STRANGENESS PRODUCTION IN MINIMUM BIAS AND JET DATA
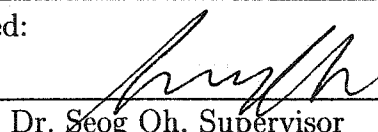
by

Justin Lancaster

Department of Physics
Duke University

Date:_____08/04/2003_____

Approved:

_____
Dr. Seog Oh, Supervisor

_____
Dr. Alfred T. Goshaw

_____
Dr. Vladimir Litvinenko

_____
Dr. Ronen M. Plesser

_____
Dr. Werner Tornow

Dissertation submitted in partial fulfillment of the
requirements for the degree of Doctor of Philosophy
in the Department of Physics
in the Graduate School of
Duke University

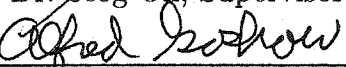2003

ABSTRACT

(Physics)

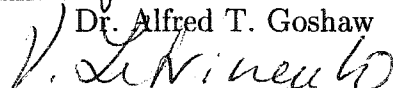# STRANGENESS PRODUCTION IN MINIMUM BIAS AND JET DATA
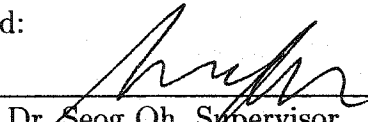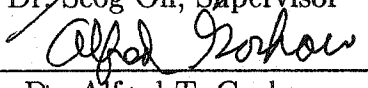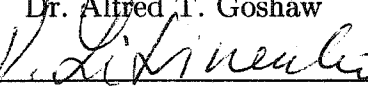
by

Justin Lancaster
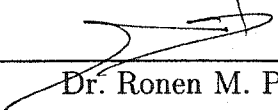
Department of Physics
Duke University

Date:_____08/04/2003_____

Approved:

_____
Dr. Seog Oh, Supervisor

_____
Dr. Alfred T. Goshaw

_____
Dr. Vladimir Litvinenko

_____
Dr. Ronen M. Plesser

_____
Dr. Werner Tornow

An abstract of a dissertation submitted in partial fulfillment of
the requirements for the degree of Doctor of Philosophy
in the Department of Physics
in the Graduate School of
Duke University

2003

Abstract

For the first time, the K_S production inside jets originating from 1.8 TeV Teva-tron proton-antiproton collisions is researched utilizing the CDF data at Fermilab. Prior to the study of K_S production inside jets, the K_S production in the Minimum Bias events is examined. The properties of K_S production, such as the values of $<p_T>$, $\frac{dN_{KS}}{d\eta}$, lifetime, and invariant cross-section, are found to be consistent with other Minimum Bias publications. After this, the number of K_S and tracks inside 0.7 jet cones are computed along with the trigger, background, and efficiency corrections for both the data and the HERWIG+QFL (event generator+detector simulator) Monte Carlo. Furthermore, the fragmentation functions are contrasted with those from the e^+e^- machines.

In the data, the number of K_S per jet increases and then reaches a plateau as a function of the jet E_T. In particular, the number of K_S per jet within $1.5 < p_T < 10.0$ GeV is determined to be 0.156+/-0.007, 0.206+/-0.011, and 0.199+/-0.011 for the 20-50 GeV, 50-100 GeV, and 100-150 GeV jets. Conversely, the number of tracks per jet in the data strictly grows with the jet E_T, and its values within $1.5 < p_T < 10.0$ GeV are 2.816+/-0.008, 5.107+/-0.009, and 5.972+/-0.008 for the 20-50 GeV, 50-100 GeV, and 100-150 GeV cases.

These data results are then compared with those from the HERWIG+QFL Monte Carlo. The Herwig+QFL Monte Carlo results are in agreement to within 10% as to the number of tracks per jet. Moreover, the number of K_S per jet, the data and the Monte Carlo agree to within 5% for the 20-50 GeV case. However, the HERWIG+QFL Monte Carlo K_S per jet values are increasingly above those of the data for K_S inside the 50-100 GeV jets (around 20% too high) and 100-150 GeV

iv

jets (approximately 35% to high). We conclude that the HERWIG generates far too many K_S inside jets at these higher energy jets. Finally, the fragmentation function is contrasted with equivalently computed quantities from e^+e^- machines, and the results from the Tevatron are below those from e^+e^- machines for all measured jet E_T ranges.

Acknowledgments

This analysis did not produce itself, nor did I, in a vacuum. It is the direct result of thousands of individuals, only a fraction of which I have had the pleasure of meeting. It is also the product of many who through their support, without knowing a quark from a toaster oven, made it possible.

For those who built the accelerator, constructed the detector, gathered the data, wrote the software, developed the field of high energy and physics (especially Galileo), I thank you.

For those always friendly and ever tolerant computer people, who saved at least a computer or two from being tossed out the window, I thank you.

For those graduate students who took time to explain a quark from a toaster oven, or simply that a toaster oven may be hot, I thank you.

For all my mentors at every level, especially my 6th grade teacher, I thank you. For those Duke professors (past and present, in and out of high energy) as well as many other professors digging their cars out of the snow at Fermilab, I thank you. For my committee, who had to read my thesis for a couple of weeks, I thank you. For my advisor, who was not only stuck with me for many years, but had to read my thesis countless times (and this thesis loses its magic after about the 100th read), I thank you.

As for my family and my friends, thank you for your love and support which made this not only possible, but likely. Many thanks.

For the person who is taking his or her time to read this thesis, I thank you.

vi

Contents

ix

List of Figures

xiii

xv

List of Tables

xviii

Chapter 1

Introduction

"The finder of a new particle used to rewarded by a Nobel Prize, but such a discovery now ought to be punished by a \$10,000 fine," said Nobel Prize winner Willis Lamb in his 1955 acceptance speech. Lamb is referring the discovery of a new class of unexpected and unpredicted "strange" particles that appeared to drop from the heavens (in this case, they actually did in the form of the earliest and still the highest energy accelerators, cosmic rays). It sent shockwaves throughout the particle physics community. "Strange" particles are produced only in pairs very quickly ($\sim 10^{-23}$ sec) and decay by themselves slowly ($\sim 10^{-10}$ sec). Rochester and Butler [1] first discovered the $K_S \to \pi^+\pi^-$ in 1947, Powell [2] found the $K_+ \to \pi^+\pi^+\pi^-$ in 1949, and Anderson discovered $\Lambda^0 \to \pi^- p^+$ in 1950, and η, ϕ, Ω, Σ, Ξ, and many other "strange" particles have been shown to exist. Today, my analysis (along with other analyses) depends on K_S as the starting point because they are produced so abundantly. In fact, my study looks at the production of K_S in objects called jets created from fragmenting quarks and gluons. Yet, at one time, as recently as 60 years ago, no one could conceive of such an analysis nor the tool necessary for its realization [3].

We will begin a very brief introduction to a field, fundamental in nature, grand in scale, precisely explaining so much and with many questions unanswered. A

discussion of the constituents of matter and how they are related to the 4 forces, the running coupling constant, parton distribution functions, and fragmentation will all be put forth in this chapter.

1.1 Quarks and Leptons

There are 3 generations of fractionally charged fermions called quarks (up,down), (strange,charm), (bottom,top), and 3 generations of charged and neutral fermions called leptons (e,ν_e), (μ,ν_μ), and (τ,ν_τ) [4]. The τ and μ particles are similar to electrons, except more massive. On the other hand, the neutrinos are extremely light neutral particles with masses of at most 20 MeV. The neutrinos regularly travel through earth without interacting with a single particle.

Through mediators, quarks and leptons interact via gravitational, electromagnetic, strong, or weak forces. Leptons do not interact through the strong force and conserve a quantity called lepton number in all interactions they participate in with the exception of "neutrino oscillation" experiments where neutrinos are believed to change flavor.

Quarks are unable to exist alone in nature. In fact, quarks and antiquarks can only exist as either quark-antiquark pairs, referred to as mesons, or 3 quark (antiquark) combinations called baryons (antibaryons). Consequently, the resulting charge is an integer. K_S and ϕ are examples of mesons, and Λ^0 and $\bar{\Lambda}^0$ are examples of baryons. Quarks also conserve a different set of quantum numbers called "truth", "beauty", "charm", and "strangeness" in all but weak interactions [3] [5] [6] [7] [8].

Table 1.1: The summary of the properties of the leptons: S(spin), L_e(lepton electron number), L_μ(lepton muon number), L_τ(lepton tau number), Q(electric charge)[1.6×10^{-19} C], m_0(mass), AP(anti-particle) [8]

		Spin	L_e	L_μ	L_τ	$Q[e]$	$m_0[MeV]$ [9]	AP
1st generation	e^-	1/2	1	0	0	-1	0.510998902±0.000000021	e^+
	ν_e	1/2	1	0	0	0	< 15x10^{-6}	$\bar\nu_e$
2nd generation	μ^-	1/2	0	1	0	-1	105.658357±0.000005	μ^+
	ν_μ	1/2	0	1	0	0	< 0.17	$\bar\nu_\mu$
3rd generation	τ^-	1/2	0	0	1	-1	1777.03±0.3	τ^+
	ν_τ	1/2	0	0	1	0	< 18.2	$\bar\nu_\tau$

Table 1.2: The summary of the properties of the quarks: S(spin), B(baryon number), I(strong isospin), s(strangeness), c(charm), b(beauty), t(truth), Q(electric charge)[1.6×10^{-19} C], m_0(mass), AP(anti-particle). The particle properties in the Standard Model for the electroweak interaction. The quantum numbers of weak isospin T, and its projection, T_3, weak hypercharge, Y, and the electric charge, Q, are given ($Q = T_3 + \frac{1}{2}Y$). The right-handed fermions (labeled by the index R) are weak-isospin singlets (T=0), while the left-handed fermions (labeled L) are weak-isospin doublets (T=1/2). Massless neutrinos appear only as left-handed particles and right-handed antiparticles. The Z^0 and the photon have the same quantum numbers ($T_3 = Y = Q = 0$) and can therefore mix. The gluons have $T = Q = Y = 0$ and therefore do not interact in the electroweak interactions [8] [10].

		Spin	B	I	s	c	b	t	$Q[e]$	$m_0[MeV]$ [9]	AP
1st generation	u	1/2	1/3	1/2	0	0	0	0	+2/3	1.5–5	$\bar u$
	d	1/2	1/3	1/2	0	0	0	0	-1/3	3–9	$\bar d$
2nd generation	c	1/2	1/3	0	0	1	0	0	+2/3	1.1x10^3–1.4x10^3	$\bar c$
	s	1/2	1/3	0	-1	0	0	0	-1/3	60–170	$\bar s$
3rd generation	t	1/2	1/3	0	0	0	0	1	+2/3	173.8x10^3±5.2x10^3	$\bar t$
	b	1/2	1/3	0	0	0	-1	0	-1/3	4.1x10^3–4.4x10^3	$\bar b$

1.2 The fundamental interactions

There are 4 fundamental interactions in nature: gravity, electromagnetic, strong, and weak. Each forces incorporates a mediator that governs how quarks and leptons

Table 1.3: Summary of the conserved quantities in the strong, electromagnetic and weak interactions [8] [9]

Conserved Quantity	Strong	Electromagnetic	Weak
I(Isospin)	Yes	No	No (ΔI=1 or 1/2)
S(strangeness)	Yes	Yes	No(ΔS=1,0)
C(charm)	Yes	Yes	No(ΔC=1,0)
P(parity)	Yes	Yes	No
C(charge–conjugation parity)	Yes	Yes	No
CP(or T)	Yes	Yes	Yes (except K^0 and B^0)
CPT	Yes	Yes	Yes

interact. The mediators for the electromagnetic, strong, and weak forces are the photon, gluon, and W/Z Bosons, respectively. Gravity has yet to be incorporated in this fundamental framework because it so much weaker than the other forces. The mediator of the gravitational force, the "graviton" has not been discovered either directly or indirectly [3] [5] [6] [7] [8].

Table 1.4: Force Carriers: S(spin), Q(electric charge), m_0(mass) [8]

	Spin	$Q[e]$	$m_0[MeV]$ [9]
γ	1	0	$< 2 \times 10^{-22}$
g	1	0	0 (assumed)
$W^\pm$	1	± 1	80419 ± 56
Z	1	0	91182 ± 2.2

1.2.1 Electromagnetism

Classical electromagnetism is connected to quantum field theory to yield what is considered the most successful and precise theory of all time: Quantum Electro-dynamics (QED). QED has the charged particles interacting through means of ex-
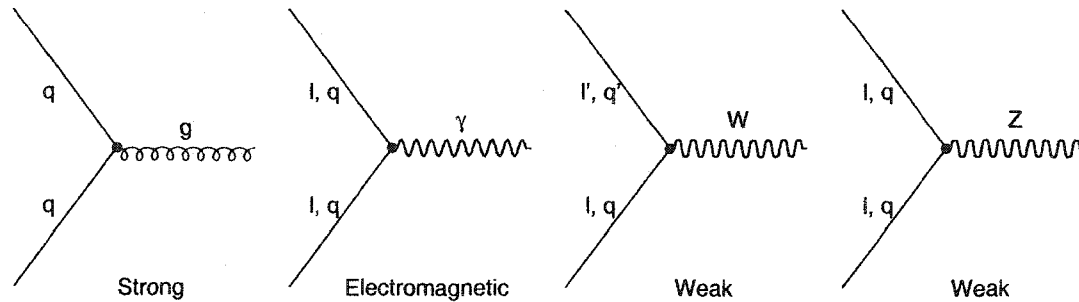
Figure 1.1: The electromagnetic, strong, and weak interaction vertices [5]

changing a field quanta called photons such that charge is conserved. So accurate is QED that the magnetic momentum of an electron is calculated to at least 10 decimal places. In addition, branching ratios and cross-sections are able to be extracted with the aid of Feynman diagrams. Feynman diagrams and charge screening will be briefly touched upon.

Feynman diagrams correlate pictures of lines and vertices to mathematical terms necessary for QED calculations. For every calculation, there are an infinite number of loops, lines, and vertices; however, QED is perturbative so the results converge because higher order terms get smaller and smaller. This is case because every vertex is associated with a factor of the electromagnetic coupling factor, $\sqrt{4\pi\alpha}$, between photons and charged particles. In particular, α is proportional to the square of the electron charge, and α is equal to the fine structure constant, $\alpha \approx \frac{1}{137}$ at low Q^2. So for a given cross-section calculation, each successive term with higher orders of α, is less significant than the preceding one.

Aside from setting the method of mathematical formulation, QED also predicts the spontaneous production of virtual e^+e^- pairs that leads to charge screening. By incorporating the uncertainty principle, conservation of energy is violated for a

brief time, $\Delta E \Delta t \sim \hbar$ where ΔE is the unconserved energy used to produce $e^+ e^-$ virtual pairs. Hence, an electron can surround itself by a cloud of virtual $e^+ e^-$ pairs by emitting virtual photons that emit virtual $e^+ e^-$ pairs with the positrons through electromagnetic interactions tending to be closer to the "bare" electron. One consequence is a smaller measured charge of an electron because of the charge screening of the cloud, and the effective charge of an electron increases as one moves through the cloud. The reduction of the effective charge due to charge screening tends to reduce the electromagnetic coupling factor. The fine structure constant is defined as the measurement of the electromagnetic coupling factor at infinity, and the electromagnetic coupling factor α asymptotically increases with energy as less charge is screened. Higher energy interactions have stronger electromagnetic coupling factors in Feynman diagrams [3] [5] [6] [7] [8].

1.2.2 Strong Interaction

The strong force is responsible for combining quarks into hadrons as well as binding neutrons and protons. The strong force behaves very similarly to QED in the manner that a charge is conserved and there is a quantized mediator present in every strong interaction, and a theory called Quantum Chromodynamics explains these types of interactions as well as empirical facts that Quantum Electrodynamics is unable to do. The questions as to why there are not any free stable quarks in nature, to why quarks combine only certain combinations of anti-quark quark pairs or in triplets of integer charge, to why the Pauli Principle appears to be violated in case of Δ^{++}, and to why the quark production rate is 3 times that of muon production rate in electron annihilation processes are all adequately addressed with Quantum Chromodynamics.
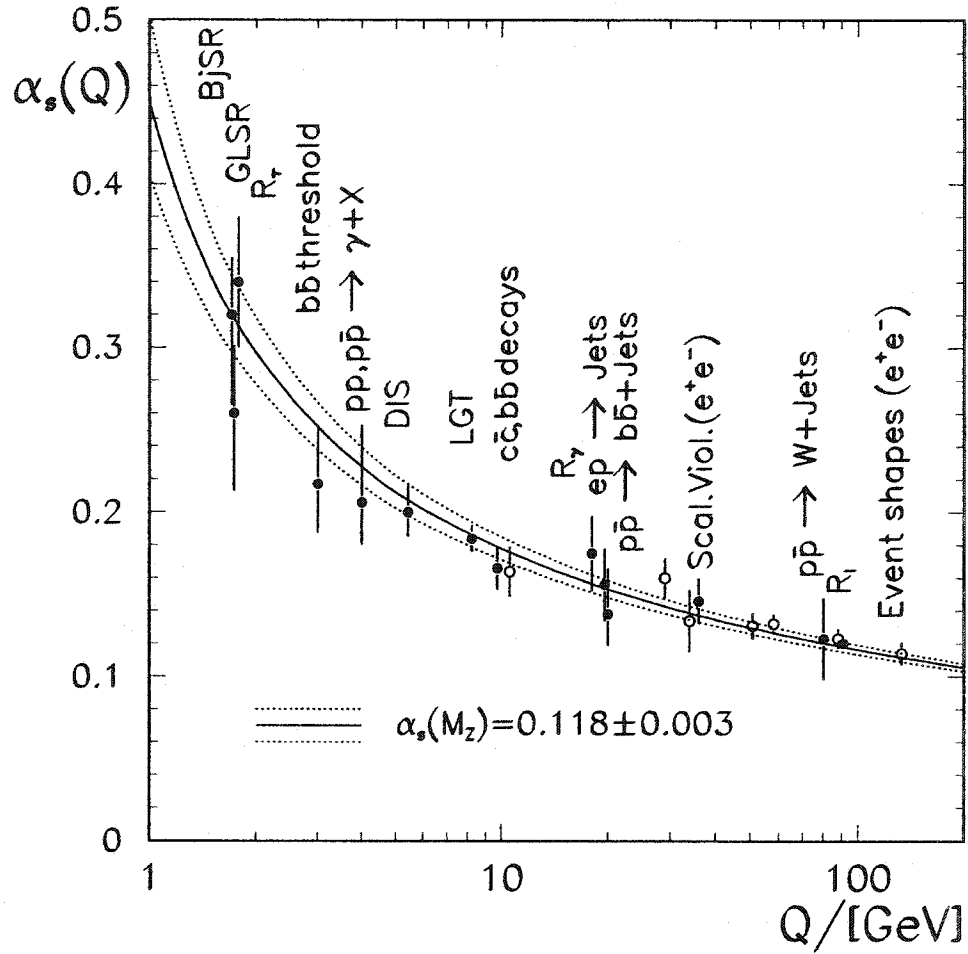
Figure 1.2: The running coupling constant α_s [11].

The nature of the strong force is complex, and it is given by equation 1.1 [12],

$$V(r) = -\frac{4}{3}\frac{\alpha_s}{r} + kr \qquad (1.1)$$

where α_s is the running coupling constant, r is the distance between quarks, k is constant approximately equal to 1.0 $GeV fm^{-1}$, and $V(r)$ is the potential between the two quarks. There are essential two separate components: the first term dominates at small interactions distances (or high momentum transfer scales) and the

second term dominates at large interactions distances (or low momentum transfer scales). The short-range term is similar in form to the electromagnetic point potential except that the α_s term is not constant, hence the term "running", but is a function of momentum transfer. The lowest order term of the α_s is given by the equation 1.2 (shown in Figure 1.2), where Q^2 is the square of the four-momentum transfer, n_f is the number of quarks allowed by energy of the interaction, and Λ_{QCD} is the approximately 200 MeV [13] (approximately the energy boundary between free quarks and hadrons) [12]:

$$\alpha_s(|Q^2|) = \frac{12\pi}{(33 - 2n_f)ln(|Q^2|/\Lambda_{QCD}^2)} \ . \tag{1.2}$$

The interpretation of these equations will now be highlighted. At large momentum transfer scales (short distances), the first term dominates. α_s decreases with energy to about 0.1, $Q^2 \gg \Lambda_{QCD}^2$, such that perturbative QCD can be applied and quarks and gluons interact with a small force. As the momentum transfer scale increases, observed charge decreases to that of just the bare value. This reduction of the strong force is known as "asymptotic freedom", and such hard scattering processes describe such high energy transfer events where higher order α_s terms have smaller and smaller effects.

At large distances dominated by the linear term of the strong force, the potential is much stronger, to the point that free quarks are more energetically likely to create quark-antiquark pairs to reduce the separation of the charges and these quarks combine to form numerous hadronic bound states. As a result, isolated quarks have not been observed in nature. This point is one of the most interesting aspects in my opinion about particle physics that the quark, a fundamental quantity of matter, have never been discovered in isolation.

The experimental evidence of the existence of color includes the existence of the Δ^{++} (uuu) particle in its lowest orbital momentum state (l=0) with its spins aligned (J=S=3/2). This state has a symmetric wavefunction (without a color wavefunction) which violates the Pauli Exclusion Principle. However, with the introduction of color wavefunction in addition to the spatial and spin wavefunctions, the overall state is still anti-symmetric, honoring the Pauli Exclusion Principle.

Furthermore, only colorless bound states of quark-antiquark pairs (mesons) and three quark combinations (baryons) have been found experimentally. Although theoretically possible for there to be other combinations of quarks (i.e. pentaquarks), none have been discovered. Moreover, the final bound states have integer charges. In addition, the octet of color-carrying gluon mediators can couple together (photons do not have this property in QED) which gives rise to the linear term of the strong interaction potential. All of these effects have been observed.

Another strong piece of evidence of color is the ratio of quark-antiquark production and muon pair production rates from electron-positron experiments. This ratio is equal to the product of the number of colors and the sum of the square of the quark charges. Since the number of flavors available is contingent on the center of mass energy of the experiment, only the quark charges kinematically allowed at the center-of-mass energy are included. The best agreement with the data occurs when the number of colors is equal to three (i.e. non-zero).

At last, for low momentum transfer interactions where perturbative QCD breaks down, individual quarks and gluons are transformed into hadrons during fragmentation processes. These clusters of bound hadrons should conserve the momenta and energy of the initial parton. Furthermore, so-called fragmentation is completely are believed to depend only upon the energy and type of the outgoing parton rather

than the particular process which generated them. Various fragmentation models are used to describe these soft QCD processes. Experimentally, 2 jet processes correspond to 2 clusters of hadrons from 2 quarks. At higher energies, there exists 3 jet processes of which 2 are jets are due to quarks and the third jet is due to a gluon. These 3 jet events, where one jet is a gluon jet, is testimony to the existence of gluons as mediators [3] [5] [6] [7] [8].

1.2.3 Weak Interaction

Electroweak interaction unifies both the weak and the electromagnetic interactions into a single theory [14]. The weak force differs from the electromagnetic force in many respects, and the weak force is necessary to explain β decay (protons turn into neutrons and visa versa) along with other processes that allow particles of one type to be transformed into another. The experimental evidence is overwhelming, including confirming the existence of 3 massive bosonic mediators in 1983 at CERN SPS with $p\bar{p}$ collisions. Other predictions such as the infamous Higgs particle, responsible for giving mass to the bosonic mediators (as well as other particles), remain to be confirmed.

Unlike QED, the mediators which interact weakly with particles have mass. The mediators include W^+, W^-, and Z^0 particles where the mass of the W boson is measured to be 81 ± 5 GeV/c^2 [15] and 80^{+10}_{-6} GeV/c^2 [16] by UA1 and UA2 (CERN experiments), respectively. The mass of the Z boson is measured to be 95.2 ± 2.5 GeV/c^2 [17] and $91.9 \pm 1.3 \pm 1.4$ GeV/c^2 [18] by UA1 and UA2, respectively. The current accepted mass measurements are shown in Table 1.4. These massive mediators give rise to weak force interactions which have a range of around $\sim 10^{-3}$ fm.

The weak force also couples to particles differently. Parity-violating and charge-conjugation violating processes are permitted in weak interactions. Also, the weak force also conserves quantities called weak isospin and weak hypercharge ($Q = T_3 + \frac{Y}{2}$ where Y is the hypercharge and T_3 is the 3rd component of the weak isospin) that distinguish between right-handed and left-handed fermions.

$W^{\pm}$ bosons not only change the charge of fermions by ± 1 but also the flavor of the fermions. These processes are called "flavor-changing charged currents". As a result, the weak force allows members of similar or different generations to interact leptonically ($\mu^- \to e^- + \bar{\nu}_e + + \nu_\mu$), hadronically ($\Lambda^0 \to \pi^- + p$), or semi-leptonically ($n \to p + e^- + \bar{\nu}_e$).

On the other hand, neutral Z bosons in "neutral current" processes may change the flavor but not the charge of the interacting particles. Furthermore, particles of similar or different generations may interact. The process $\nu_e + e^- \to \nu_e + e^-$ is an example of similar generations interacting weakly, and the process $e^+ + e^- \to q + \bar{q}$ is an example of different generations interacting weakly. Notice that through W and Z bosons (unlike photon mediators of the electromagnetic force), neutrinos also interact [3] [5] [6] [7] [8].

The weak force coupling constant (g) is proportional to the electromagnetic coupling constant (g') by the weak mixing angle (Weinberg angle θ_W) in equation 1.3, and the Weinberg angle is related to the masses of the W and Z bosons according the relation given by equation 1.4.

$$tan\theta_W = \frac{g'}{g} \tag{1.3}$$

$$cos\theta_W = \frac{M_W}{M_Z} \tag{1.4}$$

Table 1.5: The summary of the quantum numbers for the particles [8] [10]

Quarks	T	T_3	Q	Y
u_L, c_L, t_L	1/2	+1/2	+2/3	+1/3
d_L, s_L, b_L	1/2	-1/2	-1/3	+1/3
u_R, c_R, t_R	0	0	+2/3	+4/3
d_R, s_R, b_R	0	0	-1/3	-2/3
$\bar{u}_R, \bar{c}_R, \bar{t}_R$	1/2	-1/2	-2/3	-1/3
$\bar{d}_R, \bar{s}_R, \bar{b}_R$	1/2	+1/2	+1/3	-1/3
$\bar{u}_R, \bar{c}_R, \bar{t}_R$	0	0	-2/3	-4/3
$\bar{d}_R, \bar{s}_R, \bar{b}_R$	0	0	+1/3	+2/3
Leptons	T	T_3	Q	Y
ν_e, ν_μ, ν_τ	1/2	+1/2	0	-1
e_L^-, μ_L^-, τ_L^-	1/2	-1/2	-1	-1
e_R^-, μ_R^-, τ_R^-	0	0	-1	-2
$\bar{\nu}_e, \bar{\nu}_\mu, \bar{\nu}_\tau$	1/2	-1/2	0	+1
e_R^+, μ_R^+, τ_R^+	1/2	+1/2	+1	+1
e_L^+, μ_L^+, τ_L^+	0	0	+1	+2
Charged	EWK	Gauge	Bosons	
W^+	1	+1	+1	0
W^-	1	-1	-1	0
Neutral	EWK	Gauge	Bosons	
Z^0	1	0	0	0
γ	0	0	0	0

The experimental value of $sin^2\theta_W = 0.2230 \pm 0.0004$ [19] [3] [5] [6] [7] [8].

1.3 Structure Function

The current experimental evidence currently suggests that leptons are point particles. On the other hand, the proton has been shown to have a substructure from mainly lepton-hadron experiments. For example, an electron (a leptonic point particle) is used to probe the substructure of a proton. The greater the momentum

transfer of the probe and the target, denoted by Q, the more substructure of the proton can be observed. At momenta on the order of 1.0 GeV, protons appear to behave just like point particles. However, at tens of GeV, protons look to be made up of valence quarks that determine the quantum numbers of a proton. At even higher momenta, protons contain gluons from gluon emission as well as quark-antiquark pairs from gluon splitting called "sea" quarks. In the end, all "valence" quarks, "sea" quarks, and gluons must conserve the quantum numbers when averaged over all momentum space. In fact, 55% of a protons momenta is carried by gluons and not by valence quarks. Aside from a fraction of the momentum of a proton being carried by quarks and gluons, the momentum transfer Q^2 of the two interaction partons also influences the amount of momentum that takes place in a given hard scattering process because as the Q^2 increases, more of the proton is seen by the probe. Both effects are combined to yield parton distribution functions which are indispensable in calculating hard-scattering cross-sections.
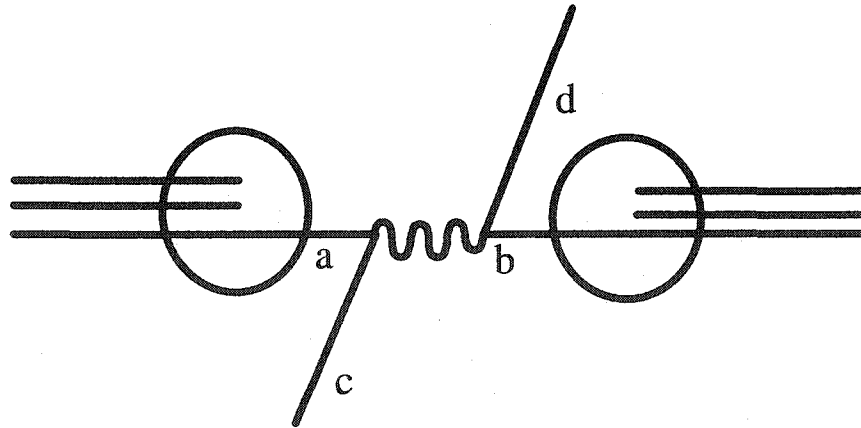
Figure 1.3: A hard scattering diagram. a and b are the incoming partons, and c and d are the outgoing partons. Other partons in the baryon (proton,antiproton) do not take part. The momentum transfer as well as the fraction of momentum of initial baryon that partons a and b have of the incoming proton and antiproton are used to determine the parton distribution function.
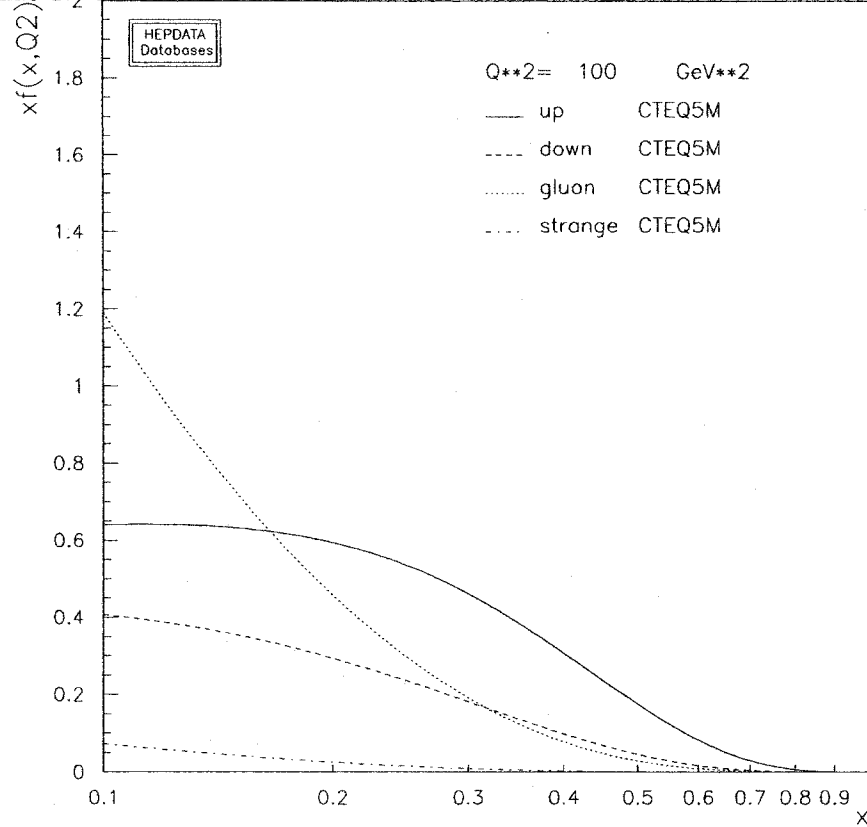
Figure 1.4: The structure functions, which are given as the product of momentum fraction and the parton distribution function, that can be used to calculate the probability of finding a quark or gluon with a momentum fraction $x > 0.1$. Notice how gluons dominate at small x [8].

Parton distribution functions are probability functions that quantify the amount of momentum a given parton of a proton carries, and parton distribution functions are important is the calculation of hard scattering $p\bar{p}$ cross-sections. If there are two interacting partons a,b each carrying x_a,x_b of the initial proton momentum, and the probability that a parton a,b has fraction x_a,x_b of the initial momentum of the proton and antiproton is given by [8]

$$f_{a/p}(x_b, Q^2), f_{b,\bar{p}}(x_b, Q^2). \tag{1.5}$$

(a)   **(b)**
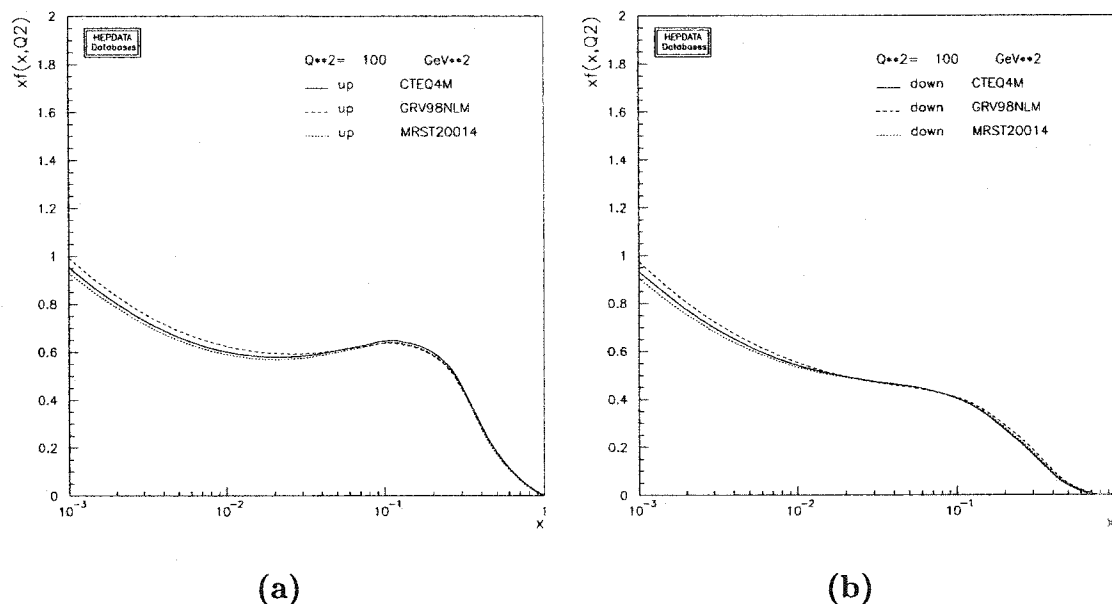
Figure 1.5: The momentum distributions for the u quark (left) and the d quark (right) as predicted by a few global PDF models (CTEQ, MRS and GRV). At very low momentum fraction, these models diverge; however, all agree for $x > 0.1$ [8].

In particular, the differential cross-section is calculated by multiplying the perturbative QCD cross-section, $\hat{\sigma}(ab \rightarrow cd)$, with both of these parton distribution functions $(f_{a/p}(x_a, Q^2), f_{b/\bar{p}}(x_b, Q^2))$ where Q^2 is the momentum transfer and x_a, x_b is the fraction of the proton momentum carried by the given parton a,b [8] [20]:

$$d^2\sigma(ab \rightarrow cd) = \hat{\sigma}(ab \rightarrow cd)f_{a/p}(x_a, Q^2)f_{b/\bar{p}}(x_b, Q^2)dx_a dx_b \ . \qquad (1.6)$$

The parton distribution also should be consistent with the quantum numbers of the proton in the form of sum rules. For example, all quark-antiquark differences when averaged over all momentum fraction space must be equal to zero with the exception of (u and $\bar{u}$) and (d and $\bar{d}$) quarks that equal 2 and 1, respectively, because a proton has two valence up quarks and one valence down quark and all other sea

quarks must average to 0. The sum rules are given by [8] :

$$\int_0^1 (f_{u/p}(x, Q^2) - f_{\bar{u}/p}(x, Q^2))dx = 2 , \qquad (1.7)$$

$$\int_0^1 (f_{d/p}(x, Q^2) - f_{\bar{d}/p}(x, Q^2))dx = 1 , \qquad (1.8)$$

$$\int_0^1 (f_{c,s,b,u,d,t/p}(x, Q^2) - f_{\bar{c},\bar{s},\bar{b},\bar{u},\bar{d},\bar{t}/p}(x, Q^2))dx = 0 . \qquad (1.9)$$

In addition, the sum of all the individuals momentum of the partons must equal to momentum of the proton, and is given by [8],

$$\sum_a \int_0^1 dx x f_{a/p}(x, Q^2) = 1 \qquad (1.10)$$

where $a = g,u,d,s,c,b,t,\bar{u},\bar{u},\bar{d},\bar{s},\bar{c},\bar{b},\bar{t}$.

The data from a multitude of experiments, each covering various regions of x and Q^2, is studied by various theoretical groups in order to model global PDF that are valid for most x and Q^2. In figures 1.4 and 1.5, different models appear to converge at high momentum fraction values where the sea quark contributions are small [3] [5] [6] [7] [8].

1.4 Fragmentation

The mechanism of producing hadrons from quarks and gluons is one of the least understood phenomenon in high energy physics. After a $p\bar{p}$ interaction, outgoing high p_T quarks and gluons cannot exist by themselves in isolation and must combine with other partons in order to form mesons and baryons. It is the consensus that fragmentation is independent upon the exact process (e^+e^- collisions, $p\bar{p}$ collisions);

instead, fragmentation depends only on the energy and type of the outgoing partons. The above assumption excludes possible color transfer issues which are dealt with in some models but may not be addressed in others. As of the effects of the type of outgoing partons, the gluons do fragment differently than the quarks. However, being difficult to distinguish between quark and gluon fragmentation, and in addition, not being the focus of this study, it will not be discussed further. So, the fragmentation theories derived from e^+e^- machines will also be assumed to be valid for $p\bar{p}$ interactions. In e^+e^- annihilation at center of mass energies $\sqrt{s}$, a hadron h along with other particles X are produced via intermediate vector bosons $V=\gamma/Z^0$ in the following process $e^+e^- \to V \to hX$. Note that the process $p\bar{p}rp \to V \to hX'$ predictions is based mostly upon the data from the $e^+e^- \to V \to hX$ process.
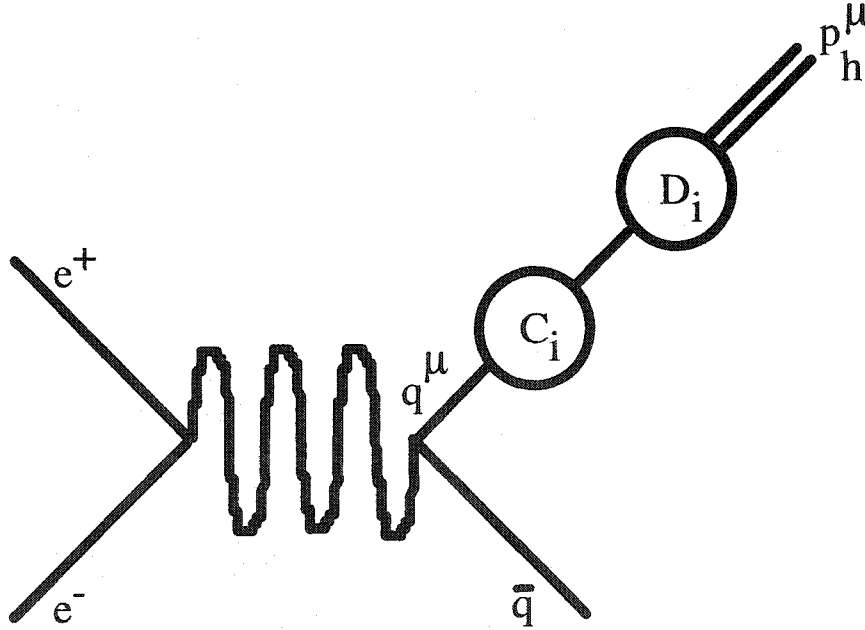
Figure 1.6: A diagram for the fragmentation for the process $e^+e^- \to hX$ [21]

The inclusive single-particle distribution of a hadron is described with a dimensionless quantity called the total fragmentation function for a hadron h, $F^h(x, s)$,

in equation 1.11 [22]:

$$F^h(x,s) = \frac{1}{\sigma_{total}} \frac{d\sigma}{dx} (e^+e^- \to V \to hX) \qquad (1.11)$$

where s = square of center of mass energy of collision and $x = \frac{2E_h}{E_{cm}}$. For a given hadron, the multiplicity of a hadron, $<n_h(s)>$, is given by integration of fragmentation function over x, shown in equation 1.12 [22]:

$$< n_h(s) >= \int_0^1 dx F^h(x,s). \qquad (1.12)$$

In particular, fragmentation functions are defined by equation 1.13 [22]:

$$F^h(x,s) = \sum_i \int_x^1 \frac{dz}{z} C_i(s;z,\alpha_s) D_i^h(\frac{x}{z},s) \qquad (1.13)$$

where the parton types are denoted by $i = u, \bar{u}, d, \bar{d},...$, and g, C_i are coefficients for a process, D_i^h is the universal fragmentation function, z is the fraction of momentum of parton i ($x < fracxz < 1$), and s and x are defined as before. This is shown in Figure 1.6. The fragmentation simplifies dramatically if only lower order α_S terms are incorporated, with gluon emission being absent. With this approximation, $C_g=0$ for gluons and $C_i = g_i(s)$ δ(1-z) for the rest of the quarks and antiquarks where $g_i(s)$ is proportional to the square of the charge of the parton i where $i = u, \bar{u}, d,$ $\bar{d},...$, and g. These approximations are not valid at Tevatron energies, and higher orders of α_S as well as gluon terms need to incorporated, and this will be elaborated later.

With the simplest approximations, a fragmentation function computed at a center of mass energy $\sqrt{s}$ is valid at all $\sqrt{s}$. However, QCD corrections introduce terms

that give rise to so-called "scaling violations" in which fragmentation functions do indeed have an $\sqrt{s}$ dependence. These scaling violations may be predicted using the DGLAP (Dokshitzer-Gribov-Lipatov-Altarelli-Parisi) evolution equation given by equation 1.14 [22] [23]:

$$t\frac{\partial}{\partial t}D_i(x,t) = \sum_j \int_x^1 \frac{dz}{z}\frac{\alpha_S}{2\pi}P_{ji}(z,\alpha_S)D_j(\frac{x}{z},t). \qquad (1.14)$$

where D_j is the fragmentation and P_{ji} are splitting functions given by perturbative expansions shown in equation 1.15 [22]:

$$P_{ji}(z,\alpha_S) = P_{ji}^{(0)}(z) + \frac{\alpha_S}{2\pi}P_{ji}^{(1)}(z) + \dots. \qquad (1.15)$$

The splitting function, P_{ji}, is defined as the probability of getting parton j from parton i when parton j has a fraction z of the momentum of parton i. These equations work for all partons where $i = u, \overline{u}, d, \overline{d},...$, and g, and j is summed over $u, \overline{u}, d, \overline{d},...$, and g. Once fragmentation functions are determined experimentally at center of mass energy $\sqrt{s}$, the fragmentation functions may be computed at another center of mass energy $\sqrt{t}$. As for the effect of the scaling violation, the x distribution is moved towards lower values as the scale increases.

Fragmentation functions are similar to structure functions. Structure functions represent the probability distribution of a parton in a hadron carrying a certain fraction of the momenta of the hadron. Likewise, fragmentation functions are the probability distributions that show the odds that a parton with a given momentum will make up a hadron with another given total momentum. Both fragmentation and structure functions are incalculable using perturbation theory. Furthermore, the simplest model would result in scale-independent x distributions with scaling

violations being derived once the QCD corrections are included. Moreover, distributions determined at a particular center of mass energy $\sqrt{s}$ may be determined for $\sqrt{t}$ using evolution equations.

At low Q^2, perturbation theory breaks down, and the running coupling constant grows. It turns out that terms which contribute to the fragmentation function that do not have log can be ignored [24]. Furthermore, for gluons, only terms on the order of $\alpha_S ln^2 Q^2$ (note: Q^2 is actually divided by a constant to make argument in the logarithm dimensionless, and this constant depends upon the details of the calculation) and above may be kept (Double Logarithmic Approximation [25]). Significant simplification of higher orders may be made by applying angular ordering. Angular ordering shows that gluons emitted successively from a parent parton are approximately equivalent to a single diagram with angular ordered emissions. In other words, partons are do not radiate at angles at greater angles than those of the prior emission. Thus, emission terms that are collinear may be summed, and the resulting calculation includes less terms than one which does not use this approximation. The Double Logarithmic Approximation with angular ordering plus some additional single log contributions comprise the Modified Leading Log Approximation (MLLA) [26] [27]. The MLLA is implemented in many Monte Carlo programs and agree quite well with the data. The DGLAP equation with the MLLA are denoted by equation 1.16 [21]:

$$t\frac{\partial}{\partial t}D_i(x,t) = \sum_j \int_x^1 \frac{dz}{z}\frac{\alpha_S}{2\pi}P_{ji}(z,\alpha_S)D_j(\frac{x}{z},z^2 t) \qquad (1.16)$$

[21] [22] [28].

1.5 Hadronization Models

Fragmentation does not speculate as to the underlying mechanism of how partons combine into hadrons; it only derives the inclusive hadron spectra and how these spectra scale with center of mass energy. Only non-perturbative and phenomenological hadronization models attempt to explain how partons merge into hadrons. Although there at least a couple major of hadronization models, when combined with fragmentation, reproduce the data quite well, only the cluster and string models will be described.

In Figure 1.7, a pictorial overview of the hadronization process will now be described. First, there is a hard scattering process that produces outgoing partons. The significant parameter which governs the energy and type of outgoing partons is the hard scattering scale M_{JJ} where M_{JJ} is the dijet mass. Then, an outgoing parton will shower into less energetic partons until the daughters would have transverse momenta below Q_{eff}. Parton showering is a perturbative process where the uncertainty increases as the value of Q_{eff} decreases. Below this threshold of Q_{eff}, the parton showering will cease, and groups of partons will combine into hadrons using one of the phenomenological hadronization models. There are two major ones, the string and cluster models; they will both discussed shortly. The last scale, order of $\frac{1}{m_\pi}$, is where hadronization terminates.

The value at which perturbative fragmentation ends and non-perturbative hadronization begins occurs, as stated above, at some transverse momenta scale factor called Q_{eff}. Since perturbative theories are quantitatively and qualitatively better understood, a lower value for Q_{eff} is more desirable because more of the calculation is based upon perturbation theories rather than phenomenological ones. However, if Q_{eff} is too low and is on the order of (200-400 MeV), the perturbative theory
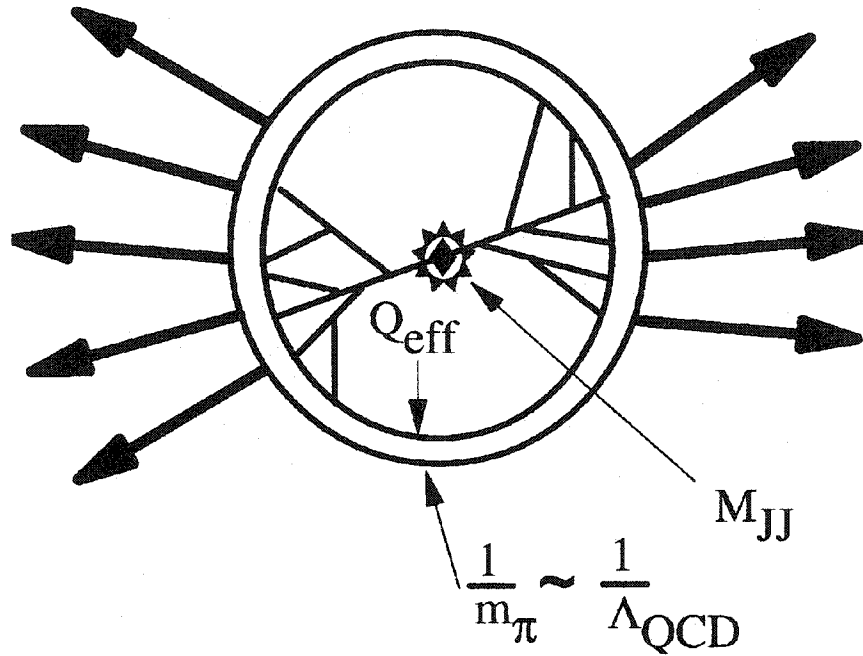
Figure 1.7: A pictorial description of jet fragmentation with the three scales M_{JJ}, Q_{eff}, and $\frac{1}{m_\pi}$. The hard-scattering scale M_{JJ} appears at the center. Q_{eff} is the scale at which the parton showering ends and the hadronization begins. The last scale, order of $\frac{1}{m_\pi}$, is where hadronization terminates [28].

begins to break down because the corrective terms become too large. One big question is how to implement the predictive parton calculations to the data through a not-well-understood non-perturbative hadronization process? Any given outgoing parton above a certain Q_{eff} will shower into other partons, then the partons at or below Q_{eff} will combine into mesons and baryons in another process called hadronization. The value Q_{eff} can only be determined experimentally. In one study, $Q_{eff} = 256 \pm 13$ MeV [28].

Hadronization models are based upon the Local Parton-Hadron Duality (LPHD) Hypothesis [29] [30]. The LPHD hypothesis assumes that hadronization occurs after parton showering. In addition, the hadrons and the partons they are derived from are closely correlated. Moreover, color effects from the two outgoing partons which

generate other hadrons are assumed to be uncorrelated. This is believed to be the case because by the time the partons fragment, they are far apart from each other. Consequently, although hadron and parton distributions differ, the inclusive average of these distributions are the same. In particular, the multiplicity and momenta distributions of hadrons and partons differ only by a normalization constant. The more particles produced (or the higher energy of the fragmenting quark or gluon), the more accurate the LPHD assumption [21] [28].
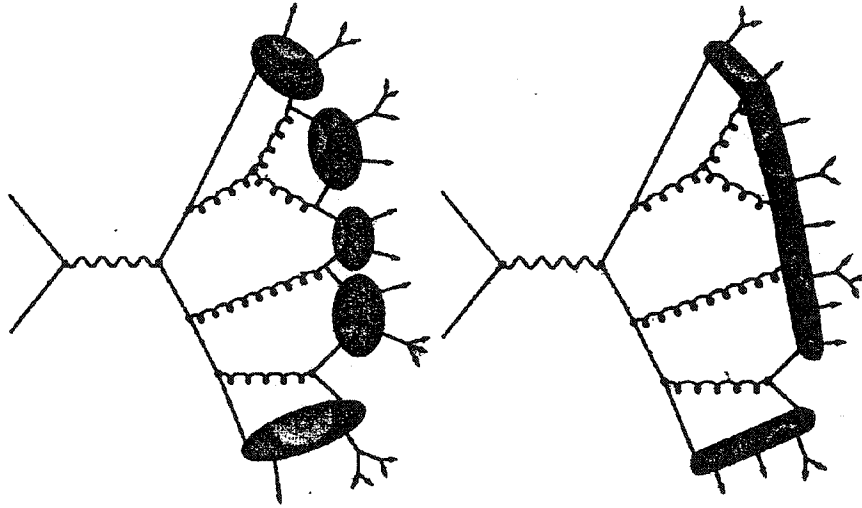
Figure 1.8: The pictorial diagrams of the cluster (left) and the string (right) hadronization models [21].

At some transverse momenta, quarks and gluons are converted to hadrons in a process called "hadronization". There are many different hadronization models that adopt the LPHD hypothesis. The cluster model will be later compared with the data in this analysis, and HERWIG (the Monte Carlo generator used in this study) adopts this hadronization model. In this method, once the parton showering process terminates, all gluons are converted into quark antiquark pairs. Each group of quarks and antiquarks in a particular region of phase space are clumped into

clusters, and depending on the mass of the cluster, can either decay directly into hadrons or divide itself into smaller clusters and decay directly into hadrons later. Unstable hadrons decay according to decay modes and branching ratios until masses of the lightest hadrons are attained. All this procedure considers allowable phase space so that the momenta and energy of all the final state hadrons is equal to the momenta and energy of the initial cluster of quarks and antiquarks. The exact ratios of lighter quarks to heavier quarks are close to that of another model, the string model (see next paragraph). The cluster model also tends not to reproduce baryon and heavy quark production well [21] [22] [28] [31] [32].

Although not compared in this analysis, the string model is another popular hadronization model worth mentioning. The many people who use the Pythia Monte Carlo generator use the string model. In this model, the color fields between partons fragments rather than the partons. In particular, as a quark-antiquark pair separates, the linear color field between them increases until there is enough energy stored up to produce two quark-antiquark pairs. The color field is represented as a string believed to have a mass density κ of approximately 1 GeV/fm. The new quark-antiquark pairs are determined via a tunneling probability function $exp(-\pi m_{q,\perp}^2/\kappa)$ where the transverse mass is given by $m_{q,\perp}^2 = m_q^2 + p_{q,\perp}^2$. It is this tunneling probability that suppresses the production of heavy quarks; u:d:s:c is generated with approximately the following ratios of $1:1:0.3:10^{-11}$. This is an iterative process that terminates once quark-antiquark pairs are no longer above the mass of hadrons. Gluon emission removes energy from the color field and appear as kinks in the string. As for baryon production, a diquark pair may also be generated via tunneling and combine with single quark to form a baryon. The string model is an improvement over the cluster model when it comes to baryon produc-

tion [21] [22] [33] [34]. Both hadronization models are shown in Figure 1.8 [21].

In the end, there are groups of particles, resulting from parton showering and hadronization process, traveling in the general direction of an initial hard-scattering parton. These particles will be considered as candidates for an entity called a "jet". Jets will be discussed at great length in Chapter 6. Of great interest in this analysis, the strangeness content contained with these jets.

1.6   Motivation of the Analysis

The motivation of this study is to test the treatment of the production of strangeness in the fragmentation and the hadronization models supported by earlier experiments. Most strangeness production theories are derived from e^+e^- machines such as LEP, and there is the question of whether these models are also valid for $p\bar{p}$ collisions of the Tevatron. In particular, there are two competing hadronization models: the cluster model and the string model. The cluster model and the string model are incorporated in HERWIG and Pythia generators, respectively. Although not discussed further, the string model is not expected to vary much from the HERWIG Monte Carlo cluster model. In order to test the cluster model, certain physics quantities will be computed in the data and contrasted with those predicted by the HERWIG Monte Carlo based upon the cluster model. In addition, other physics values will be compared directly to those from e^+e^- experiments. This is the first time anyone has studied strangeness in jets in $p\bar{p}$ collisions.

The object mostly closely tied with that of a fragmenting quark or gluon is a cluster of particles going in the same direction as the initial quark or gluon, and this quantity is called a "jet". Typically, jets consists of charged and neutral particles within a region of space and whose identification depends mostly upon

energy deposition in the calorimeter. By computing the number of particles having a strange quark inside jets, the data may be measured against those from the HERWIG Monte Carlo.

In this analysis, the production of K_S in jets will be taken as the barometer of strangeness production since K_S are abundant and contain a strange quark. Thus, the number of K_S per jet, $\frac{N_{KS}}{jet}$, will be one of the key measurements. In one mode, a K_S conveniently decays into two charged pions. Although the K_S may not be traced using the tracking chamber because it is neutral, the parent mass of K_S may be reconstructed from its two charged pions daughters. In this manner, the production of K_S may be calculated.

Also, the number of charged particles within a jet, $\frac{N_{track}}{jet}$ quantities can be compared to the cluster model. This value is a check on the overall particle generation of the cluster model. The same can be said about the momenta spectra of the K_S and tracks inside jets and their production ratio to each other, the number of K_S divided by the number of charged tracks, $\frac{N_{KS}}{N_{track}}$. It is important not only examine strangeness production but also its production relative to those of charged particles. Others have studied track production in dijets and track production of jets defined strictly with tracks, but nobody at the CDF has examined track production in jets determined via calorimetry as a stand-alone entity.

One great test of any model is its ability to accurately predict the data in regions that were previously inaccessible. With e^+e^- machines, only strangeness production in jets below 50 GeV has been published and the upper limit of jet E_T for future LEP publications may confidently be placed at 100 GeV. On the other hand, the Tevatron collisions are at much higher center of mass energies, and consequently, strangeness production will be studied in jets up 150 GeV in this analysis. The

strangeness content in jets may be extended 30% higher over all other experimental data.

If the cluster model is accurate, those values calculated from the HERWIG Monte Carlo will be similar to the data. A discrepancy between HERWIG and the data would imply that the cluster model would need to adjust the strangeness content of fragmenting quarks and gluons. Furthermore, disagreements may arise from an increase in jet E_T or from an overall difference in particle production. In any case, currently for the string model (and cluster model is comparable), the production ratios of the up, down, and strange quarks are approximately set at 1:1:0.3 for all jet E_T.

Moreover, through fragmentation plots, these results may be directly measured against other experiments. Being just the p_T of the K_S divided by the jet E_T, the fragmentation is a measure of overall K_S production. The fragmentation function is believed to be independent of initial energy of the partons. These $p\bar{p}$ Tevatron results may be contrasted with those from e^+e^- collisions. If the shape of the spectra are similar and there is an offset (the Tevatron plot lower than the others), this may be evidence of a jet E_T dependence (scaling violation).

Prior to any jet analysis, K_S production in the Minimum Bias set is studied and compared to other analyses in order to support the K_S production in jets analysis. For example, the $c\tau$ measurement of K_S will test the reliability of the efficiencies. Other quantities such as invariant cross-section are contrasted to other publications among quantities.

There are many questions: Is the cluster model correct? Is K_S production too high or too low in jets? Are these ratios of up:down:strange quarks correct? If so, are particles generated at the appropriate p_T spectra? If K_S production is too low,

is that because the cluster model generates too few K_S or too few particles overall? If these ratios are correct, are do they hold for all measured jet E_T? How do the Tevatron's $p\bar{p}$ and the e^+e^- collisions from other experiments compare? Is there evidence of scaling? Are these results consistent with those of predecessors?

Much discussion and work to be done. Let us begin with the tools in this analysis, the Tevatron and the CDF detector.

Chapter 2

The Experiment

The Fermi National Laboratory is one of the world's most renowned science research facilities. Located 35 miles west of Chicago on 7000 acres of land, over 2200 scientists from 36 states and 20 countries push both science and technology to new limits. From particle physics to astrophysics, from detector design to accelerator innovations, and from the development of theoretical models to the discovery of the top and bottom quarks, Fermilab has been and will continue to be an excellent place for first-class research. From 1991-1996, trillions of $p\bar{p}$ collisions at center of mass energies of 1.8 TeV took place using the 6.28 km circumference Tevatron accelerator buried 30 ft underground. Since then, the Tevatron and its detectors, CDF and D0, have undergone complex upgrades. In particular, by replacing the Main Ring with the Main Injector, the ability of recycling protons was achieved. This new feature should not only increase the center of mass collision energy to 1.96 TeV but also increase the number of collisions by an order of magnitude. Detector improvements were mainly aimed at advancing resolution, acceptance, and readout. Although the Run II detector is extremely interesting, this analysis is based on Run I data (1991-1996 data). Hence, only the manner in which $p\bar{p}$ interact at 1.8 TeV, the Run I CDF detector, and the data acquisition system will be briefly described [6] [7] [8] [35].
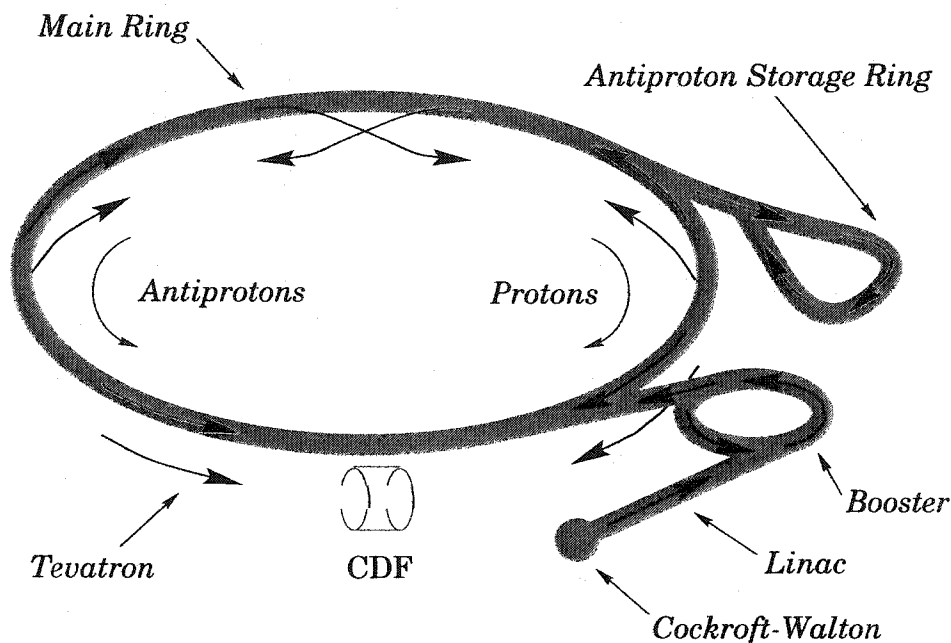
Figure 2.1: A schematic of the Tevatron accelerator at the Fermi National Accelerator Laboratory. The Cockcroft-Walton, Linac, Booster, Main Ring, and the Tevatron are used to collide protons and antiprotons at center of mass energies of 1.8 TeV. Note that CDF is located at one of the collision points.

2.1 The Fermilab Tevatron

To have $p\bar{p}$ collisions at center of mass energies of 1.8 TeV, protons and antiprotons are accelerated to 900 GeV using a five stage accelerator process as well as use sophisticated techniques to accumulate and store antiprotons. The first stage of the process consists of a Cockcroft-Walton accelerator taking negative Hydrogen to energies of 750 keV, and then a linear accelerator (LINAC) ramps up the energy of these ions to 400 MeV. Electrons from the H^- ions are removed leaving only the protons to be injected into the Booster. The Booster brings protons up to 8.0 GeV using its magnetic dipoles to force the particles to follow circular orbits at almost constant orbital radius and constant orbital frequency by increasing the dipole fields with the momentum of the particles. From the Booster, protons are brought up to
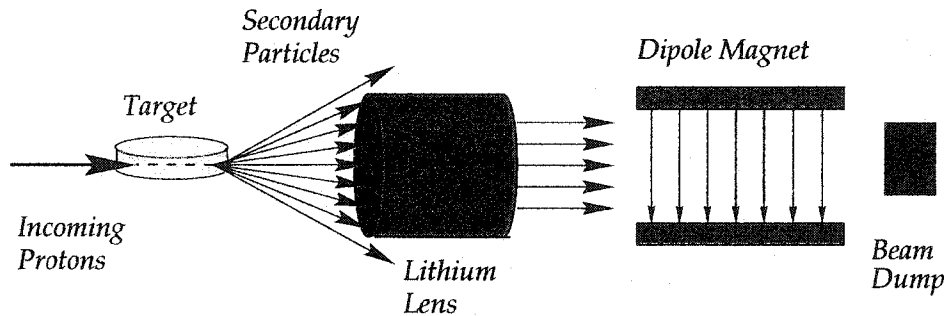
Figure 2.2: In order to produce antiprotons, protons collide into a Nickel target to generate secondary particles from which antiprotons are filtered and focused into a beam using a cylindrical Lithium lens.

150 GeV with 774 dipole magnets and 240 quadrupole magnets in the Main Ring. The dipole magnets are for steering, as stated earlier, and the quadrupole magnets are for focusing the beam.

By directing 120 GeV proton into a Nickel target to create many secondary particles, antiprotons are filtered out and focused into a beam using a cylindrical Lithium lens. This process generates 10^7 antiprotons with every collision with the fixed target. The antiprotons are stored in the Debuncher at energies of 8 GeV where the momentum spread is reduced, and the antiprotons are then stockpiled in the accumulator until approximately 10^{10} antiprotons are collected. From here, the antiprotons are placed into the Main Ring rotating counter to the protons until both are at energies of 150 GeV. The last acceleration stage is when both protons and antiprotons are accelerated to energies of 900 GeV inside the Tevatron, with protons orbiting counterclockwise and antiprotons orbiting clockwise, until center of mass collisions of 1.8 TeV can be attained. The Tevatron is concentric with the Main Ring, but it incorporates 774 superconducting dipole magnets and 216 superconducting quadrupole magnets.

6 bunches of protons and 6 bunches of antiproton collide every 3.5 μs at up

to 4 interaction points. However, there are only 2 collider detectors, CDF and D0, so electrostatic separators are used to prevent bunch crossings at the other collision points. A collision can occur only when a proton and an antiproton bunch overlap. Each bunch has an average radius of 40(25) μm for Run 1A(B) and a Gaussian distribution with a σ of 30 cm in z. Also, there are 2.0×10^{11} protons in the a proton bunch, and normally there are about 10 times less antiprotons in an antiproton bunch.

The number of collisions can be calculated using

$$R = \mathcal{L}\sigma_{int} \tag{2.1}$$

where R is the rate of events , σ_{int} is the cross-section of a given interaction, and $\mathcal{L}$ is a quantity called the luminosity. The luminosity is approximately given by

$$\mathcal{L} = \frac{f n_p n_{\bar{p}}}{4\pi \sigma_p \sigma_{\bar{p}}} \tag{2.2}$$

where n_p and $n_{\bar{p}}$ are the number of particles in each bunch, f is the frequency of collisions, and σ_p and $\sigma_{\bar{p}}$ are the Gaussian transverse beam profiles. In general, nature fixes the cross-section of a given process, and increasing luminosity is very important in order to increase the data used for analyses. Reducing the beam profiles, increasing the collision rate, and increasing the number of particles in each bunch are ways to achieve this goal. For example, with a given $p\bar{p}$ σ_{int} of 50 mb at 1.8 TeV, and a Run 1B average $\mathcal{L}$ of $1.6 \times 10^{31} cm^{-2} s^{-1}$, the collision rate is 800 thousand interactions per second. Since only a few events can be written onto 8 mm tape per second, triggers are used to select events of interest as much as the acceptance rate will permit. Luminosity decreases with time because protons and antiprotons
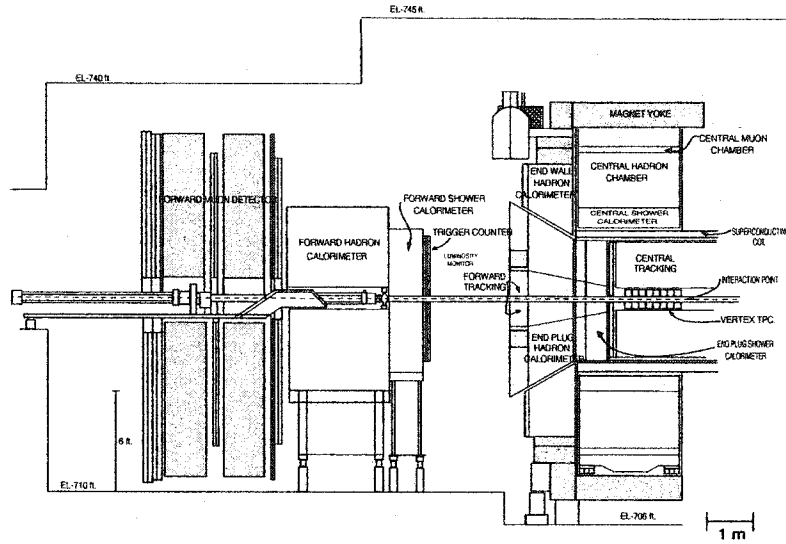
Figure 2.3: The forward half of the CDF detector. The CDF detector is azimuthally and forward-backward symmetric about the nominal interaction point.

are lost either to beam gas collisions or $p\bar{p}$ collisions as well as the beam increases its beam profiles σ_p and $\sigma_{\bar{p}}$. Hence, each Tevatron store of protons and antiprotons lasts about 20 hours before replacing the bunches becomes necessary [6] [7] [8] [35].

2.2 Collider Detector at Fermilab (CDF)

The Collider Detector at Fermilab (CDF) is centered around one of six nominal interaction points around the Tevatron, and CDF collects a wide range of data from 1.8 TeV $p\bar{p}$ collisions. Using the charge, position, momentum, and energy deposition information obtained from the 27 m long, 10 m high, and over 2300 kg detector, a wide variety of events can be analyzed. In the rest of the chapter, CDF will be briefly discussed with special emphasis on the components which are relevant to this analysis.
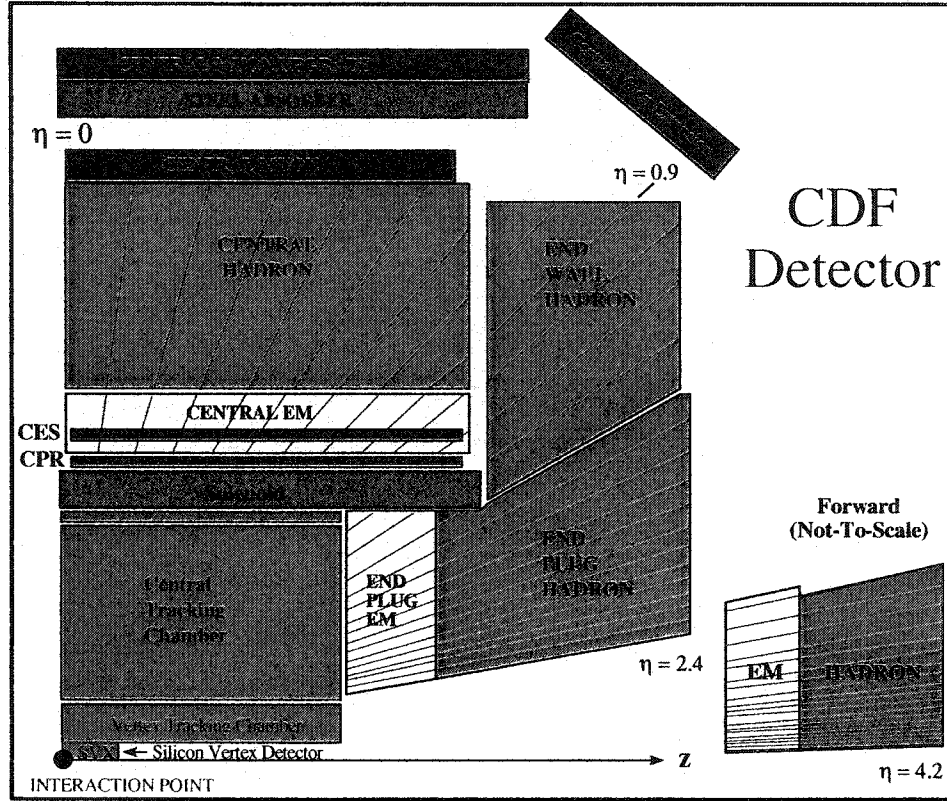
Figure 2.4: A quadrant of the CDF detector.

Since CDF is forward-backward and azimuthally symmetric, cylindrical coordinates are employed. CDF uses a right-handed coordinate system where the positive z-axis is the direction of the beam of protons, the y-axis is directly upward, and the x-axis is radially outwards. The polar angle θ is measured with respect to the z-axis, and the azimuthal angle ϕ is the angle viewed from the $+z$-axis is measured counter-clockwise.

One particularly useful quantity called rapidity is defined as

$$y = \frac{1}{2} ln(\frac{E + P_z}{E - P_z}).$$ (2.3)

Under Lorentz boosts with a velocity β along the z-axis in reference to an inertial
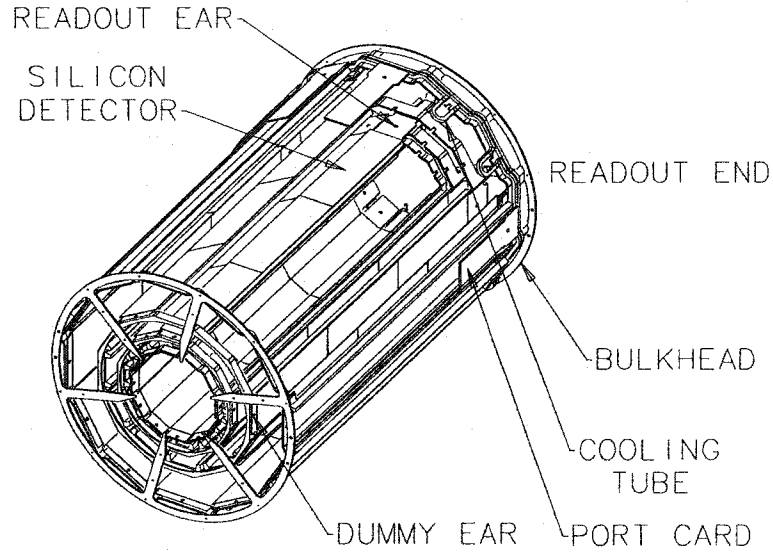
Figure 2.5: The diagram of a single SVX barrel.

frame, the transformation of rapidity is $y \rightarrow y + tanh^{-1}\beta$ and the difference between two rapidity quantities is Lorentz invariant. For highly relativistic particles, $p \gg mc$, rapidity can be simplified to

$$\eta = -ln(tan\frac{\theta}{2}) \ . \tag{2.4}$$

This quantity is called pseudorapidity and is approximately equal to rapidity. There are actually two useful forms of pseudorapidity. The first is called detector pseudorapidity ($\eta_{detector}$), and it is calculated using the nominal interaction point as the origin (geometric center of the detector). The latter is called event pseudorapidity (η) and this quantity is measured with respect to the interaction vertex of $p\bar{p}$ collisions. The distribution of the interaction vertex in z closely resembles a Gaussian

PIG TAIL

READOUT EAR

MECH. ALIGNMENT
HOLE

CHIP

WIREBONDS

WIREBONDS

SILICON DETECTOR

ROHACELL AND CARBON
FIBER SUPPORT

DUMMY EAR

MECH. ALIGNMENT HOLE
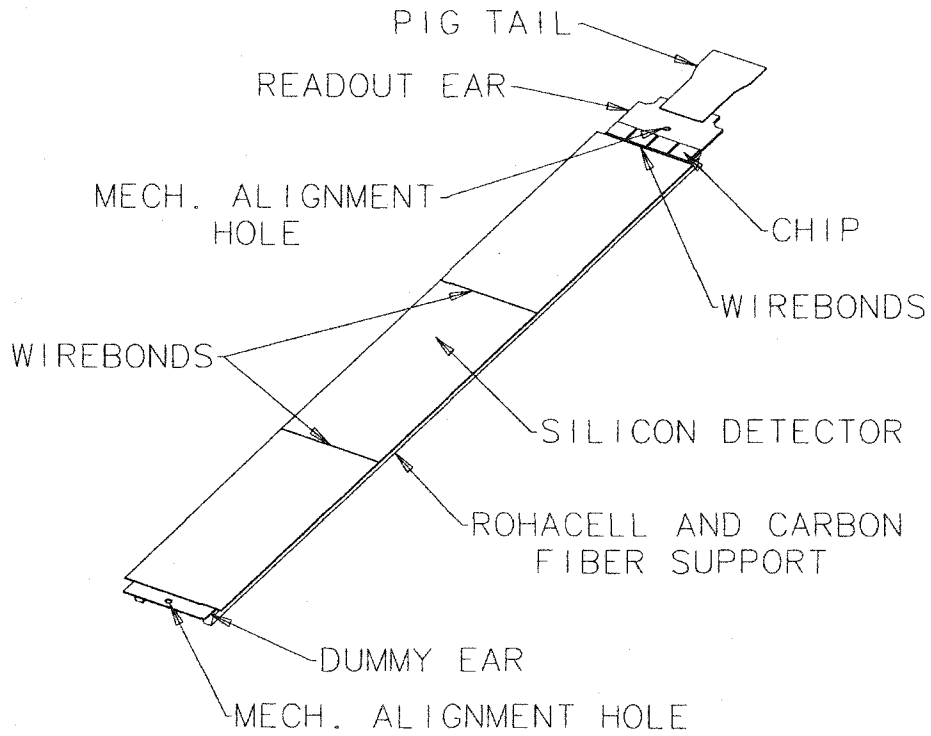
Figure 2.6: A figure of a SVX ladder.

Fake Secondary
Vertex

d.

True Secondary
Vertex

-L$_{xy}$

+L$_{xy}$

Displaced
Tracks

Primary
Vertex

Jet Axis

Displaced
Tracks

Prompt
Tracks
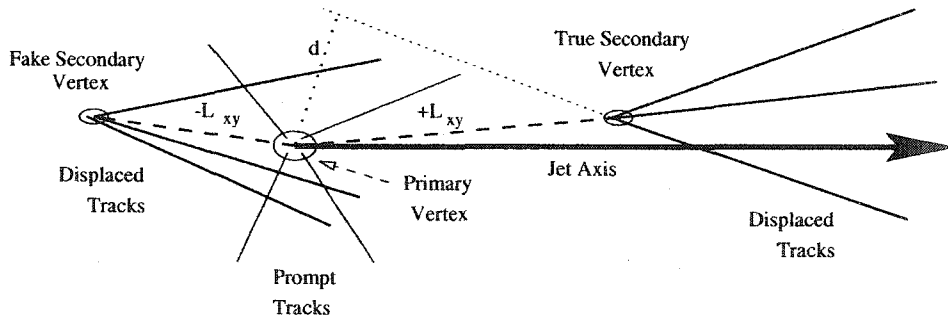
Figure 2.7: A picture of tracks intersecting at a secondary vertex which is displaced L_{xy} from the primary vertex.

with σ of 30 cm [6] [7] [8] [35].

2.2.1 Central Tracking Systems

The Central Tracking systems are designed to determine the trajectories of charged particles for the purpose of momentum and charge measurements. In addition, electromagnetic clusters without tracks can be used for photon identification. The Silicon Vertex Detector (SVX) is positioned closest to the beamline. The SVX is a series of silicon microvertex detectors which yield high precision measurements near the interaction region. Beyond the SVX, the Vertex Tracking Chamber (VTX) gives r-z information of the tracks. The Central Tracking Chamber, which surrounds both the SVX and VTX, is instrumental in 3D track reconstruction. The latter two detectors are wire drift chambers. Enclosing all of the Central Tracking systems is a 4.8 m long NbTi/Cu superconducting solenoid with a radius of 1.5 m that generates the 1.41 Tesla axial magnetic field. This field causes the charged particles to follow the helical trajectories from which momenta and charge can be extracted.

Silicon Vertex Systems (SVX)

The Silicon Vertex Detector (SVX) primary purpose is to precisely determine tracking in r-ϕ in order to identify tracks intersecting away from the primary vertex, called "secondary vertices", that are useful in locating B-hadrons with $c\tau$ on order of 300-400 μm. It is important to note that although this analysis depends heavily on secondary vertices for K_S identification, the SVX is not used in this analysis. SVX can indeed be used to find K_S and studies have been done at CDF. However, the $c\tau$ of the K_S are on the order of 2.6786 ± 0.0024 cm [9] so these particles have long enough $c\tau$ for the resolution of the CTC to be more than sufficient.

The SVX consists of a pair of 25.5 cm long barrels that have a gap of 2.15 cm between them. Each barrel is divided azimuthally into 12 wedges, and each wedge has 4 layers of single-sided silicon called ladders. Every ladder has 3 silicon wafers,

Table 2.1: Summary of the SVX characteristics. Given below is the crystal width, active area, the number of readout strips, and the number of readout chips for a given layer of SVX.

Layer	Crystal Width (cm)	Active Area Width (cm)	Readout Strips	Readout Chips
0	1.6040	1.5360	256	2
1	2.3720	2.3040	384	3
2	3.1400	3.0720	512	4
3	4.2930	4.2240	768	6

which are 300 μm thick and 8.5 cm long, and is rotated by $3°$ about its length to provide overlap. In addition, each ladder increases in width, the number of readout strips, and the number of readout chips as the position of the ladder increases radially. Each wafer has a strip pitch of 60 μm for the first 3 layers closest to the beampipe and 55 μm for the outer most layer, and every wafer is surrounded with conducting strips. All silicon strips are parallel to the z-axis, and hence can only obtain r-ϕ information of the tracks. The SVX covers 60% of the $p\bar{p}$ interactions with its detector pseudorapidity coverage of $|\eta_{detector}| < 1.9$.

Once the silicon is biased with a potential and an ionizing particle goes through the silicon, a large quantity of electron-hole pairs are generated. The electrons which are excited to the conduction band are attracted to the large potential difference of the conducting strips. The voltage drop of the strip is proportional to that of the ionization, and the strips are readout with electronics. In total, there are 46,080 strips channels in the SVX that result in a resolution of about 10 μm [6] [7] [8] [35].

Vertex Detector (VTX)

The VTX detector is a drift-time proportional chamber used to more accurately describe where ,in the 30 cm Gaussian of $p\bar{p}$ collisions, an event actually took place
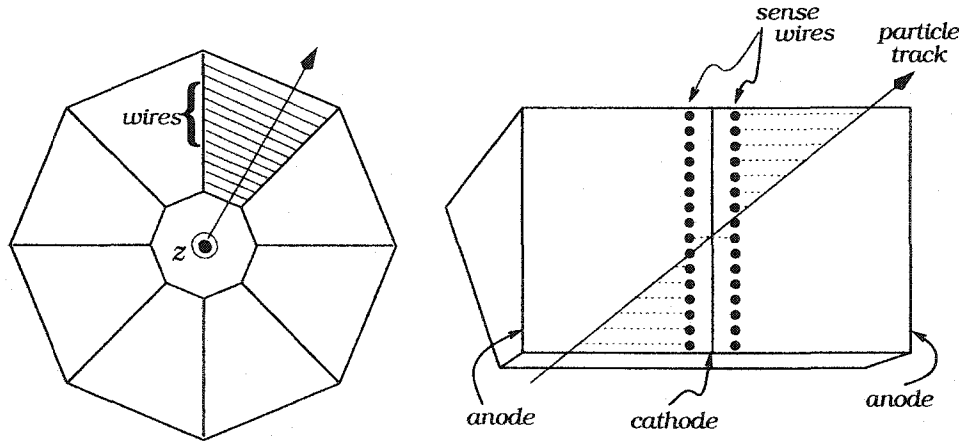
Figure 2.8: A figure of a particle leaving behind an ionization trail as it transverses the VTX. The electrons from the ionization trail are drawn to the sense wires for readout.

to within a resolution of 2.0 mm. Furthermore, identification of multiple vertices can help correct the calorimetry for multiple interactions, and the z-vertex information obtained is used to calculate the polar production angle θ. The z-vertex calculated by the VTX is also a seed in the pattern recognition software which matches hits in the other tracking chambers. Even in the latter stages of the analysis, many variables depend on the event vertex, such as lateral displacement (L_{xy} in Figure 1.7).

The VTX detector is located just outside the SVX and extends to an outer radius of 22 cm. With 28 side-by-side modules, each 9.4 cm long, encircling the beam line as a chain of octant-shaped annuluses. Each chamber is split in half by a voltage plane to reduce the drift distance of charge particles in the 50%-50% Argone-Ethane gas mixture that has a drift velocity of 46 $\mu m/ns$. As a particle travels through the module, the gas is ionized, and the ions travel parallel to the z-axis until a sense wire is hit. Signals can then be read out and amplified to measure the r-z of a charged particle. To get rudimentary r-ϕ measurements, each octant

is rotated $\pm 15°$ with respect to each adjacent module. In this manner, a charged track can be isolated to be within $\frac{1}{8}^{th}$ of an octant. The VTX covers $|\eta_{detector}| < 3.5$.

The hits of the charged particles are entered into the pattern recognition software to form tracks segments which are extrapolated to the beam-line to yield a primary z-vertex measurement. The quality of a vertex depends on the number of hits and the number of track segments used in the pattern recognition. The resulting graded scale of classes of vertices are used to rank a vertex with respect to others. For example, a class 12 vertex is the highest quality vertex with more than 180 hits [6] [7] [8] [35].

Central Tracking Chamber (CTC)

Surrounding both the SVX and the VTX is an open cell drift chamber called the Central Tracking Chamber (CTC). The purpose of the CTC is to obtain the information necessary for the reconstruction software to precisely measure the 3D-tracks within $|\eta_{detector}| < 1.1$. The 3.2 m long cylinder has an inner radius of 0.28 m, and the detector extends out to 1.38 m. There are 30,504 gold-plated tungsten wires grouped into 84 layers. Furthermore, these 84 layers are grouped into 9 superlayers, 5 axial superlayers which are parallel to the beamline as well as 4 stereo superlayers that are $\pm$ 3° from the beamline. Each axial superlayer has 4,392 wires (12 sense wire layers), and each stereo superlayer has 1,764 wires (6 sense wire layers). The axial layers yields r-ϕ values and the stereo layers measures r-z so together both extract information used to calculate the helixes of many charged particles.

The detector is also subdivided azimuthally into cells by stainless steel HV field-shaping wires. Potential wires alternate with the sense wires inside each cell. Consequently, there is a 1350 V/cm electric field in the CTC in addition to a 1.41 T magnetic field from the solenoid.
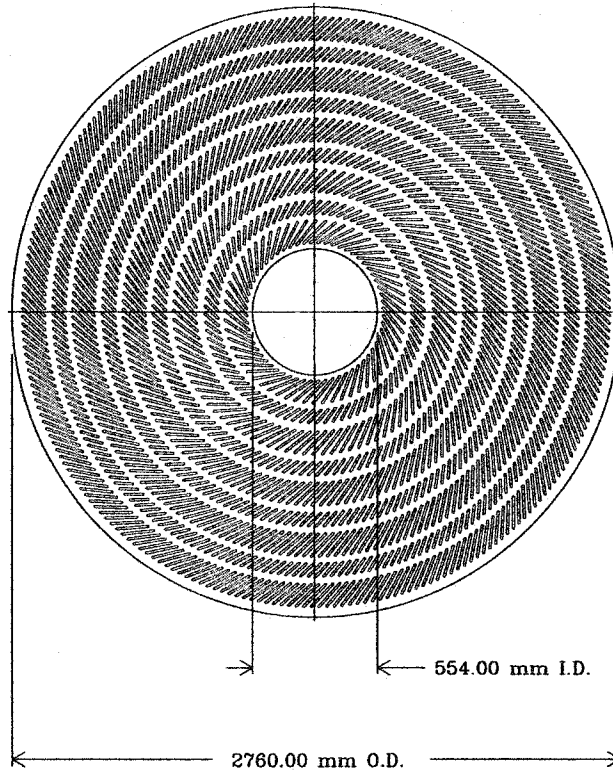
Figure 2.9: A figure of the endplate of the CTC. There are 9 tilted superlayers of sense wires. 5 superlayers measure r-ϕ, and 4 superlayers measure r-z.

The entire chamber volume is filled with a 50/50 Argon-Ethane gas with trace amounts of isopropyl alcohol that has a drift velocity of 46 μm/ns. The drift velocity of the gas dictates the cell size because the CTC recovery time (0.8 μs) must be less than the beam crossing time in the Tevatron (3.5 μs). Otherwise, data from the previous events would still be present in subsequent events.

As a charged particle passes through the CTC, the gas becomes ionized so that electrons drift to the sense wires within 706 ns (or a maximum drift distance of 40 mm). Using this hit information as well as primary vertex information from the VTX, the reconstruction code calculates the 5 tracking parameters of a given helix:

z_0, ϕ_0, θ_0, impact parameter d_0, and the radius of curvature R in the transverse plane. In particular, the hit information from the axial layers determine r-ϕ measurements. Then, the algorithm uses axial hits and the primary vertex, as measured by the VTX, to reconstruct 3D tracks.

In Figure 1.9, the rotation of the cell structure by 45° appears odd; however, there are motivations for this. Because of the E and B fields crossing, the electrons will drift at a Lorentz angle of 45° from the radial direction. By rotating the cells by this Lorentz angle, the drift time of the electrons is proportional to drift distance to the wire plane. In addition, for any given hit on a sense wire, there is an ambiguity in the drift direction of the electrons. This "ghost" track can be distinguished from the true trajectory by observing that the true path passes through the primary vertex. The rotation accomplishes the same purpose by simply matching segments across superlayers.

The CTC has an azimuthal spatial resolution of approximately 200 μm and a spatial resolution of 6 mm in the axial direction. Momentum measurement resolution is

$$\frac{\delta p_T}{p_T} \sim 0.002 p_T \tag{2.5}$$

if only the CTC is used, and when the CTC is used in conjunction with SVX, the resolution is

$$\frac{\delta p_T}{p_T} \sim 0.0009 p_T \tag{2.6}$$

where p_T is given in GeV/c.

In summary, a charged track passing through the CTC ionizes the gas enclosed. The electrons from the ionized gas drift to sense wires, and the drift time is measured with electronics. These hit times are used to yield helix trajectories. It is interesting
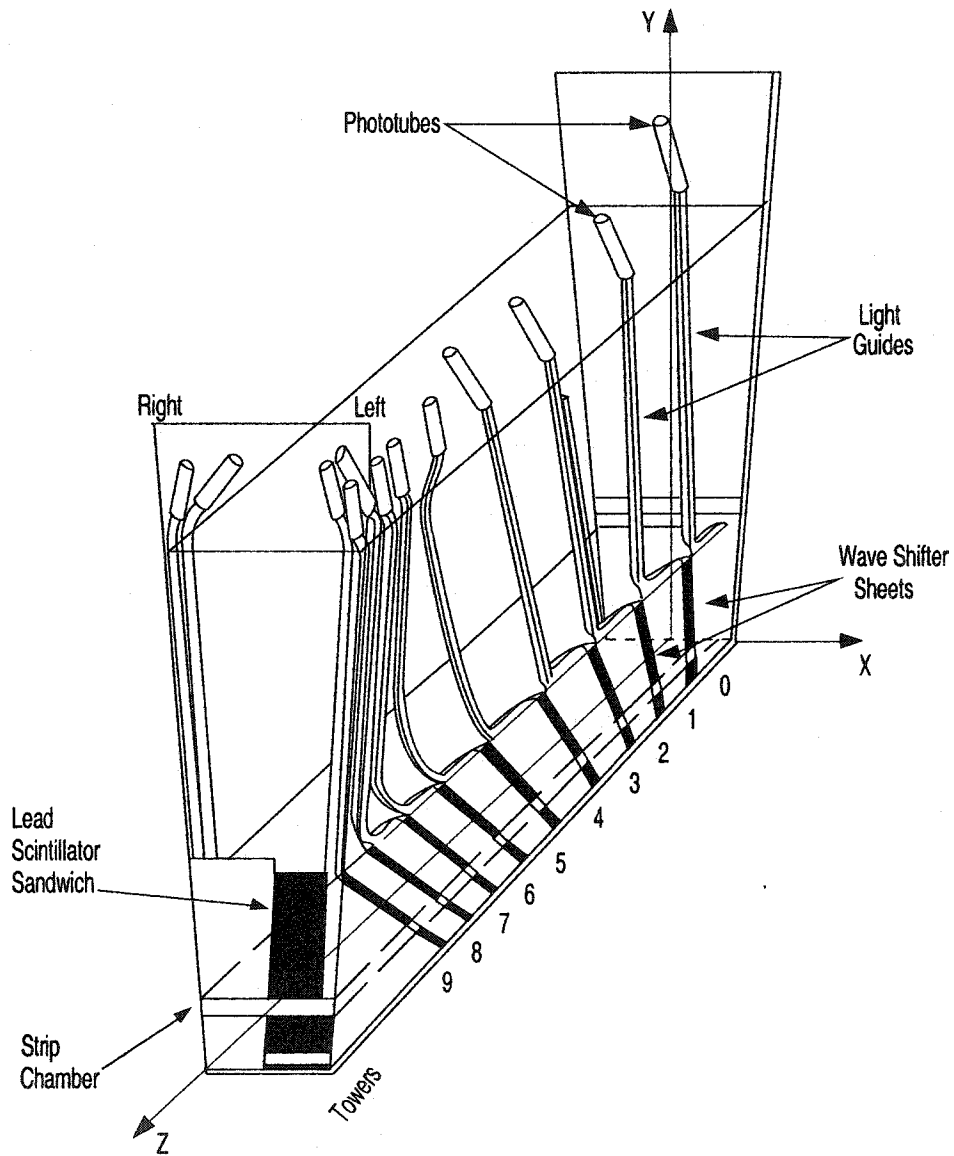
Figure 2.10: A single wedge of the CEM. Lead-scintillator sandwich converts initial particle energy into light which is collected by the waveguides and transferred to the phototubes.

to note that K_S , being neutral particles, are not detected directly, but through their charged decay products. This analysis depends heavily on the CTC [6] [7] [8] [35].
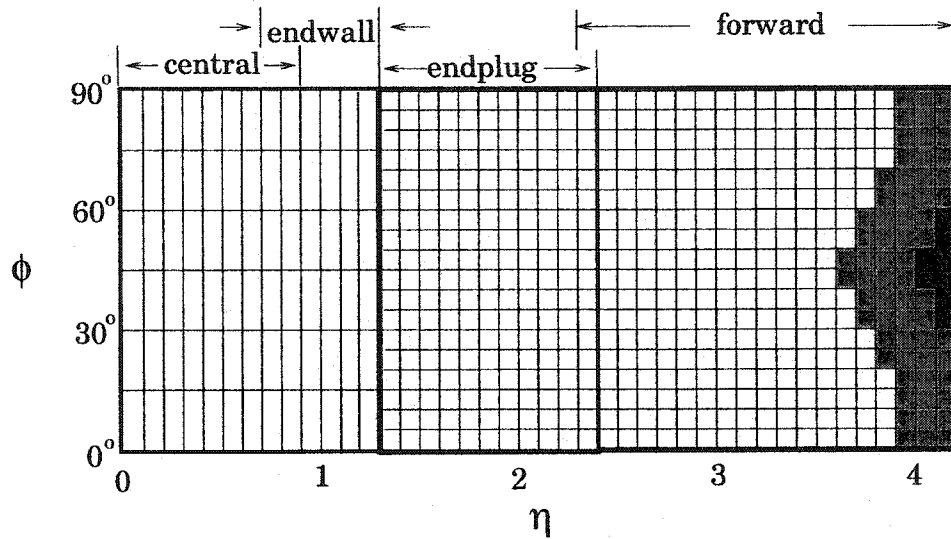
Figure 2.11: A quadrant of the calorimeters showing the η-ϕ tower segmentation. EM calorimeters have coverage of $0<\eta<4.2$. The area shaded in gray denotes to regions where the HAD has partial coverage due to the low β magnets. The black region is where there is no coverage because the beampipe is positioned here.

2.2.2 Calorimetry

There are several electromagnetic and hadronic calorimeter subsystems that cover different regions of pseudorapidity. Each is designed to measure the energy of electrons, photons, and hadrons. By causing either electromagnetic or hadronic showers with absorbers and converting particles into light with scintillators, the light that is collected with waveguides and is carried to the phototubes is proportional to the energy of the incident particle. The segmentation of the detector has almost complete azimuthal coverage and about $|\eta_{detector}|<4.2$ coverage in pseudorapidity. Only "cracks", areas of the calorimeters without electronic readout, at every $15°$ in ϕ and at $|\eta_{detector}|<0.13$, $1.1<|\eta_{detector}|<1.4$, and $2.3<|\eta_{detector}|<2.4$, are insensitive to incident particles. These cracks usually coincide with adjacent detector cells or detector subsystems. Detection and formation of energy clusters is crucial
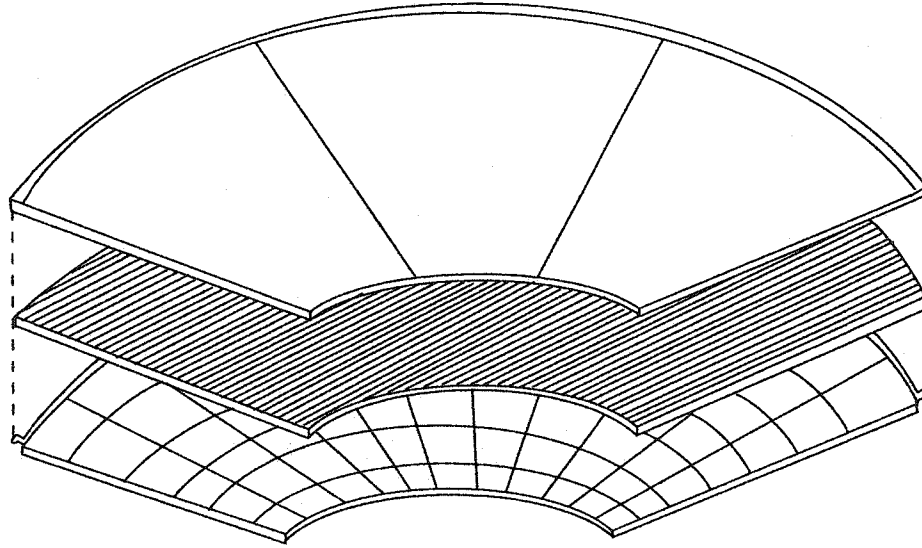
Figure 2.12: A diagram of a quadrant of the PEM where the top layer is that of proportional tubes, the middle layer is that of a lead absorber, and the bottom layer shows the copper etching which gives rise to the segmentation of the cathode pads in η (radial lines) and ϕ (arcs).

in the identification of jets. The central calorimeter and strip chambers, the plug calorimeters, and the forward calorimeters will all be discussed.

Central Calorimeter, Central Electromagnetic Strip Chambers, Wall Calorimeters (CEM,CES,WHA)

The Central Electromagnetic Calorimeters (CEM) consists of 4 modules, and each pair surrounds both the solenoid and the central tracking systems on either side of the nominal interaction point, $z = 0$. Each modular pair has 24 wedges, every $15°$ in ϕ, and each wedge has 10 projective towers, every .1 in η. The projective tower property of the calorimeters refers to each tower pointing back to the interaction region. The entire CEM is 5.0 m long and 35 cm thick, and its volume consists of 31 alternating layers of 3.175 mm thick lead absorbers and 5mm thick layers of

scintillator. There are 2 wavelength shifters per tower that guides green waveshifted light (490 nm) to the phototubes. Hence, when a high E_T photon or electron hits a lead absorber, the particle interacts with shell electrons to yield Bremsstrahlung γ 's. These high energy γ convert to electron-positron pairs. The electromagnetic shower cycle continues until all the initial energy of the parent is transferred to e^+e^- pairs. The scintillating layers convert these electrons and positrons into light which is directed by the waveguides to the phototubes. Overall, the CEM is 18 radiation lengths thick.

Between the 8th lead layer and the 9th scintillator layer, the Central Electromagnetic Strip Chamber (CES) is situated. The location of the CES marks the average maximum transverse depth of an electromagnetic shower, 5.9 radiation lengths into the CEM. The CES is able to measure the position and transverse shower distributions of electromagnetic clusters in z and r-ϕ with a detector which is part strip chamber and part gas proportional chamber. The strip chamber consists of 128 cathode strips that are oriented perpendicular to the beam and 64 anode wires which lie parallel the beam. The gas proportional chamber is filled with a 95%-5% Ar-CO_2 mixture, and its wires are separated by 2 mm. There is a 1420 V potential applied to the wires. The position measurement resolution of CES is 2 mm. The CES is particularly useful in identifying γ in a electromagnetic shower by studying the shower profile obtained from the strip chamber.

Encompassing the CEM, the Central Hadronic Calorimeter and the Wall Hadronic Calorimeter absorb hadrons, create hadronic showers, and in principle, are very similar to the CEM. Each projective tower of the CHA and WHA corresponds to a tower in the CEM with the pseudorapidity coverage being $|\eta_{detector}|<0.9$ for the CHA and $1.7>|\eta_{detector}|>1.3$ for the WHA. The CHA consists of 32 layers of

Table 2.2: Summary of the CDF calorimeters characteristics [7].
The table shows for every calorimeter system, the pseudorapidity coverage, the average energy resolution with energy dependent and systematic uncertainties added in quadrature as calculated directly from electron (for EM) and pion (for HAD) test beam data, the position resolution, and its thickness in term of the radiation lengths (EM calorimeters) or interaction lengths (HAD calorimeters).

Calorimeter subsystem	$\|\eta\|$ coverage	Energy resolution $\sigma(E)/E$	Position resolution (cm^2)	Depth
CEM	0–1.1	$13.5\%/\sqrt{E_T} \oplus 1.7\%$	0.2×0.2	$18\ X_0$
CHA	0–0.9	$75\%/\sqrt{E_T} \oplus 3\%$	10×5	$4.5\ \lambda_0$
WHA	0.7–1.3	$75\%/\sqrt{E_T} \oplus 3\%$	10×5	$4.5\ \lambda_0$
PEM	1.1–2.4	$28\%/\sqrt{E_T} \oplus 2\%$	0.2×0.2	$18\text{–}21\ X_0$
PHA	1.3–2.4	$130\%/\sqrt{E_T} \oplus 4\%$	2×2	$5.7\ \lambda_0$
FEM	2.2–4.2	$25\%/\sqrt{E_T} \oplus 2\%$	0.2×0.2	$25\ X_0$
FHA	2.3–4.2	$130\%/\sqrt{E_T} \oplus 4\%$	3×3	$7.7\ \lambda_0$

steel absorber interleaved with 1.0 cm thick plastic scintillator. The WHA has 15 layers of 5.1 cm steel absorbers with alternating layers of 1.0 cm thick plastic scintillator. The extra thickness in the WHA is due to the fact that a particle will on average have 1.4 times more total energy in the WHA than in the CHA for a given E_T [6] [7] [8] [35].

Plug Calorimeters (PEM/PHA)

Enclosing the ends of the conical volume defined by $\theta = 30°$ left by the WHA, two separate plug calorimeters fit snuggly. Each endcap consists of 4 90° azimuthal quadrants with a 10° hole to permit the beam pipe to run through the center. The radius of a quadrant is 1.4 m. The plug electromagnetic calorimeter is nearest to the interaction point and is 50 cm deep, and the plug hadronic calorimeter is just beyond. Both PEM and PHA have readout cathode pads etched in a projective geometric scheme, having a segmentation of 5° in phi and 0.09 in η. However, the

pads near the shower max have 4 to 5 times more segmentation to allow a more precise measurement of the profiles of showers. The PEM has 34 layers of gas proportional tubes sandwiched with 2.7 mm thick lead absorbers, and the PHA has 20 layers of proportional tubes intermixed with 5.1 cm thick steel absorbers. Each tube is composed of conductive plastic and is filled with a 50%-50% Argone-Ethane gas mixture. For proportional tubes, the quantity of charge collected on the wires is directly proportional to the ionization of the gas which is itself proportional to the initial energy of the hadron. The PEM has a coverage of $1.1 < |\eta_{detector}| < 2.4$ whereas the PHA has a coverage of $1.32 < |\eta_{detector}| < 2.4$. Energy and position resolutions of all the calorimeters are listed in Table 2.1 [6] [7] [8] [35].

Forward Calorimeters (FEM/FHA)

To include the $2.2 < |\eta_{detector}| < 4.2$ projective geometric region, FEM and FHA detectors enclose the ends of the cylindrical portion of the CDF detector, enabling measurements of the energies of particles to be found as close as $2°$ from the beamline. The tower segmentation of both the FEM and FHA are 0.1 in η and $5°$ in ϕ, in this high η region. The 1.0 m deep FEM is 6.5 m from the center of the detector, with each side 3 m in length. In the FEM, there are 30 sampling layers of proportional tube chambers alternating with 0.48 cm thick layers of 94%-6% Lead-Antimony alloy absorbers. The FHA, located just behind the FEM, has 27 sampling layers of proportional tube chambers with 5.1 cm thick steel absorbers interspersed. Since the eta region of interest is $|\eta_{detector}| < 1.0$ in this analysis, the forward and plug calorimeters are not very useful [6] [7] [8] [35].

2.2.3 Muon Detector

The Central Muon Chambers (CMU), the Central Muon Upgrade Chambers (CMUP), the Central Extension Muon Chambers (CMX), and the Forward Muon System (FMU) provide muon detection. If a muon track can be associated with a low energy cluster in the calorimeter, a muon can be identified. The muon chambers are proportional chambers which detect tracks which traverse the steel filters, the central tracking systems, the calorimeter systems, and the solenoid. Even a muon with a p_T as low as 1.5 GeV/c can pass through all other parts of the detector (3.487 m from the beam axis), depositing little energy in the calorimeters. The number of interaction lengths of steel are 5, 8, and 6 between the beam axis and the CMU, CMUP, and CMX, respectively. The ϕ coverage is 85%, 80%, and 67% for the CMU, CMUP, and the CMX, and the η coverage is $|\eta_{detector}|<0.6$ for the combined CMU and CMUP systems, $0.6<|\eta_{detector}|<1.0$ for the CMX, and $2.0<|\eta_{detector}|<3.6$ for the FMU. The CMU and CMUP systems are steel filters in front of 4 layers of drift chambers, and the CMX two pairs of arches with drift chambers located behind the central and wall calorimeters. The FMU system is a pair of magnetized iron toroids (used also as steel filters) in which the drift chambers and scintillators for the toroid instrumentation are also used for muon measurements [6] [7] [8] [35].

2.2.4 Beam-Beam Counters

Mounted on the front of the forward calorimeters, there four scintillating counters confined to the same plane on opposite sides of the beam pipe, 5.4 m from the interaction point. The coverage is $3.2<|\eta_{detector}|<5.9$. If both BBC counters have coincident hits within 15.0±0.2 ns of a bunch crossing, then a legitimate $p\bar{p}$ collision is believed to have occurred. This provides a veto for beam interactions with
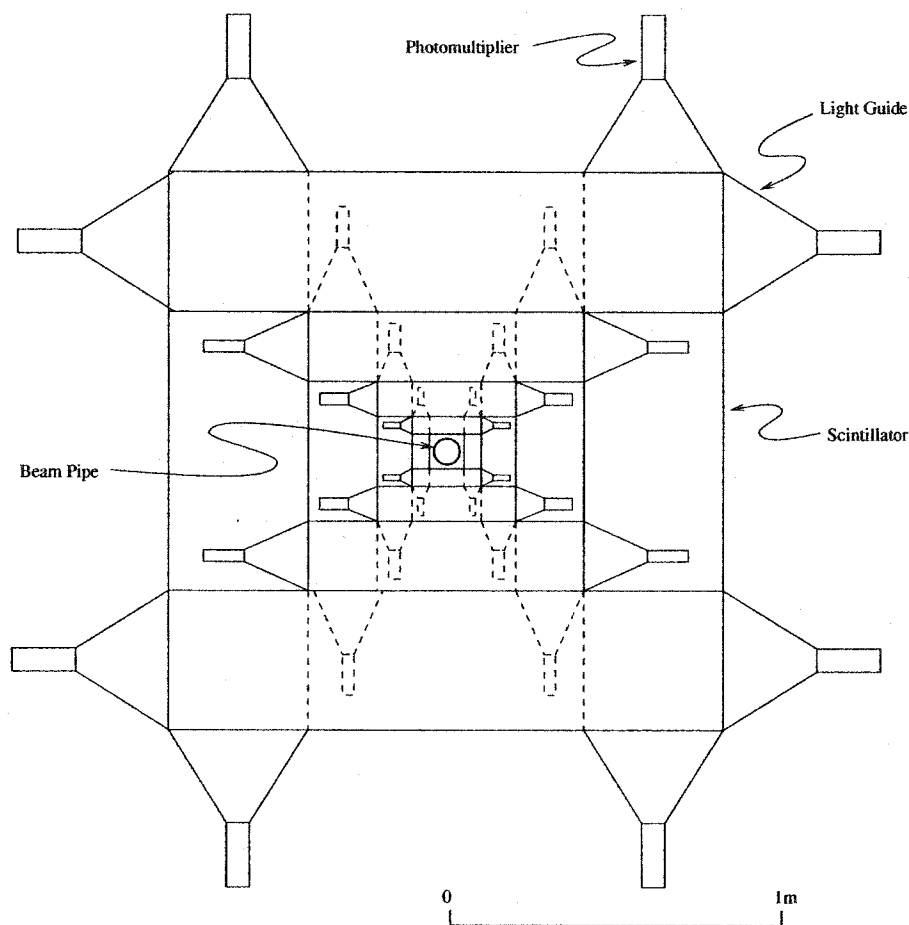
Figure 2.13: A diagram of one set of Beam-Beam Counters (BBC).

beam-pipe gas. Furthermore, successful readout from the beam-beam counters is equivalent of passing the Minimum Bias Trigger. Also, instantaneous luminosity is derived from the quotient of the rate of coincident hits and the effective σ_{BBC}. In this analysis, the track embedding sample used the same instantaneous luminosity distribution as the data to prevent skewed efficiencies [6] [7] [8] [35].

2.3 Data Acquisition and Trigger Systems

When the 6 proton and 6 antiproton bunches collide every 3.5 μs (or at frequency of 285 kHz) with an average of 3.0 $p\bar{p}$ interactions per bunch crossing for Run 1B, there can be several hundred thousand interactions per second of which only a few events per second can be written onto tape. Most of these events are diffractive events whereas the events of most interest are usually hard-scattering events; hence, there are a series of hardware and software event cuts that reject "uninteresting" events at rates of 10^4-10^5 while retaining most of the "interesting" events. For example, a $t\bar{t}$ event (σ of about 5 pb) occurs once every 5 hours and an inclusive W boson event (σ of 25 nb) occurs once every 4 seconds, and these events are not the ones you want to throw away with the other 10^4-10^5 "uninteresting" events every second. To accomplish this feat, each trigger stage has stricter event criteria which allows fewer events for longer processing during the next stage. It is important to make decisions and readout data quickly in order to reduce the amount of time which the Data Acquisition System (DAQ) cannot readout data (dead time). There are 3 general types of triggers for an event to pass in order to be written to tape. They are called the Level 1, Level 2, and Level 3 triggers.

2.3.1 Level 1 Trigger

The Level 1 Trigger is a hardware trigger which evaluates every event before the next beam-crossing, within 3.5 μs. Without any deadtime, it brings the event rate from several hundred thousand per second to only a few kHz. This trigger selects mostly hard scattering events by making sure there are hits in the BBC counters and either basic energy deposition in a calorimeter or hits in the muon chambers. Only 1-2% of the events are passed onto the L2 trigger [6] [7] [8] [35].

2.3.2 Level 2 Trigger

The Level 2 trigger decision process takes longer than the bunch-crossing frequency, 25-35 μs, and there is not an option to buffer the data (storage of information for latter processing). Hence, the next 7-10 bunch crossings are ignored upon a Level 1 accept, and few percent of deadtime is a result. Tracking, photon, jet, electron, and other higher order objects are processed at this stage, and upon a L2 accept, the data from the detector is digitized by the Front-end electronics and readout by scanners with the aid of a data acquisition system. This process takes 3 ms, during which the DAQ is unable to take data, and this is responsible for another few percent of deadtime. The Trigger Supervisor checks the digitization of the event while the Event Builder assembles digitized data into an event structure. Events are passed onto the L3 trigger at rates of 22 Hz for Run 1A and 44-55 Hz for Run 1B. However, for some types of events, in which more events pass than can be processed by Level 3, only a fraction of events are taken, and the resulting sample is prescaled [6] [7] [8] [35].

2.3.3 Level 3 Trigger

The Level 3 trigger buffers and processes events in parallel without deadtime using only software triggers. It uses simpler and quicker versions of tracking algorithms in order to fully reconstruct electron, jet, muon, and photon objects, and if it passes the designed L3 trigger, the data is then written to staging disks and latter stored onto 8mm tape at a rate of up to 5-7 Hz for Run 1A and 10 Hz for Run 1B. The L3 trigger system employs 48 parallel CPU's which can operate with the computing power of 1000 MIPs (Millions of Instructions Per second).

This analysis depends primarily on the minimum bias triggers and jet triggers,

which will be discussed in more detail in the next two subsections. In addition, due to acceptance and detector efficiencies, even a smaller fraction of events that pass the triggers are studied [6] [7] [8] [35].

2.3.4 Minimum Bias Triggers

The run 1B minimum bias data stream, XMBB5P, has coincident hits (within 15.0 ± 0.2 ns of a beam crossing) in the BBC counters [7] [36] [37]. This is the only hardware requirement for a minimum bias event. Other event selection criteria will be discussed in the minimum bias selection chapter.

2.3.5 Jet Triggers

The jet data sample is taken from 4 different types of tape sets: QJ2B_P, QJ5B_P, QJ7_P, and QJ0_P. Events on the QJ2B_P tapes must pass the JET_20_TEX_0_PRE_25_V2 Level 2 trigger and the QCDB_JET4_20_TEX_0 Level 3 triggers. First, the event must pass L1_4_Prescale_40 Level 1 trigger that prescales the sample by a factor of 40. Then, at least one jet at Level 2 must have at least 20 GeV as well as have more than 0.5 GeV on transverse energy for each electromagnetic tower (JET_20_TEX_0_PRE_25_V2 trigger). The prescale at this stage is 25. Finally, after the Level 3 jet clustering algorithm, at least one jet with at least 10 GeV must be present to pass the QCDB_JET4_20_TEX_0 Level 3 trigger.

The QJ5B_P events must pass the same Level 1 prescale trigger, the Level 2 clustering algorithm must have at least one jet above 50 GeV (JET_50_V3 trigger), and the Level 3 clustering algorithm must have at one jet with at least 35 GeV (QCDB_JET3_50 trigger). The QJ7_P events must pass the JET_70_V3 Level 2 trigger and the QCDB_JET3_70 Level 3 trigger. An event must have at least one

jet with at least 70 GeV at Level 2 and at least one jet having at least one jet above 70 GeV. A QJ7B_P event is prescaled by a factor 8 at Level 2.

The QJ0B_P events actually consist of 2 non-prescaled Level 3 triggers: QCDB_JET1_100 and QCDA_JET_140. The first must have at least one jet (after the Level 2 Jet_100_V13 trigger) above 80 GeV, and the second must have at least one jet have at least 140 GeV and pass an online cosmic filter (note this a different cosmic filter than one described below). As for the Level 2 Jet_100_V13 trigger, at least one jet must be above 100 GeV [36] [37].

Chapter 3

Minimum Bias: The Selection Criteria

As mentioned in the previous chapter, the Minimum Bias events have coincident hits in the BBC counters. As a consequence of such a wide acceptance criteria, the odds that any given Minimum Bias event contains either W bosons, Z bosons, or high energy jets is remote. Moreover, the Minimum Bias events also have a lower track multiplicity than the events which pass one of the jet triggers. Consequently, this permits K_S to be examined in an isolated environment, and the knowledge attained here can later be employed to the more complicated jet events. Upon contrasting K_S properties and production to earlier publications, the focus will return to the primary purpose of this analysis which is the production of K_S in jets. In the first of three chapters having to do with K_S found inside Minimum Bias events, the event and track selection criterion, the method of identifying both primary and secondary vertices, and a description of the cuts necessary for the isolation of K_S will all be discussed.

3.1 The Event Selection Criteria

The Run 1B Minimum Bias data stream, XMBB5P, is run through and about 1.4 million events are processed. Aside from having coincident hits (within 15.0 ± 0.2 ns of a beam crossing) [7] in the BBC counters, each Minimum Bias event satisfies certain criteria such as pass the cosmic filter, "bad run", and primary vertex cuts.

Every event must first pass a cosmic filter that vetoes events with more than 6.0 GeV of "out-of-time" energy. "Out-of-time" energy refers to a cluster in the hadronic calorimeters that is outside a timing window of the CTC for a given event; this "out-of-time" energy is not restricted to eliminating cosmic events but also main-ring splash events, monojet events, and dijets with small missing E_T. In looking at 8669 minimum bias events, all but one event passes the cosmic filter. The cosmic filter has much more of an effect with the jet events and will be discussed later [38] [39].

Each event must also meet certain criteria in order to be considered a good event which is acceptable for study. First, the delivered integrated luminosity must be greater than 1.0 nb^{-1} with stable beams conditions. The solenoid, the temperatures, the voltages, the trigger rates, and the electronics must be within design specifications. In addition, the offline data is analyzed to check for unacceptable detector behavior that would indicate a problem with the data. The events that meet these requirements are said to have passed "bad run" cuts [7].

Finally, the leading primary vertex must be contained within 60.0 cm from the $z = 0$ of the detector in order to ensure that the particles of an event are in the region where the CDF detector is most efficient [7]. In Table 3.1, the number of events after each event cut is listed along with the K_S efficiency. Only approximately 8% of the K_S in the data are lost after these event cuts.

Table 3.1: The number of Minimum Bias events after each successive cut.

Cuts	Number of Minimum Bias Events	Fraction of Events Remaining
Only Cosmic Filter	1,381,935	1.000
Bad Run	1,379,960	0.999
$|z_{primary}|$<60.0 cm	1,272,470	0.921

3.2   The Track Selection Criteria

Track must first be reconstructed from hits in the CTC with the pattern recognition software. The software starts by combining the hits within each superlayer, fitting the axial hits to a circle and the stereo hits to a line. The stereo fit takes the z_{vertex} from the VTX as the input, and in this manner, the 3D track efficiencies are dictated by both the resolutions of the VTX and the CTC.

Once the axial "segments" are found for each superlayer, two independent algorithms work to match segments across superlayers to find 2D tracks. Whenever track results from the two algorithms are unique, the 2D track solution is combined with the stereo fit to calculate a 3D track. If the two algorithms yield two solutions with hits in common, the 2D track that has the most hits in the fit will be passed along for 3D fitting. However, if the two algorithms yield two solutions with over-lapping hits with the same number of hits in each fit, then one 2D track is chosen at random for 3D fitting.

In particular, a segment within a given cell must have at least 5 hits and pass through the sense wire plane. To match segments across cells, 8 hits have their resid-uals (the absolute value of the difference between the fit values and the projected fit values with the hits) less than 500 μm. These hits are added to the segment, and this new segment is used as a seed for further calculations. The resulting arc

or circle is fit to a straight line that must pass through the beam position. The hits within a 2 mm "road" about a circle are added to the fit, another circular fit is done, and the process repeats. The calculation terminates if either there are 3 wire layers between the beam axis and the seed segment or until the beam is reached. The best $\frac{3}{4}$ of residuals are averaged and the hits which are 3 times this average are removed, and then the circle fit is performed again. There is one caveat. If a fit has 20 hits without any of the hits below superlayer 3, the process is repeated without the beam constraint. The result of this procedure is a 2D track ready for 3D fitting. The r-ϕ of the nearest circle to the beamline and the z_{vertex} from the VTX is combined to form a trial trajectory. Stereo hits within 1.5 mm of the trial trajectory are added, and the trial trajectory is recalculated, again with the hits with large residuals removed. In the end, a 3D track defined by 5 track parameters is found [40] [41].

A 3D track is a helical trajectory of a charged particle in a constant magnetic field with the axis of the helix along the solenoidal field. On an event display, looking down the beampipe, the arcs and the circles are the tracks (solid lines) derived from the hits (dots). The larger the transverse momenta of the charged particle, the less the magnetic field will deflect its trajectory and the straighter the path. With the lower momenta tracks (below 400 MeV), some of the low momenta charged tracks can spiral inward and do not pass enough CTC superlayers to be reconstructed. The neutral particles pass straight through the CTC undetected [41].

There are 5 parameters that define a helix, and hence a 3D track: d_0 (the impact parameter), c (the signed half-curvature), ϕ (the angle between the closest approach and the x-axis), $cot\theta$ (the cotangent of the spiral angle), and z_0 (the closest approach to the beamline). Figure 3.1 illustrates a few of them in the r-ϕ plane. Although

all of the parameters are indispensable, the impact parameter and the curvature usually have additional cuts further along the analysis process. First, a cut on the impact parameter is incorporated in quite of few analyses since the prompt tracks have impact parameters very close to the primary vertex whereas secondary tracks have impact parameters that are further away from the origin. For K_S production, the tracks are typically displaced from the origin so requiring tracks to exceed some minimum impact parameter value does indeed reduce the background. It is possible to increase the signal to noise ratio where the number of K_S is the signal and the number of background candidates is the noise. However, the number of K_S is reduced substantially and the impact parameter cut biases the p_T of the K_S (the greater the p_T of the K_S , the further the tracks are from the primary vertex, and thus, the greater the impact parameter values). As a result, an impact parameter cut is not implemented in this analysis. As for the curvature parameter value, the sign of c indicates the charge of the particle while the magnitude is inversely proportional to the diameter of the projected circle on the plane perpendicular to the beam. The half-curvature is also inversely proportional to the p_T, and later, there will be track cuts made on the p_T of each pion track from the K_S in order to optimize the efficiency of the CTC [41] [42].

3.3 The Primary Vertex Selection Criteria

As discussed earlier, of up to several primary z-vertices, only a single primary vertex is selected from where to initiate the search for the secondary vertices. Although it is possible to find the secondary vertices without the primary vertices, certain K_S variables (to be described later) depend upon identifying the "correct" primary vertex. Finding the "correct" primary vertex is complicated by multiple vertices from
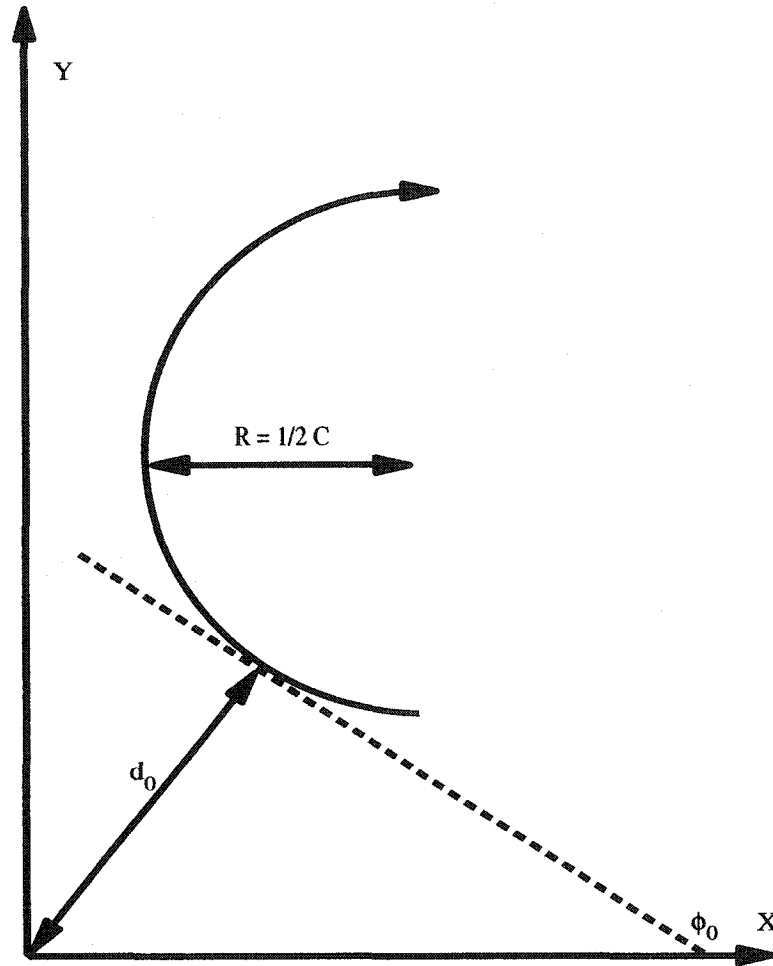
Figure 3.1: The track parameters

any given interaction as well as the multiple vertices from the multiple interactions. Depending upon the analysis, there are different methods of selecting an event vertex from a list of primary vertices for each event. Some select only the events with one event vertex [43], and some select the primary vertex nearest to the secondary vertex of the particle of interest [44]. Others correlate certain high momentum objects with the primary vertices, i.e. the z-coordinate of either a high p_T muon [44], electron [41], or jet [8]. Too many events are lost if the first method is selected. As for the second method, the sample may be biased by selecting only those K_S which
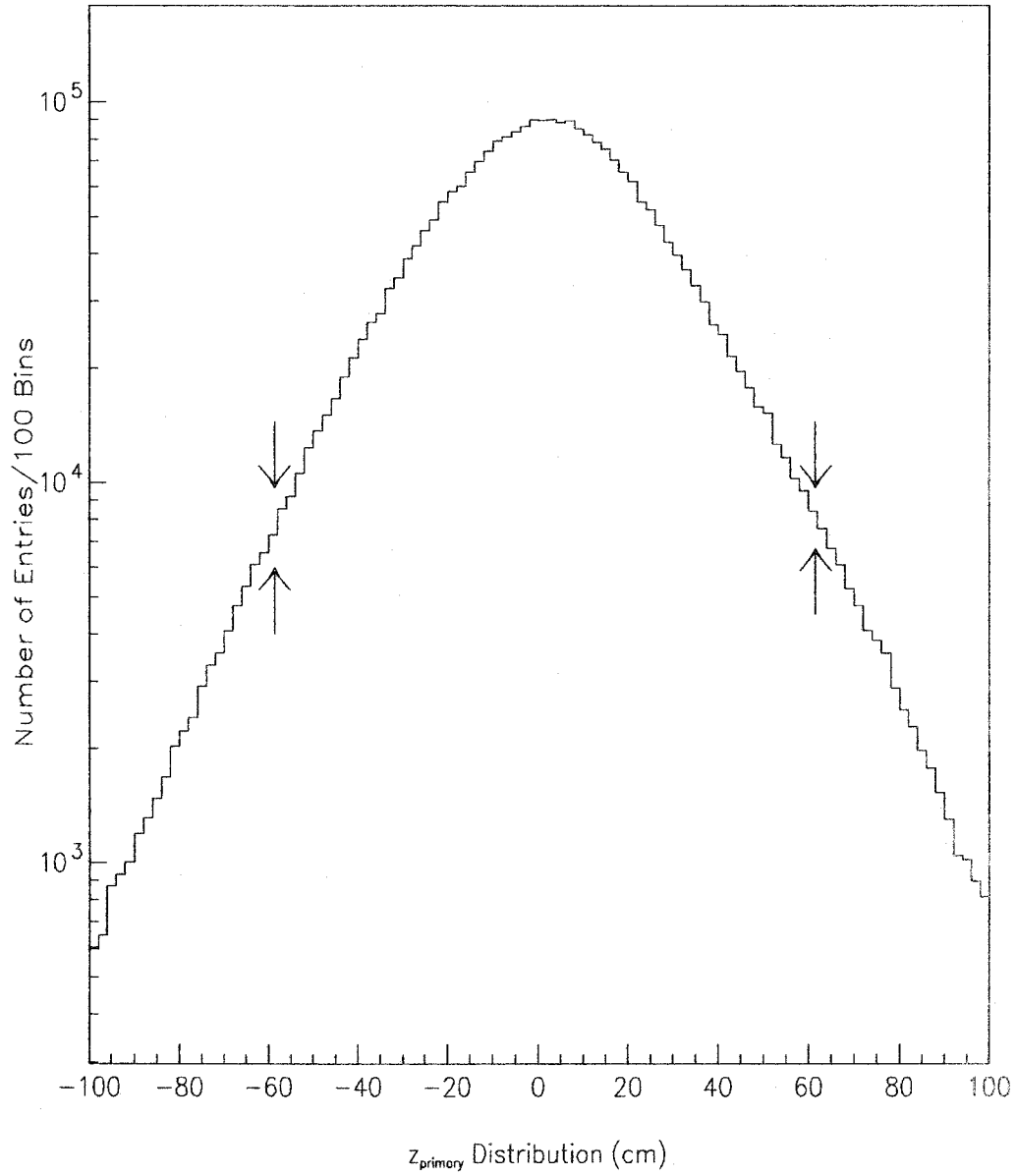
Figure 3.2: The $z_{primary}$ distribution. The cut of $|z_{primary}|<60.0$ cm is used.

decay close to the primary. There are just not enough high p_T objects in order to implement the third method without a tremendous loss of Minimum Bias events.

In this analysis, only the best quality vertex is used for each event, and this is quite common. The quality of a vertex is proportional to the number of hits in the VTX associated with a given vertex [6] [7] [8] [35].

One question which comes to mind immediately is what if the wrong vertex is chosen? The short answer is that a given K_S may be found to have a secondary vertex, but the particle is unlikely to point back to the primary vertex. There is a "pointing constraint" in the fitting routine. Whenever a secondary vertex is found, this "pointing constraint" checks to see that it appears to have originated from the selected primary vertex. In particular, this pointing constrait is enforced when a cut is made on the value of the χ^2 (the χ^2 will be discussed later) [45].

As for the other vertex components, they are considered to be linearly related to the beam spot size and the slope of the beam along the z direction in many analyses. However, the beam spot size is usually less than 40 μm [44], and the $c\tau$ of a K_S is on the order of a couple of centimeters [9]; hence, a $v_x = v_y = 0.0$ approximation is sufficient. On the other hand, for B-particles having $c\tau$ of about a few hundred microns [9], this approximation is not good.

3.4 The Secondary Vertex Selection Criteria

The secondary vertices are the crux of the analysis. A combined geometric and kinematic fitting routine called CVTMFT is utilized to recognize when a group of tracks originate from a given space point other than the primary vertex. CTVMFT looks for the arcs that intersect at any point in the x-y plane given the track parameters of the potential daughters. Then, the 3D secondary vertex reconstruction incorporates the remaining coordinate information. Other physical constraints, such as either daughter particles having certain masses or the momentum of the parent

must point back to the primary vertex, are applied in order to reduce the errors of the result.

The best manner to understand how CTVMFT locates the secondary vertices is to discuss an example, $K_S \rightarrow \pi^+\pi^-$. First, the daughter tracks must originate from the same space point. In this case, the pions must originate at the point where the K_S decays. If either the particle or its daughters has its mass known, additional mass constraints can be set to find the secondary vertex. Here, the K_S decaying into pions is the process sought, so the known masses of the pions is added to the kinematic constraints of the fit. Usually, the daughter masses are fixed and the unknown parent mass is left as a floating value. This is optional in CVTMFT, but this analysis depends on this feature. Also, there exists another optional constraint that the secondary vertex must point back to the primary vertex (or another arbitrary direction). This assumption is reasonable since most K_S will be originating directly from the primary vertex or from another particle that points back to the primary vertex. Once the constraints are settled upon, CTVMFT can sort through pairs of tracks to check which meet all the constraints.

The CVTMFT algorithm begins with the initial track parameters of the two tracks and adjusts the track parameters in order to minimize χ^2 equations consisting of all constraints applied concurrently. To elaborate, in its simplest form, χ^2 is the sum of a set of linear equations that are the functions of the differences between geometric and kinematic values of the tracking parameters as well as the error matrix of these tracking parameters. Other constraints such as a pointing constraint only add to the number of free parameters. In order for χ^2 to be minimized, these non-linear derivative equations of χ^2 with respect to every free parameter is equal to zero. These χ^2 derivative equations are thus expanded into a Taylor series with only

Table 3.2: The number of K_S after each successive cut. Errors are taken from the fit of the area of the Gaussian.

Cuts	Number of K_S	Fraction of K_S Remaining
Only Cosmic Filter	125992 ± 1323	1.063 ± 0.016
Badrun	125991 ± 1323	1.063 ± 0.016
$\|z_{primary}\| < 60.0$ cm	118570 ± 1291	1.000
$\chi^2_{KS} < 20.0$	95490 ± 938	0.805 ± 0.012
$\|z_{KS} - z_{primary}\| < 3.0$ cm	92186 ± 911	0.777 ± 0.011
$p_T^{TracksfromKS} > 300$ MeV	82957 ± 813	0.700 ± 0.010
$\|\eta^{KS}\| < 1.0$	67221 ± 696	0.567 ± 0.009
3D Displacement$^{KS} > 1.0$ cm	61562 ± 562	0.519 ± 0.007
$\cos\theta_{PD}{}^{KS} < 0.990$	56941 ± 441	0.480 ± 0.006

the linear terms being kept. Then, these linear χ^2 equations are solved, and the solutions are substituted again for the generation of a new set of the χ^2 derivative equations. Again, the process of Taylor expanding and solving these sets of linear χ^2 equations is iterated several times. Convergence of the solutions is not guaranteed. Later, a $\chi^2 < 20.0$ cut is applied in this analysis to reduce the number of diverging fits for K_S candidates.

In the end, when a pair of tracks is found to have originated from a secondary vertex, then the adjusted track parameters, the adjusted vertices, and the coordinates of the secondary vertex are returned. It is very important to state that the track parameter values and displacement values are altered by CTVMFT during the secondary fitting process. However, the differences are slight. Most of the candidates CVTMFT keeps are not K_S, or any real particles for that matter, but rather just background of pairs of tracks. If these adjusted tracks can both be extrapolated back to the secondary vertex, then the mass and the momentum of the parent is calculated [45].

3.5   The K_S Selection Criteria

To reiterate, only the first in a list of primary vertices is considered as the event vertex. By convention, this is the best quality vertex. In addition to the primary vertex, every oppositely charged pair of "good" 3D CTC tracks (with each track p_T above 200 MeV) is put through a V-Finder (CTVMFT) to be considered as candidates for K_S . A "good" 3D track has either at least 2 axial superlayers with at least 4 hits each and 1 stereo superlayer or some other stringent combination of axial hits and stereo information [46]. The V-Finder checks to see whether a given pair of tracks, whose masses are assumed to be those of pions, intersect within a region of 3D space and their summed total momentum points back to the primary vertex. In addition, each individual track must not only intersect but also to have originated from the calculated secondary vertex returned by the V-Finder. If these criteria are satisfied, the tracks of the daughter particles are taken by another routine that reconstructs the 4-vector of the parent particle. If the "parent" mass calculated is within 0.45 and 0.55 GeV, approximately ± 50 MeV around the mass of a K_S , then it is booked according to the mass window it falls under and is considered as a valid candidate that can be further studied [41] [43] [47] [48].

These candidates undergo successive cuts in order to increase the signal to noise ratio. The effect of each cut is shown in Table 3.2, and a description of each cut will be detailed below.

The χ^2 Cut

For every fit, a χ^2 is returned from the fitting routine, and this value is considered as a check to the accuracy of the fit. The rapidly decreasing tail distribution runs from 0.0 to a number that increases with the added constraints. In particular, the pointing back criteria broadens this distribution because it includes the primary

vertex errors in this calculation. The χ^2 cut is not a particularly useful one; it acts on both the background and the signal in the same manner and does little to significantly enhance the signal to noise ratio. However, a $\chi^2 < 20.0$ does eliminate candidates with extremely bad CTVMFT fits. In the top of Figure 3.3, the cut at $\chi^2 = 20.0$ is denoted by arrows as well as the effect of the reconstructed mass spectrum after the cut [41] [43] [45] [47] [48].

The $|z_{KS}\text{-}z_{primary}|$ Cut

The z_{KS} value refers to z-coordinate obtained after extrapolating the momentum of the K_S back to the beamline. This value is calculated using a slope equation in the following manner:

$$z_{KS} = v_z^{KS} - v_x^{KS} \frac{p_z^{KS}}{p_x^{KS}}. \tag{3.1}$$

The smaller the scalar difference between z_{KS} and the primary vertex, the more likely the K_S originates from the primary vertex. In the bottom of Figure 3.3, the difference between the extrapolated z_{KS} and the primary vertex is plotted along with arrows at ± 3.0 cm to indicate the cut values [41] [43] [47] [48].

The Cut on the p_T of the Tracks

Although the CTC can measure the individual track momenta down to 200 MeV and many other studies utilize a 400 MeV track cut, this analysis will implement a 300 MeV track cut. Low momenta tracks, below 400 MeV, are more likely to loop in circles inside the CTC rather than emerge from it when compared to charged tracks with higher momenta. Moreover, the lower the track p_T, the more likely the track will not have as many hits in the CTC. Both of these effects cause not only a decrease in the single track efficiency (and consequently the K_S efficiency) but also produces a large charge asymmetry for low momenta tracks. However, the K_S have a large dependence on the track p_T cut. This is because most K_S are generated

with relatively low p_T (below 3.0 GeV), and since the track efficiencies have a strong track p_T dependence, it follows that the K_S also have a strong dependence on the track p_T. Far too many K_S would be lost in the Minimum Bias set because the K_S are produced more abundantly with lower momenta. In particular, a 400 MeV track cut would have 70556 ± 827 K_S and a 300 MeV track cut 104673 ± 1133 K_S ; this difference between the two cuts is about a third of the K_S . To reduce the charge asymmetry and move into a p_T track range where the CTC functions more efficiently without losing too many K_S , a 300 MeV track cut is selected. In top of Figure 3.4, the track cut is shown with the arrows as is the effect on the reconstructed K_S mass spectra from the preceding cut [41] [43] [47] [48].

The η Cut

The K_S must have an η less than 1.0. Beyond this η range, the acceptance of the CTC is more limited, and hence, the track efficiency, along with the K_S efficiency, drops significantly. The η cut is displayed in the bottom of Figure 3.3 along with the mass distribution following the this cut [41] [43] [47] [48].

The 3D Displacement Cut

The 3D displacement is defined as the magnitude of the displacement between the secondary and the primary vertices. In particular, in the following equation:

$$3D\,Dis = \sqrt{(v_x^{secondary} - v_x^{primary})^2 + (v_y^{secondary} - v_y^{primary})^2 + (v_z^{secondary} - v_z^{primary})^2}$$

$$(3.2)$$

where $v_x^{primary}$, $v_y^{primary}$, and $v_z^{primary}$ denote the location of the primary vertex, and $v_x^{secondary}$, $v_y^{secondary}$, and $v_z^{secondary}$ give the coordinates of the secondary vertex. Both vertices are measured with the respect to the origin of the detector. The 3D displacement of the K_S candidates, 3D Dis, is must be greater than 1 cm to kept

for further study. In the top of Figure 3.5, the 3D displacement is histogramed with the value of the cut being denoted by the arrows, and the effect of the cut on the reconstructed mass spectrum is also shown [41] [43] [47] [48].

The Pointing Vector ($\mathbf{Cos(\theta_{PD})}$) Cut

The pointing vector value is just the dot product of the 2D momentum vector and the 2D displacement divided by the product of the scalar values of the 2D momentum and 2D displacement. This value ensures that the momentum is along the displacement and is just the cosine of the angle between the 2D momentum and 2D displacement vectors. The pointing vector clusters around either -1 or 1. If the value is around -1, the candidate is traveling in the direction opposite to its displacement. In this case, the candidate is probably background. The closer the pointing vector value is to 1.0, the better the candidate. In the bottom right of Figure 3.5, the 2D pointing vector is plotted and beside the K_S which pass a 0.990 pointing vector cut. The 2D version of this cut has better resolution than the 3D version because of the differences between the z-r-ϕ and r-ϕ resolution. Again, the momentum and secondary vertex values are calculated using the CTVMFT fitting routine, and the primary vertex is taken from the VTX [41] [45].

Below is a summary of the cuts used for K_S .

- K_S Cuts

    - $\chi^2_{KS} < 20.0$

    - $|z_{KS}\text{-}z_{primary}| < 3.0$ cm

    - $p_T^{tracks\ from\ KS} > 300$ MeV

    - $|\eta^{KS}| < 1.0$

    - 3D Displacement$^{KS} > 1.0$ cm

$$- \cos\theta_{PD}{}^{KS} > 0.990$$
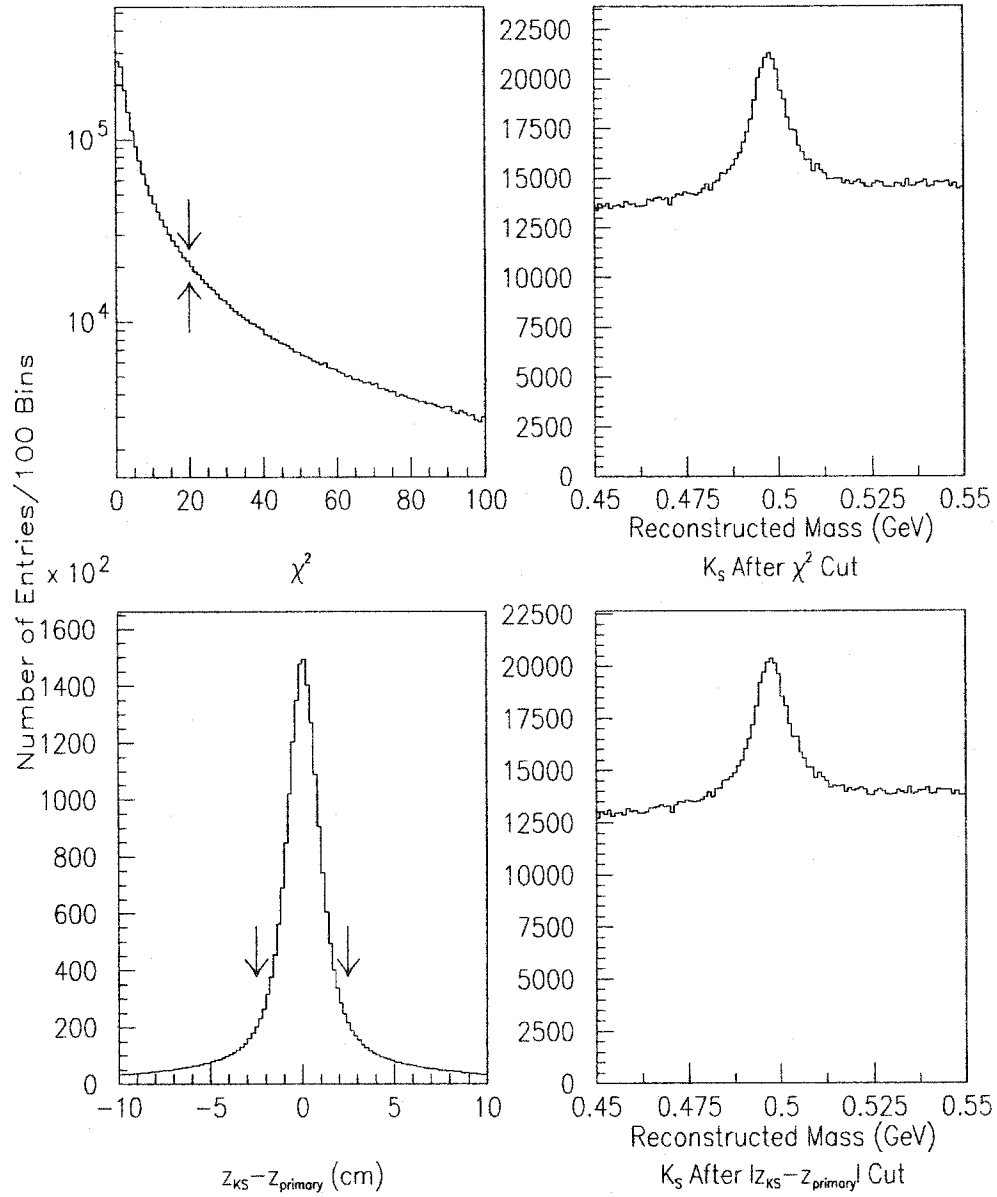
Figure 3.3: The χ^2 distribution (upper left) and the $|z_{KS}\text{-}z_{primary}|$ pointback distribution (lower left) are shown with arrows indicating the cut values. On the right side, the K_S mass distribution after each cut.
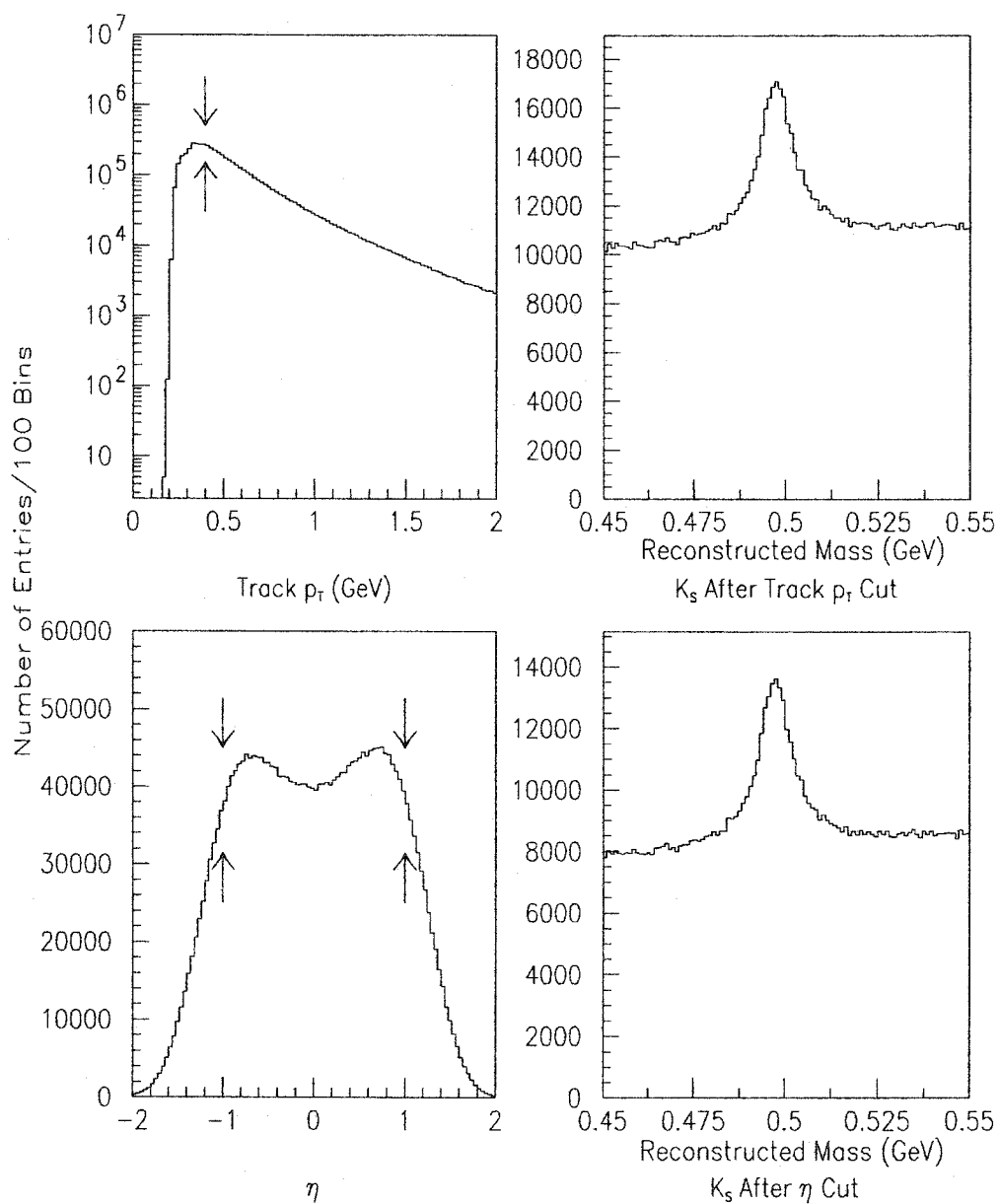
Figure 3.4: The track p_T distribution (upper left) and the η distribution (lower left) are shown with arrows indicating the cut values. On the right side, the K_S mass distribution after each cut.
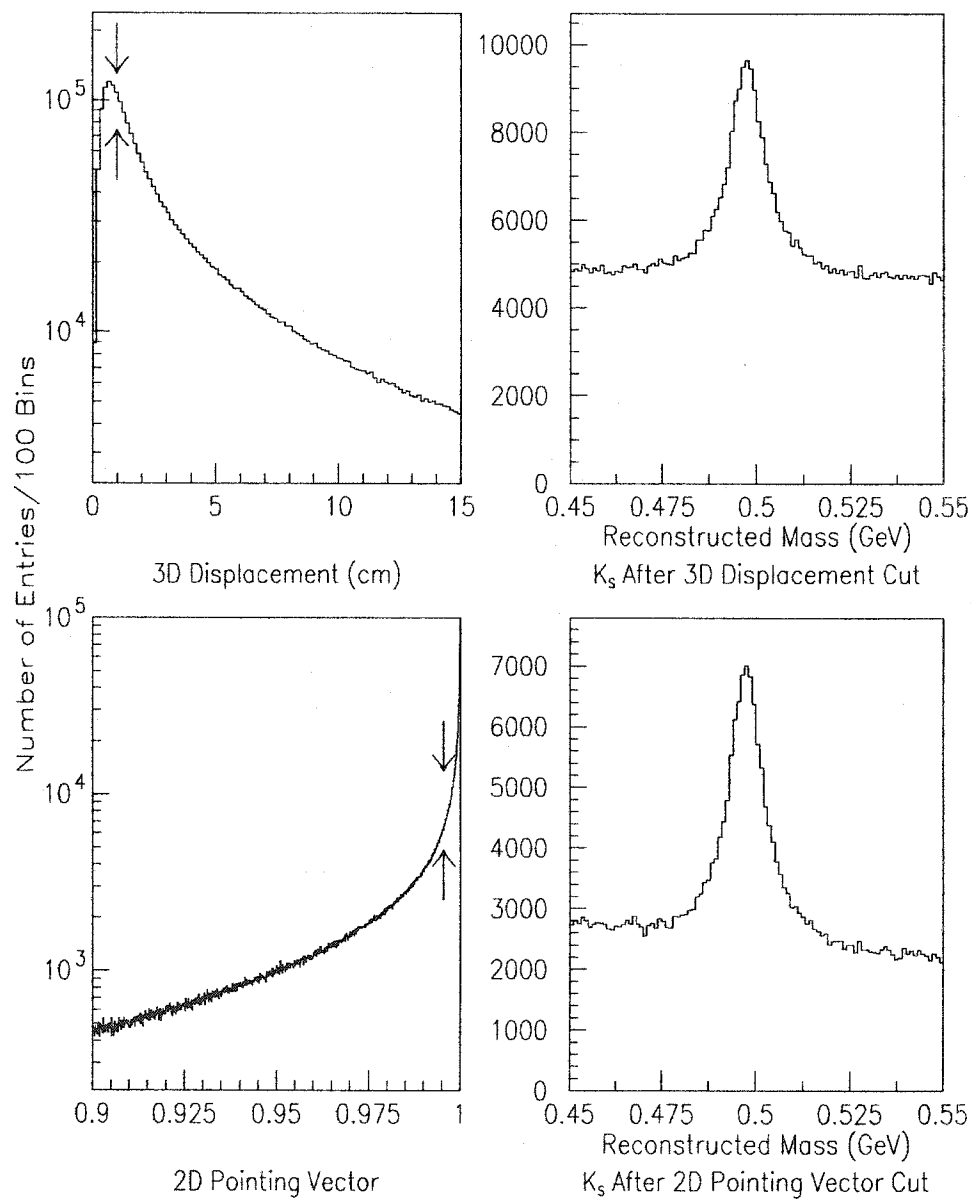
Figure 3.5: The 3D displacement distribution (upper left) and the 2D pointing vector distribution (lower left) are shown with arrows indicating the cut values. On the right side, the K_S mass distribution after each cut.

Chapter 4

Minimum Bias: Track Embedding Efficiencies

Not every particle produced in $p\bar{p}$ collisions is found by the CDF detector. So for every K_S within a given p_T range in the data, there are some that are missing. Hence, to correctly understand the physics, physics variables, such as the p_T spectrum, must be corrected for the efficiency. Many are lost due a variety of reasons: holes in coverage, lost hits, extra hits causing reconstruction software to incorrectly reproduce tracks, secondary vertices not found, and the cuts to reduce background that also diminish the signal. Every explanation of an efficiency loss depends on the plethora of conditions such as the properties of the particles, the resolution, and the coverage of the detector. It is quite impractical to account for every loss in efficiency. Instead, one variable is selected to correct for the efficiency of the K_S, and all other factors for every property for every reason are integrated together to yield an overall correction factor for a given p_T. The p_T variable is chosen because the CTC efficiency of finding a K_S is strongly correlated to the p_T of the individual daughter tracks from the parent particle which is itself is directly related to the p_T of the K_S. Another efficiency correction on a variable, called the $c\tau$ and will be defined later, is computed in order to check the Monte Carlo. The main goal of this chapter is to describe how and why the efficiency curves are generated [41].

73

4.1 An Overview

The information obtained from creating Monte Carlo K_S at a given p_T is converted into hits in the CTC; and, after rerunning reconstruction software, the K_S efficiency in data is determined for a given p_T. Once K_S p_T curves have been extracted from data, this efficiency curve as a function of p_T is employed to correct for the inefficiency of the CTC. In addition, with the identical track embedding data, $c\tau$ efficiency as function of p_T will also be determined.

Before describing the exact procedure, it is nice to visualize the track embedding concept. In Figure 4.1, a transverse view of the CTC is given for an event selected for track embedding. The dots in the event display are the actual hits in the CTC, and the fitting of these hits yields the tracks given by solid lines. Also, the greater the p_T, the less visible the curvature of a track. In Figure 4.2, the event in Figure 4.1 has had 3.0 GeV K_S embedded into it. The high p_T pion track is the new straight track, and the low p_T pion track is the new curved track. These new track embedded pion tracks intersect, forming a V, at the same space point the K_S decays. Note since only charged particles create hits in the CTC, only the charged pions from the embedded K_S can be seen directly. Thus, the neutral K_S are invisible to the CTC. However, some events in which track embedding is attempted does not successfully reveal a K_S even indirectly. The K_S , if the p_T is too large, can decay outside the CTC. Moreover, the K_S can escape down the beamline or slip through a crack so that it is never found. The daughter particles also may escape the detection of CTC, especially if the p_T of the individual tracks is too soft. This is quite often the case with pions and explains most of the loss of efficiency for K_S . The efficiency is given as the number of K_S found divided by the number of the events that K_S were track embedded into, and the next section outlines the procedure [41].

4.2 The Track Embedding Procedure

Step 1) Create text files of 4-vector and vertice data of K_S daughters.

Since K_S are assumed not to prefer any particular direction in either η ($|\eta|<2.0$) or ϕ ($0 \leq \phi < 2\pi$), K_S are generated one particle at a time at a specific p_T at random ϕ ($0 \leq \phi < 2\pi$) and random η ($|\eta|<2.0$) using a generator called FAKEEVENT [49]. Only K_S are present after the generator level, and K_S are actually decayed into charged pions in the CDFSIM detector simulator [50]. This is the case because it is possible that either the K_S may live long enough to decay in a region beyond the CTC or its daughters have low enough p_T so that the magnetic field of the solenoid might have a considerable effect on the tracks. Using the 4-vectors of the K_S from FAKEEVENT as input, the CDFSIM detector simulator determines where the particle decays inside the detector as well as calculates the 4-vectors of the daughters and the decay vertices. After both the FAKEEVENT generator and the CDFSIM detector simulator, a list of daughter 4-vectors, primary vertices, and secondary vertices are placed into a text file for K_S with a particular p_T. It is this information that will be ultimately be converted into CTC hits in a real data event [51].

Step 2) Select a Minimum Bias data embedding sample.

About 8,000 to 16,000 actual Minimum Bias events are needed for the track embedding study. The Minimum Bias events just pass the Minimum Bias triggers of the CDF detector, and hence each Minimum Bias event usually has a lower track multiplicity and fewer CTC hits when compared with higher p_T events such as jet events. The Minimum Bias sample comprising of the data described in Chapter 3 will not suffice because CTC hit information is dropped prior to the creation of this data set. Instead, the Minimum Bias sample actually taken for this Minimum Bias

track embedding analysis is the parent set of the Minimum Bias data in Chapter 3, before the hit information is lost. The track embedding sample is also checked to have a luminosity distribution similar to the actual data as well as pass all the criteria specified for a good Minimum Bias event. The event must pass quality event cuts outlined in Chapter 3, and a tally of good track embedding events is kept [41] [51].

Step 3) Embed K_S in Minimum Bias data.

For each data event, the daughter information from a Monte Carlo generated and detector simulated K_S at a given p_T is taken from the text file. First, both the primary and secondary vertices are translated so the primary vertices of the data and Monte Carlo event coincide. Then, the 4-vectors of the daughter particles are converted into track parameters using a routine called QTRKPR [52]. From these output track parameters, hits are then added to the CTC taking into account multiple scattering, $\frac{dE}{dx}$ effects, and wire hit efficiencies using another CDF program called CTADDH [53] developed for this purpose. Once hits are added to the data, reconstruction is rerun to produce a new list of tracks which code can then be applied to discover whether K_S can be found [28] [42] [51] [54] [55] [56] [57] [58].

Step 4) Finding the K_S in the track-embedded data.

The technique implemented in the search for K_S in the track embedding sample is for the most part identical to that outlined in Chapter 3 with the exception of employing a reconstructed K_S p_T window cut. Since the p_T of track embedded particle is known, the information can be utilized to separate the embedded K_S from K_S already present in the data set. Since CTC resolution is generally a decreasing function of p_T and would give rise to a broadening of the p_T distribution as p_T of the K_S increases, the p_T window must become larger as the p_T of K_S

increases. The p_T windows applied to each K_S p_T range is given by Table 4.1.

In Figure 4.3, the p_T windows are clearly marked by arrows in K_S p_T spectra produced after track embedding. Just as in the case with the reconstructed masses, 0.7 GeV, 1.6 GeV, 3.0 GeV, and 10.0 GeV embedded K_S with a 50 MeV, 100 MeV, 250 MeV, and 1.0 GeV p_T window cut values about the embedded p_T values are shown. Each peak in the p_T spectra represents the track embedded K_S , and its value shifts depending upon the embedded p_T value. Similarly, the resolution is directly proportional to the embedded p_T. In fact, in Figure 4.4, the p_T resolution increases from approximately 0.0045 GeV for 0.7 GeV track embedded K_S to about 0.1748 GeV for 10.0 GeV track embedded K_S . Again, the p_T windows should be wide enough to accept the embedded K_S as well as be sufficiently narrow in order to reduce the number of candidates already in the data set for being mistaken for those being embedded. It should be noted that the track embedded K_S resolutions are slightly narrower than the resolutions found in the Minimum Bias data.

Prior to p_T window cuts, the reconstructed masses of K_S candidates are shown in Figure 4.5. To help illustrate the effectiveness of the p_T window cut, in Figure 4.6, the reconstructed masses of K_S candidates are plotted for K_S that pass (dashed line) and fail (solid line) the p_T window cut. In this plot, 0.7 GeV, 1.6 GeV, 3.0 GeV, and 10.0 GeV embedded K_S with a 50 MeV, 100 MeV, 250 MeV, and 1.0 GeV p_T window cuts about the embedded p_T values are displayed. The peak in the solid line distribution are the K_S already present in the data prior to track embedding. Those K_S candidates that meet the p_T window criteria are fitted simultaneously with a 1st order polynomial and a Gaussian. Then, the 1st order polynomial, basically the fit of the background, is needed in order to subtract out the background from the mass plots which pass the p_T window cuts. The resulting fitted plots of the mass

distributions with the background subtracted out from them are shown in Figure 4.7. The resolution of the K_S approximately doubles from about 0.005 GeV for the 0.7 GeV case to approximately 0.010 GeV for the 10.0 GeV track embedded K_S .

The other K_S cuts along with the p_T window cut used in the generation of the p_T efficiency curve are given below:

- K_S in p_T efficiency study

    - Event Cuts

    - K_S must pass the p_T window cut given by Table 4.1.

    - $\chi^2_{KS} < 20.0$

    - $|z_{KS}\text{-}z_{primary}| < 3.0$ cm

    - $p_T^{tracks\ from\ KS} > 300$ MeV

    - $|\eta^{KS}| < 1.0$

    - 3D Displacement$^{KS} > 1.0$ cm

    - $\cos\theta^{KS}_{PD} > 0.990$

In Figures 4.8 through 4.10, the various cut values are shown for both the K_S candidates within a given p_T window (dashed line) and those K_S candidates which lie outside the p_T window (solid line). The solid line can be for the most part be considered as the background distribution whereas the dashed line contains mostly track embedded K_S candidates. The arrows indicate the cut values for each variable specified in the itemized list above. Moreover, this is done for both 1.6 GeV and 3.0 GeV track embedded K_S with p_T window cuts of 100 MeV and 250 MeV respectively. To be more specific, Figure 4.8 shows the χ^2_{KS} and $z_{KS}\text{-}z_{primary}$ distributions, Figure 4.9 displays the $p_T^{tracks\ from\ KS}$ and η^{KS} distributions, and Figure

4.10 histograms 3D Displacement^{KS} and $\cos\theta^{KS}_{PD}$ distributions. Furthermore, since the number of background is far greater than the track embedded K_S , these distributions are normalize to unity.

In Tables 4.2 through 4.4, the effect of each cut on the track embedded Monte Carlo is compared with the data for a p_T range that is approximately around the track embedded p_T value. The motivation of these ranges in the data is that there lacks sufficient statistics to compute K_S within extremely narrow p_T windows. As a result, K_S from the 0.7 GeV track embedded Monte Carlo are matched with K_S with p_T between 650 and 750 GeV in the data. Likewise, 1.6 GeV track embedded K_S are equated with 1.5-1.7 GeV K_S in data, and the 3.0 GeV track embedded K_S are set against the 2.75-3.25 GeV K_S in data. The percentage drops in Tables 4.2 through 4.4 are measured with respect to the χ^2_{KS} in order to demand K_S in the data to originate from the primary just like the K_S in track embedding sample. There is a very small effect of the χ^2_{KS} cut on the track embedded K_S , but the χ^2_{KS} cut effects the data by 20-40%. This is believed to be due to K_S in the data not originating from the leading primary vertex. These K_S that would fail the pointing criteria, and subsequently, the χ^2_{KS} cut. However, the agreement after the χ^2_{KS} is good to a few percent with the exception of the 0.7 GeV case of the $\cos\theta^{KS}_{PD}$ cut where the difference is on the order of 15%.

Step 5) Calculate efficiencies with the new track-embedded data set. For every track embedded p_T value, the number of K_S found after cuts is divided by the number of track embedded events, and this process repeats for a multitude of different p_T values between 0.5 GeV and 10.0 GeV. In particular, the number of K_S after cuts is computed by summing K_S candidates between 0.48 and 0.52 GeV after the background has been subtracted out. For cases where the efficiencies

Table 4.1: The p_T window ranges for a given K_S p_T.

p_T Range of K_S (GeV)	p_T Window Range (MeV)
$p_T \leq 1.4$	50.0
$1.4 < p_T \leq 1.8$	100.0
$1.8 < p_T \leq 2.3$	150.0
$2.3 < p_T \leq 3.0$	250.0
$3.0 < p_T \leq 5.0$	500.0
$5.0 < p_T \leq 10.0$	1000.0

Table 4.2: The number of K_S after each successive cut for $p_T = 0.7$ GeV. Errors are taken from the fit of the area of the Gaussian. There are 16677 K_S embedded in $|\eta| < 2.0$, and events pass all cuts.

Cuts	Number of K_S in MC	%	% in Data (.65-.75 GeV)
After Event Cuts	$2186. \pm 61.$	1.015 ± 0.0384	1.421 ± 0.0384
$\chi^2_{KS} < 20.0$	$2153. \pm 55.$	1.000	1.000
$|z_{KS} - z_{primary}| < 3.0$ cm	$2092. \pm 54.$	0.972 ± 0.0353	0.943 ± 0.0353
$p_T^{tracks\ from\ KS} > 300$ MeV	$1556. \pm 46.$	0.723 ± 0.0282	0.740 ± 0.0282
$|\eta^{KS}| < 1.0$	$1261. \pm 40.$	0.586 ± 0.0239	0.576 ± 0.0239
3D Displacement$^{KS} > 1.0$ cm	$1075. \pm 36.$	0.499 ± 0.0210	0.507 ± 0.0210
$\cos \theta^{KS}_{PD} > 0.990$	$998. \pm 33.$	0.464 ± 0.0194	0.412 ± 0.0194

are low (i.e. p_T below 1.0 GeV), about 16,000 Minimum Bias events are needed to calculate the efficiency for those p_T intervals. Then, every computed efficiency point is plotted against p_T with errors from the fit in order to produce plots in Figures 4.11. In Figure 4.11, the upper portion consists of each efficiency point as a function of p_T. The lower left plot has the front end (below 4 GeV) fitted with a 6th order polynomial, and the lower right plot has the back end (above 4 GeV) fitted with a 1st order polynomial. These fitted curves are later taken to correct the background subtracted p_T distribution of the K_S in the data.

Table 4.3: The number of K_S after each successive cut for $p_T = 1.6$ GeV. The errors are taken from the fit of the area of the Gaussian. There are 8028 K_S embedded in $|\eta| < 2.0$, and events pass all cuts.

Cuts	Number of K_S in MC	%	% in Data (1.5-1.7 GeV)
After Event Cuts	$3222. \pm 62.$	1.026 ± 0.0278	1.174 ± 0.0278
$\chi^2_{KS} < 20.0$	$3141. \pm 60.$	1.000	1.000
$|z_{KS}\text{-}z_{primary}| < 3.0$ cm	$3109. \pm 59.$	0.990 ± 0.0267	0.972 ± 0.0267
$p_T^{tracks\ from\ KS} > 300$ MeV	$2961. \pm 58.$	0.943 ± 0.0258	0.944 ± 0.0258
$|\eta^{KS}| < 1.0$	$2397. \pm 51.$	0.763 ± 0.0218	0.775 ± 0.0218
3D Displacement$^{KS} > 1.0$ cm	$2219. \pm 49.$	0.706 ± 0.0206	0.736 ± 0.0206
$\cos\theta^{KS}_{PD} > 0.990$	$2221. \pm 48.$	0.707 ± 0.0204	0.715 ± 0.0204

Table 4.4: The number of K_S after each successive cut for $p_T = 3.0$ GeV. The errors are taken from the fit of the area of the Gaussian. There are 8028 K_S embedded in $|\eta| < 2.0$, and events pass all cuts.

Cuts	Number of K_S in MC	%	% in Data (2.75-3.25 GeV)
After Event Cuts	$3978. \pm 68.$	1.011 ± 0.0242	1.199 ± 0.0242
$\chi^2_{KS} < 20.0$	$3937. \pm 66.$	1.000	1.000
$|z_{KS}\text{-}z_{primary}| < 3.0$ cm	$3912. \pm 67.$	0.994 ± 0.0238	0.979 ± 0.0238
$p_T^{tracks\ from\ KS} > 300$ MeV	$3831. \pm 66.$	0.973 ± 0.0234	0.968 ± 0.0234
$|\eta^{KS}| < 1.0$	$3131. \pm 58.$	0.795 ± 0.0198	0.823 ± 0.0199
3D Displacement$^{KS} > 1.0$ cm	$3008. \pm 57.$	0.764 ± 0.0193	0.768 ± 0.0193
$\cos\theta^{KS}_{PD} > 0.990$	$3005. \pm 57.$	0.763 ± 0.0193	0.748 ± 0.0193

4.3   The $c\tau$ Corrections

One efficiency correction that will not appear again when studying jet events is that of the proper lifetime, $c\tau$, of K_S . The proper life time, $c\tau$, is given by the following equation:

$$c\tau = \frac{M_{KS}D_{KS}}{P_{KS}} \tag{4.1}$$

where P_{KS} is the 3D momentum of the K_S , D_{KS} is the 3D displacement of the K_S , and M_{KS} is the mass of the K_S . Although $c\tau$ is regarded as a positive quantity, a measurement error in any component in either P_{KS} or D_{KS} can give rise to negative values [40] [59] [60]. Since the statistics are typically much smaller for negative $c\tau$ values, the positive $c\tau$ values are studied. These $c\tau$ efficiency corrections will be incorporated into the $c\tau$ measurements in Chapter 5. The goal is not to measure the $c\tau$ itself but instead to check the accuracy of the efficiency corrections. The more precise the resulting efficiency-corrected $c\tau$, the better the efficiency curve actually is.

The experimental check is not actually the $c\tau$ distribution itself but rather the negative of the reciprocal of the slope of the decaying exponential of the $c\tau$ distribution. For K_S , the accepted value is about 2.6786 ± 0.0024 cm [9]. Although the $c\tau$ of particle depends upon the weighted average of each decay channel, the experimental value is sufficient for comparison since most decay channels have the same $c\tau$. It is important to note that K_S decaying from other particles, such as $B^0 \rightarrow K_S + J/\Psi$ or $D_0 \rightarrow K_S +$ anything, will have a $c\tau$ that will be slightly larger than the prompt experimental value. However, B^0 and D_0 have very small $c\tau$ themselves [9] [61], so the difference is negligible.

The $c\tau$ distributions of K_S at specific p_T values are produced with the following

K_S cuts:

- Sample K_S in $c\tau$ Study

    - Event Cuts

    - K_S must pass the p_T window cut given by Table 4.1.

    - $\chi^2_{KS} < 20.0$

    - $|z_{KS} - z_{primary}| < 3.0$ cm

    - $p_T^{tracks\ from\ KS} > 300$ MeV

    - $|\eta^{KS}| < 1.0$

    - 3D Displacement$^{KS} > 1.0$ cm

These cuts are looser than those taken to calculate the K_S p_T efficiencies since some cuts are more likely to sculpt the $c\tau$ spectrum than others. Moreover, applying all cuts may not yield enough statistics at certain p_T values in order to get an accurate enough measurement of the absolute value of the slope of the $c\tau$. Regardless of cuts, the efficiency curves once applied to the data would yield approximately the same result with the exception of mild discontinuities in the final efficiency-corrected $c\tau$ plot. The cuts incorporated here do not bias the $c\tau$ measurement beyond 1.0 cm, and in the end, the slope of the final $c\tau$ spectrum in Chapter 5 is relatively smooth without dips or bumps above a $c\tau$ of 1.0 cm.

A subtle problem will now be described. After the p_T window cut, the $c\tau$ can be plotted for K_S masses between 0.48 and 0.52 GeV (central region). Similarly, the $c\tau$ distributions can also be plotted from 0.45 to 0.48 GeV as well as 0.52 to 0.55 GeV (sideband regions). Ideally, the $c\tau$ distributions would be null histograms in sideband regions; however, they are not. Instead, there exists background $c\tau$ values

that appear in the sidebands. This is not the concern. The issue is that there are such background $c\tau$ in the central region as well. Hence, when the $c\tau$ of this central region is plotted, it includes the $c\tau$ of the K_S plus a very unwanted fraction of $c\tau$ from the background candidates. Background subtraction is a process employed in order to remove unwanted background $c\tau$ from the central mass region.

Background subtraction is process outlined as follows. First, compute the total number of K_S in both of the sidebands (N_{s1}^{total}, N_{s2}^{total}), the central region (N_c^{total}), and the total number of K_S in the central region after subtracting the background (N_{KS}). Second, calculate the fraction of the background within the central peak as follows:

$$fraction = \frac{N_c^{total} - N_{KS}^{total}}{N_{s1}^{total} + N_{s2}^{total}} \tag{4.2}$$

Then, subtract from the $c\tau$ of the central region the sum of the $c\tau$ distributions of the sidebands by the fraction calculated from equation 4.2. Similarly, propagate the errors bin by bin with this fraction accordingly:

$$error = \sqrt{N_c^{bin} + fraction * (N_{s1}^{bin} + N_{s2}^{bin})} \tag{4.3}$$

where the number of particles in a given bin for the central region and the two sidebands are expressed as N_c^{bin}, N_{s1}^{bin}, and N_{s2}^{bin}. After this background procedure, the resulting $c\tau$ of the central region has had these background $c\tau$ removed. The slopes from each $c\tau$ distributions at a given p_T are plotted against the p_T of the embedded K_S in Figure 4.12.

Again, the slope of the $c\tau$ distribution is actually the negative reciprocal of the experimental measured $c\tau$. For the implementation of these adjustments, it simpler to correct for the positive inverse of the experimental value, or in other words, just

the absolute value of the slope of the $c\tau$ distribution. At large $c\tau$, particles decay deeper into the CTC such that the inner layers of the CTC have less hits. This explains the drop from the expectation value at high $c\tau$ (or increase in the absolute value of the slope), see Figure 4.12. The high $c\tau$ corrections effect the tail of the data distribution the most (high absolute value of the slope), where there are few K_S . In Chapter 5, the efficiency-corrected $c\tau$ will be computed from the data [62].

```
Run 59911 Event 8147    testbefore.ybs              6JUN94 12:34:27 25-Nov-02

      Pt    Phi   Eta    Et(-vec)=    1.0 GeV
z_1= -19.1,  3 trk        Phi = 180.0 Deg          Emax =    0.9 GeV
    -0.6    56  1.77     Sum Et =    0.0 GeV
     0.2   137  0.99
     0.2    37 -0.14




Hit & to refresh                                          PHI:    147.
                                                          ETA:    1.77
```
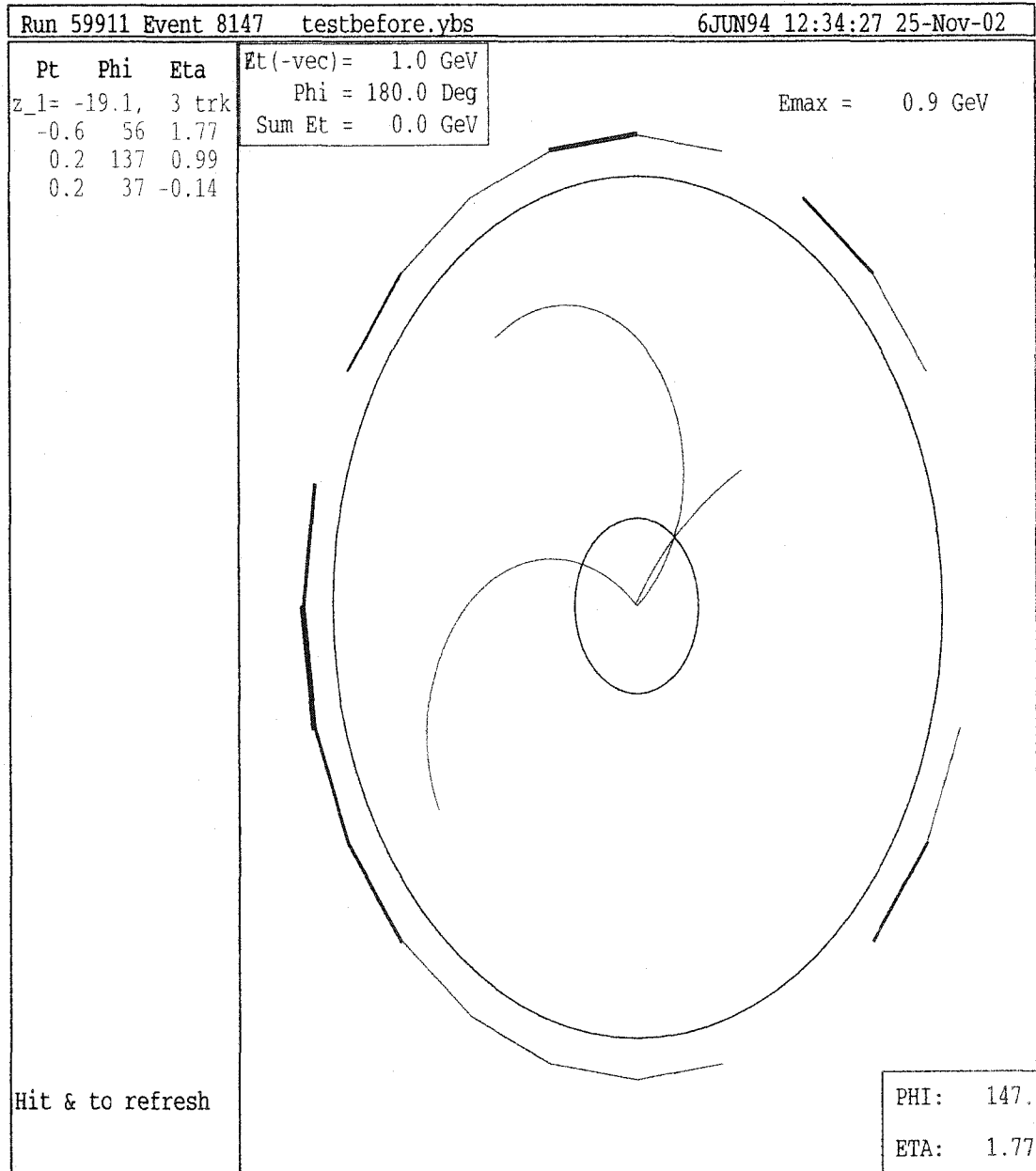
Figure 4.1: A transverse view of a Minimum Bias event. A K_S has not yet been track embedded.
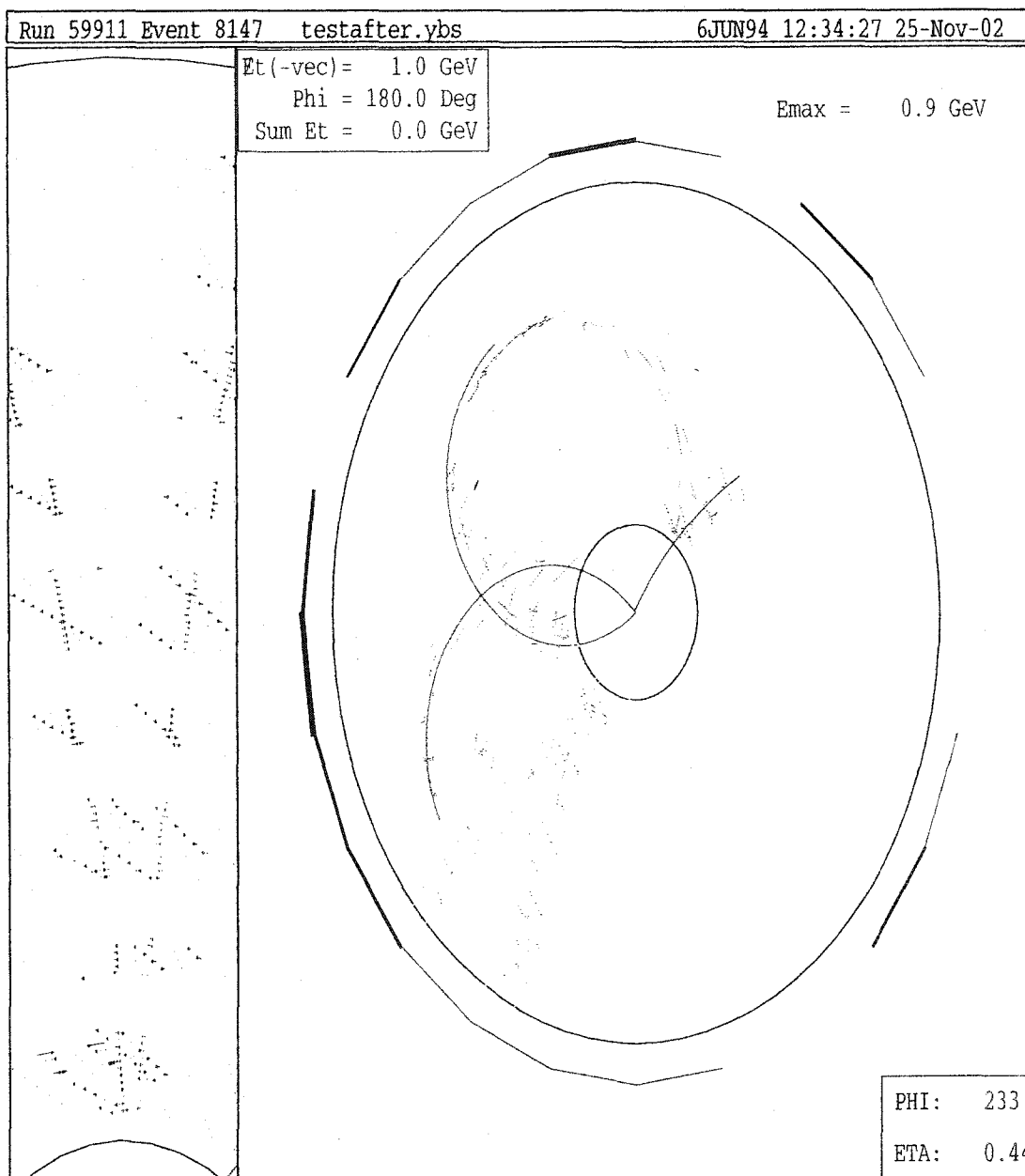
Figure 4.2: A transverse view of a Minimum Bias event with a 3.0 GeV track-embedded K_S. The K_S consists of two tracks intersecting to form a "V". This is not seen in Figure 4.1. The curved tracks have less transverse momenta than the tracks with less curvature.
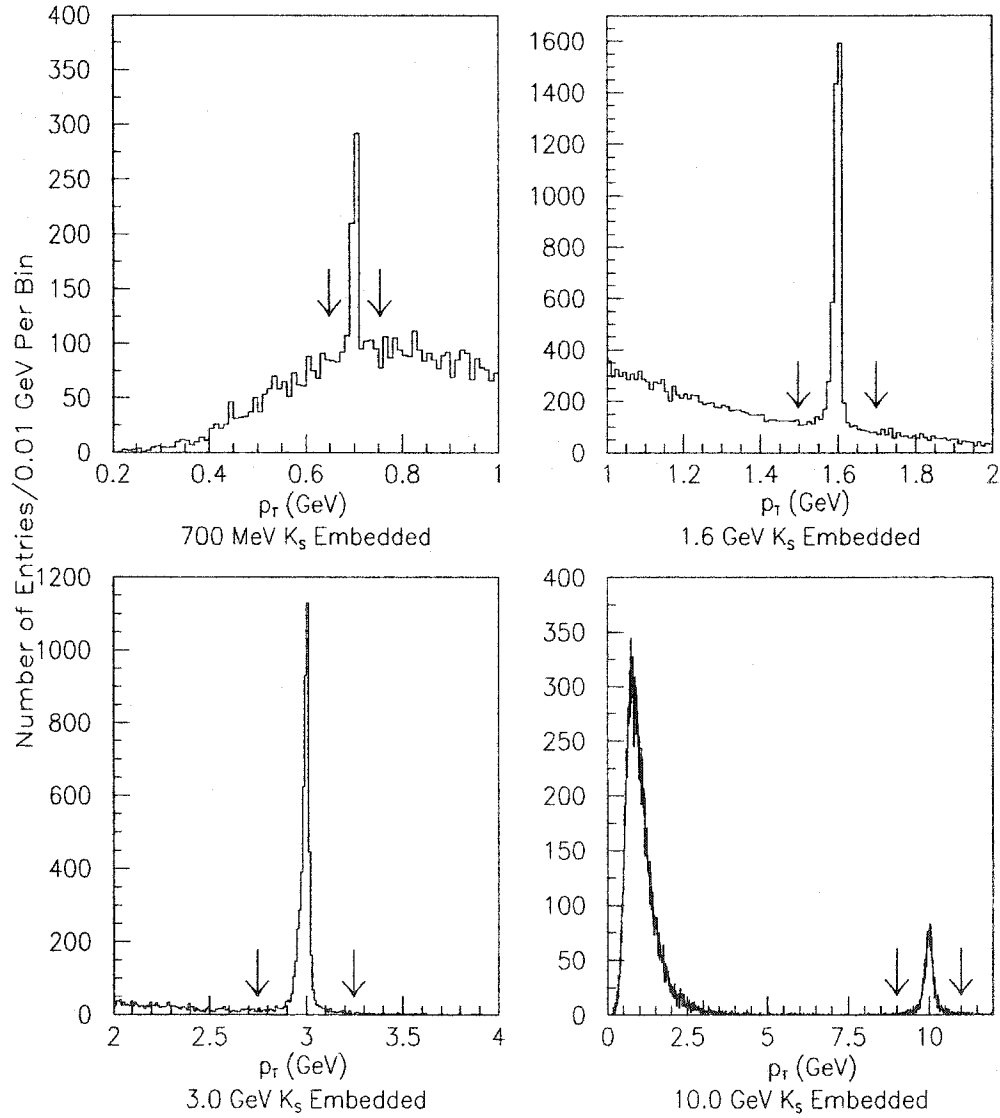
Figure 4.3: The p_T distribution of K_S candidates after track embedding. The p_T distributions of 0.7 GeV, 1.6 GeV, 3.0 GeV, and 10.0 GeV K_S candidates with arrows indicating p_T window cuts. The p_T windows are 50 MeV, 100 MeV, 250 MeV, 1.0 GeV for 0.7 GeV, 1.6 GeV, 3.0 GeV, and 10.0 GeV K_S. These are based upon 10004 events for the 0.7 GeV case and 8668 events for the 1.6 GeV, 3.0 GeV, and 10.0 GeV cases. These distributions are of K_S embedded into $|\eta|<2.0$ prior to the event cuts.
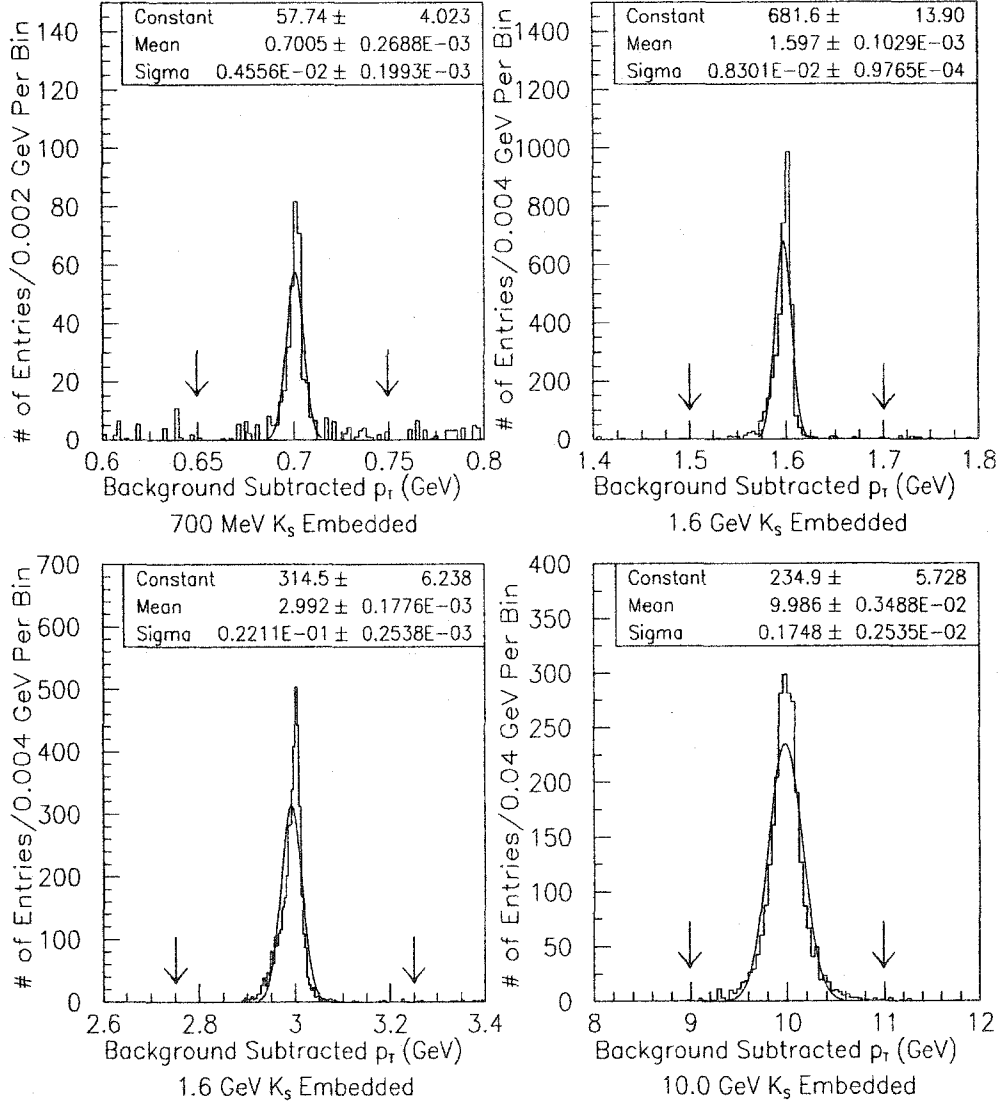
Figure 4.4: The p_T distributions of K_S candidates after background subtraction fitted with a gausian. The fitted background subtracted p_T distributions of 0.7 GeV, 1.6 GeV, 3.0 GeV, and 10.0 GeV K_S candidates with the p_T windows being 50 MeV, 100 MeV, 250 MeV, 1.0 GeV for 0.7 GeV, 1.6 GeV, 3.0 GeV, and 10.0 GeV K_S. These are based upon 10004 events for the 0.7 GeV case and 8668 events for the 1.6 GeV, 3.0 GeV, and 10.0 GeV cases. These distributions are of K_S embedded into $|\eta|<2.0$ prior to the event cuts.
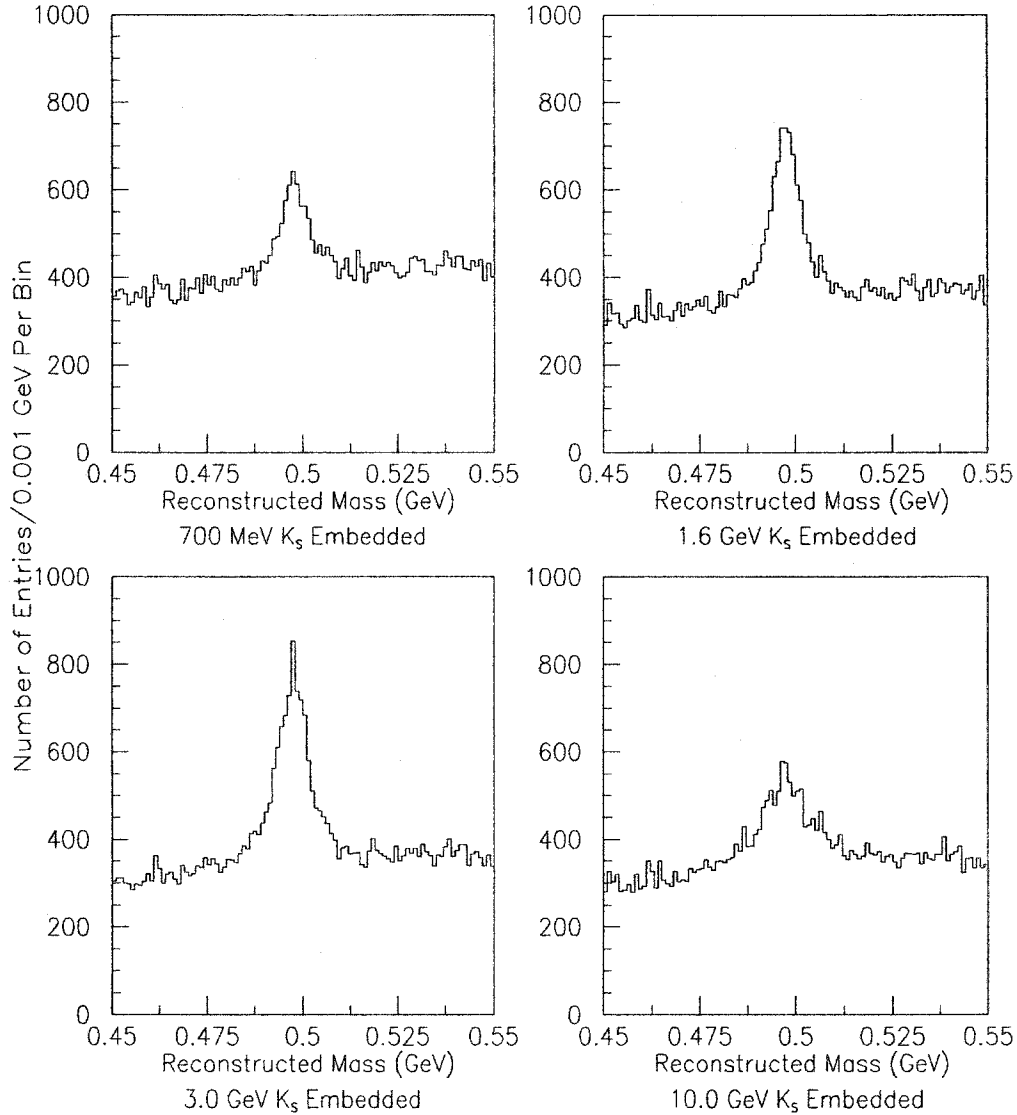
Figure 4.5: The mass distribution of K_S candidates after track-embedding. The mass distributions of 0.7 GeV, 1.6 GeV, 3.0 GeV, and 10.0 GeV K_S candidates that pass (dashed line) and fail (solid line) p_T window. The p_T windows are 50 MeV, 100 MeV, 250 MeV, 1.0 GeV for 0.7 GeV, 1.6 GeV, 3.0 GeV, and 10.0 GeV K_S. These are based upon 10004 events for the 0.7 GeV case and 8668 events for the 1.6 GeV, 3.0 GeV, and 10.0 GeV cases. These distributions are of K_S embedded into $|\eta|<2.0$ prior to the event cuts.
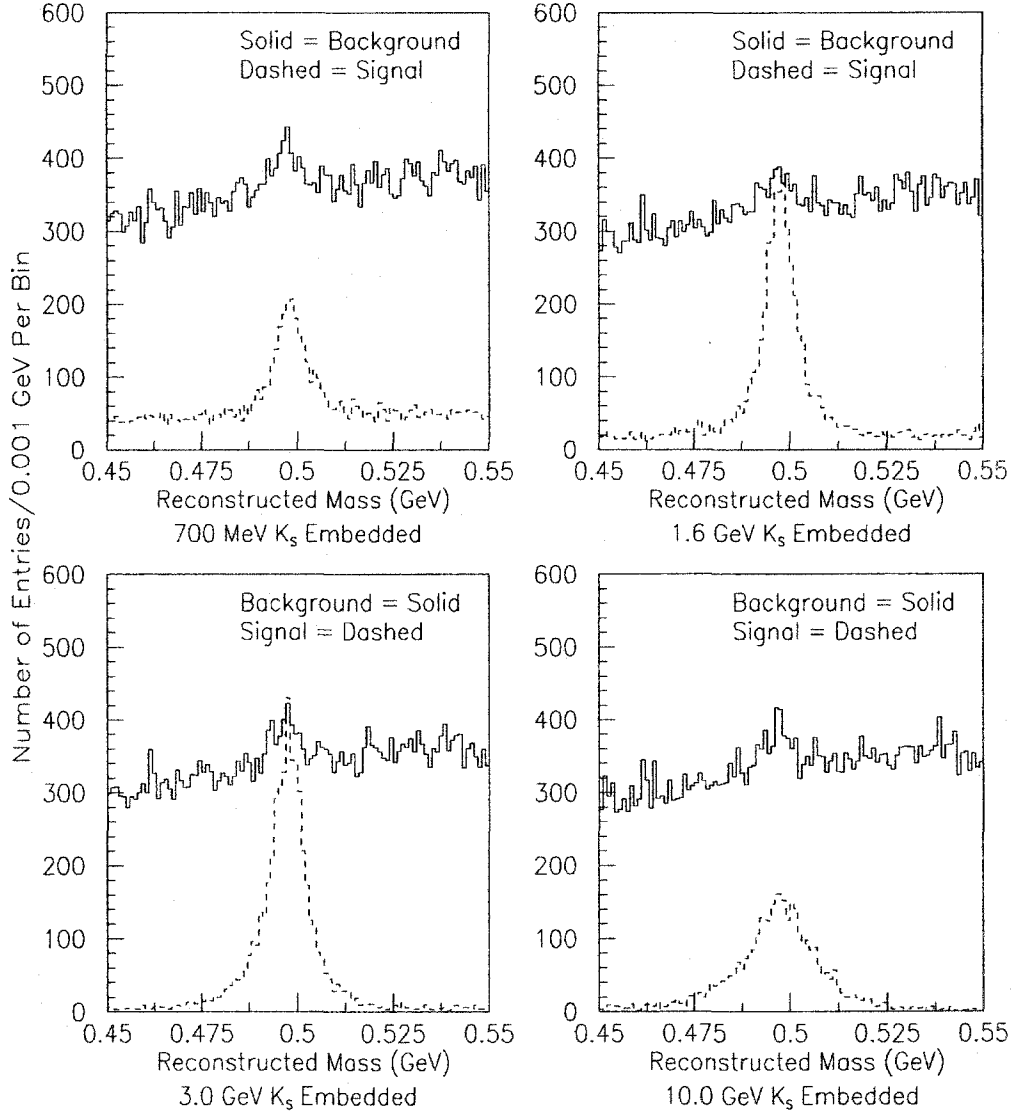
Figure 4.6: The mass distribution of K_S candidates after track-embedding (with and without the p_T window cut). The mass distributions of 0.7 GeV, 1.6 GeV, 3.0 GeV, and 10.0 GeV K_S candidates that pass (dashed line) and fail (solid line) p_T window. The p_T windows are 50 MeV, 100 MeV, 250 MeV, 1.0 GeV for 0.7 GeV, 1.6 GeV, 3.0 GeV, and 10.0 GeV K_S. These are based upon 10004 events for the 0.7 GeV case and 8668 events for the 1.6 GeV, 3.0 GeV, and 10.0 GeV cases. These distributions are of K_S embedded into $|\eta|$<2.0 prior to the event cuts.
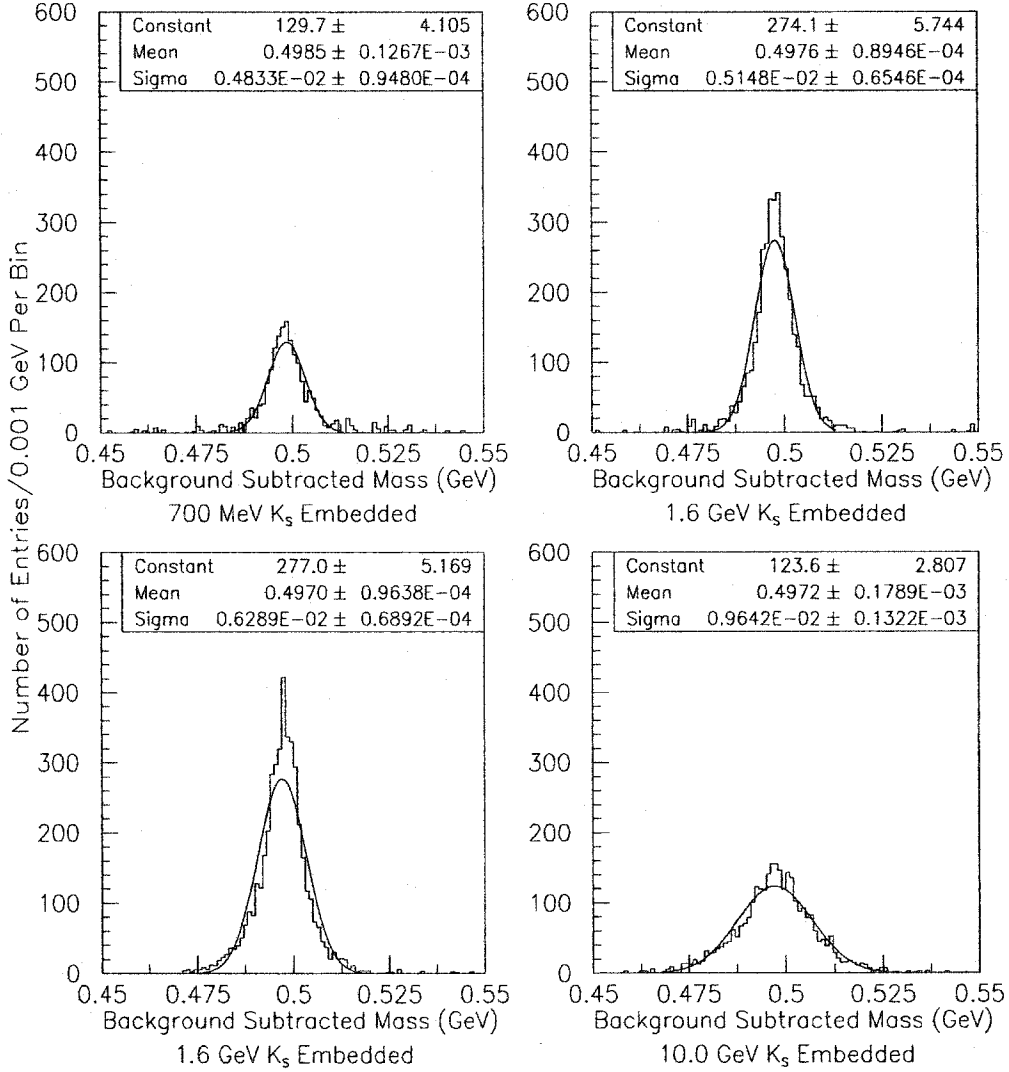
Figure 4.7: The mass distribution of K_S candidates after background subtraction within the p_T window. The fitted background subtracted mass distributions of 0.7 GeV, 1.6 GeV, 3.0 GeV, and 10.0 GeV K_S candidates that pass (dashed line) and fail (solid line) p_T window. The p_T windows are 50 MeV, 100 MeV, 250 MeV, 1.0 GeV for 0.7 GeV, 1.6 GeV, 3.0 GeV, and 10.0 GeV K_S. These are based upon 10004 events for the 0.7 GeV case and 8668 events for the 1.6 GeV, 3.0 GeV, and 10.0 GeV cases. These distributions are of K_S embedded into $|\eta|<2.0$ prior to the event cuts.
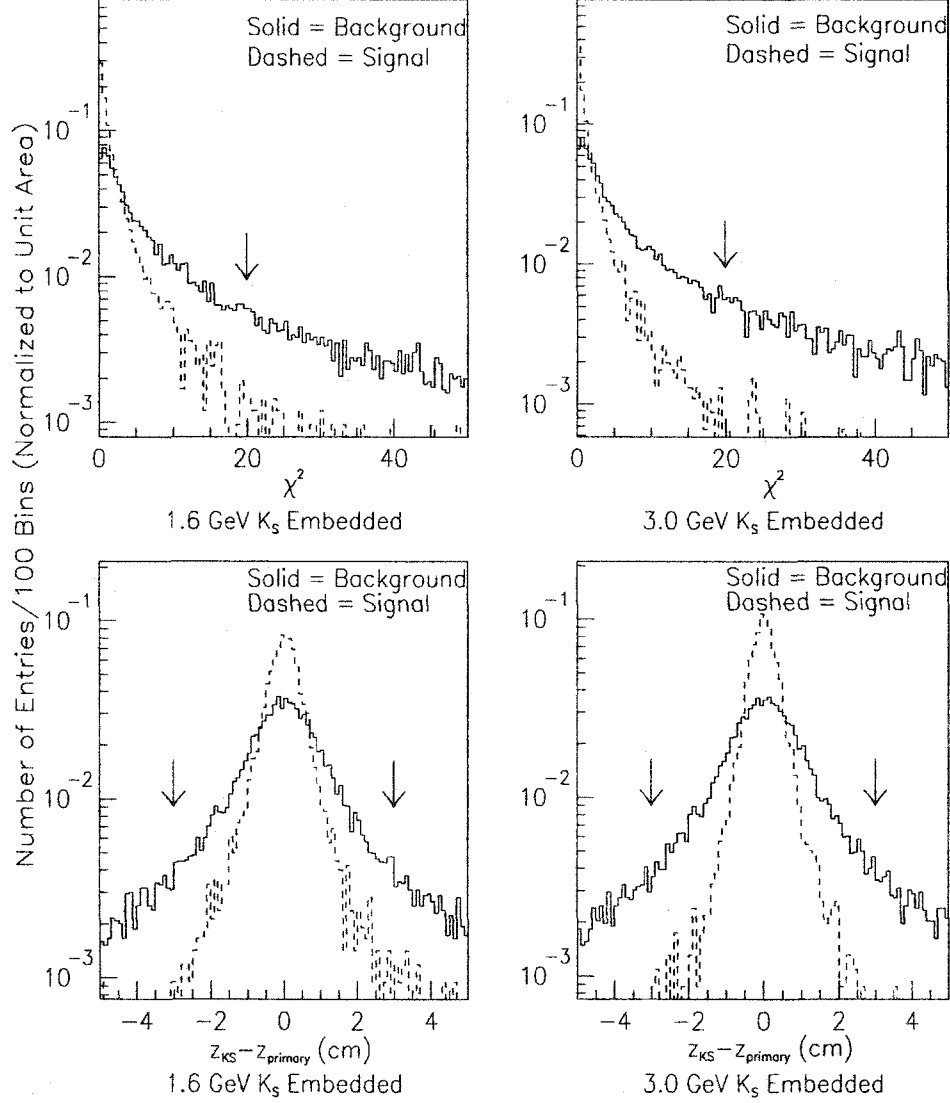
Figure 4.8: In the top half, the χ^2_{KS} distributions of the 1.6 GeV (left) and 3.0 GeV (right) candidates which pass (dashed line) and fail (solid line) the p_T window cut. The arrows indicate the $\chi^2_{KS} < 20.0$ cut. In the bottom half, the $|z_{KS} - z_{primary}|$ distributions are shown similarly with the arrows indicating the $|z_{KS} - z_{primary}| < 3.0$ cm cut. All distributions are based 8028 K_S embedded into $|\eta| < 2.0$ after passing the event cuts. The distributions are normalized to unit area.
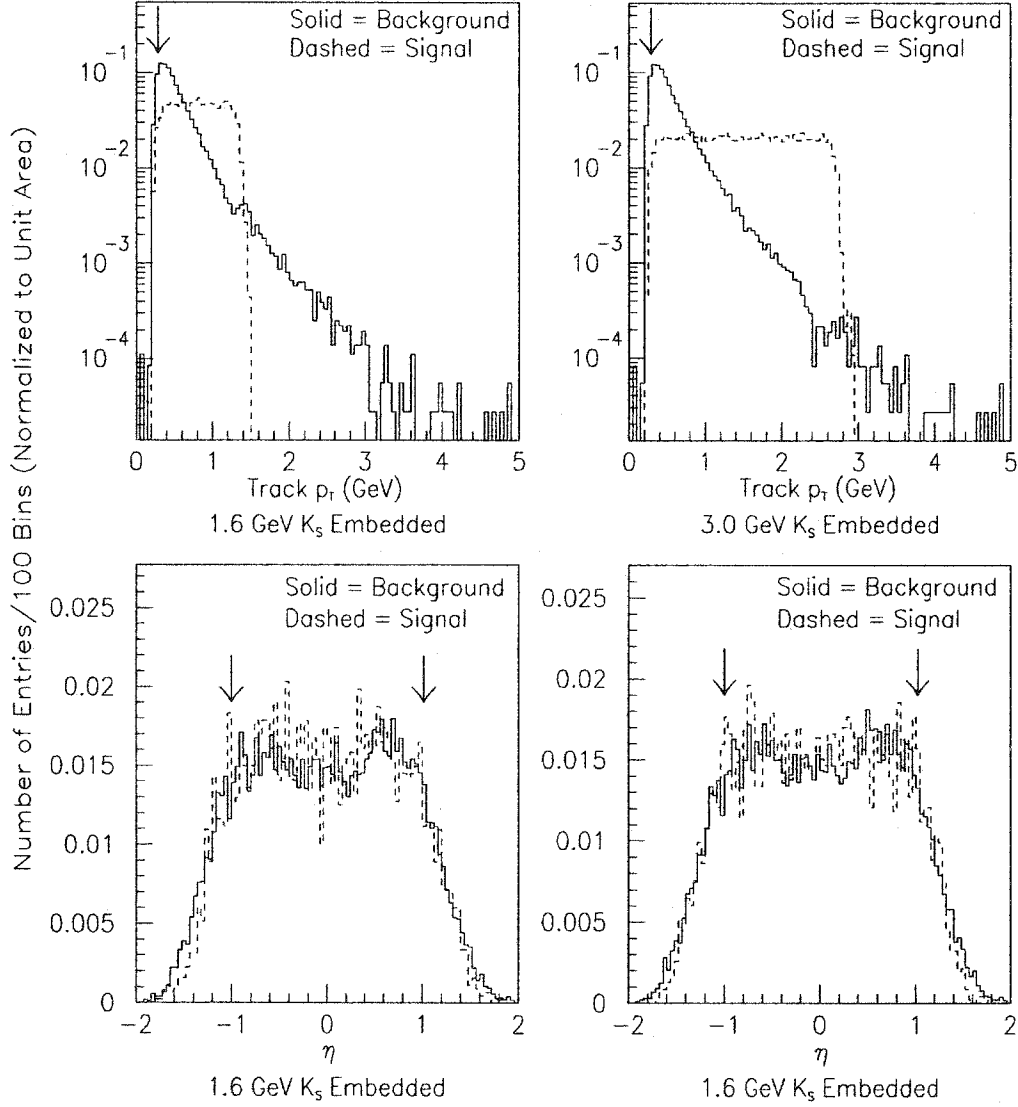
Figure 4.9: In the top half, the daughter track p_T distributions of the 1.6 GeV (left) and 3.0 GeV (right) candidates which pass (dashed line) and fail (solid line) the p_T window cut. The arrows indicate the $p_T^{tracksfromKS}>300.0$ MeV cut. In the bottom half, the η^{KS} distributions are shown similarly with the arrows indicating the $|\eta^{KS}|<1.0$ cut. All distributions are based 8028 K_S embedded into $|\eta|<2.0$ after passing the event cuts. The distributions are normalized to unit area.
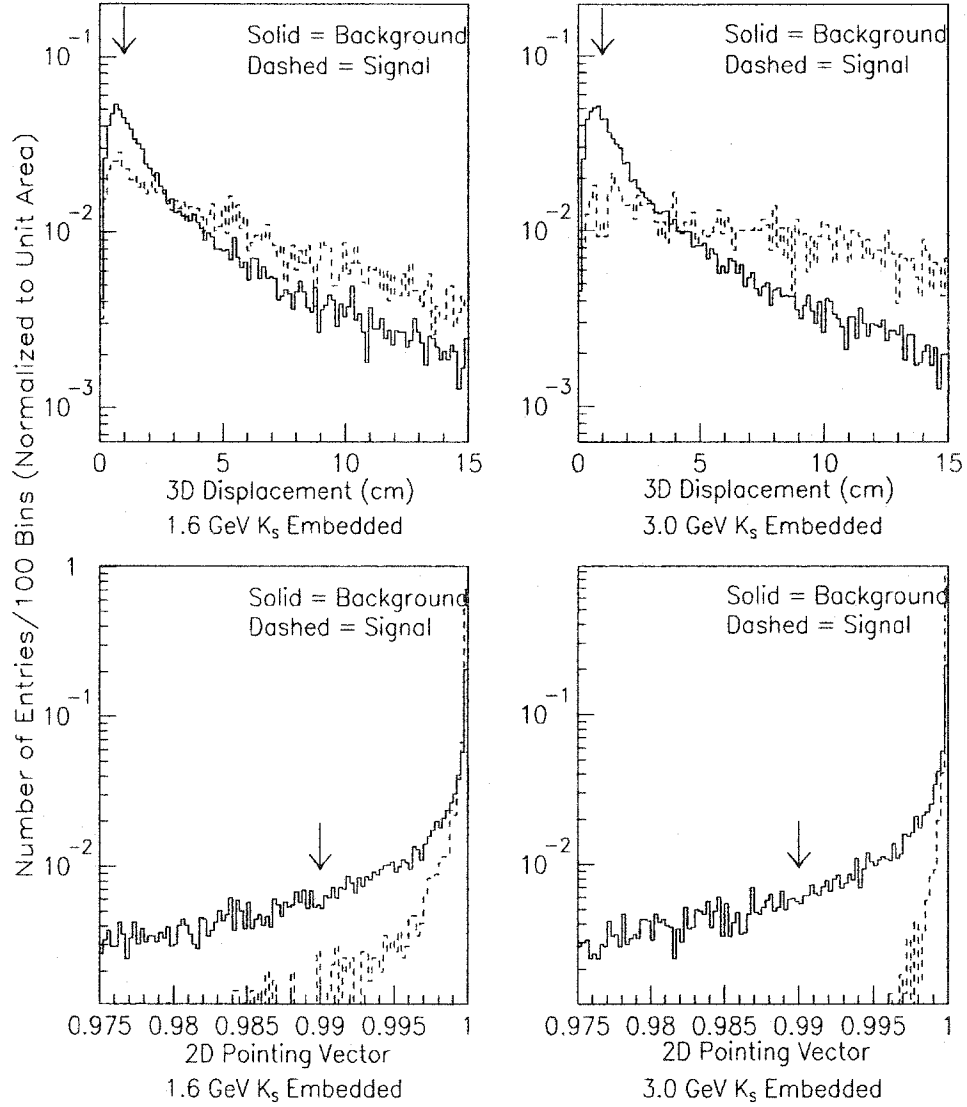
Figure 4.10: In the top half, the 3D displacement^{KS} distributions of the 1.6 GeV (left) and 3.0 GeV (right) candidates which pass (dashed line) and fail (solid line) the p_T window cut. The arrows indicate the 3D displacement^{KS}>1.0 cm cut. In the bottom half, the 2D pointing vector $(\cos\theta_{PD}^{KS})$ distributions are shown with the arrows indicating the $\cos\theta_{PD}^{KS}$>0.990 cut. All distributions are based 8028 K_S embedded into $|\eta|$<2.0 after passing the event cuts. The distributions are normalized to unit area.

Efficiency vs. p_T

Efficiency vs. p_T Efficiency vs. p_T
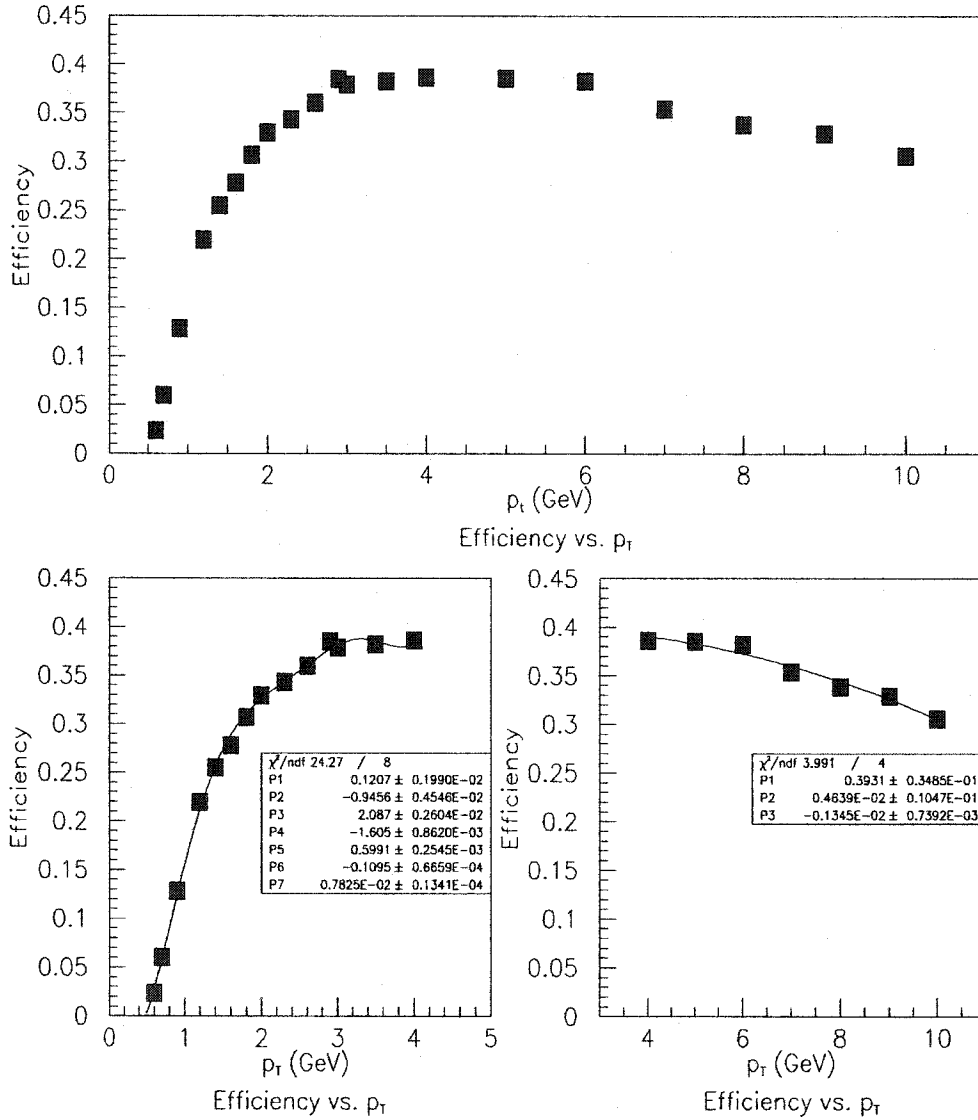
Figure 4.11: The K_S efficiency vs. p_T curve for the Minimum Bias set. Each point in the top figure represents a p_T value which implemented track-embedding, and these points are divided into 2 distinct fit regions shown in the bottom diagrams. This efficiency curve does not implement the branching ratio correction, and the K_S are embedded between $|\eta|<2.0$. For embedded K_S with p_T below 1.0 GeV, 16677 events passing the event cuts are used. For embedded K_S with p_T above 1.0 GeV, 8028 events passing the event cuts are used.
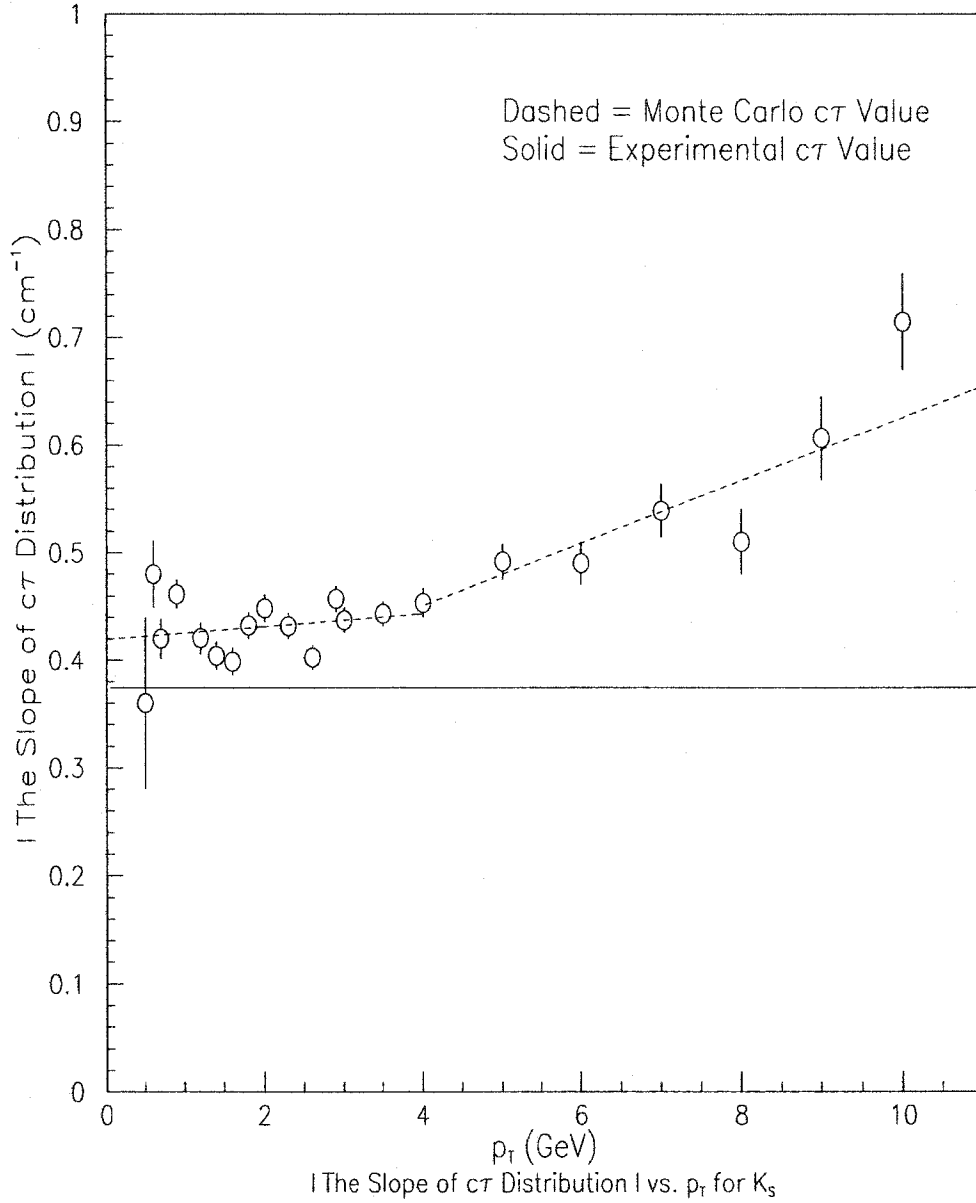
Figure 4.12: The |slope of the $c\tau$ distribution| vs. p_T. This curve is implemented in the $c\tau$ calculation. The solid line is the expected value, and the dashed line is the efficiency value extracted from the track embedding. (bottom right).

Chapter 5

Minimum Bias: Results

The efficiency corrections will now be applied to the K_S sample in order to produce plots which offer greater insight into K_S production in Minimum Bias events. In the first section, the efficiency adjusted $c\tau$ measurement will be highlighted along with its implications regarding the reliability of the Monte Carlo. Then, the mass spectrum, the number of K_S , the uncorrected $\frac{dN_{K_S}}{dp_T}$ spectrum, the $\frac{E}{N_{event}} \frac{d^3 N_{K_S}}{d^3 p}$ curve, the track density $\frac{dN_{K_S}}{d\eta}$, the $<p_T>$, and the invariant cross-section will be among a list of items to be discussed. Bear in mind, the results obtained from the Minimum Bias set are not the primary objective, but rather they are only intended to compare with previously publications.

5.1 $c\tau$ Measurement

The efficiency adjusted $c\tau$ measurement is compared to the accepted value so that the accuracy of the efficiency corrections may be gauged. The first topic of discussion will be a review of what transpired in Chapter 4 followed by stating the unadjusted $c\tau$ value, then the implementation of the $c\tau$ efficiency is to be described, and to end this section, the efficiency corrected $c\tau$ will be presented along with what may be inferred as to the precision of the Monte Carlo and the p_T efficiency curve.

As in section 4.3 which pertains to $c\tau$ efficiency calculation, the proper lifetime is denoted by the following equation:

$$c\tau = \frac{M_{KS}D_{KS}}{P_{KS}} \qquad (5.1)$$

where P_{KS} is the 3D momentum of the K_S , D_{KS} is the 3D displacement of the K_S , and M_{KS} is the mass of the K_S [40] [63] [64]. Again, the experimental check is the reciprocal of the slope of the decaying exponential of the positive $c\tau$ distribution, and the accepted value is 2.6786 ± 0.0024 cm for K_S [9]. Furthermore, the K_S are selected with the cuts employed in the $c\tau$ efficiency calculation, except for the p_T window cut, and these cuts are given below:

- Sample K_S in $c\tau$ Study

  - Event Cuts

  - $\chi^2_{KS} < 20.0$

  - $|z_{KS} - z_{primary}| < 3.0$ cm

  - $p_T^{tracks\ from\ KS} > 300$ MeV

  - $|\eta^{KS}| < 1.0$

  - 3D Displacement$^{KS} > 1.0$ cm

Background subtraction is likewise needed to remove background $c\tau$ values from the central region (0.48 to 0.52 GeV). To review, the method involves adding the $c\tau$ values from the sideband mass regions (0.45-0.48 GeV and 0.52-0.55 GeV), and then subtracting the combined histogram from the $c\tau$ distribution containing both the K_S and background candidates having central region (0.48-0.52 GeV) mass values. When the sum of the sideband $c\tau$ distributions is subtracted from the central $c\tau$

distribution, the sum of the sidebands must be weighted with the fraction denoted
by Equation 5.2:

$$fraction = \frac{N_C^{total} - N_{KS}^{total}}{N_{S1}^{total} + N_{S2}^{total}} \tag{5.2}$$

where N_{S1}^{total} and N_{S2}^{total} are the total number of candidates in each of the sideband
regions $S1$ and $S2$, N_C^{total} is the total number of K_S and background candidates in
the central region, and N_{KS}^{total} is the total number of K_S in the central peak. The
errors are propagated bin by bin utilizing the following equation:

$$error = \sqrt{N_C^{bin} + fraction(N_{S1}^{bin} + N_{S2}^{bin})} \tag{5.3}$$

After the background subtraction procedure, the resulting $c\tau$ of the central region
has had these background $c\tau$ removed, and this is the distribution from which
the slope of the decaying exponential is computed. In particular, $N_{S1}^{total} = 139769$,
$N_{S2}^{total} = 132707$, $N_C^{total} = 244948$, and $N_{KS}^{total} = 61790$ yield a fraction of approximately
0.672. N_{S1}^{total} is within 5% of N_{S2}^{total}, and nothing is gained by having them equal.
The resulting value is quite robust, and the divisions of the sidebands and central
regions are not important so long as they are reasonable. Moreover, it best to keep
the regions consistent with those in the p_T calculation.

In Figure 5.1, the fitted $c\tau$ distribution is shown after background subtraction
and before efficiency adjustments. The proper lifetime prior to efficiency corrections
is 2.3736 ± 0.0116 cm. The number is slightly smaller than the accepted measured
value of 2.6786 ± 0.0024 cm [9] because some of the K_S with longer lifetimes are lost
due to the lack of hits in inner layers of the CTC. Therefore, before the efficiency
corrections, the widely accepted quantity and this experimental value differ by about
15%. Hopefully, the $c\tau$ determined with the $c\tau$ efficiencies from Chapter 4 will

improve the agreement.

The efficiency corrected $c\tau$ is generated in the identical matter as the unadjusted $c\tau$ with one exception: before booking histograms, every $c\tau$ and mass value is weighted by a function of the efficiency correction from the p_T vs. $c\tau$ plot studied in Chapter 4. The number of K_S is extracted from the weighted mass plot as is the number of background candidates in the sideband and central regions. The adding and subtracting histograms proceeds similar as before with the N_C^{total}, N_{KS}^{total}, N_{S1}^{total}, and N_{S2}^{total} being calculated from histograms with these correction factors. There also exists a p_T cut of 0.5 GeV for the K_S, since below this value, the efficiencies are not well understood. In addition, all K_S with $p_T > 10$ GeV have adjustments equal to the efficiency at 10.0 GeV. The correction factor is expressed in Equation 5.4:

$$weight = exp((c\tau^{slope}(p_T) - c\tau^{slope}_{experimental}) * c\tau(p_T)) \tag{5.4}$$

where $c\tau^{slope}(p_T)$ is taken from Figure 4.12 as a function of p_T, the $c\tau^{slope}_{experimental}$ variable is just the constant $\frac{1}{2.6786}$ ($\frac{1.0}{c\tau_{experimental}}$), and $c\tau(p_T)$ is a given $c\tau$ value to be booked.

To fill in the details, the weighted sideband values are 149900 (N_{S1}^{total}) and 140400 (N_{S2}^{total}) for 0.45 to 0.48 GeV and 0.52 to 0.55 GeV, respectively, the weighted central value is 267000 (N_C^{total}), the weighted number of K_S is 71650 (N_{KS}^{total}), and the weighted fraction is 0.67292. The sidebands are within 7% of each other and making them to be equal would not alter the result.

The final background subtracted $c\tau$ corrected for efficiencies is given in Figure 5.2, and the efficiency corrected $c\tau$ is computed to be 2.6882 ± 0.0124 cm, and the value is inline with expectations and is within errors of the experimental value of 2.6786 ± 0.0024 cm [9]. Other people at CDF have conducted similar lifetime

studies and also found the experimental value to be consistent with the expected $c\tau$. First, Schub's result is within 30% of expected value with as little as 500 K_S candidates [41] [65] More recently, another study quotes the $c\tau$ of K_S as being 2.643 ± 0.018 cm [43]. This latter result is slightly lower than K_S $c\tau$ derived here because the fit of [63] includes all regions of the $c\tau$ spectrum, even those, obviously departing from the exponential. The agreement indicates that the Monte Carlo accurately accounted for the decreasing $c\tau$ tail of the data, and the p_T efficiency curve may be considered to be reliably generated.

5.2 Reconstructed Mass Peak

Before any quantity may be computed, the K_S sample must be obtained. As described in Chapter 3, K_S candidates have already met the following criteria:

- K_S in p_T sample

  - Event Cuts

  - $\chi^2_{KS} < 20.0$

  - $|z_{KS} - z_{primary}| < 3.0$ cm

  - $p_T^{tracks\ from\ KS} > 300$ MeV

  - $|\eta^{KS}| < 1.0$

  - 3D Displacement$^{KS} > 1.0$ cm

  - $\cos\theta^{KS}_{PD} > 0.990$

After these cuts have been applied, the reconstructed mass distribution appears approximately as a Gaussian resting upon a smooth background, and this is plotted

in Figure 5.3. The mass distribution of K_S candidates consists of a mixture of K_S along with particles which, although they satisfy the requirements, are not K_S. Unfortunately, such background particles are indistinguishable from real K_S. With each additional cut, the number of K_S per background K_S may increase; however, this may reduce the number of K_S too much. For example, an impact parameter cut would increase the Signal to Noise ratio, but it would also reduce the number of K_S dramatically.

All the analysis from this point is based upon deriving K_S properties from the shapes of the K_S plus background histogram and the sideband histograms. First, the K_S plus background histogram is fitted with a Gaussian and a 1st order polynomial. The 1st order polynomial represents the background. Then, this 1st order polynomial is subtracted from the K_S plus background histogram shown in Figure 5.3. The resulting K_S mass peak distribution is shown in Figure 5.4.

Ideally, the K_S mass distribution in Figure 5.4 would be a perfect delta function. It is only the actual measurement error of the particle that gives rise to the spreading of the delta function to yield approximately a Gaussian. The fitted Gaussian in Figure 5.4 reveals the mean of the mass peak to be 0.4974 GeV with a mass resolution of 5.293 MeV. This result agrees quite well with the world average of 0.497672 ± 0.000031 GeV [9]. The number of K_S candidates after cuts and unadjusted for efficiencies is evaluated by summing the number of K_S candidates between 0.48 and 0.52 GeV in Figure 5.4. In this case, there are 56940 ± 441 uncorrected K_S where the error is taken as the Gaussian area error obtained directly from the combined Gaussian and polynomial fits.

5.3 p_T Spectrum

After first calculating the background subtracted p_T curve with cuts described in the previous section, the p_T curve is corrected with the efficiency spectrum. Using this efficiency adjusted p_T curve, the number of K_S in the sample can be determined.

In a procedure which closely mirrors that of the production the unadjusted $c\tau$ plot, the uncorrected p_T spectrum of the K_S are computed via background subtraction. The technique is identical with mass ranges (0.45 to 0.48 GeV and 0.52 to 0.55 for the sidebands and 0.48 to 0.52 for the central regions) and errors evaluated similarly; however, p_T distributions are substituted for the $c\tau$ distributions. Moreover, there is a slight difference in K_S candidate selection criteria with the $c\tau$ case lacking the 2D pointing vector cut as well as having an additional p_T constraint on the K_S . To be more specific, with the p_T background subtraction, $N_{S1}^{total} = 82400$, $N_{S2}^{total} = 69169$, $N_C^{total} = 159696$, and $N_{KS}^{total} = 56940$ yield a fraction of approximately 0.6778. It should be obvious that N_{S1}^{total} is 20% greater than N_{S2}^{total}, and this can be resolved by altering the mass ranges for N_{S1}^{total}, N_C^{total} and N_{KS}^{total}, and N_{S2}^{total} to be 0.45 to 0.48 GeV, 0.48 to 0.515 GeV, and 0.515 to 0.55 GeV respectively. Another solution would include slightly different weights when adding and subtracting p_T distributions, but in the end, nothing is gained by doing so because the normalized p_T distributions of sidebands are the same. It is also should mentioned that additional 2D pointing vector cut causes the asymmetry in the sidebands. The resulting unadjusted p_T spectrum is displayed in Figure 5.5.

The next step in continuing the understanding K_S production is to convert the unadjusted $\frac{dN_{KS}}{dp_T}$ spectrum into the efficiency corrected $\frac{dN_{KS}}{dp_T}$ curve by applying the fitted efficiency curve obtained from Chapter 4. To reiterate, K_S efficiency is a function of p_T, and the function is defined with a different set of parameters for two

distinct fit regions in the bottom of Figure 4.11. Therefore, the number of K_S in a given bin in Figure 5.5 is multiplied by the reciprocal of the K_S efficiency given at the value of the p_T at the midpoint of the bin. In addition, these corrections are applied only to the p_T region between 550 MeV and 10 GeV where the efficiency corrections are greater than 5% and statistics in the unadjusted bins are reasonable. Moreover, this number is multiplied by 0.6861±0.0028 [9] to take the branching ratio into account. Although the resulting curve is not presented here because the $\frac{E}{N_{event}} \frac{d^3 N_{KS}}{d^3 p}$ distribution is usually preferred, the number of K_S in the adjusted curve is calculated by summing the K_S in each bin. The number of K_S between 550 MeV and 10 GeV is 250339 ± 4984 where the total error is the result of error propagation of each bin. The number of K_S prior to the efficiency corrections between 550 MeV and 10 GeV is 56873 ± 238 where the error is determined statistically [41].

5.4 The $\frac{E}{N_{event}} \frac{d^3 N_{KS}}{d^3 p}$ Spectrum

The $\frac{E}{N_{event}} \frac{d^3 N_{KS}}{d^3 p}$ can be expressed in terms of the efficiency corrected $\frac{dN_{KS}}{dp_T}$ curve, and once the $\frac{E}{N_{event}} \frac{d^3 N_{KS}}{d^3 p}$ is obtained and fitted, variables such as $<p_T>$ and $\frac{dN_{KS}}{d\eta}$ may be evaluated.

To get $\frac{E}{N_{event}} \frac{d^3 N_{KS}}{d^3 p}$ in terms of $\frac{dN_{KS}}{dp_T}$, first substitute the cylindrical coordinate form of dp^3, $d^3 p = p_T \, dp_T \, d\phi \, dz$, to yield Equation 5.5:

$$\frac{E}{N_{event}} \frac{d^3 N_{KS}}{d^3 p} = \frac{E}{N_{event}} \frac{d^3 N_{KS}}{p_T dp_T d\phi dz}. \tag{5.5}$$

Then, using $d\eta = \frac{dp_z}{E}$, Equation 5.5 can be rewritten as Equation 5.6:

$$\frac{E}{N_{event}} \frac{d^3 N_{KS}}{d^3 p} = \frac{1}{N_{event}} \frac{d^3 N_{KS}}{p_T dp_T d\phi d\eta}. \tag{5.6}$$

Since the number of K_S are efficiency adjusted in the region of space confined by $0 \leq \phi < 2\pi$ and $|\eta| < 2.0$ and the K_S efficiency can be considered to be uniform over the variables ϕ and η, it follows that $d\phi = 2\pi$ and $d\eta = 4$. Accordingly, in Equation 5.7, $\frac{E}{N_{event}} \frac{d^3 N_{KS}}{d^3 p}$ is successfully transformed into a function of $\frac{dN_{KS}}{dp_T}$:

$$\frac{E}{N_{event}} \frac{d^3 N_{KS}}{d^3 p} = \frac{1}{N_{event}} \frac{d^3 N_{KS}}{8\pi p_T dp_T}. \tag{5.7}$$

The $\frac{E}{N_{event}} \frac{d^3 N_{KS}}{d^3 p}$ spectrum in Figure 5.6 is obtained by dividing the number of K_S in each bin of the efficiency corrected $\frac{dN_{KS}}{dp_T}$ curve with the p_T value at the midpoint of the bin and by multiplying every bin with the constant $\frac{1}{8\pi N_{event}}$ where $N_{event} = 1272552$.

The $\frac{E}{N_{event}} \frac{d^3 N_{KS}}{d^3 p}$ spectrum is fit with a power law, and the extracted fit parameters are used to calculate important quantities such as $\frac{dN_{KS}}{d\eta}$ and $<p_T>$ [41]. The power law equation is given by $\frac{A p_0^n}{(p_0 + p_T)^n}$ where A and n are free parameters and p_0 is a commonly accepted fixed constant equal to 1.3. Furthermore, the $\frac{E}{N_{event}} \frac{d^3 N_{KS}}{d^3 p}$ spectrum is fitted from 0.7 GeV to 10.0 GeV, and this is displayed in Figure 5.7. It is believed that an exponential would fit the data better for extremely low p_T; however, this analysis does not contain points in this range. In the next section, $\frac{dN_{KS}}{d\eta}$ and $<p_T>$ will be computed.

5.5 $\frac{dN_{KS}}{d\eta}$ and $<p_T>$

The calculations of track density $\frac{dN_{KS}}{d\eta}$ and $<p_T>$ will be illustrated by explaining Table 5.1. As mentioned before, the $\frac{E}{N_{event}} \frac{d^3 N_{KS}}{d^3 p}$ spectrum in Figure 5.7 is fitted with a power law from 0.7 GeV to 10.0 GeV. The top of Table 5.1 displays not only the fit range and fit parameters but also the form of the power law. These fit

parameters can then be substituted into the functions of the power law equations, to be described below, and integrated over p_T to yield both the $\frac{dN_{KS}}{d\eta}$ and $<p_T>$ quantities. By changing the limits of integration, $\frac{dN_{KS}}{d\eta}$ and $<p_T>$ values may be computed for different p_T ranges.

The integration of the product of the power law and $2\pi\, p_T$ would compute $\frac{dN_{KS}}{d\eta}$. This is shown in Equation 5.8:

$$\frac{dN_{KS}}{d\eta} = 2\pi\left(\int_{0.7GeV}^{10.0GeV} \frac{Ap_0^n p_T dp_T}{(p_T + p_0)^n}\right). \tag{5.8}$$

The fit parameters are substituted into Equation 5.8 prior to integration. In Table 5.1, equation 5.8 is integrated from 0.7 GeV to 10.0 GeV as well as from 0.5 GeV to 10.0 GeV. In the end, $\frac{dN_{KS}}{d\eta} = 0.129 \pm 0.005$ for 500.0 MeV$<p_T<$10.0 GeV and $\frac{dN_{KS}}{d\eta} = 0.084 \pm 0.003$ for 0.7 GeV$<p_T<$10.0 GeV.

The $<p_T>$ is slightly more complicated, it is given by Equation 5.9 for 0.7 GeV$<p_T<$10.0 GeV:

$$< p_T > = \frac{\int_{0.7GeV}^{10.0GeV} \frac{Ap_0^n p_T^2 dp_T}{(p_T+p_0)^n}}{\int_{0.7GeV}^{10.0GeV} \frac{Ap_0^n p_T dp_T}{(p_T+p_0)^n}}. \tag{5.9}$$

Again, for the 0.5 GeV to 10 GeV case, the limits of integration in the above equation need to be changed. The $<p_T> = 1.022 \pm 0.005$ for 500.0 MeV$<p_T<$10.0 GeV, and the $<p_T> = 1.251 \pm 0.005$ for 700.0 MeV$<p_T<$10.0 GeV. The errors are propagated with approximations in order to reduce the number of terms.

One way to compare the results with others such as Schub [41] and Rimondi, Moggi, and Deninno [43] is to study the $<p_T>$ over all p_T. The previous analyses cite $<p_T> = 0.60 \pm 0.03$ [41] and $<p_T> = 0.61 \pm 0.02$ [43]. Over all p_T, the number here is within their errors, $<p_T> = 0.59 \pm 0.005$. There are different methods of fitting the $\frac{E}{N_{event}} \frac{d^3N_{KS}}{d^3p}$ spectrum, and the method utilized for this comparison consists of

fixing $p_0 = 1.3$ and proceeding as described in this section. In addition, Schub [41] computes $\frac{dN_{KS}}{d\eta}$ over all p_T to be 0.29 ± 0.04, and in this analysis, $\frac{dN_{KS}}{d\eta} = 0.30\pm0.01$. Hence, these results are all within 5% of each other.

It is important to mention that there are many other fitting techniques for methods $\frac{E}{N_{event}} \frac{d^3 N_{KS}}{d^3 p}$ spectra. First, p_0 does not necessarily need to be constant. In [43], when it is not, p_0 increases to 3.16 ± 0.06 (as opposed to $p_0 = 1.3$), and $<p_T>$ over all p_T increases to 0.74 ± 0.07. Moreover, the power law may be the only function to fit the $\frac{E}{N_{event}} \frac{d^3 N_{KS}}{d^3 p}$. For example, an exponential may be implemented with or without a power law. If both an exponential and a power law are used, below a given p_T, the exponential fits the spectra, and above a transition point, a power law may be used. This transition point need not be where data exists as long as continuity of the functions and their derivatives is enforced. This $<p_T>$ depends tremendously on the systematics of the given method, and [41] is an excellent reference to continue this discourse. However, the point is not focus exclusively on the K_S production in Minimum Bias events. Hence, with the agreement with previous published $<p_T>$ and $\frac{dN_{KS}}{d\eta}$ for the case of fixing p_0, fitting the $\frac{E}{N_{event}} \frac{d^3 N_{KS}}{d^3 p}$ with a power law, and integrating the fit over all p_T being sufficient, contrasting the invariant cross-section with these analyses will be described in the subsequent section.

5.6 Invariant Cross-Section

The invariant cross-section will be the last topic. This involves multiplying the $\frac{E}{N_{event}} \frac{d^3 N_{KS}}{d^3 p}$ spectrum by the $\sigma_{effective}$. For $p\bar{p}$ collisions, the $\sigma_{effective} = 43\pm6$ mb. In Figure 5.8, [41] overlaps the invariant cross-section computed in this thesis, and the two curves are within 5% of each other. Also, the explicit values are compared for various p_T in Table 5.6. The agreement is approximately 15% on a point-by-

point basis except when p_T>3.0 GeV where statistics are limited [41]. Moreover,

the cross-section measurement from [43] is quite comparable. Since the consistency

with a few Minimum Bias K_S measurements has been shown, the K_S production

in jets will studied next.

Table 5.1: $\frac{dN_{KS}}{d\eta}$ and $<p_T>$ for K_S in the Minimum Bias set.

Fit Range	700 MeV$<p_T<$10.0 GeV
Function Fitted	$\frac{Ap_0^n}{(p_0+p_T)^n}$
Resulting Fit Parameters	$A = 0.991 \pm 0.030$ $n = 7.427 \pm 0.037$ $p_0 = 1.3$ (fixed)
$\frac{dN_{KS}}{d\eta}$ from 0.5$<p_T<$10.0 (GeV)	0.129 ± 0.005
$\frac{dN_{KS}}{d\eta}$ from 0.7$<p_T<$10.0 (GeV)	0.084 ± 0.003
$<p_T>$ from 0.5$<p_T<$10.0 (GeV)	1.022 ± 0.005
$<p_T>$ from 0.7$<p_T<$10.0 (GeV)	1.251 ± 0.005

Table 5.2: The invariant cross-section comparison .

p_T (GeV)	Schub's [41] $E\frac{d^3\sigma}{d^3p}$ (mb/GeV^2)	Derived Here $E\frac{d^3\sigma}{d^3p}$ (mb/GeV^2)
0.85	0.900 ± 0.200	0.915 ± 0.058
1.15	0.310 ± 0.050	0.350 ± 0.019
1.45	0.180 ± 0.020	0.159 ± 0.009
1.75	0.065 ± 0.009	0.075 ± 0.005
2.05	0.032 ± 0.006	0.030 ± 0.003
2.35	0.019 ± 0.004	0.022 ± 0.002
2.65	0.009 ± 0.002	0.010 ± 0.002
2.95	0.005 ± 0.002	0.006 ± 0.001
3.30	0.003 ± 0.001	0.003 ± 0.0008
3.75	0.0004 ± 0.0005	0.002 ± 0.0008
4.50	0.0004 ± 0.0002	0.0007 ± 0.0002
5.50	0.0002 ± 0.0001	0.00002 ± 0.00008
7.00	0.00009 ± 0.00006	0.00003 ± 0.00004
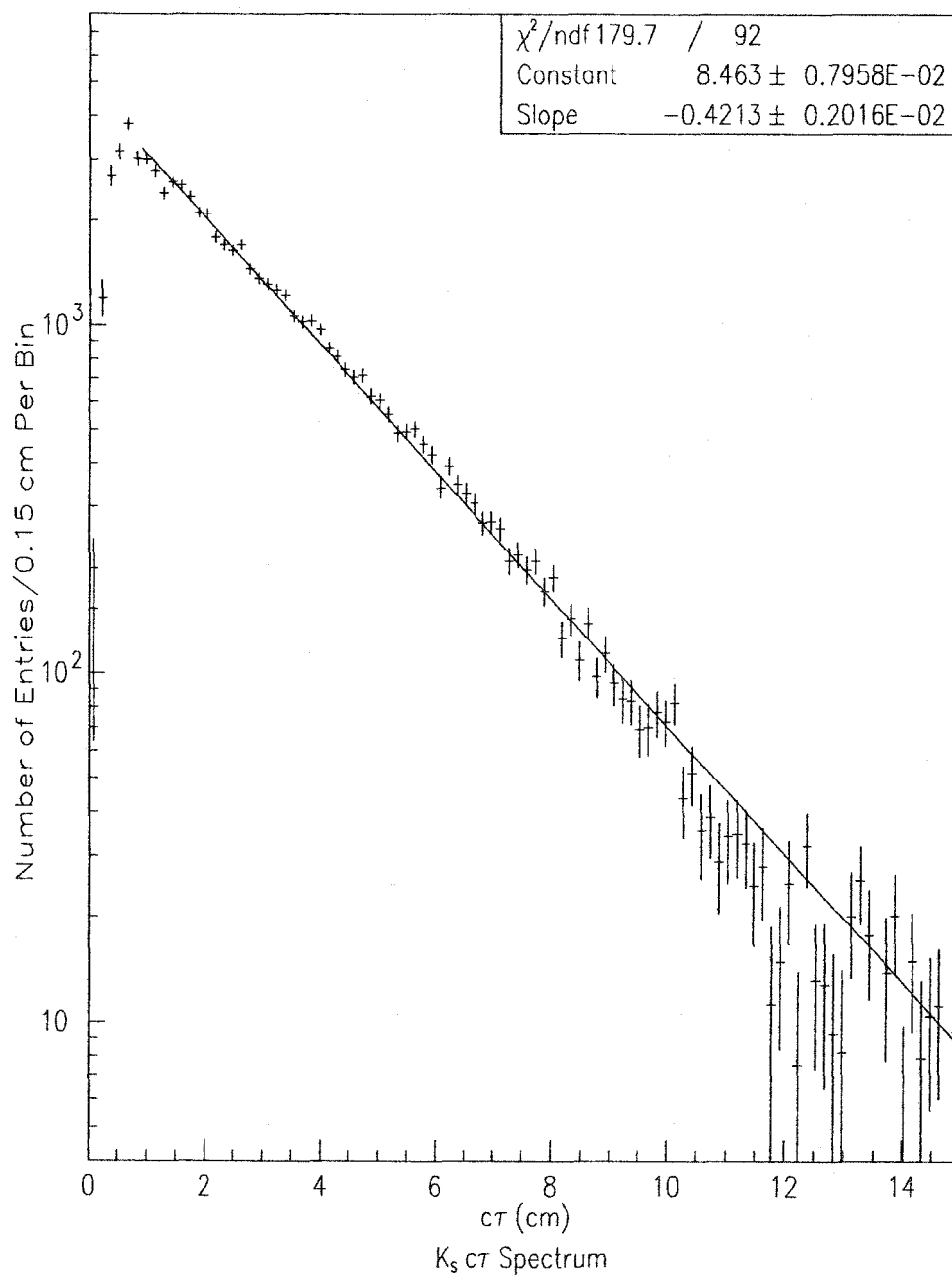
Figure 5.1: The K_S $c\tau$ spectrum. The curve is obtained after background subtraction and is not corrected for efficiencies.
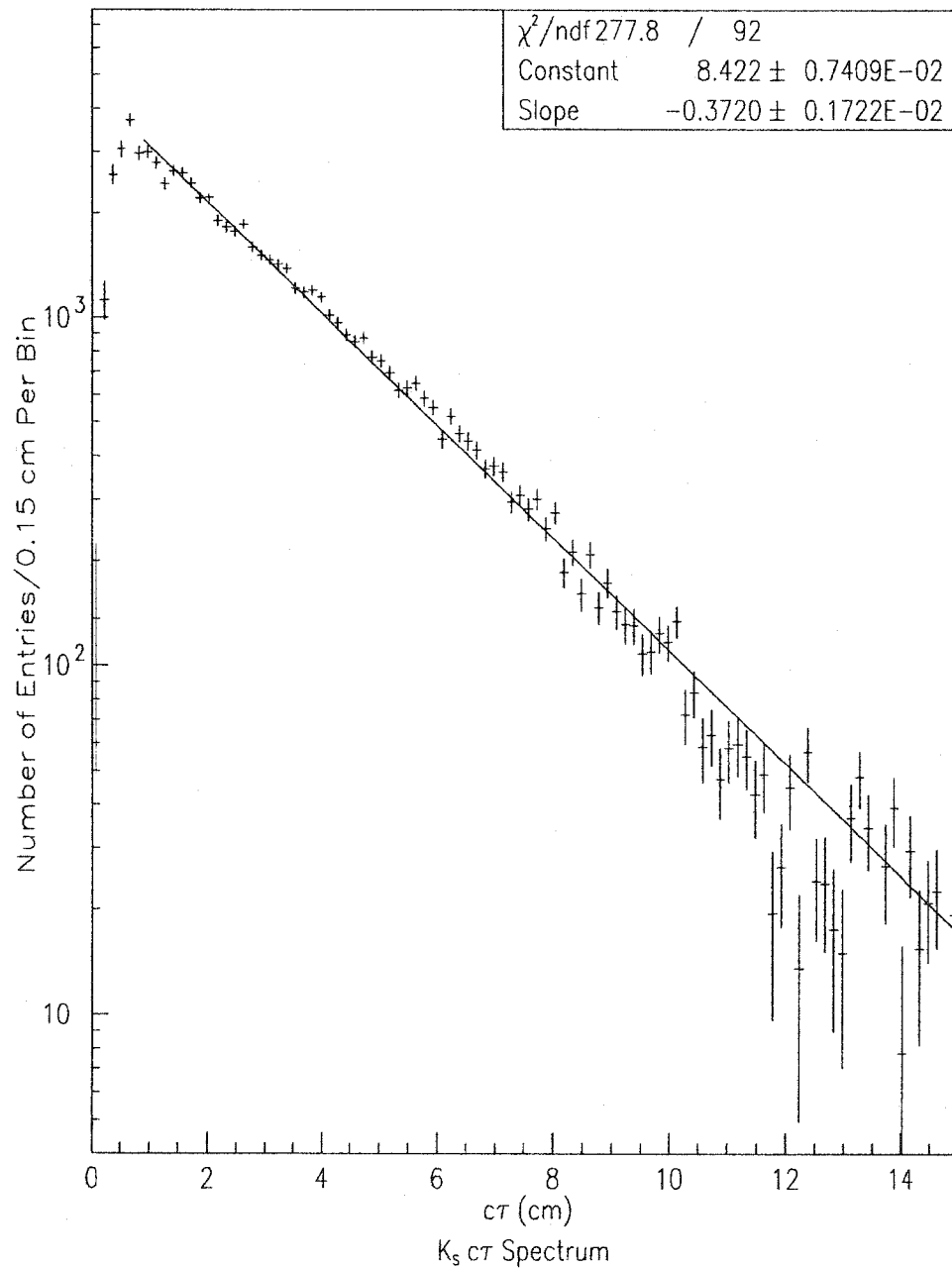
Figure 5.2: The K_S $c\tau$ spectrum. The curve is obtained after background subtraction and is corrected for efficiencies.
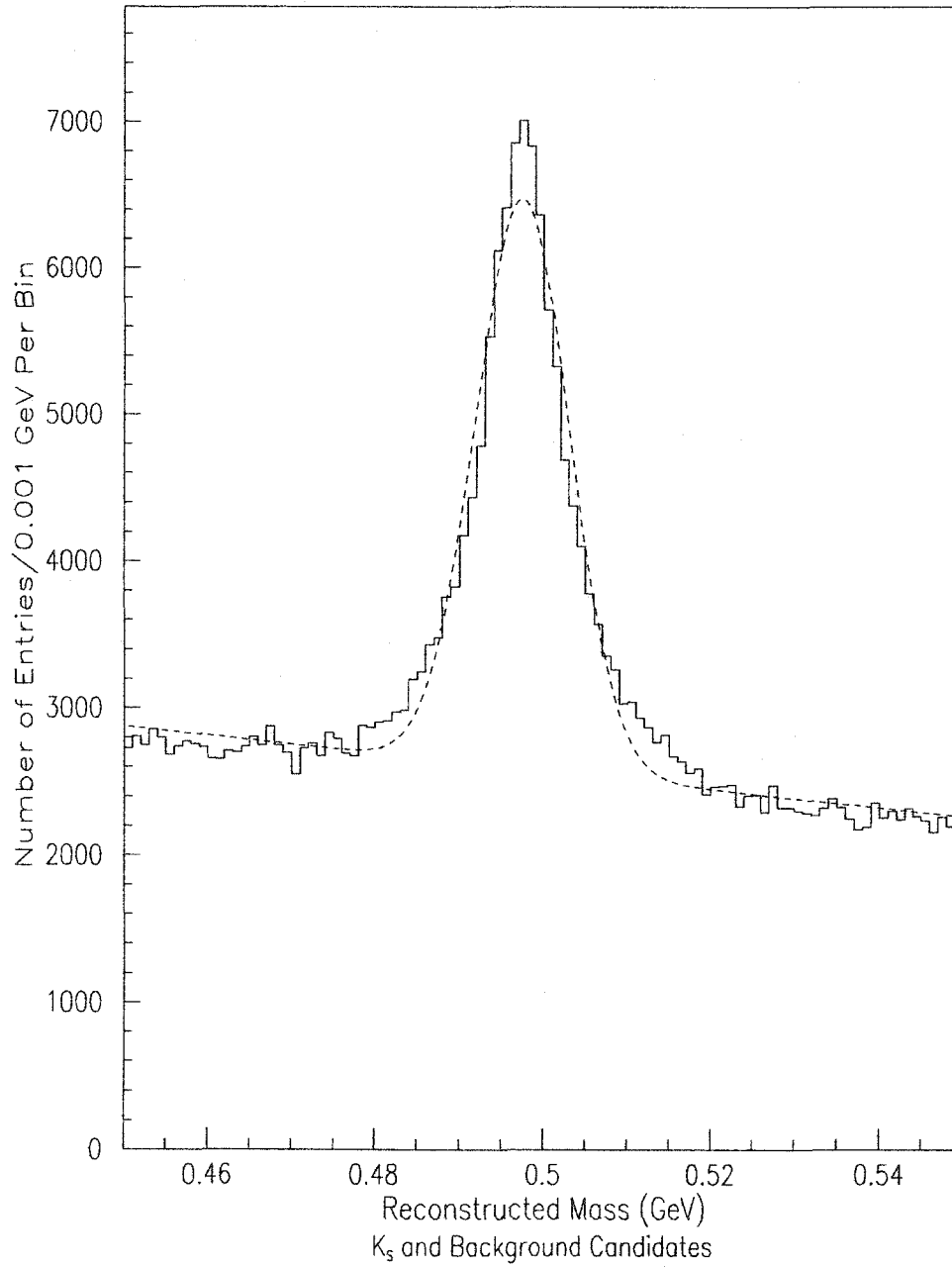
Figure 5.3: The mass distribution of K_S candidates before background subtraction and after Cuts.
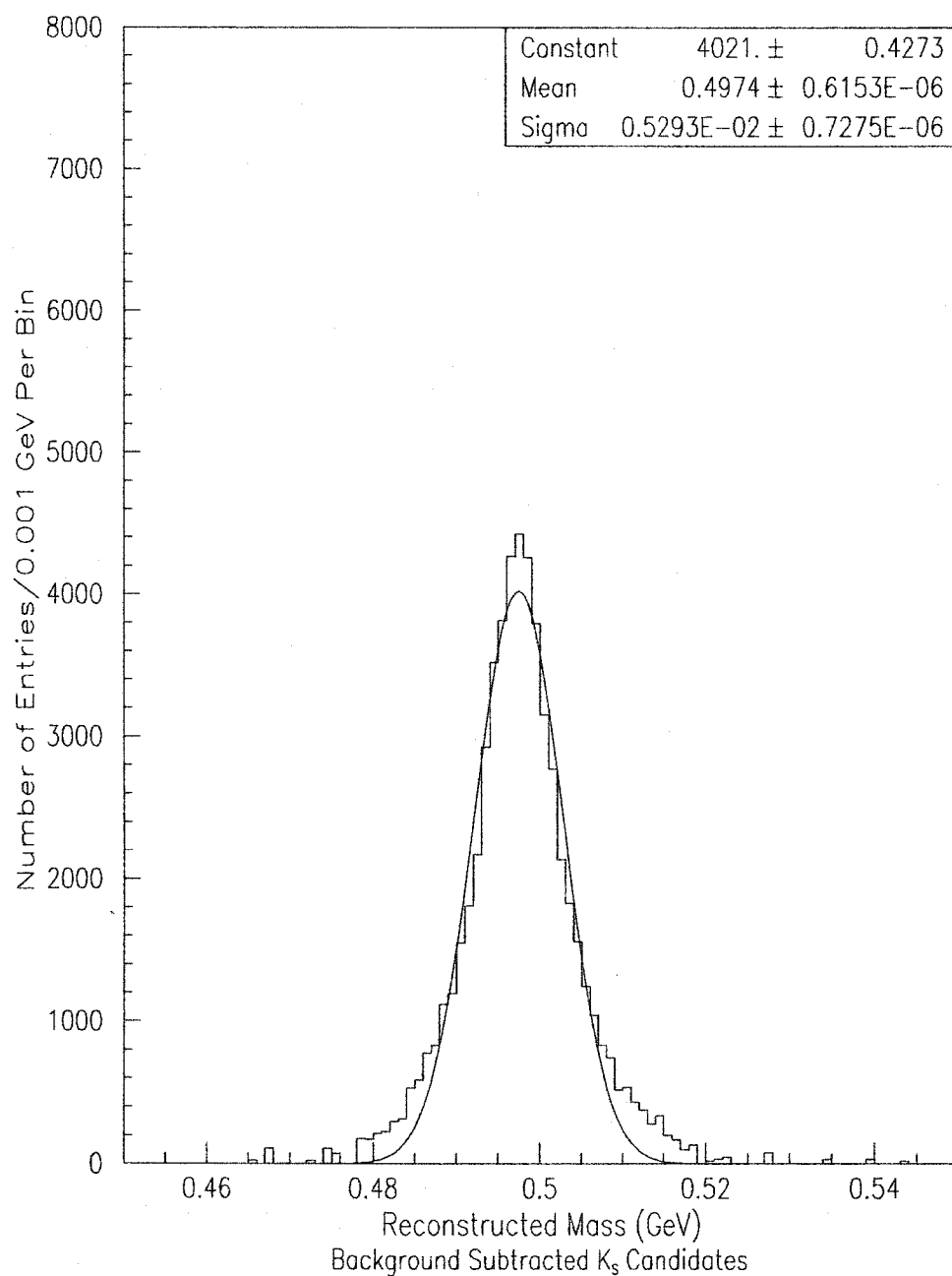
Figure 5.4: The mass distribution of K_S candidates after background subtraction and after cuts.

Uncorrected K_S p_T Spectrum
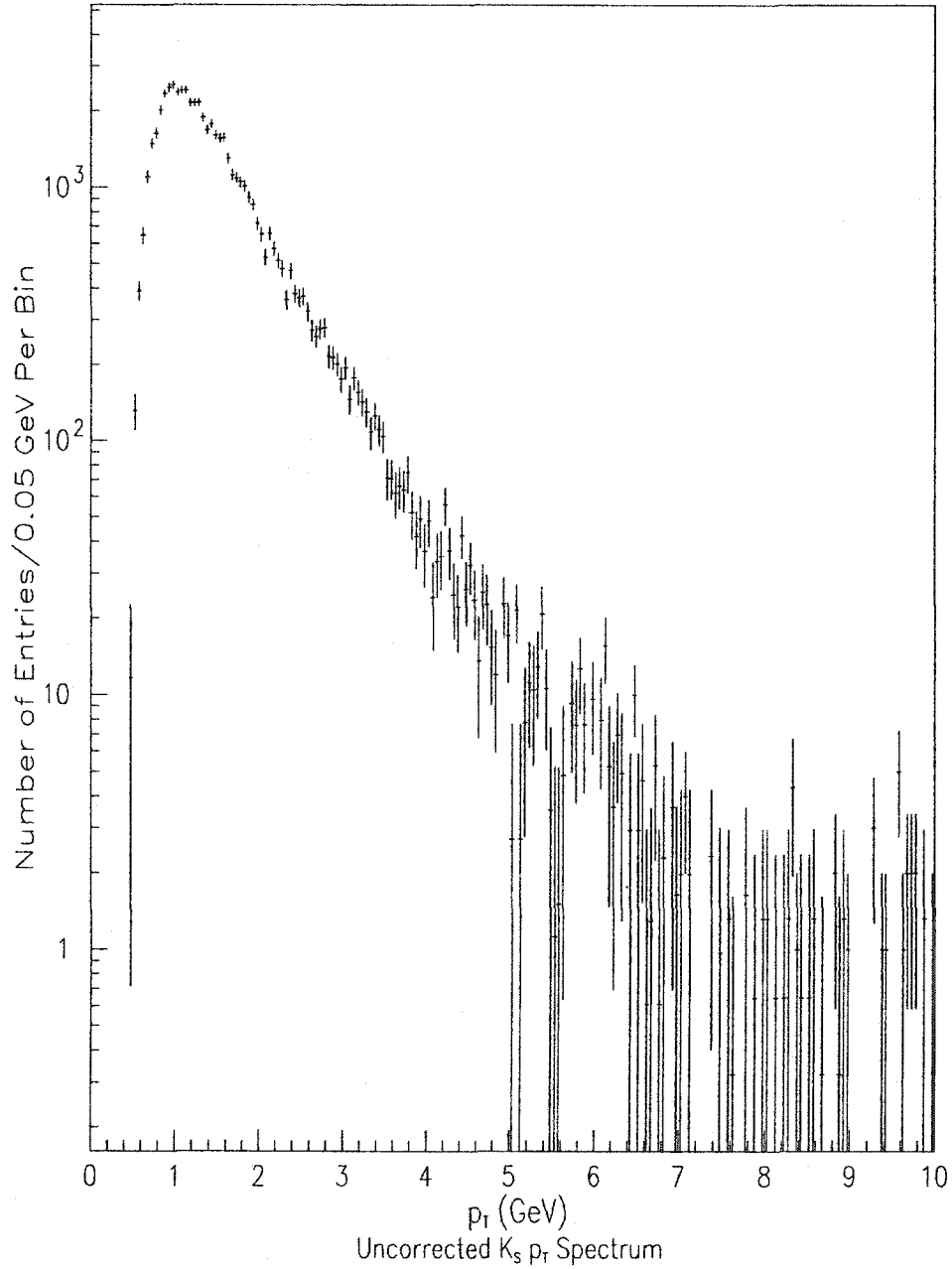
Figure 5.5: The K_S $\frac{dN}{dp_T}$ spectrum. The curve is obtained after background subtraction and is not corrected for efficiencies.
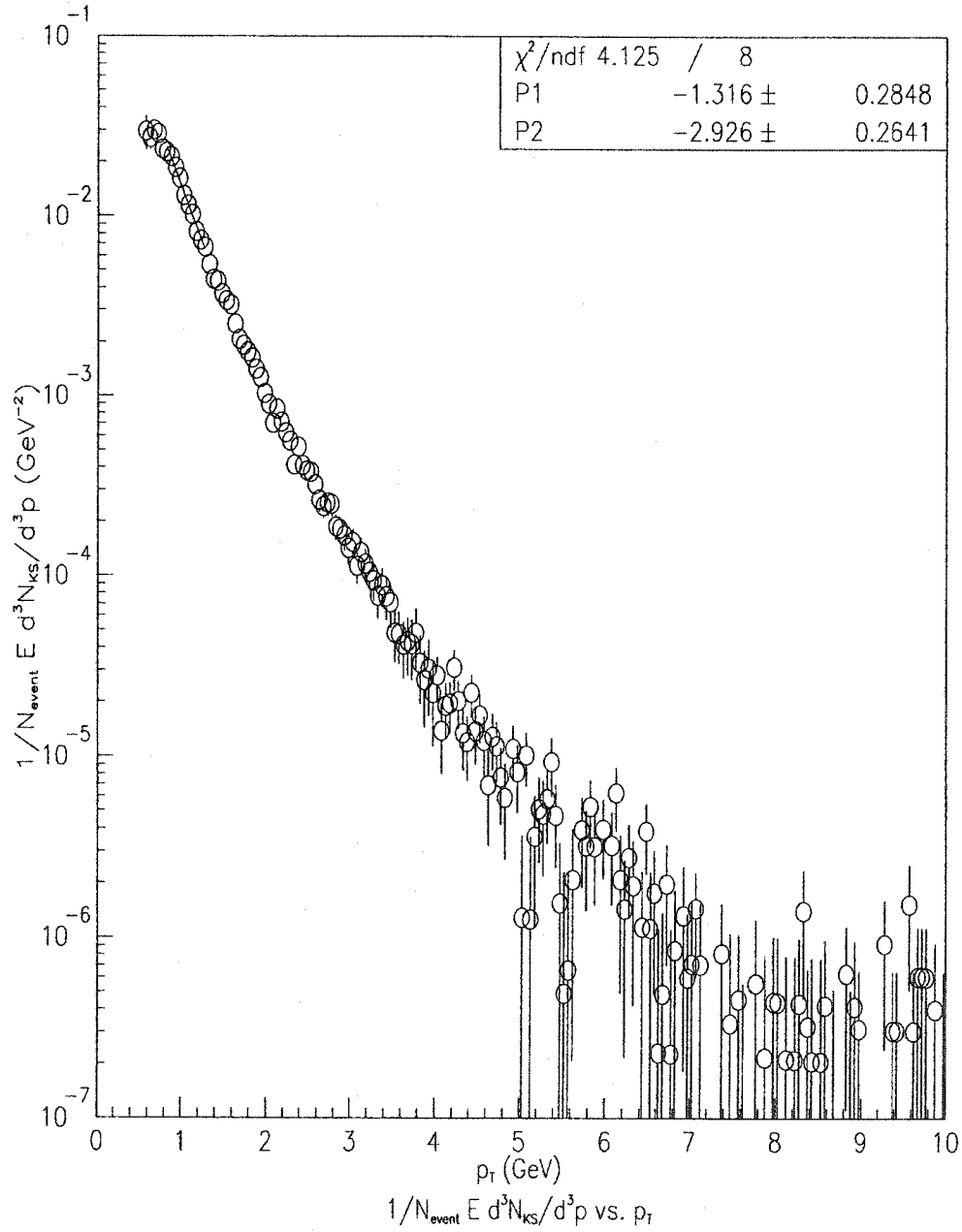
Figure 5.6: The $\frac{E}{N_{event}}$ $\frac{d^3 N_{KS}}{d^3 p}$ spectrum. The spectrum is obtained after background subtraction and is corrected for efficiencies. The curve is fitted with an exponential.
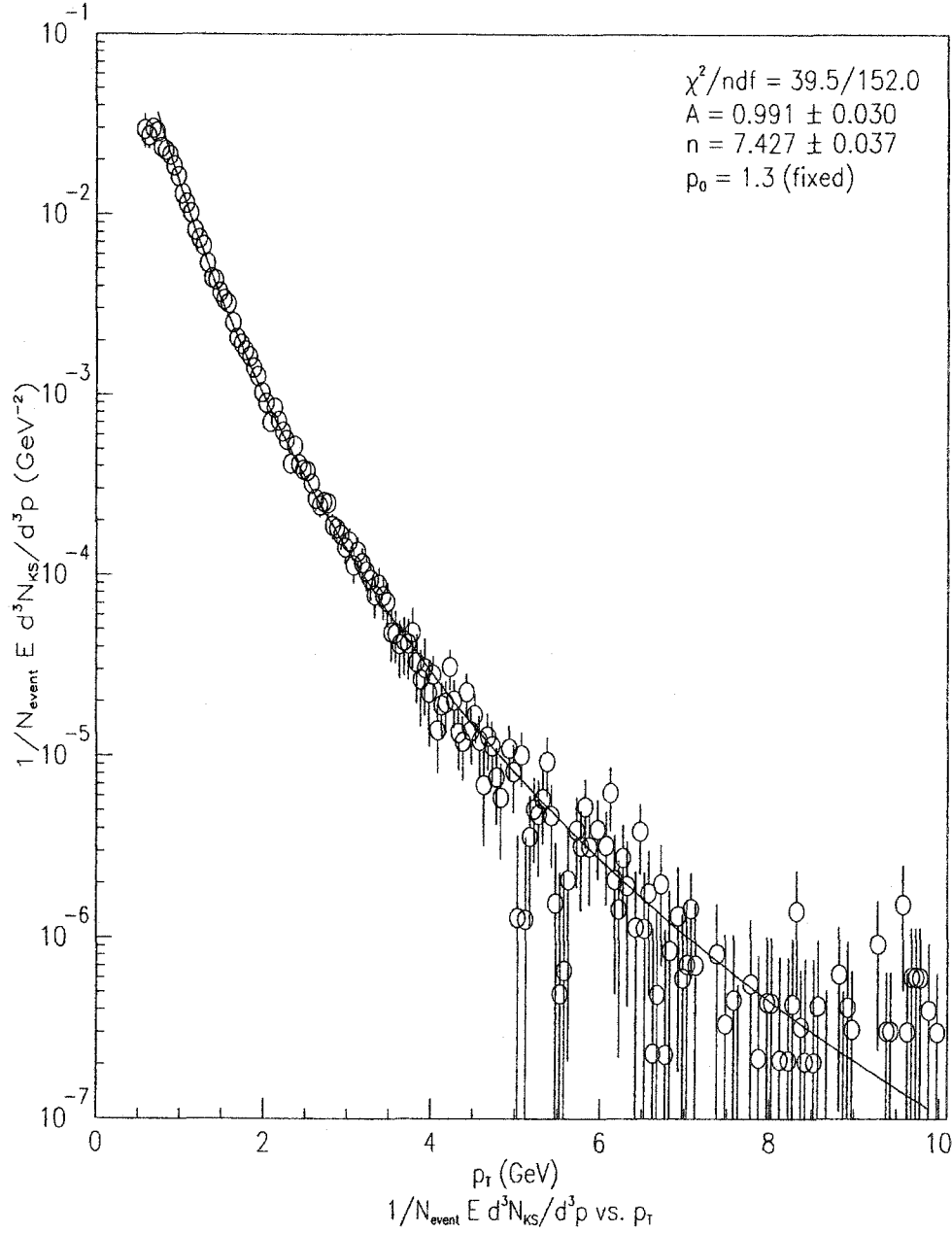
Figure 5.7: The $\frac{E}{N_{event}}$ $\frac{d^3N_{KS}}{d^3p}$ spectrum. The spectrum is obtained after background subtraction and is corrected for efficiencies. The curve is fitted with a power law from 0.7 GeV to 10.0 GeV.
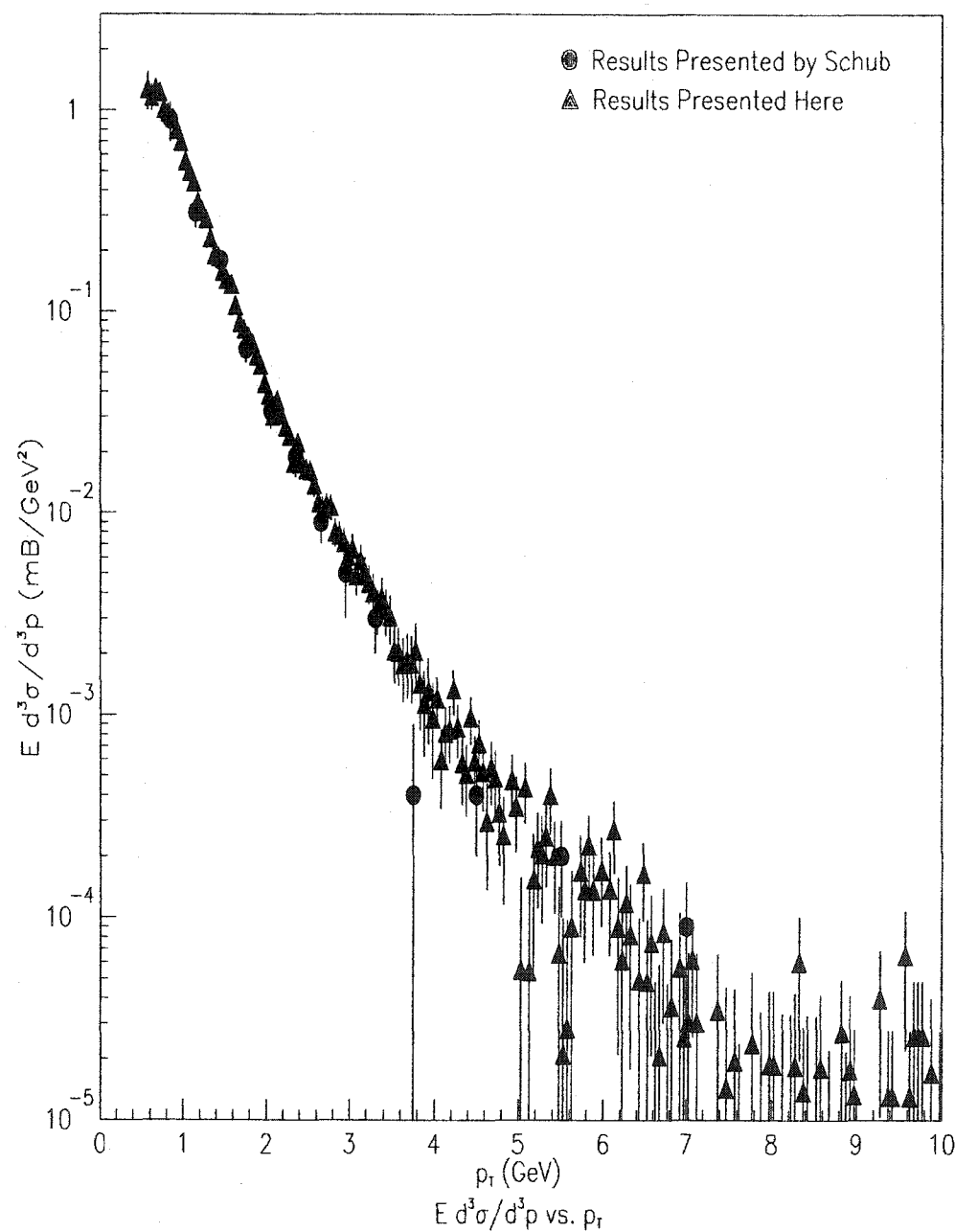
Figure 5.8: The $\frac{Ed^3\sigma}{d^3p}$ spectrum for K_S . The curve is obtained after background subtraction and is corrected for efficiencies.

Chapter 6

Jets: Selection Criteria

The same Minimum Bias event selection cuts are applied to the jet events that pass the jet triggers. The good run cut, the primary vertex cut, and the cosmic filter are employed. The cosmic filter will be described more thoroughly here because the effects are more prevalent. In addition, there is a jet trigger cut that is necessary to prevent double counting of jet events from different jet data samples. The jet selection as well as K_S selection will also be discussed.

6.1 Event Selection

As mentioned previously, the bad run cut, the primary vertex cut, the cosmic filter, and jet trigger cuts are used. Since only the last two cuts are not discussed in the "Minimum Bias Event" chapter, the effects of the cosmic filter and the jet trigger cuts will be described here.

6.1.1 Cosmic Filter

The idea behind the cosmic filter is to reduce the ntuple size by eliminating events that do not appear to be $p\bar{p}$ collisions. The effectiveness of the filter scales with energy; hence, the filter is negligible for the Minimum Bias events and is most

119

effective for events that pass the jet70 and jet100 triggers. It would be good for the filter to remove bad events with bad jets without significantly altering the number of K_S found inside jets as well as the $\frac{N_{KS}}{jet}$ values.

The cosmic filter looks for more than 6.0 GeV of energy in the hadronic calorimeters that is "out-of-time" from the CTC readout. In addition to vetoing cosmic events, monojet, Main Ring splash, and dijets with small missing E_T are removed from the sample. Others studying the effect of the cosmic filter records that 99.75% of the jet20 events, 90.11% of the jet50 events, 77.74% of the jet 70 events, and 77.91% of the jet100 events pass the cut without altering the jet E_T spectrum. Taking this into account, only a study is preformed on the jet100 set since this would give an upper limit the effect.

Of 52025 jet100 events, 43699 events (84% of the total number of events in this small sample) pass the cosmic filter. Dividing the jets into three energy ranges (>100 GeV,50-100 GeV, and 20-50 GeV), Tables 6.1, 6.2, and 6.3 show the effect the cosmic filter has on the number of jets, the number of K_S in jets, and $\frac{N_{KS}}{jet}$. The cosmic filter cuts less than 6% of the jets, less than 2% of the K_S, and tends to increase the $\frac{N_{KS}}{jet}$ by at most 6%. All K_S in the sample must be between 1-10 GeV and $|\eta|<1.0$. The errors on the number of the K_S and the $\frac{N_{KS}}{jet}$ are all less than 5%. Overall, the $\frac{N_{KS}}{jet}$ ratio increases at most 5% because of the cosmic filter and is believed to be the result of not the rejection of K_S but rather the reduction of bad jets in bad events [38] [39]. In Tables 6.1-6.3, the effect of the cosmic filter is shown on the number of jets, the number of K_S inside jets, and the $\frac{N_{KS}}{jet}$ for 20-50 GeV, 50-100 GeV, and greater than 100 GeV jets, respectively.

Table 6.1: The number of jets, K_S in jets, and $\frac{N_{KS}}{jet}$ in 20-50 GeV jets in the Jet100 sample before and after the cosmic filter.

20-50 GeV	Before	After	%
Jets	9848	9469	96.2
K_S in Jets	1222	1209	98.9
$\frac{N_{KS}}{jet}$	0.1223	0.1290	105.5

Table 6.2: The number of jets, K_S in jets, and $\frac{N_{KS}}{jet}$ in 50-100 GeV jets in the Jet100 sample before and after cosmic filter.

50-100 GeV	Before	After	%
Jets	16001	15743	98.4
K_S in Jets	2054	2042	99.6
$\frac{N_{KS}}{jet}$	0.1276	0.1300	101.9

Table 6.3: The number of jets, K_S in jets, and $\frac{N_{KS}}{jet}$ in >100 GeV jets in the Jet100 sample before and after cosmic filter.

>100 GeV	Before	After	%
Jets	30947	29336	94.8
K_S in Jets	3469	3455	99.6
$\frac{N_{KS}}{jet}$	0.1120	0.1178	105.2

6.1.2 Trigger Cut

Since the jet sample actually consists of 4 different tape samples with 5 different L3 triggers, it is not uncommon that one event to be recorded in one or more data sets. In fact, about 15% of the events which pass the jet70 trigger can also be found in the either the jet20, jet50, or jet100 data sets. One might suspect that every event which satisfies the jet100 trigger would automatically pass the jet20 trigger, but because of prescaling, this is often not the case and is not as straightforward.

For this double counting to avoided, the trigger bit string for each event is examined. A sequence of bit values of 0 in the string becomes equal to 1 if an event passes a particular trigger; the string is quite long because there are dozens of possible triggers. To simplify, let us say an event has a bit string denoted by 1111 (1 = pass jet20, 1 = pass jet50, 1 = pass jet70, and 1 = pass jet100) passes all of the jet triggers. If the event passes only the jet20 and jet50 triggers, the string is equal to 1010. There are few different algorithms that would be just as effective to rid the sample of double-counted events, all are equivalent because there is only a unique set. By vetoing events based upon there L3 bit pattern, the resulting data sample contains only unique events. It is important to note this not a "real" cut that removes any events but rather just those that appear more than once [48].

6.2 Jet Selection

When a quark or a gluon fragments, many particles directed toward a particular direction are contained within a cone. Ideally, if all particles are contained within this cone, all momentum and energy of the jet are equal to that of the initial fragmented quark or gluon. In order to account for as much of the energy of the

initial quark or gluon, all particles, charged and neutral, need to be accounted for. Hadronic and electromagnetic energy clusters in the calorimeter can be correlated to that of the energy of the initial fragmented quark or gluon to yield an object called a "jet". A jet is a very well-studied entity and is just as real a physics object as a photon, electron, or muon, except the exact definition is a matter of constant debate and varies much more from analysis to analysis.

A given jet is characterized by the clustering algorithm implemented. A good place to begin is with the cone size of a jet, ΔR, and this variable is defined in units of η and ϕ by $\Delta R = \sqrt{\Delta \eta^2 + \Delta \phi^2}$. Some people prefer $\Delta R = 1.0$, others like $\Delta R = 0.4$, but the most common at CDF is $\Delta R = 0.7$. In this analysis, K_S must be within a jet having a cone size of 0.7.

The idea of jet clustering is to group energy towers together to form bigger and bigger clusters of energy within a cone of 0.7 until all energy towers are associated with either itself or another cluster. The cluster algorithm firsts lists all the towers in both the hadronic and electromagnetic calorimeters having $E_T > 1.0$ GeV. The largest cluster is then taken as the center of a circle having radius of $\Delta R = 0.7$. If there are other towers with $E_T > 1.0$ GeV confined within this circle, this energy is grouped with the initial seed energy and the procedure is repeated until all towers are accounted for. Whenever an energy cluster does not have any additional clusters within the 0.7 cone, the highest energy tower is selected as the new seed.

After this initial stage of the clustering process, various clusters may either be within the cone size of other clusters or overlap with other clusters. Some neighboring clusters are two distinct jets, others should be merged into one. The manner in which this is done is to assign a 4-vector to every tower so that the direction of the 4-vector points from the event vertex to the center of the towers

shower maximum and the magnitude is that of the deposited energy of the tower. The 4-vectors components are summed together according to the following equations

$$E_x = \sum E_x^i, \ E_y = \sum E_y^i, \ E_z = \sum E_z^i, E = \sum E^i \qquad (6.1)$$

$$E_T = E sin\theta, \ \eta = -ln(tan\frac{\theta}{2}), \ \phi = tan^{-1}\frac{E_y}{E_x}. \qquad (6.2)$$

The 4-vectors of each cluster of towers are calculated to give the value of the centroid of every cluster. After the centroids are identified, a circle radius of $\Delta R = 0.7$ is constructed with the centroid as the center. If other clusters are within the circle of another centroid, they either need to be separated or merged together. If the overlap function (shared $\frac{E_T}{min(E_1, E_2)}$) is less than 0.75, the two clusters are distinct and overlapping towers are associated with the cluster nearest in η. If either the overlap function is greater than 0.75 or one cluster is completely within the ΔR of another cluster, the clusters are merged. Centroids are then recalculated as clusters are merged or separated until a jet has the same stable set of towers [6] [7] [8] [66] .

It is worth mentioning that clusters identified as photons and electrons can be taken out of the jet energy calculations either directly or before a reclustering process. The jets in this sample do not do this because the number of photons and electrons is relatively small compared to the number of jets. Muons, depositing little energy in the calorimeters, are not taken into account [6] [7] [8].

6.2.1 Jet Energy Corrections

Clustering itself is insufficient to correctly determine the transverse energy of a jet. Some extra energy from other sources finds its way into the 0.7 cone (underlying

events/multiple interaction corrections), and some energy from the parent-parton escapes the 0.7 cone (out-of-cone corrections). In addition, there are calorimeter energy response questions needed to be applied. Charged particle trajectories bent by the magnetic field so that they lie outside the jet cone are taken into account at this time.

The absolute response correction adjusts for the central calorimeter response to charged and neutral particles. By tuning Monte Carlo to data, a given cluster with a given p_T from the data is compared to the p_T of particles lying within a cone in the Monte Carlo. To compute the mean jet response as a function of E_T for various cone sizes, a quadratic spline is applied for parameterization. In this analysis, the default absolute scalings are implemented [6] [7] [8] [67].

The relative response corrections refer to the scaling of the forward and plug energies to be the equivalent of being measured by the central calorimeters. This correction is obtained from jet events with one central jet and a second jet located elsewhere in the calorimeter. The imbalance between the two jets as a function of p_T and η of the second jet yields a correction factor. Once the jet energy is rescaled to central calorimeter, the jet energy is then adjusted using the response of the central calorimeter [6] [7] [8] [68].

As for extra energy inside the 0.7 cone not originating from the parent-parton, a quantity of energy is removed from every jet tower. The energy has two sources: 1) underlying event energy from spectator partons and 2) energy associated with multiple interactions. The first is isotropically distributed throughout the detector, and the correction factor is determined by employing a dijet sample. The second is a linear function of the number of event vertices as derived from the calorimeter information from the minimum bias samples. The average value of underlying event

contamination is 1.01 GeV. In addition, multiple interactions also contribute extra energy inside the cone. Both are relatively independent of jet E_T for fixed cone size.

The above corrections can be parameterized using the following equation:

$$E_T' = A(R(E_T, \eta))E_T - n_{VTX}b - 1.6a \qquad (6.3)$$

where

E_T' = corrected transverse jet energy

E_T = initial transverse jet energy

$R(E_T, \eta)$ = relative jet corrections

n_{VTX} = number of vertices from extra interactions

b = average energy for a given jet per vertex

$A(R(E_T, \eta))$ = absolute energy correction

a = average energy from a primary interaction as well as additional interaction energy without an additional vertex.

1.6 = accounts for detector response.

The out-of-cone energy adjusts for energy of the parent parton lost from the cone due to fragmentation effects and soft gluon radiation. Since jets tend to be more collimated at higher energies, the out-of-cone energy correction added to each jet decreases with cone-size and jet E_T. The parameterization is obtained from Monte Carlo data and is given by the following equation where a,b,c depend on cone-size:

$$E_T'' = E_T' + a(1 - be^{-c}E_T') \qquad (6.4)$$

where

E_T'' = corrected transverse jet energy for out-of-cone losses.

$E_T' = $ corrected transverse jet energy for underlying events, response, and multiple interactions.

$a = 8.382$

$b = 0.846$

$c = 0.00740$

There is another set of jet energy corrections not incorporated into this analysis, but common enough to deserve mentioning. In cases where muons, electrons, and photons are identified, these objects can be taken out of the jet energy calculation either directly from the energy of the jet or from the energy of towers associated with its cluster. However, the number of electrons, photons, and muons objects candidates is less than 5% of the events in the jet data samples and this small effect is does not warrant this energy correction in either of its forms [6] [7] [8] [69] [70].

In Figure 6.2, the number of jets is histogramed as a function of jet E_T for each trigger sample, both before and after jet energy corrections.

6.2.2   Jet Vertex Selection

To avoid having K_S satisfying the criteria of being inside a jet cone, but in fact may be displaced along the z-axis, some constraint on the primary and jet vertex is necessary. Having already calculated the primary vertex, the tracking information is applied to compute the jet vertices. Each track in the CTC, within $|\eta_{detector}| < 1.1$, with transverse momenta between 0.200 GeV/c and 250 GeV/c, is checked to see whether it falls inside a $\Delta R = 0.7$ jet cone. The z_0 values of these tracks contained within a given jet are averaged to yield a single jet vertex. Every track beyond 60 cm from this jet vertex are removed and the average is recalculated. This process is repeated until all tracks are within 33.75 cm of the jet vertex or until 3 iterations

of the procedure. The root mean square (RMS) of the distribution tracks about the jet vertex indicates the quality of the jet vertex [71] [72].

As for the resolution, by comparing the computed jet vertices to vertices of the two electrons from Z boson events, it was shown the jet vertex resolution increases with the jet energies. For example, for E_T cuts of 10, 15, 20, and 40 GeV, the jet vertex resolutions were 0.87, 0.85, 0.72, and 0.54 cm [8].

Only one primary vertex is selected as the origin of the K_S production, and K_S efficiencies drop significantly as K_S are produced further and further away from the primary vertex. Hence, the jet vertex must be within 5.0 cm of the primary vertex. In addition, a good quality cut on the jet vertex is that it has a $z_{jet}^{rms} < 5.0$ cm.

There are a group of tables that render greater details of how the cuts effect the number of events and jets for each trigger sample. First, in Table 6.5, the number of events after each cut is tallied. Approximately 8-15 % of the events are lost due to these cuts. As for the effect of the selection criteria on the number of jets in each sample, Tables 6.5-6.8 record the number of jets and the fraction of jets left after each cut for each jet sample. Where there are good statistics, about 25% of the 20-50 GeV jets, 30-40 % of the 50-100 GeV jets, and 35-45 % of the 100-150 GeV jets remain after the cuts. On the bottom of the Figure, 6.3, the difference between the primary and jet vertices is plotted for jet 50 sample.

6.3 K_S in Jet Selection Criteria

The cuts are similar to those in the "Minimum Bias Selection" chapter with the exception that K_S must be within a 0.7 cone of a jet having its vertex within 5.0 cm of the primary vertex. For the jet vertex to be more credible, the root mean

square of this calculation must be less than 5.0 cm. In addition, a 0.5 GeV track cut replaces the 300 MeV track cut because K_S originated inside jets have much higher p_T than K_S found in Minimum Bias events. Also, the 2D pointing vector cut is reduced from 0.995 to 0.990 since low p_T K_S in jets have lower 2D pointing vector values than K_S found in the Minimum Bias set. The K_S inside jets are further divided into 20-50 GeV, 50-100 GeV, and 100-150 GeV jet energy ranges.

In Tables 6.9-6.12, the total number of K_S and the number of K_S inside 20-50, 50-100, 100-150 GeV jets is recorded after each cut for each jet sample. Moreover, the fraction of the remaining K_S after in each cut is shown in Figure 6.1 for all data sets. The case for all K_S is plotted in the upper left corner; K_S inside 20-50, 50-100, and 100-150 GeV jets are plotted in the upper right corner, the lower left corner, and the lower right corner, respectively. Later, in Chapter 7, the effect of the cuts on the data and the Monte Carlo will be compared. Finally, the cosine of the angle between the K_S inside a jet and the jet axis is plotted on the top of Figure 6.3. Notice that the K_S are mostly within 30° of the jet axis.

In Figure 6.4, the uncorrected reconstructed mass spectra of the K_S contained within 20-50 GeV, 50-100 GeV, and 100-150 GeV jets are displayed. These K_S have passed the cuts detailed in this section, and the means of the mass distributions are independent of the jet E_T and agree with the measured mass [9]. The mass resolutions vary little from 0.6848E-02 GeV to 0.7432E-02 GeV between the 20-50 GeV and the 100-150 GeV cases. This will be better understood once the efficiencies in Chapter 7 are studied. In short, only 20-50 GeV case has higher efficiencies (see Figure 7.16), and this explains why the mass resolution is slightly narrower for the K_S inside 20-50 GeV jets.

In summary, the cuts are listed below.

Table 6.4: The number of events in the Jet20, Jet50, Jet70, and Jet100 samples after each successive cut.

Cuts	Jet 20 Events	%	Jet 50 Events	%	Jet 70 Events	%	Jet 100 Events	%
Only Cosmic Filter	541,158	100.0	320,177	100.0	307,891	100.0	1,381,935	100.0
Trigger Cut	526,158	97.2	299,986	93.7	256,559	83.3	1,381,935	100.0
Badrun	525,822	97.2	296,496	92.6	250,571	81.4	1,379,960	99.9
$|z_{primary}|<60$ cm	488,177	90.2	273,674	85.5	231,468	75.2	1,272,470	92.1

- K_S Cuts

  - K_S within $\Delta R = 0.7$ jet cone

  - $z_{jet}^{rms} < 5.0$ cm

  - $|z_{primary} - z_{jet}| < 5.0$ cm

  - $\chi_{KS}^2 < 20.0$

  - $|z_{KS} - z_{primary}| < 3.0$ cm

  - $p_T^{tracks \; from \; KS} > 500$ MeV

  - $|\eta^{KS}| < 1.0$

  - 3D Displacement$^{KS} > 1.0$ cm

  - $\cos \theta_{PD}{}^{KS} > 0.990$

  - $1.5 < p_T^{KS} < 10.0$ GeV

Table 6.5: The number of jets in the Jet20 sample after each successive cut for 20-50, 50-100, 100-150 GeV E_T ranges.

Cuts	20-50 GeV Jets	%	50-100 GeV Jets	%	100-150 GeV Jets	%
Cosmic Filter and Trigger Cut	856,235	100.0	139,186	100.0	512	100.0
Badrun	856,209	100.0	139,047	99.9	331	64.6
$\|z_{primary}\|<60.0$ cm	794,726	92.8	130,436	93.7	249	48.6
$\|\eta_{jet}^{detector}\|<1.0$	418,093	48.8	72,358	52.0	142	27.7
$z_{jet}^{rms}<5.0$ cm	274,642	32.1	47,383	34.0	98	19.1
$\|z_{primary}\text{-}z_{jet}\|<5.0$ cm	245,167	28.6	42,032	30.2	86	16.8

Table 6.6: The number of jets in the Jet50 sample after each successive cut for 20-50, 50-100, 100-150 GeV E_T ranges.

Cuts	20-50 GeV Jets	%	50-100 GeV Jets	%	100-150 GeV Jets	%
Cosmic Filter + Trigger Cut	215,604	100.0	453,249	100.0	70,390	100.0
Badrun	215,364	99.9	451,176	99.5	65,195	92.6
$\|z_{primary}\|<60.0$ cm	196,379	91.1	417,999	92.2	65,032	92.4
$\|\eta_{jet}^{detector}\|<1.0$	94,230	43.7	268,263	59.2	42,647	60.6
$z_{jet}^{rms}<5.0$ cm	60,040	27.8	186,763	41.2	29,108	41.4
$\|z_{primary}\text{-}z_{jet}\|<5.0$ cm	54,267	25.2	168,951	37.3	26,131	37.1

Table 6.7: The number of jets in the Jet70 sample after each successive cut for 20-50, 50-100, 100-150 GeV E_T ranges.

Cuts	20-50 GeV Jets	%	50-100 GeV Jets	%	100-150 GeV Jets	%
Cosmic Filter + Trigger Cut	147,902	100.0	247,841	100.0	257,864	100.0
Badrun	147,424	99.7	246,535	99.5	253,878	98.5
$|z_{primary}| < 60.0$ cm	134,909	91.2	222,567	89.8	241,343	93.6
$|\eta_{jet}^{detector}| < 1.0$	67,365	45.5	140,498	56.7	180,045	69.8
$z_{jet}^{rms} < 5.0$ cm	41,700	28.2	98,285	39.7	124,148	48.1
$|z_{primary} - z_{jet}| < 5.0$ cm	38,376	25.9	90,657	36.6	113,808	44.1

Table 6.8: The number of jets in the Jet100 sample after each successive cut for 20-50, 50-100, 100-150 GeV E_T ranges.

Cuts	20-50 GeV Jets	%	50-100 GeV Jets	%	100-150 GeV Jets	%
Cosmic Filter + Trigger Cut	1,137,327	100.0	1,443,838	100.0	1,707,897	100.0
Badrun	1,124,784	98.9	1,435,133	99.4	1,672,636	97.9
$|z_{primary}| < 60.0$ cm	1,015,976	89.3	1,265,212	87.6	1,569,682	91.9
$|\eta_{jet}^{detector}| < 1.0$	511,508	45.0	743,847	51.5	1,175,526	68.8
$z_{jet}^{rms} < 5.0$ cm	313,346	27.6	504,708	35.0	805,874	47.2
$|z_{primary} - z_{jet}| < 5.0$ cm	286,431	25.2	463,542	32.1	736,875	43.1

Table 6.9: The number of K_S in the Jet20, Jet50, Jet70, and Jet100 samples after each successive cut.

Cuts	Number of K_S in Jet 20	Number of K_S in Jet 50	Number of K_S in Jet 70	Number of K_S in Jet 100
Only Cosmic Filter + Trigger Cut	143217 ± 1584	97372 ± 1394	86619 ± 1405	594055 ± 3656
Badrun	143167 ± 1584	97202 ± 1394	86120 ± 1400	587459 ± 3644
$|z_{primary}| < 60.0$ cm	134531 ± 1540	91150 ± 1346	80664 ± 1367	543020 ± 3507
$\chi^2_{KS} < 20.0$	113811 ± 1162	77689 ± 1056	70211 ± 1100	472911 ± 2807
$|z_{KS}\text{-}z_{primary}| < 3.0$ cm	110787 ± 1142	75925 ± 1041	68575 ± 1078	460783 ± 2771
$p_T^{tracks} > 500$ MeV	70522 ± 778	52332 ± 796	48592 ± 854	327799 ± 2160
$|\eta^{KS}| < 1.0$	61340 ± 703	46332 ± 738	43692 ± 804	293571 ± 2032
3D $\text{Dis}^{KS} > 1.0$ cm	58175 ± 544	42340 ± 572	40397 ± 624	270102 ± 1580
$\cos\theta_{PD}{}^{KS} > 0.990$	56651 ± 497	41476 ± 535	39590 ± 581	262582 ± 1450
$1.5 < p_T^{KS} < 10$ GeV	47027 ± 450	34924 ± 467	32998 ± 498	221953 ± 1304

Table 6.10: The number of K_S in 20-50 GeV jets in the Jet20, Jet50, Jet70, and Jet100 samples after each successive cut.

Cuts	Number of K_S in Jet 20 20-50 GeV Jets	Number of K_S in Jet 50 20-50 GeV Jets	Number of K_S in Jet 70 20-50 GeV Jets	Number of K_S in Jet 100 20-50 GeV Jets
Cosmic Filter + Trigger Cut	49126 ± 918	12789 ± 506	8579 ± 429	64166 ± 1121
Badrun	49122 ± 918	12792 ± 506	8561 ± 426	63845 ± 1121
$|z_{primary}| < 60.0$ cm	46551 ± 893	11940 ± 487	7954 ± 426	59245 ± 1082
$|\eta_{jet}^{detector}| < 1.0$	41408 ± 818	10293 ± 439	7270 ± 403	52384 ± 1008
$z_{jet}^{rms} < 5.0$ cm	29756 ± 650	7087 ± 346	4918 ± 300	35870 ± 795
$|z_{primary}\text{-}z_{jet}| < 5.0$ cm	28401 ± 627	6940 ± 335	4778 ± 292	34826 ± 765
$\chi_{KS}^2 < 20.0$	27461 ± 560	6544 ± 307	4666 ± 264	33631 ± 692
$|z_{KS}\text{-}z_{primary}| < 3.0$ cm	26710 ± 550	6431 ± 304	4594 ± 260	32916 ± 683
$p_T^{tracks} > 500$ MeV	21151 ± 435	5024 ± 229	3572 ± 218	26048 ± 548
$|\eta^{KS}| < 1.0$	20159 ± 427	4746 ± 214	3463 ± 215	24786 ± 528
3D Dis$^{KS} > 1.0$ cm	19066 ± 310	4452 ± 173	3275 ± 160	22895 ± 397
$\cos\theta_{PD}{}^{KS} > 0.990$	18721 ± 316	4356 ± 165	3157 ± 143	22126 ± 366
$1.5 < p_T^{KS} < 10.0$ GeV	16886 ± 297	3995 ± 161	2807 ± 127	20026 ± 332

Table 6.11: The number of K_S in 50-100 GeV jets in the Jet20, Jet50, Jet70, and Jet100 samples after each successive cut.

Cuts	Number of K_S in Jet 20 50-100 GeV Jets	Number of K_S in Jet 50 50-100 GeV Jets	Number of K_S in Jet 70 50-100 GeV Jets	Number of K_S in Jet 100 50-100 GeV Jets
Cosmic Filter + Trigger Cut	9879 ± 524	35254 ± 912	19437 ± 729	108992 ± 1767
Badrun	9879 ± 524	35249 ± 912	19423 ± 729	108910 ± 1766
$|z_{primary}|{<}60.0$ cm	9453 ± 517	33119 ± 898	18070 ± 737	98859 ± 1722
$|\eta_{jet}^{detector}|{<}1.0$	8435 ± 487	30683 ± 848	16533 ± 710	87980 ± 1568
$z_{jet}^{rms}{<}5.0$ cm	5734 ± 357	23070 ± 686	12468 ± 599	65563 ± 1285
$|z_{primary}\text{-}z_{jet}|{<}5.0$ cm	5466 ± 339	22252 ± 663	12100 ± 585	63912 ± 1250
$\chi_{KS}^2{<}20.0$	5236 ± 304	21341 ± 603	11525 ± 534	61481 ± 1121
$|z_{KS}\text{-}z_{primary}|{<}3.0$ cm	5171 ± 296	20862 ± 597	11262 ± 524	59989 ± 1095
$p_T^{tracks}{>}500$ MeV	4131 ± 236	16938 ± 518	9154 ± 443	49206 ± 933
$|\eta^{KS}|{<}1.0$	3937 ± 227	16302 ± 512	8661 ± 424	46652 ± 921
3D Dis$^{KS}{>}1.0$ cm	3670 ± 178	14722 ± 400	8161 ± 330	42954 ± 711
$\cos\theta_{PD}{}^{KS}{>}0.990$	3566 ± 173	14316 ± 374	8089 ± 317	42220 ± 676
$1.5{<}p_T^{KS}{<}10.0$ GeV	3038 ± 150	12388 ± 323	6937 ± 269	36961 ± 593

Table 6.12: The number of K_S in 100-150 GeV jets in the Jet20, Jet50, Jet70, and Jet100 samples after each successive cut.

Cuts	Number of K_S in Jet 20 100-150 GeV Jets	Number of K_S in Jet 50 100-150 GeV Jets	Number of K_S in Jet 70 100-150 GeV Jets	Number of K_S in Jet 100 100-150 GeV Jets
Cosmic Filter + Trigger Cut	NA	5421 ± 390	23159 ± 906	148828 ± 2184
Badrun	NA	5419 ± 392	23153 ± 907	148433 ± 2182
$|z_{primary}| < 60.0$ cm	NA	5311 ± 385	22135 ± 881	140523 ± 2155
$|\eta_{jet}^{detector}| < 1.0$	NA	4954 ± 390	20955 ± 866	131467 ± 2082
$z_{jet}^{rms} < 5.0$ cm	NA	3597 ± 390	16021 ± 734	97180 ± 1718
$|z_{primary}\text{-}z_{jet}| < 5.0$ cm	NA	3561 ± 437	15442 ± 720	94075 ± 1662
$\chi_{KS}^2 < 20.0$	NA	3377 ± 332	15007 ± 646	90778 ± 1506
$|z_{KS}\text{-}z_{primary}| < 3.0$ cm	NA	3309 ± 314	14594 ± 602	88699 ± 1477
$p_T^{tracks} > 500$ MeV	NA	2551 ± 269	11540 ± 523	72328 ± 1267
$|\eta^{KS}| < 1.0$	NA	2525 ± 262	11205 ± 519	69816 ± 1235
3D $\text{Dis}^{KS} > 1.0$ cm	NA	2293 ± 188	9977 ± 392	63826 ± 962
$\cos\theta_{PD}{}^{KS} > 0.990$	NA	2337 ± 186	9798 ± 366	62173 ± 902
$1.5 < p_T^{KS} < 10.0$ GeV	NA	1973 ± 131	8300 ± 305	53398 ± 760
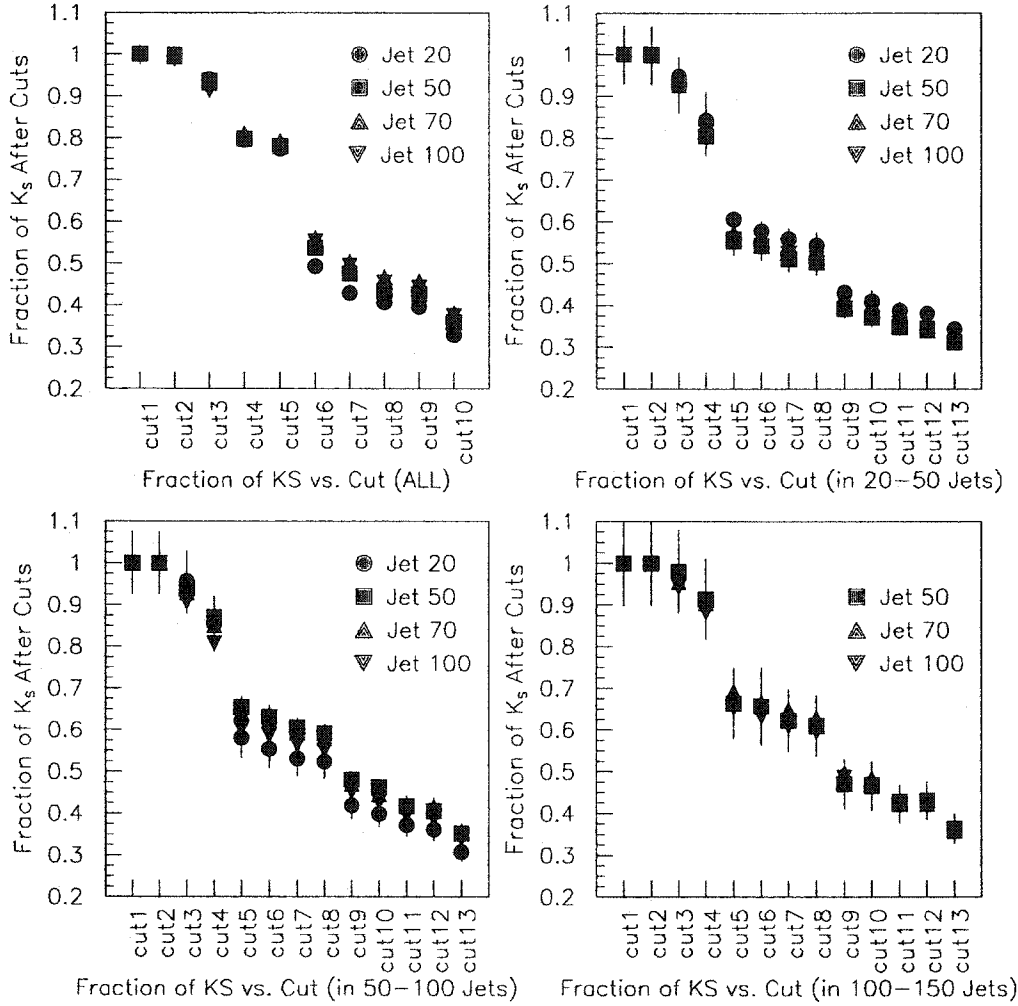
Figure 6.1: The fraction of the K_S left after each cut in each jet sample. In the upper left corner, the fraction of the K_S left after every cut for all K_S is plotted. In the upper right corner, the fraction of the K_S left after every cut for all K_S inside 20-50 GeV jets is plotted. In the lower left corner, the fraction of the K_S left after every cut for all K_S inside 50-100 GeV jets is plotted. In the lower right corner, the fraction of the K_S left after every cut for all K_S inside 100-150 GeV jets is plotted. The cut labels are defined in the following manner: cut1 = Cosmic Filter + Trigger Cut, cut2 = Badrun, cut3 = $|z_{primary}| < 60.0$ cm, cut4 = $\eta_{jet}^{detector} < 1.0$, cut5 = $z_{jet}^{rms} < 5.0$ cm, cut6 = $|z_{primary} - z_{jet}| < 5.0$ cm, cut7 = $\chi^2_{KS} < 20.0$, cut8 = $|z_{KS} - z_{primary}| < 3.0$ cm, cut9 = $p_T^{tracks\ from\ KS} > 500$ MeV, cut10 = $|\eta^{KS}| < 1.0$, cut11 = 3D Displacement$^{KS} > 1.0$ cm, cut12 = $\cos\theta_{PD}{}^{KS} < 0.990$, and cut13 = $1.5 GeV < p_T^{KS} < 10.0$ GeV.
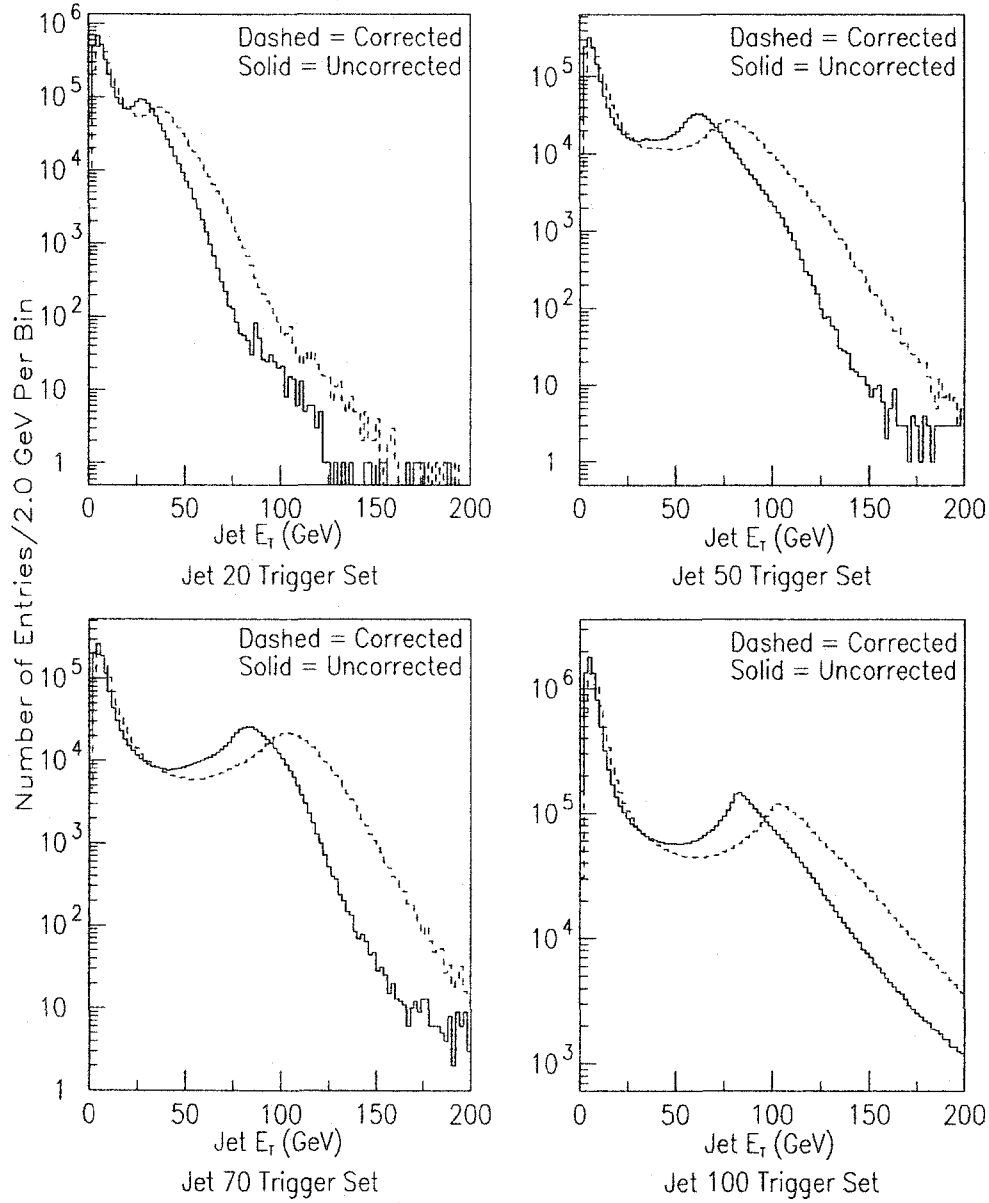
Figure 6.2: The jet E_T distribution for the Jet20, Jet50, Jet70, and Jet100 sets. The solid line is the uncorrected jet energy distribution, and the dashed line is the corrected jet energy distribution.
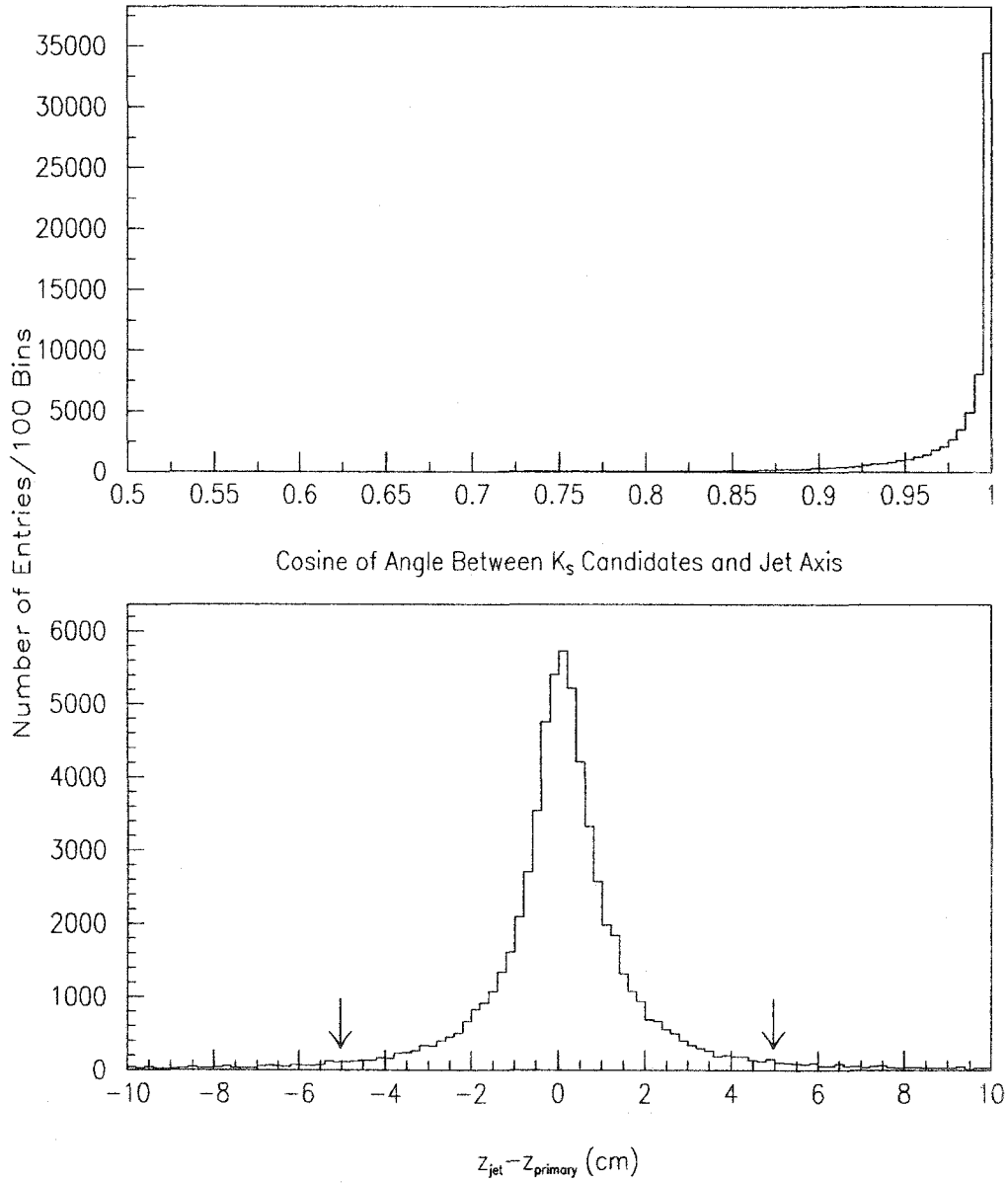
Figure 6.3: In the upper figure, the cosine of the angle between the K_S and the jet axis is plotted for K_S inside 0.7 cone jets in Jet 50 sample. In the lower figure, the difference between the jet vertex and primary vertex is plotted for the Jet 50 sample.
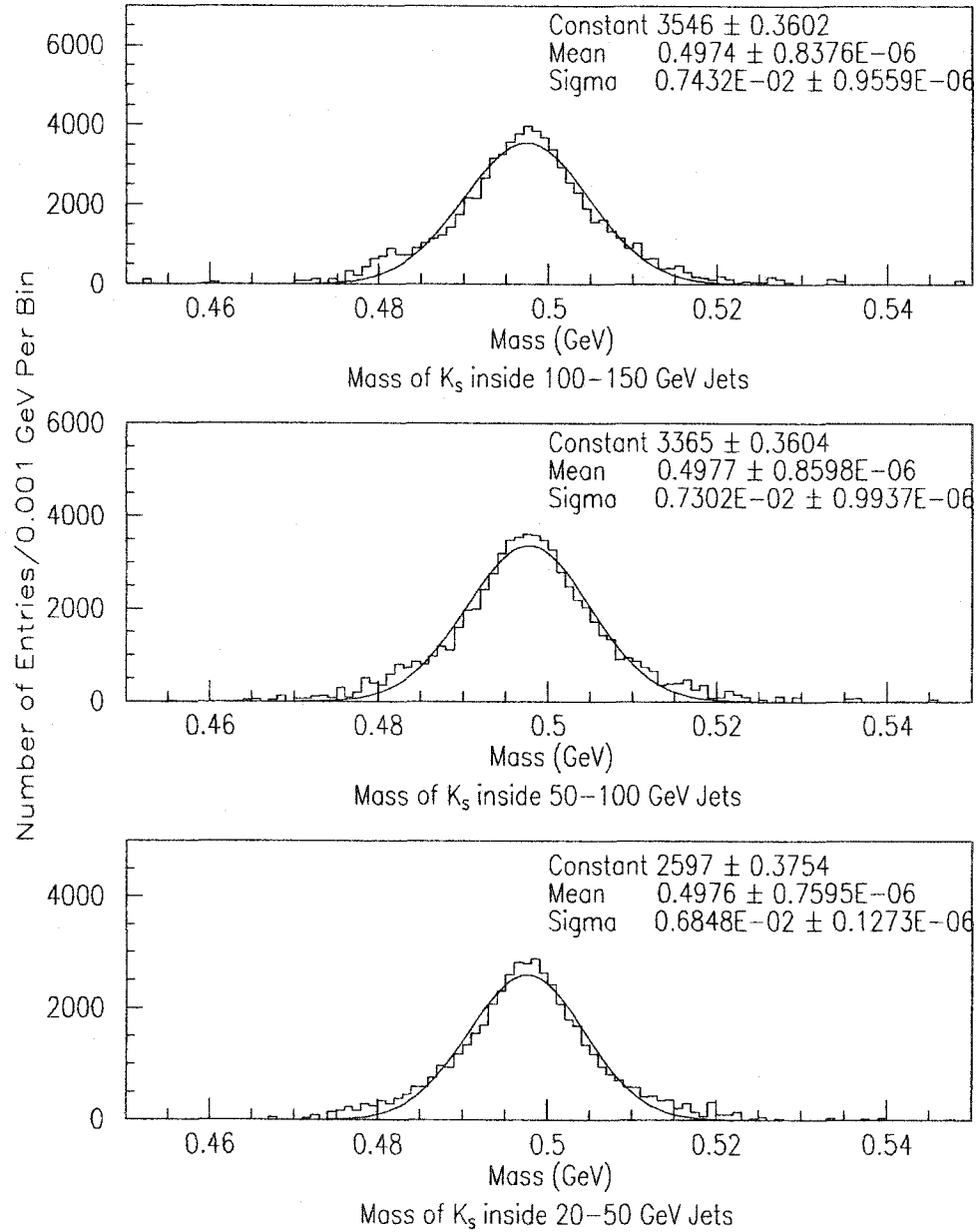
Figure 6.4: The mass distribution of K_S candidates after background subtraction after cuts. These particles are found inside 100-150 GeV jets (top), 50-100 GeV jets (middle), and greater than 20-50 GeV Jets (bottom).

Chapter 7

Jets: Efficiencies From Track Embedding

There are many similarities and differences between track embedding in the Minimum Bias and jet samples. Just as in the case for K_S in the Minimum Bias data, not all K_S are found inside jets in the jet sample. Like the track-embedding K_S in the Minimum Bias sample, the efficiency of finding K_S in the CDF detector is strongly correlated to the p_T of the K_S . Again, once the K_S have been extracted from the data, these efficiency curves are used to correct for the inefficiency of the CTC. However, correcting for K_S in jets introduces additional complications than in the Minimum Bias case that must be taken into account.

Since the goal is to study K_S production in jets, K_S can no longer be placed with random η and ϕ in the jet data as is done in the Minimum Bias sample, but rather K_S must be placed inside 0.7 jet cones. Furthermore, K_S are not put in jets with random η and ϕ anywhere inside 0.7 jet cones. Instead, the K_S are deposited in jets similar to other particles. Also, K_S are not embedded in any jet in the jet data sample. K_S have to be embedded in jets that have jet vertices relatively close to the primary vertices so that the secondary vertex algorithm can find them (i.e. K_S would fail the pointing back criteria). Additional factors include depositing K_S inside jets and finding them, but the K_S are reconstructed outside the jet

141

cones would be considered lost. Moreover, K_S efficiency is now dependent on jet properties such as jet E_T. Another important factor is that K_S must be embedded in a jet sample having luminosity along with jet properties similar to those of the data.

In this chapter, a review of track-embedding will be reiterated, followed by a detailed track-embedding procedure that addresses some issues described above. Then, comparisons between K_S and background distributions will be made as well as comparisons between K_S in data and K_S in track-embedded Monte Carlo. K_S in jet efficiencies as a function of luminosity, η_{jet}, ϕ_{phi}, $|z_{primary}-z_{jet}|$, and the number of tracks per jet will also be presented along with the actual efficiency curves needed to correct the K_S inside jets in the jet data. Finally, since K_S production will be compared to charged particle production, the calculation of single track efficiency in jets curves will be described in order to later correct the single track p_T spectrum in jets.

7.1 Track-embedding Reiterated

By depositing hits of Monte Carlo K_S into the CTC data and rerunning reconstruction, the efficiency of finding K_S in data can be determined. The efficiency of CDF detector of finding K_S is strongly correlated to the p_T. Once K_S p_T curves have been extracted from data, these efficiency curves as a function of p_T can be used to correct for the inefficiency of the CTC.

About 10,000 actual jet events are employed for the track embedding study. The sample is checked to have a similar luminosity distribution to actual jet data as well as pass all criteria specified for jet events. A simple tally of good track-embedding events is kept (events in which one K_S is embedded into one jet in one event). Jet

events just pass the QCDB triggers (one trigger before the triggers used to produce the JET20, JET50, JET70, and JET100 sets) because later triggers drop the banks needed to embed hits. Since events pass jet triggers, each event is more likely to have high track multiplicity and many more CTC hits than Minimum Bias events. In Figure 7.2, a transverse view of the CTC is given for a typical jet event selected prior to track embedding. The dots are the actual hits in the CTC, and the fitting of the hits yields the tracks given by solid lines. Only charged particles create hits in the CTC, and only charged particles can be seen directly with CTC. K_S being all neutral would themselves be invisible. Only the daughter pions can be seen directly. Also, the greater the p_T of a track, the less visible the curvature.

In Figure 7.3, the event in Figure 7.2 has had 3.0 GeV K_S embedded into a 136.9 GeV jet. If you compare the 1:00 position of Figure 7.2 and Figure 7.3, you should count 10 tracks in Figure 7.2 and 12 tracks in Figure 7.3. The additional 2 tracks are the embedded 3.0 GeV K_S. The high p_T pion is new straight track, and the low p_T pion track is the new curved track. The tracks of the pions intersect at the approximately the same point the K_S decays forming a "V". However, some events in which track embedding is attempted does not successfully reveal K_S. A K_S, if it has too much p_T, can decay outside the CTC; a K_S may also slip through a crack so that it is never found. The daughter particles can also escape the detection of CTC, especially if the p_T of the individual tracks are too soft. This is quite often the case with pions and explains most of the loss of efficiency for K_S. The efficiency is given as the number of a K_S in jets found divided by the number of the events that have had K_S track-embedded into them.

Since the embedding procedure in jets is complex and will be discussed in greater detail in the next section, for now the daughter particles of K_S are "magically",

details saved for the next section, embedded inside jets at the primary vertex as hits in the CTC. "Magically", kinematic and vertice information of daughter particles of K_S are saved in text files after K_S are produced and decayed in FAKEEVENT and CDFSIM, and the daughters of the K_S are then embedded inside jets such that K_S a distribution similar to other particles. The distributions of jets incorporated for track-embedding is similar to the distributions of the other jets in the jet data, and the embedding jet events are liken to the events found in jet events. The information in the text file is adjusted in order to embedded the daughters of the K_S at the primary vertices close to the jet vertices, and 4-vector and vertice information from the daughters of the K_S are converted to track parameters, and track parameters are converted to hits in the CTC. Once hits are added to the data, reconstruction is rerun to produce a new list of tracks from which code can then be applied to discover whether K_S in a specified embedded jet can be found.

In determining K_S inside jets in the track-embedded data, identical selection criteria are utilized as described in Chapter 6 with the exception of using a reconstructed K_S p_T window cut. As before in the Minimum Bias track-embedding, since the p_T of track-embedded K_S is known, the information is necessary in order to separate the K_S candidate from K_S already present in the data set. Table 7.2 has the ranges of the K_S shown along with the p_T window for each range. In Figure 7.4, 1.6 GeV and 6.0 GeV track-embedded K_S candidates are displayed. The solid line represents the K_S that fail the p_T window cut and may be K_S already present in the data, and the dashed line shows the embedded K_S that pass the p_T window cut. K_S already inside the embedding data may or may not be within jets, and these K_S give rise to solid line K_S mass peak. For 1.6 GeV K_S , the p_T window is 30 MeV, and for the 6.0 GeV K_S , the p_T window is 0.5 GeV. On the

bottom figures of Figure 7.4, the fitted background subtracted mass plots of K_S passing the p_T window cut are plotted. Figure 7.4 shows that the mass resolution of K_S in jets increases from approximately 0.006 GeV for 1.6 GeV embedded K_S to approximately 0.008 GeV for 6.0 GeV embedded K_S . Figure 7.5 contains the p_T of the K_S along with arrows indicating the range of the p_T window. The bottom figures in Figure 7.5 reveals the background subtracted fitted p_T of K_S that are within the p_T window. In Figure 7.5 (below), the resolution of the p_T increases from approximately 0.006 GeV for 1.6 GeV embedded K_S to about 0.07 GeV for 6.0 GeV embedded K_S .

The number of K_S in jets are calculated at a range of p_T intervals. In top of Figure 7.4, there is a small mass peak (dashed line) that passes the p_T window cuts as well as the event and jet cuts. Once the background has been subtracted from this peak, the resulting mass peaks (fitted plots on the bottom of Figure 7.4) can be fitted and the number of K_S can be summed from 0.48 to 0.52 GeV. The efficiency is given by the number of K_S found within jets divided by the number of K_S embedded inside jets. The points are then plotted against p_T using fitting errors to produce plots in Figures 7.16-7.18. The upper portion of each figure consists of each point as a function of p_T, and lower portions of Figure 7.16-7.18 are each fitted for two different p_T ranges. These curves are needed to correct the p_T spectra of the K_S in the data. Note that in Minimum Bias case, there is only a single efficiency curve, and now there are three efficiency curves, one for each jet E_T range. This is done because K_S in jet efficiency is also a function of jet E_T. The next section will describe the track-embedding procedure in much more detail.

7.2 Track-embedding Jet Procedure

Step 1) Obtaining the $\Delta R_{jet-track}$ distribution of tracks in jets.

The K_S will be placed inside jets in a manner similar to all other particles since there is not any reason that K_S should be distributed differently. The distribution of tracks as function of $\Delta R_{jet-track}$ is defined by:

$$\Delta R_{jet-track} = \sqrt{(\eta_{jet} - \eta_{track})^2 + (\phi_{jet} - \phi_{track})^2} \tag{7.1}$$

Also, only the shape of the distribution is of interest, and this changes slightly for efficiency corrections (CTC track efficiency is high), track p_T cuts, η cuts, number of events, etc. Many of these cuts are studied as to what effect each has on the shapes of the $\Delta R_{jet-track}$ distribution, and one variable that has a significant effect is that of the jet E_T. The $\Delta R_{jet-track}$ distribution can be a strong function of jet E_T, especially at low jet E_T.

The entire jet set is ran through with the following cuts and is the first step in producing the distributions:

- Track cuts for the production of $\Delta R_{jet-track}$ distributions.

    - Event Cuts

    - $|z_{primary}\text{-}z_{jet}| < 5.0$ cm

    - $|z_{primary}\text{-}z_{track}| < 5.0$ cm

    - Track is associated with the nearest jet within $\Delta R_{jet-track} < 1.0$

    - Booked according to Jet E_T Ranges

There are over 25 $\Delta R_{jet-track}$ distributions corresponding to different jet E_T ranges, and each distribution is subtracted by a flat constant function which yields

0.0 at $\Delta R_{jet-track} = 0.7$. These are the distributions implemented in the track embedding. In Figure 7.1, $\Delta R_{jet-track}$ are grouped into just 3 energy ranges, 20-50 GeV, 50-100 GeV, and 100-150 GeV, and are normalized to unit area. As jet E_T increases, the shape of the $\Delta R_{jet-track}$ distribution becomes broader as the peak of the distribution moves to larger values of $\Delta R_{jet-track}$. This is not a particularly large efficiency effect.

Step 2) Create text files of 4-vector and vertice data of K_S daughters. Create the text files of 4-vectors and primary and secondary vertice information of daughters from K_S at random η, $|\eta|<2.0$, and random ϕ, $0\leq\phi<2\pi$. These are the exact text files incorporated into the Minimum Bias track-embedding produced with FAKEEVENT and CDFSIM.

Step 3) Select an embedding data sample. The embedding sample consists of events from a data set that has CTC hit banks. Unfortunately, the CTC hit banks are not found in the JET20, JET50, JET70, and JET100 sets (they are dropped as these sets are created). Hence, the parent set (QJTB) for the jet trigger samples is needed for the track embedding. In addition, not any subset of QJTB would do, but the sample has to include events with a instantaneous luminosity distribution similar to that of the jet data set. Otherwise, luminosity efficiency corrections would be needed. The events must satisfy the criteria of cosmic filter (all other event cuts will be applied later). The event also must have at least one of the two highest energy jets with a primary vertex within 5.0 cm of the jet vertex. This last requirement is to optimize the track embedding process (virtually all jet vertices that are within 5.0 cm of the primary vertex are from the 2 highest E_T jets).

Step 4) Select jets for track-embedding.

First, jets must have $|\eta_{jet}|<2.0$ before being considered because the CTC coverage is approximately $|\eta|<1.0$. Since for every event, there is only one K_S embedded into only one jet, some caution must be exercised to avoid having all K_S embedded into jets of a particular energy range. In particular, there is an algorithm and "cap" designed to limit the number of events with a certain jet energy. For example, if there are 10000 jets between 100-150 GeV and 500 jets between 50-100 GeV, the program will keep the 500 jets between 50-100 GeV and up to 2000 jets between 100-150 GeV. The jet E_T are corrected prior to this selection process; all other jet cuts are applied later. It is important to clarify that the properties of the jet taken for embedding are saved for later and are denoted by ϕ_{embed}, η_{embed}, and jet E_T^{embed}.

Step 5) Selecting an embedding direction in a jet for track-embedding. Once an embedding jet is selected, applying Monte Carlo techniques to the $\Delta R_{jet-track}$ distribution for the particular jet E_T sets an embedding direction with a given $\phi_{direction}$ and $\eta_{direction}$ with respect to ϕ_{embed} and η_{embed} of the selected jet where the K_S will be embedded. This is the embedding direction is where the K_S should be placed.

Step 6) Selecting a K_S closest to the embedding direction in $\Delta R_{KS-direction}$. The text file is ran through until a K_S closest to the embedding direction is found. The text file is used over and over again without K_S being removed from the list. The "randomness" of the $\phi_{direction}$ and $\eta_{direction}$ ensures the randomness of the ϕ and η of the K_S. The "randomness" of $\phi_{direction}$ and $\eta_{direction}$ depends on ϕ_{embed} and η_{embed}, and the η_{embed} is not a perfectly flat distribution between $|\eta_{embed}|<2.0$. However, the η_{embed} are distributed enough to result in a similar η_{KS} spectrum to

prevent the same K_S from being selected repeatedly. $\Delta R_{KS-direction\ jet}$ is given by

$$\Delta R_{KS-direction} = \sqrt{(\eta_{KS} - \eta_{direction})^2 + (\phi_{KS} - \phi_{direction})^2} \qquad (7.2)$$

$\Delta R_{KS-direction}$ is mostly less than 0.05, and the distribution peaks at 0.025. Hence, the embedding of the K_S is not precisely at the embedding direction but about 0.025 $\Delta R_{KS-direction}$ from it.

Step 7) Smear the primary vertex.

Now that the identity of the K_S to be embedded is known, the K_S must be embedded using the vertex and 4-vector information from the text file. In particular, just like the Minimum Bias case, the K_S must be embedded at the primary with the x and y components of the vertex set to 0.0. Unlike the Minimum Bias case, this time the primary vertex will be smeared by a Gaussian having the sigma given by the distribution of the measurement error of the primary vertex (around 0.25 cm). This has a negligible effect on the overall efficiencies and only slightly widens the width of the K_S . The vertex smearing can be removed from the jet track embedding as well as be added to the Minimum Bias track embedding, both without much of an effect. By virtue of selecting primary vertices from events, the primary vertex distribution of the embedding sample is similar to the primary vertex distribution of the data.

Step 8) Embed K_S just as in Minimum Bias track embedding.

The K_S vertice and 4-vector information is converted into hits into the CTC. First, the vertice information from the text file needs to be translated so that its origin is identical to that of the smeared primary. Then, the 4-vector information is converted into the 5 track parameters. After these steps, hits are embedded into the CTC using CTADDH. All embedded jet variables are kept at this stage as well and

will be denoted by either the superscript or the subscript "embed". Reconstruction is reran to yield a new data set with K_S embedded into it.

Step 9) Calculate Efficiencies with new track-embedded data set.

It is at this stage that efficiencies are calculated. The efficiency consists of a numerator (number of K_S in jets after cuts) divided by a denominator (number of events passing certain embedding criteria). In all cases, there is a unique track embedded jet in a unique track embedded event, so in the denominator the phrase "track embedded event" is interchangeable with "track embedded jet". To be consistent, the phrase "track embedded event" will be used to remain consistent with the Minimum Bias discussion.

The number of events must pass the following cuts to be counted as a track embedding event (Denominator):

- Track-embedding Event Cuts

    - Event Cuts

    - $|z_{primary} - z_{embedded\ jet}| < 5.0$ cm

    - $z^{rms}_{embedded\ jet} < 5.0$ cm

    - $|\eta^{detector}_{embedded\ jet}| < 1.0$

    - $20\,\mathrm{GeV} < \mathrm{Jet}\,E_T < 50\,\mathrm{GeV}$, $50\,\mathrm{GeV} < \mathrm{Jet}\ E_T < 100\,\mathrm{GeV}$, or
      $100\,\mathrm{GeV} < \mathrm{Jet}\,E_T < 150\,\mathrm{GeV}$

The event cuts are identical to the data event cuts. The $|z_{primary} - z_{embedded\ jet}| < 5.0$ cm criteria ensures that K_S are reasonable close to the primary vertex from where the search for K_S will begin and that K_S are within jet cones at approximately the same z-position as the jet. The $z^{rms}_{embedded\ jet} < 5.0$ cm criteria checks to see that

$z_{embedded\ jet}$ is carefully measured. For example, a $z_{embedded\ jet}$ having $|z_{primary}$-$z_{embedded\ jet}|$<0.1 cm having $z^{rms}_{embedded\ jet}$>20.0 cm should not be counted. The $|\eta^{detector}_{embedded\ jet}|$<1.0 should keep the jets within the CTC coverage. Finally, a cut is made on the jet E_T to allow for three separate efficiency vs. p_T^{KS} curves, one for each jet E_T range: 20-50 GeV, 50-100 GeV, and 100-150 GeV jets. The values are calculated for each embedded p_T^{KS} point, and this number is taken as the denominator in calculation of the efficiency at each embedded p_T^{KS} point.

The number of K_S must pass the following cuts to be counted as a track embedding event (Numerator):

- Number of K_S in jets (Numerator)

    - All Cuts Listed in the Above Table (Denominator)

    - K_S must be inside the embedded jet.

    - K_S must pass the p_T window cut given by Table 7.1.

    - χ^2_{KS}<20.0

    - $|z_{KS}$-$z_{primary}|$<3.0 cm

    - $p_T^{tracks\ from\ KS}$>500 MeV

    - $|\eta^{KS}|$<1.0

    - 3D Displacement^{KS}>1.0 cm

    - $\cos\theta^{KS}_{PD}$>0.990

Out of the jets that pass all of the event and jet cuts, the number of embedded K_S found the embedded jets determines the numerator of the efficiency calculation. To ensure that a given jet is the embedded jet, a strict $|E_T^{jet}$-$E_T^{embedded\ jet}|$<0.001 GeV is necessary along with event and jet cuts. As before in the Minimum Bias set,

a p_T window cut which varies according p_T of the embedded K_S (see Table 7.1) is applied to reduce the contamination of K_S already in the data set. Only those K_S within the p_T window cut along with all other cuts are tallied. By dividing the numerator term by the denominator term, the efficiency of K_S at a particular p_T value can be determined.

In addition, all Minimum Bias K_S cuts appear again with the same cut values with the exception of the 2D pointing vector cut (decreases from 0.995 to 0.990) and the $p_T^{tracks\ from\ KS}$ (increases from 300 MeV to 0.5 GeV). The increase in the $p_T^{tracks\ from\ KS}$ is due to the overall increase in p_T of the K_S in jets as well as keeping the individual p_T cut in the region where the CTC track efficiency is more reliable. The change in the 2D pointing vector takes into account the widening of the distribution between the minimum bias and jet samples, and the differences between the two cut values is not significant.

All cut variables for both 1.6 GeV and 6.0 GeV K_S in jets are shown in Figures 7.6-7.9. The dashed line indicates candidates satisfying the p_T window cut, and the solid line denotes candidates that fail the p_T window cut. The arrows point to the actual cut values. In addition to the cuts seen before in the Minimum Bias scenario, there are the $z_{primary}$-z_{jet} and z_{jet}^{rms} distributions (Figure 7.6).

7.3 Efficiency Dependencies

In this section, the K_S inside jets efficiency as a function of E_T^{jet}, η_{jet}, ϕ_{jet}, luminosity, $|z_{KS}$-$z_{primary}|$, and jet track multiplicity (the number of tracks within a jet) will be discussed. For each of these variables, the K_S in jets are subdivided by whatever property that is being studied after the K_S cuts have been applied. To illustrate, for the generation of the efficiency vs. ϕ_{jet} plot (see figure 7.12), the K_S in jets

(numerator) are calculated just as before with the exception that the K_S in jets is further subdivided into K_S in jets with particular ranges of ϕ_{jet}. Similarly, the number of embedded events (denominator) are determined but instead the events are subdivided into events having jets with particular ϕ_{jet} values. In this case, the five ϕ_{jet} ranges are 0-1, 1-2, 2-3, 3-4, and $5-2\pi$.

If there were not an jet E_T dependence, there would be 5 ϕ_{jet} efficiencies for every K_S embedded p_T. However, there is a known K_S efficiency dependence on jet E_T, so the K_S in jets (numerator) and the events for each ϕ_{jet} range is further subdivided in to three jet energy ranges, 20-50 GeV, 50-100 GeV, and 100-150 GeV for each K_S embedded p_T. This would result in three plots for each K_S p_T value: K_S in 20-50 GeV jets vs. ϕ_{jet}, K_S in 50-100 GeV jets vs. ϕ_{jet}, K_S in 100-150 GeV jets vs. ϕ_{jet}. Unfortunately, statistics do not allow this since there are far too few embedded K_S at each p_T range to be subdivided into 5 ϕ_{jet} ranges and 3 jet E_T ranges. Hence, groups of K_S embedded p_T are combined into three K_S embedded p_T groups given by the Table 7.2. The low K_S embedded p_T combines more embedded p_T values than either the high or mid K_S embedded p_T groups because of the lower K_S efficiency at the low p_T.

By combining embedded p_T values, the K_S in jet efficiency can be studied for 20-50 GeV, 50-100 GeV, 100-150 GeV as a function of ϕ_{jet} for three separate groups of K_S embedded p_T (low,mid,high). In Figure 7.12, there are three resulting plots for ϕ_{jet} for the three groups. Although the ϕ_{jet} efficiency is approximately constant for a given group of embedded p_T ranges for 20-50 GeV, 50-100 Gev, and 100-150 GeV jets (any plot in figure 7.12), the value of this constant varies for each group (low,mid,high) because the efficiency of K_S p_T varies for each group (i.e. low p_T group has a lower efficiency than the mid p_T group).

Table 7.1: The groups of embedded K_S in jets ranges

Groups of Embedded K_S p_T values	Embedded p_T Values
Low	900 MeV,1.2 GeV,1.4 GeV, 1.6 GeV, 1.8 GeV, 2.0 GeV, 2.3 GeV, 2.6 GeV
Mid	2.9 GeV, 3.0 GeV, 3.5 GeV, 4.0 GeV, 5.0 GeV
High	6.0 GeV, 7.0 GeV, 8.0 GeV, 9.0 GeV, 10.0 GeV

Table 7.2: The p_T window ranges for a given K_S p_T.

p_T Range of K_S (GeV)	p_T Window Range (MeV)
$p_T \leq 1.4$	25.0
$1.4 < p_T \leq 1.8$	30.0
$1.8 < p_T \leq 2.3$	50.0
$2.3 < p_T \leq 2.6$	75.0
$2.6 < p_T \leq 3.0$	100.0
$3.0 < p_T \leq 3.5$	150.0
$3.5 < p_T \leq 5.0$	200.0
$5.0 < p_T \leq 7.0$	500.0
$7.0 < p_T \leq 8.0$	750.0
$8.0 < p_T \leq 10.0$	1000.0

For figure 7.10, the K_S efficiency as a decreasing function of jet energy is shown for each of the three groups. As a result, three separate K_S efficiency curves will be made for K_S in 20-50 GeV, 50-100 GeV, and 100-150 GeV jets. The K_S efficiency as function of η_{jet} (Figure 1.11), luminosity (Figure 7.13), $|z_{primary}-z_{jet}|$ (Figure 7.14), and tracks per jet (Figure 7.15) are also shown. The K_S efficiency curve for each jet E_T integrates over all other efficiency dependencies.

Table 7.3:

Cuts	Number of K_S in MC	%	% in Data (1.5-1.7 GeV)
After Event Cuts	495. ± 23.	1.032 ± 0.0685	1.068 ± 0.0946
$\chi^2_{KS} < 20.0$	480. ± 23.	1.000	1.000
$\|z_{KS}\text{-}z_{primary}\| < 3.0$ cm	476. ± 23.	0.993 ± 0.0663	0.983 ± 0.0857
$p_T^{tracks\ from\ KS} > 500$ MeV	288. ± 18.	0.601 ± 0.0462	0.692 ± 0.0624
$\|\eta^{KS}\| < 1.0$	282. ± 17.	0.588 ± 0.0454	0.657 ± 0.0593
3D Displacement$^{KS} > 1.0$ cm	258. ± 17.	0.537 ± 0.0427	0.629 ± 0.0513
$\cos\theta^{KS}_{PD} > 0.990$	255. ± 16.	0.531 ± 0.0423	0.561 ± 0.0428

Table 7.4: The number of K_S after each successive cut for $p_T = 1.6$ GeV inside 50-100 GeV jets. The errors are taken from the fit of the area of the Gaussian.

Cuts	Number of K_S in MC	%	% in Data (1.5-1.7 GeV)
After Event Cuts	801. ± 30.	1.031 ± 0.0550	1.017 ± 0.0816
$\chi^2_{KS} < 20.0$	777. ± 29.	1.000	1.000
$\|z_{KS}\text{-}z_{primary}\| < 3.0$ cm	773. ± 29.	0.995 ± 0.0534	0.973 ± 0.0753
$p_T^{tracks\ from\ KS} > 500$ MeV	522. ± 24.	0.672 ± 0.0398	0.644 ± 0.0536
$\|\eta^{KS}\| < 1.0$	508. ± 23.	0.654 ± 0.0390	0.598 ± 0.0506
3D Displacement$^{KS} > 1.0$ cm	462. ± 22.	0.595 ± 0.0364	0.571 ± 0.0427
$\cos\theta^{KS}_{PD} > 0.990$	459. ± 22.	0.592 ± 0.0362	0.512 ± 0.0369

Table 7.5: The number of K_S after each successive cut for $p_T = 1.6$ GeV inside 100-150 GeV jets. The errors are taken from the fit of the area of the Gaussian.

Cuts	Number of K_S in MC	%	% in Data (1.5-1.7 GeV)
After Event Cuts	578. ± 25.	1.019 ± 0.0625	1.069 ± 0.0975
$\chi^2_{KS} < 20.0$	568. ± 25.	1.000	1.000
$|z_{KS} - z_{primary}| < 3.0$ cm	564. ± 25.	0.994 ± 0.0611	0.971 ± 0.0848
$p_T^{tracks\ from\ KS} > 500$ MeV	373. ± 20.	0.656 ± 0.0451	0.656 ± 0.0604
$|\eta^{KS}| < 1.0$	365. ± 20.	0.642 ± 0.0444	0.634 ± 0.0588
3D Displacement$^{KS} > 1.0$ cm	343. ± 19.	0.603 ± 0.0424	0.563 ± 0.0477
$\cos \theta_{PD}^{KS} > 0.990$	339. ± 18.	0.597 ± 0.0420	0.510 ± 0.0391

Table 7.6: The number of K_S after each successive cut for $p_T = 6.0$ GeV in 20-50 GeV jets. The errors are taken from the fit of the area of the Gaussian.

Cuts	Number of K_S in MC	%	% in Data (5.5-6.5 GeV)
After Event Cuts	515. ± 27.	1.010 ± 0.0744	1.006 ± 0.0726
$\chi^2_{KS} < 20.0$	510. ± 27.	1.000	1.000
$|z_{KS} - z_{primary}| < 3.0$ cm	508. ± 26.	0.997 ± 0.0732	0.976 ± 0.0701
$p_T^{tracks\ from\ KS} > 500$ MeV	508. ± 26.	0.997 ± 0.0732	1.039 ± 0.0746
$|\eta^{KS}| < 1.0$	495. ± 26.	0.971 ± 0.0717	0.996 ± 0.0725
3D Displacement$^{KS} > 1.0$ cm	488. ± 26.	0.957 ± 0.0715	0.968 ± 0.0707
$\cos \theta_{PD}^{KS} > 0.990$	487. ± 26.	0.955 ± 0.0716	0.956 ± 0.0672

Table 7.7: The number of K_S after each successive cut for $p_T = 6.0$ GeV in 50-100 GeV jets. The errors are taken from the fit of the area of the Gaussian.

Cuts	Number of K_S in MC	%	% in Data (5.5-6.5 GeV)
After Event Cuts	868. ± 35.	1.000 ± 0.0569	1.032 ± 0.0869
χ^2_{KS}<20.0	868. ± 35.	1.000	1.000
$\|z_{KS}\text{-}z_{primary}\|$<3.0 cm	866. ± 35.	0.998 ± 0.0564	0.982 ± 0.0800
$p_T^{tracks\ from\ KS}$>500 MeV	867. ± 35.	0.999 ± 0.0565	1.123 ± 0.0914
$\|\eta^{KS}\|$<1.0	847. ± 34.	0.976 ± 0.0554	1.089 ± 0.0875
3D Displacement^{KS}>1.0 cm	823. ± 33.	0.948 ± 0.0540	1.046 ± 0.0812
$\cos\theta_{PD}^{KS}$>0.990	820. ± 33.	0.944 ± 0.0535	1.010 ± 0.0778

Table 7.8: The number of K_S after each successive cut for $p_T = 6.0$ GeV in 100-150 GeV jets. The errors are taken from the fit of the area of the Gaussian.

Cuts	Number of K_S in MC	%	% in Data (5.5-6.5 GeV)
After Event Cuts	603. ± 29.	1.015 ± 0.0698	0.993 ± 0.0886
χ^2_{KS}<20.0	594. ± 29.	1.000	1.000
$\|z_{KS}\text{-}z_{primary}\|$<3.0 cm	592. ± 29.	0.997 ± 0.0686	0.969 ± 0.0860
$p_T^{tracks\ from\ KS}$>500 MeV	597. ± 29.	1.004 ± 0.0689	1.144 ± 0.1029
$\|\eta^{KS}\|$<1.0	580. ± 28.	0.976 ± 0.0674	1.124 ± 0.1016
3D Displacement^{KS}>1.0 cm	570. ± 28.	0.960 ± 0.0662	1.062 ± 0.0917
$\cos\theta_{PD}^{KS}$>0.990	570. ± 28.	0.959 ± 0.0660	1.029 ± 0.0881
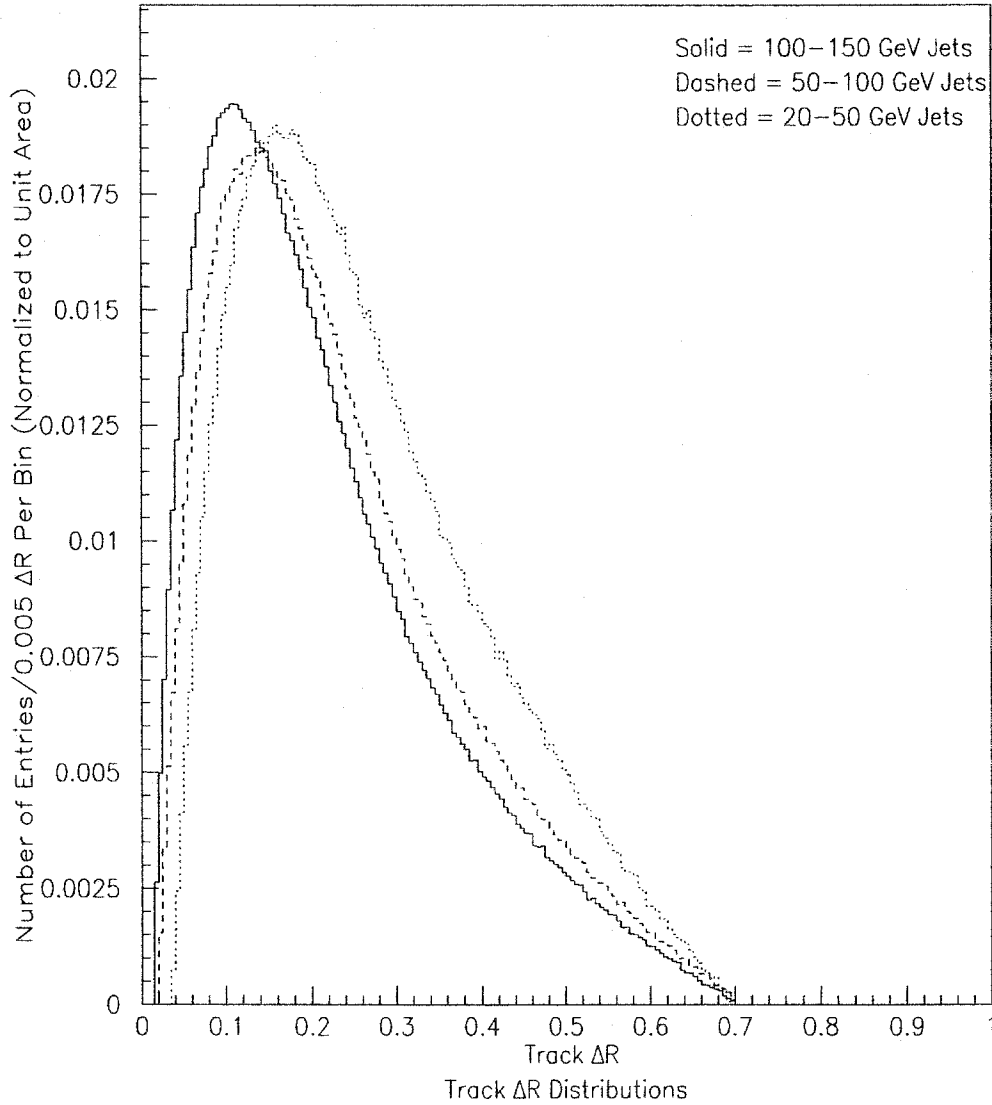
Figure 7.1: A few $|\Delta R_{jet-track}|$ distributions normalized to unit area. In order of decreasing peaks, the $|\Delta R_{jet-track}|$ distribution inside jet energies of 100-150 GeV, between 50 GeV and 100 GeV, and between 20 GeV and 50 GeV. K_S are embedded into jets according to $|\Delta R_{jet-track}|$ distributions.
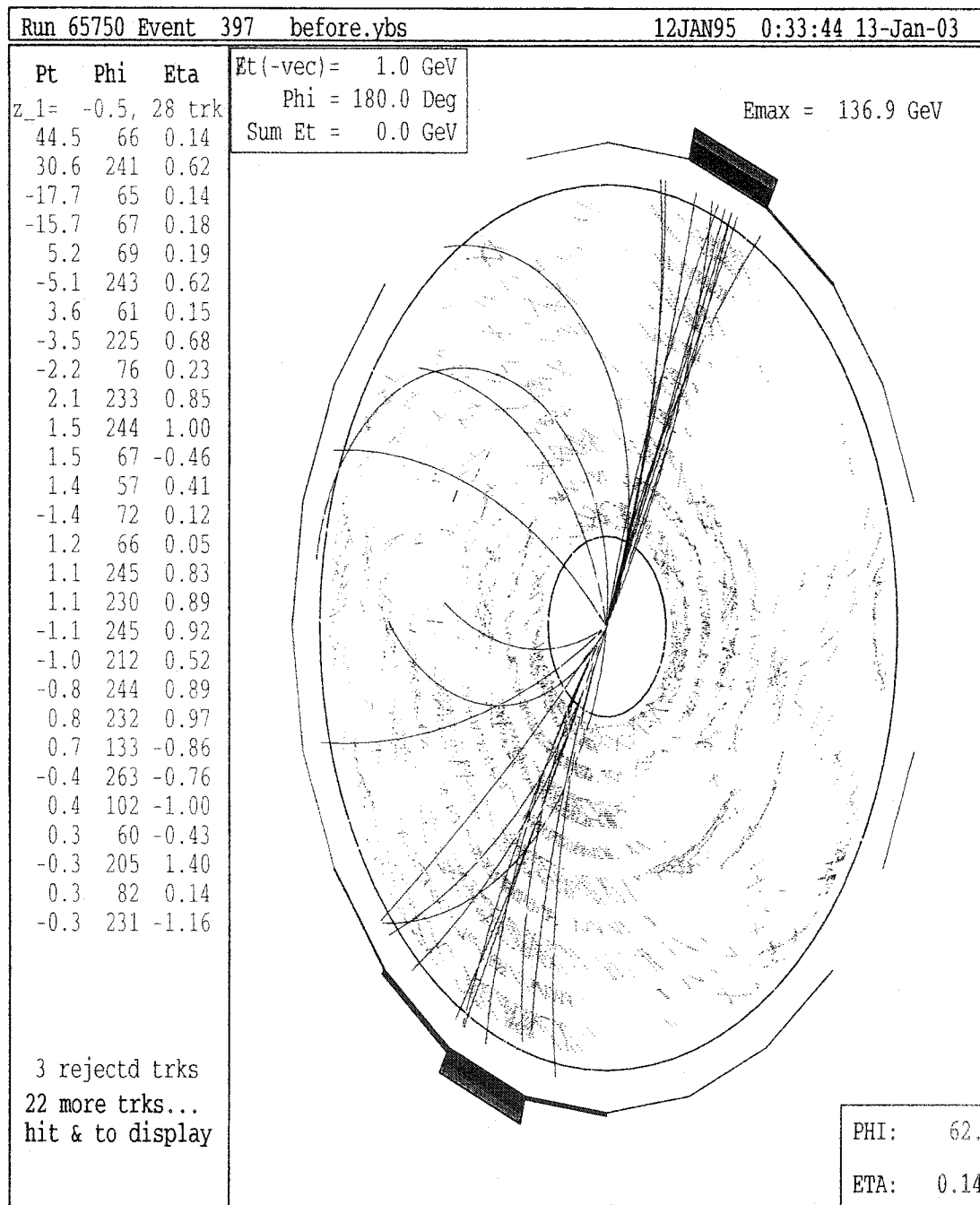
Figure 7.2: A transverse view of a jet event. A K_S has not yet been track embedded.
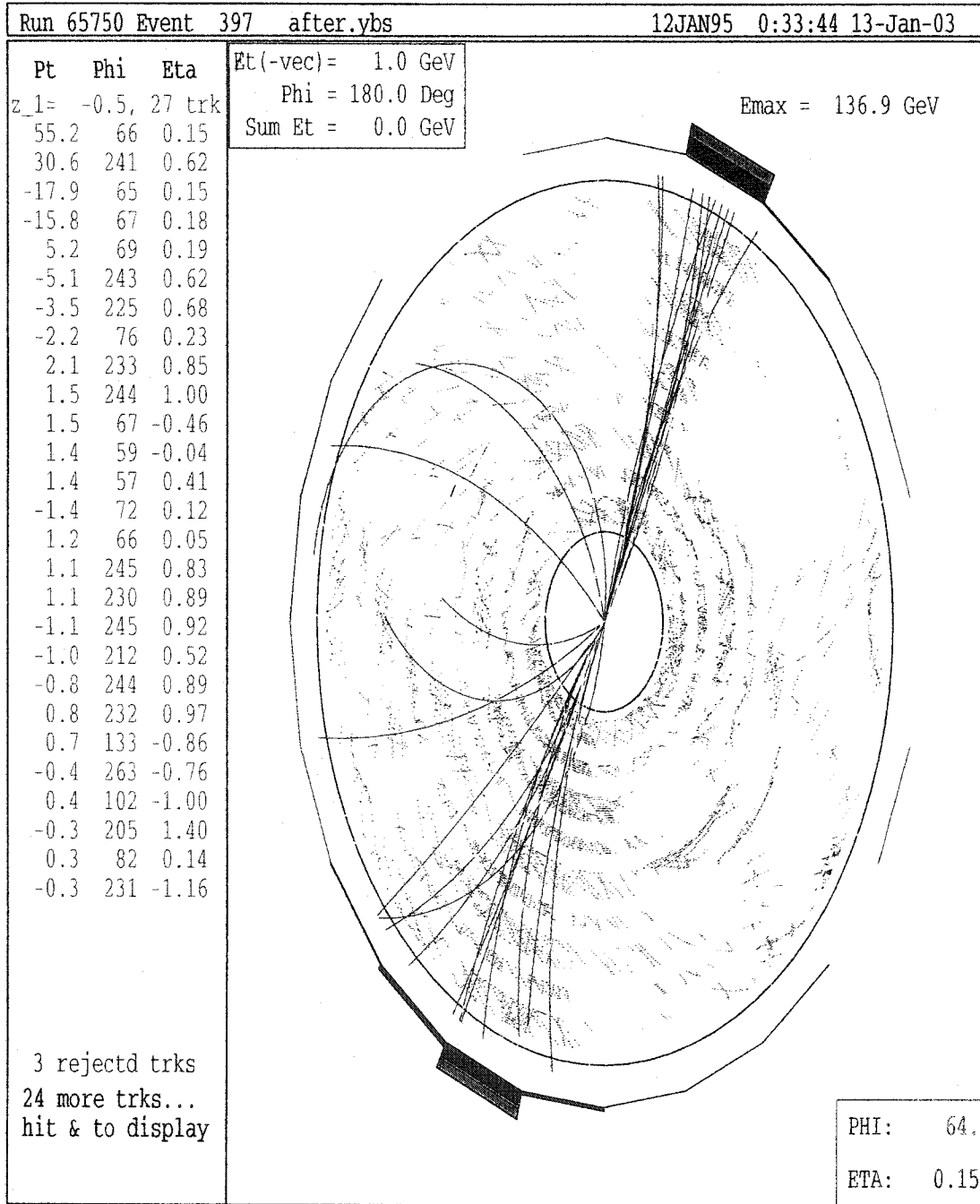
Figure 7.3: A transverse view of a jet event with a 3.0 GeV track-embedded K_S. The K_S consists of a straight track and a curved track not seen in Figure 7.1. The straight track is the higher p_T pion track, and the curved track is the softer p_T pion track.

7.4 Comparison with Jets in Data

Tables 7.3-7.8 compare after each cut the embedded K_S at a given p_T value in jets to K_S in jets within a particular p_T range in the data. The 1.6 GeV and 6.0 GeV embedded K_S in the track-embedding are matched with K_S having p_T ranges within 1.5-1.7 GeV and 5.5-6.5 GeV. This is done again for 20-50 GeV, 50-100 GeV, and 100-150 GeV jet E_T ranges. For the 6.0 GeV case, the agreement is quite good whereas for the 1.6 GeV case, the data and MC agree to approximately 15%. The disagreement either appears to originate with the track cut and continues throughout the rest of the table or appears at the end of the table with the appearance of the pointing cut. The comparisons are normalized with respect to K_S in jets pointing to the primary vertex (i.e. the $\chi^2_{KS} < 20.0$ cut). This discrepancy is not fully understood although it has been studied.

7.5 Single Track Efficiency

The primary reason to why the single track in jets efficiencies are calculated is in order to correct the single track p_T spectra so that $\frac{N_{track}}{jet}$ number may be computed (done in later Chapter 8). This number can also be compared with the $\frac{N_{KS}}{jet}$. Another reason is a cross-check for the K_S efficiency curves since the track efficiency in jets has been studied. In addition, the product of the single track efficiencies along with the secondary vertex reconstruction efficiency should yield the K_S efficiency.

The procedure of single track-embedding is very similar to the procedure of the K_S in jet track-embedding with the exception of instead of embedding 2 pion tracks from the K_S at a particular p_T with the K_S directed according to the $\Delta R_{jet-track}$ distribution, a single pion track at a particular p_T is embedded into a jet according

to the $\Delta R_{jet-track}$ distribution. Moreover, the text files of pions at a particular p_T are produced rather than K_S at a particular p_T. To compute each efficiency point, background subtraction is applied to the p_T to yield the number of pions found at that particular p_T. Typically, the single track efficiency is done separately for positive and negative pions, but since the efficiencies converge above 400 MeV, the single track efficiency uses only negative pions.

In Figure 7.19, the single track efficiency vs. p_T for tracks inside 20-50 GeV, 50-100 GeV, and 100-150 GeV is shown. The single track is approximately a constant of 95% for 20-50 GeV and 100-150 GeV ranges whereas the single track efficiency is about 90% for the 50-100 GeV range.

It should be noted that aside from the track-embedding references in Chapter 5, [28] [42] [51] [54] [55] [56] [57] [58], the only analysis which embeds tracks in jets is [28]. This method applied here closely resembles this analysis with the exception that tracks (and K_S) are embedded according to the track density distributions and jet vertices. However, the single track efficiencies, even with different cuts, are similar as well as their dependence on η and ϕ variables. The comparisons are good to 5-10%.
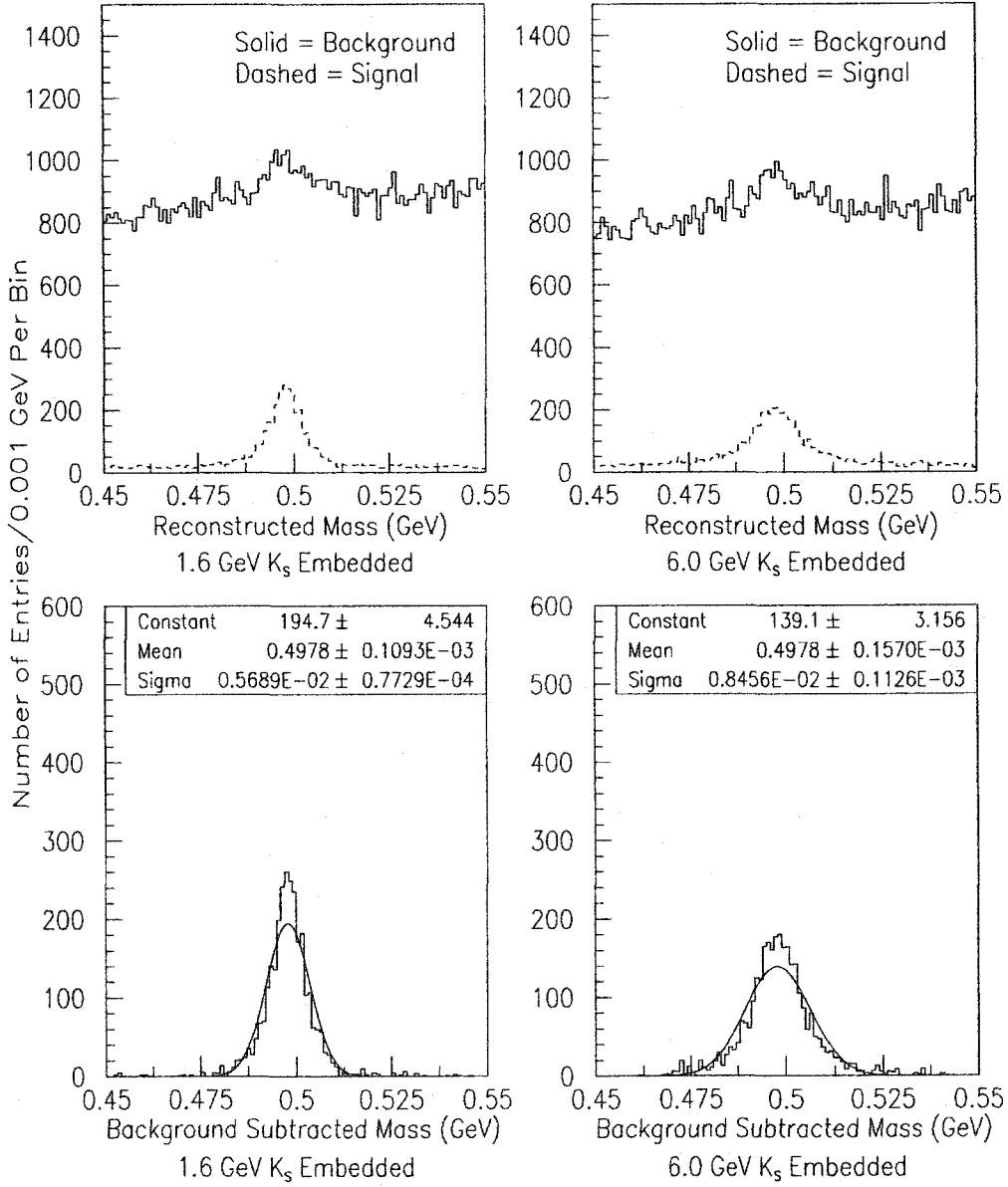
Figure 7.4: The mass distribution of K_S candidates after track-embedding. The mass distributions of 1.6 GeV (top left) and 6.0 GeV (top right) K_S candidates that pass (dashed line) and fail (solid line) p_T window. The p_T windows are 30 MeV and 0.5 GeV for 1.6 GeV and 6.0 GeV K_S. Below are the fitted background subtracted mass distributions.
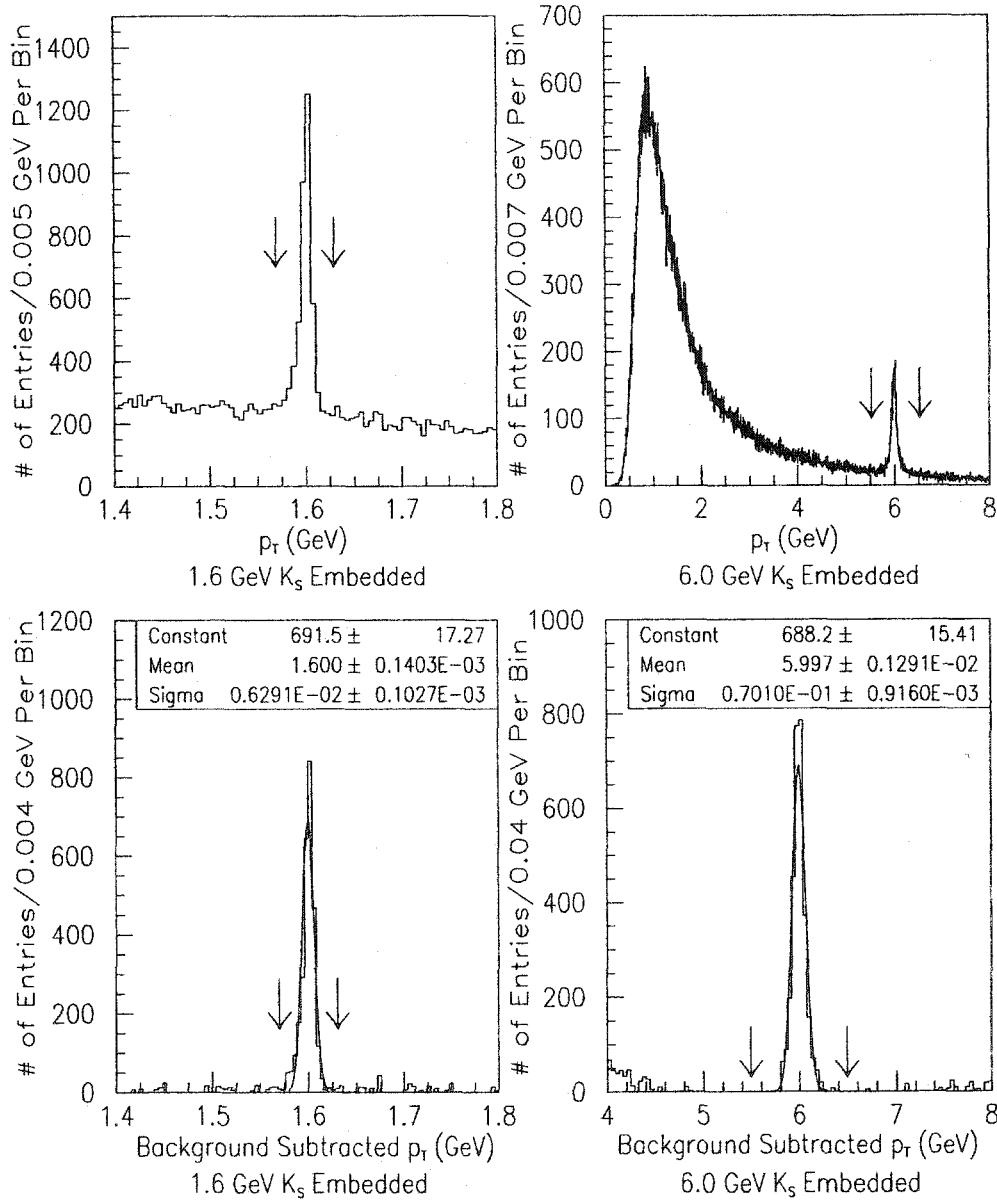
Figure 7.5: The p_T distributions of K_S candidates after track-embedding. The p_T distributions of 1.6 GeV (top left) and 6.0 GeV (top right) K_S candidates that pass (dashed line) and fail (solid line) p_T window. The p_T windows are 30 MeV and 0.5 GeV for 1.6 GeV and 6.0 GeV K_S. Below are the fitted background subtracted p_T distributions.
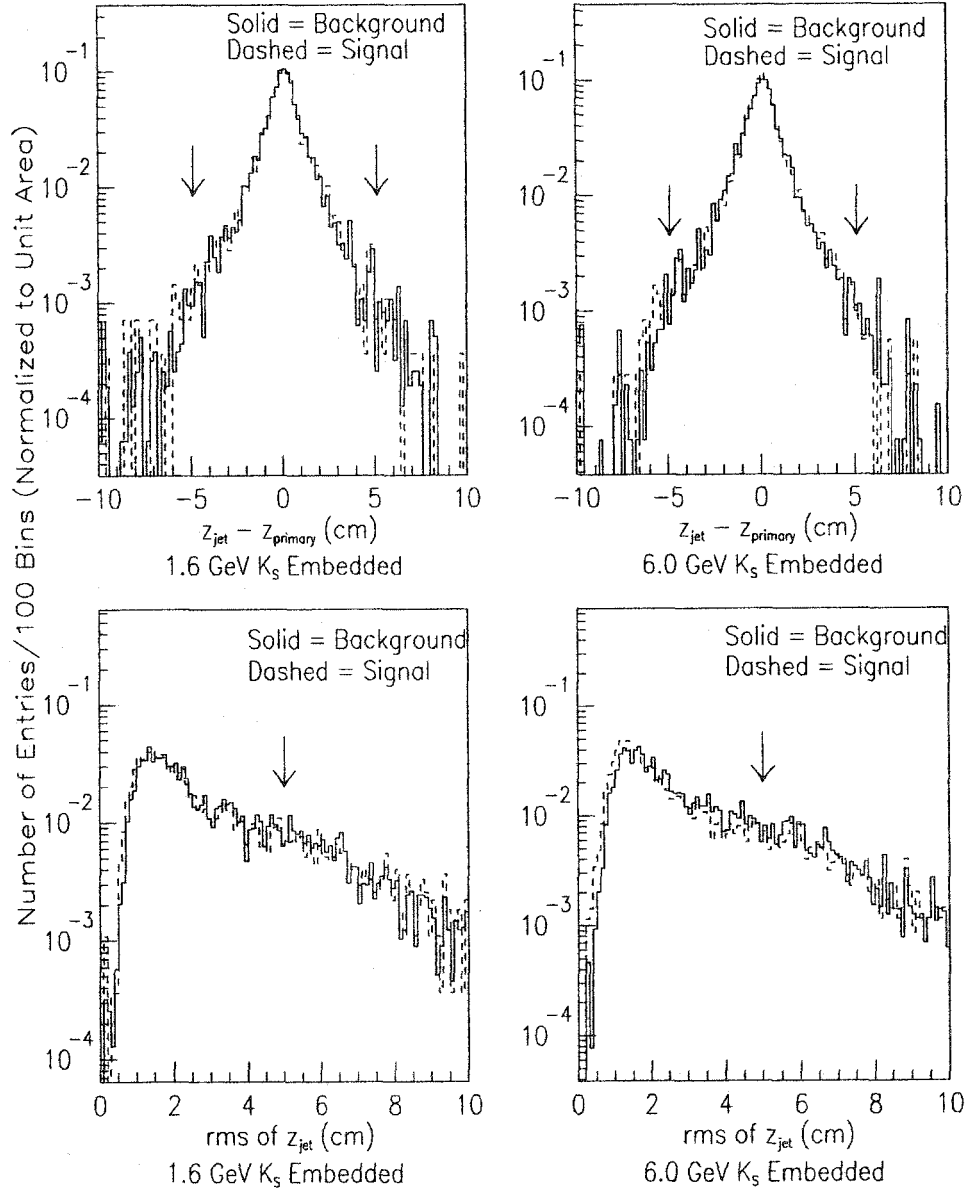
Figure 7.6: In the top half, the $z_{primary}$-z_{jet} distributions of the 1.6 GeV (left) and 6.0 GeV (right) candidates which pass (dashed line) and fail (solid line) the p_T window cut. The arrows indicate the $|z_{primary}$-$z_{jet}| < 5.0$ cm cut. In the bottom half, the z_{jet}^{rms} distributions are shown similarly with the arrows indicating the $z_{jet}^{rms} < 5.0$ cut.
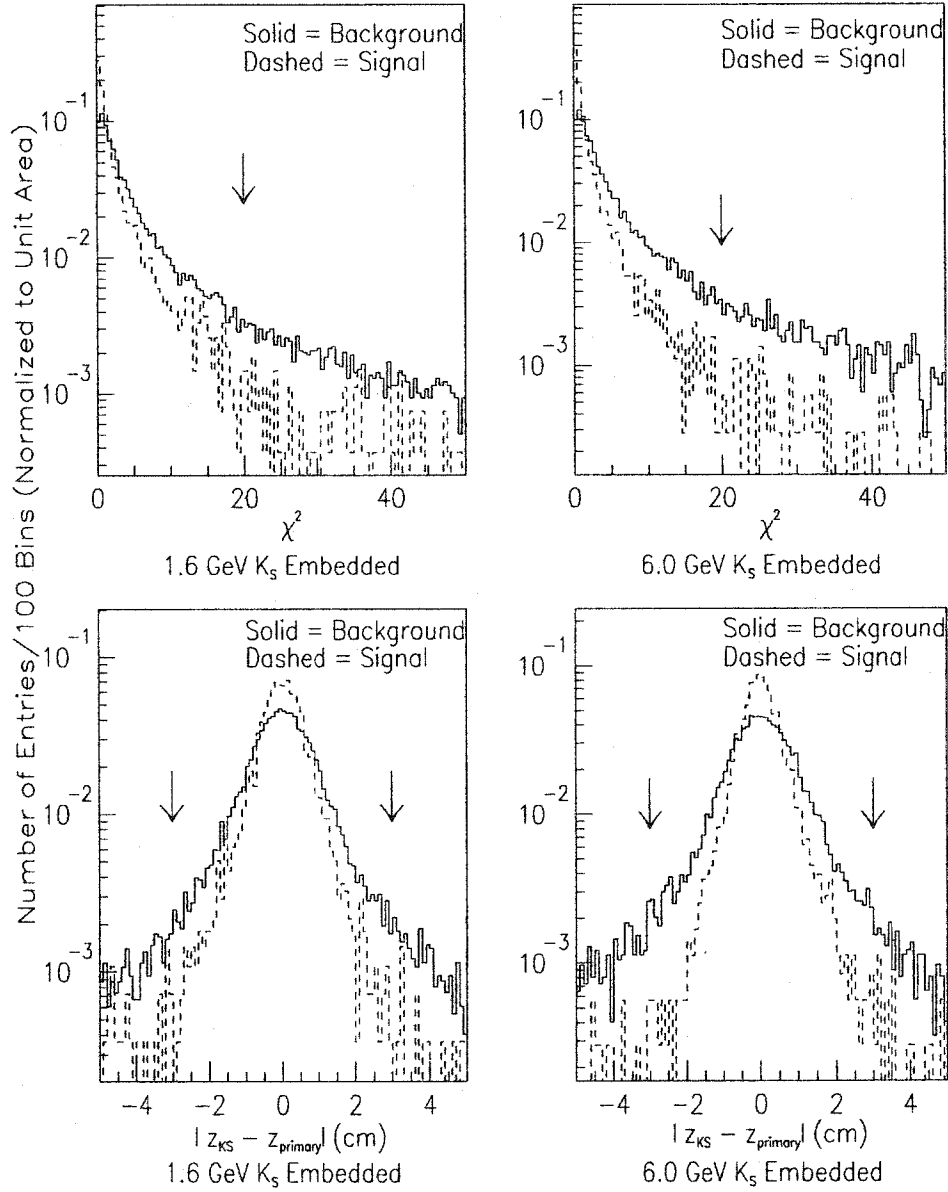
Figure 7.7: In the top half, the χ^2_{KS} distributions of the 1.6 GeV (left) and 6.0 GeV (right) candidates which pass (dashed line) and fail (solid line) the p_T window cut. The arrows indicate the χ^2_{KS}<20.0 cut. In the bottom half, the $|z_{KS}\text{-}z_{primary}|$ distributions are shown similarly with the arrows indicating the $|z_{KS}\text{-}z_{primary}|$<3.0 cm cut.
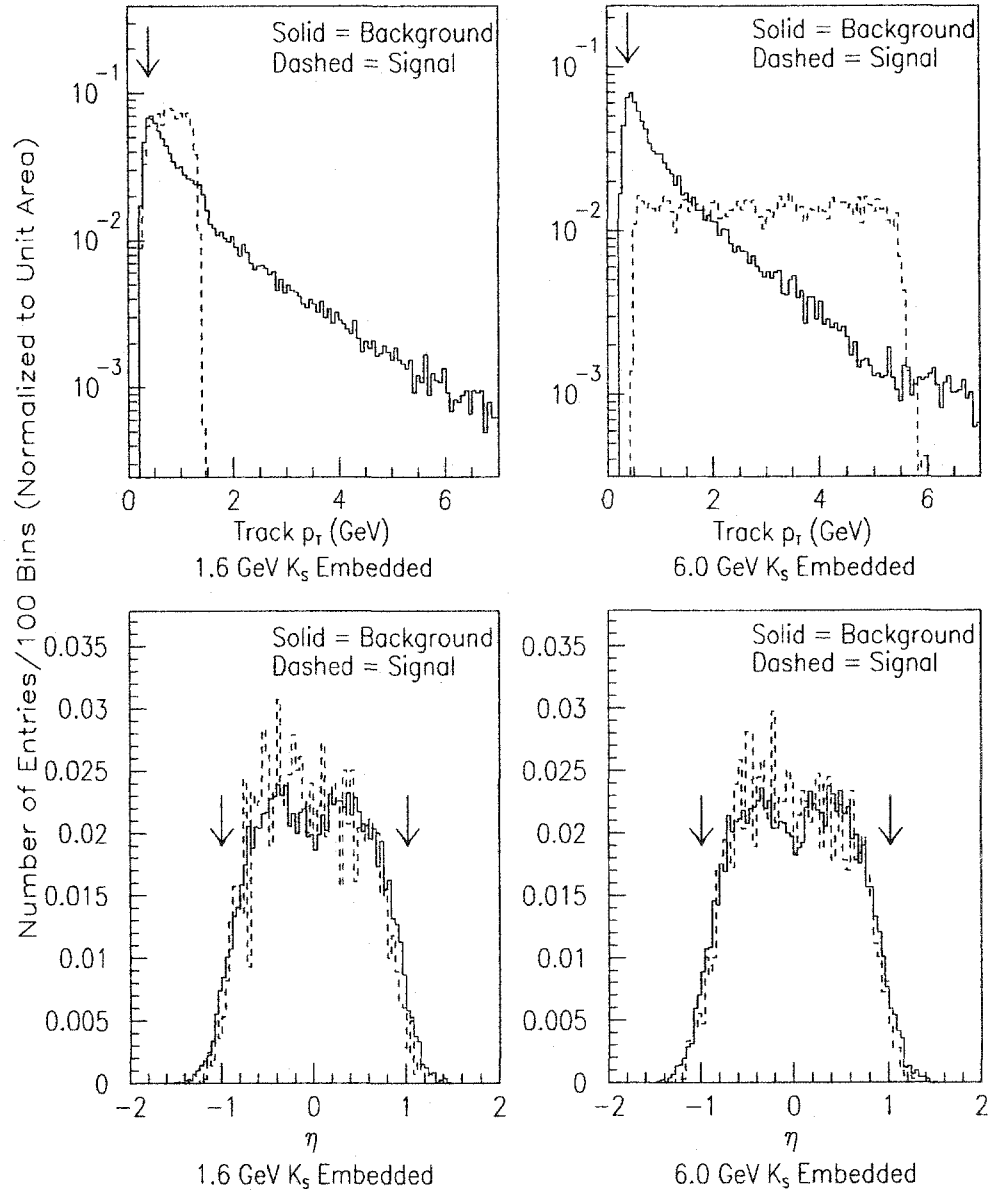
Figure 7.8: In the top half, the daughter track p_T distributions of the 1.6 GeV (left) and 6.0 GeV (right) candidates which pass (dashed line) and fail (solid line) the p_T window cut. The arrows indicate the $p_T^{tracks\ from\ KS} > 500.0$ MeV cut. In the bottom half, the η^{KS} distributions are shown similarly with the arrows indicating the $|\eta^{KS}| < 1.0$ cut.
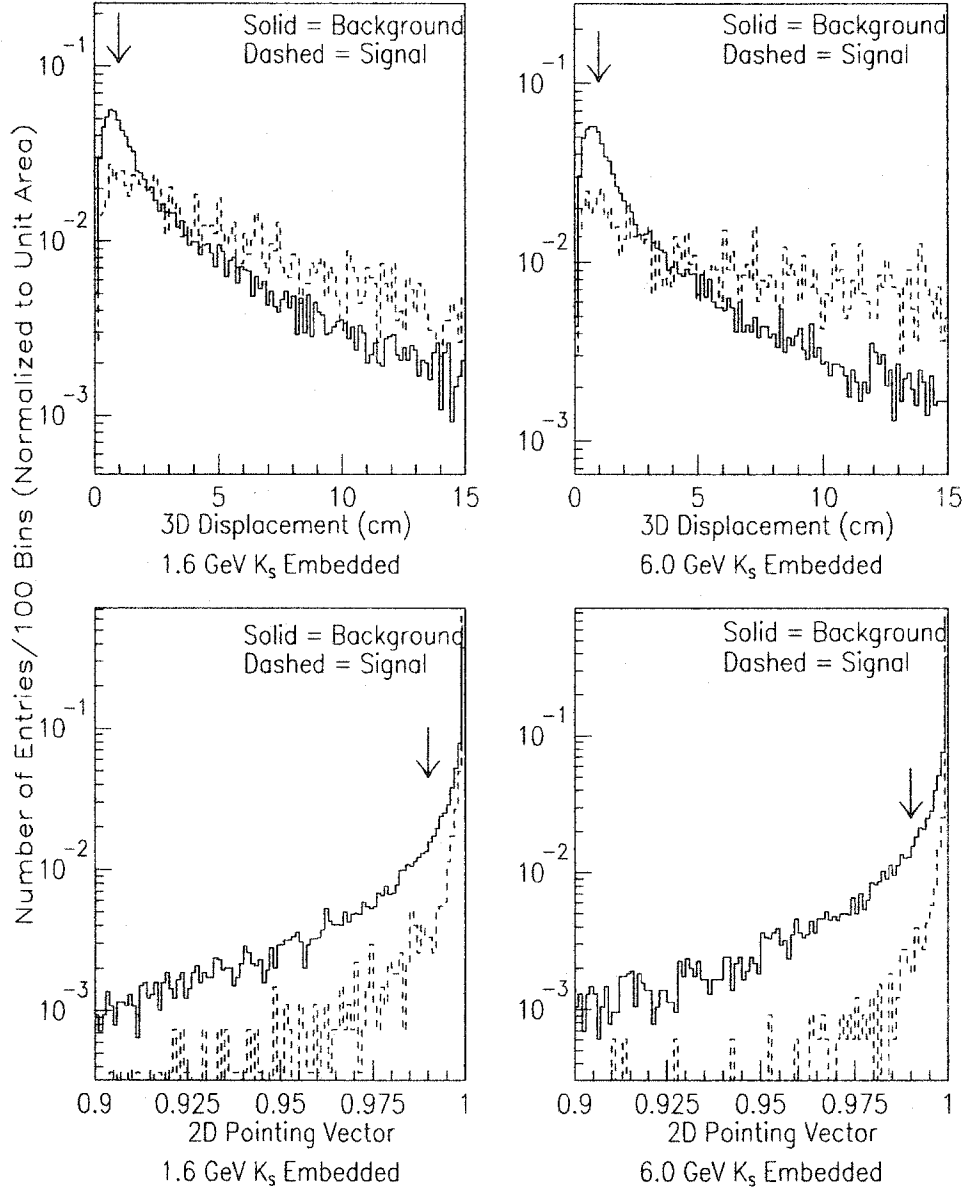
Figure 7.9: In the top half, the 3D displacement^{KS} distributions of the 1.6 GeV (left) and 6.0 GeV (right) candidates which pass (dashed line) and fail (solid line) the p_T window cut. The arrows indicate the 3D displacement^{KS}>1.0 cm cut. In the bottom half, the 2D pointing vector($\cos\theta_{PD}^{KS}$) distributions are shown similarly with the arrows indicating the $\cos\theta_{PD}^{KS}$>0.990 cut.

Efficiency vs. Jet E_T for Low,Mid,and High p_T K_s
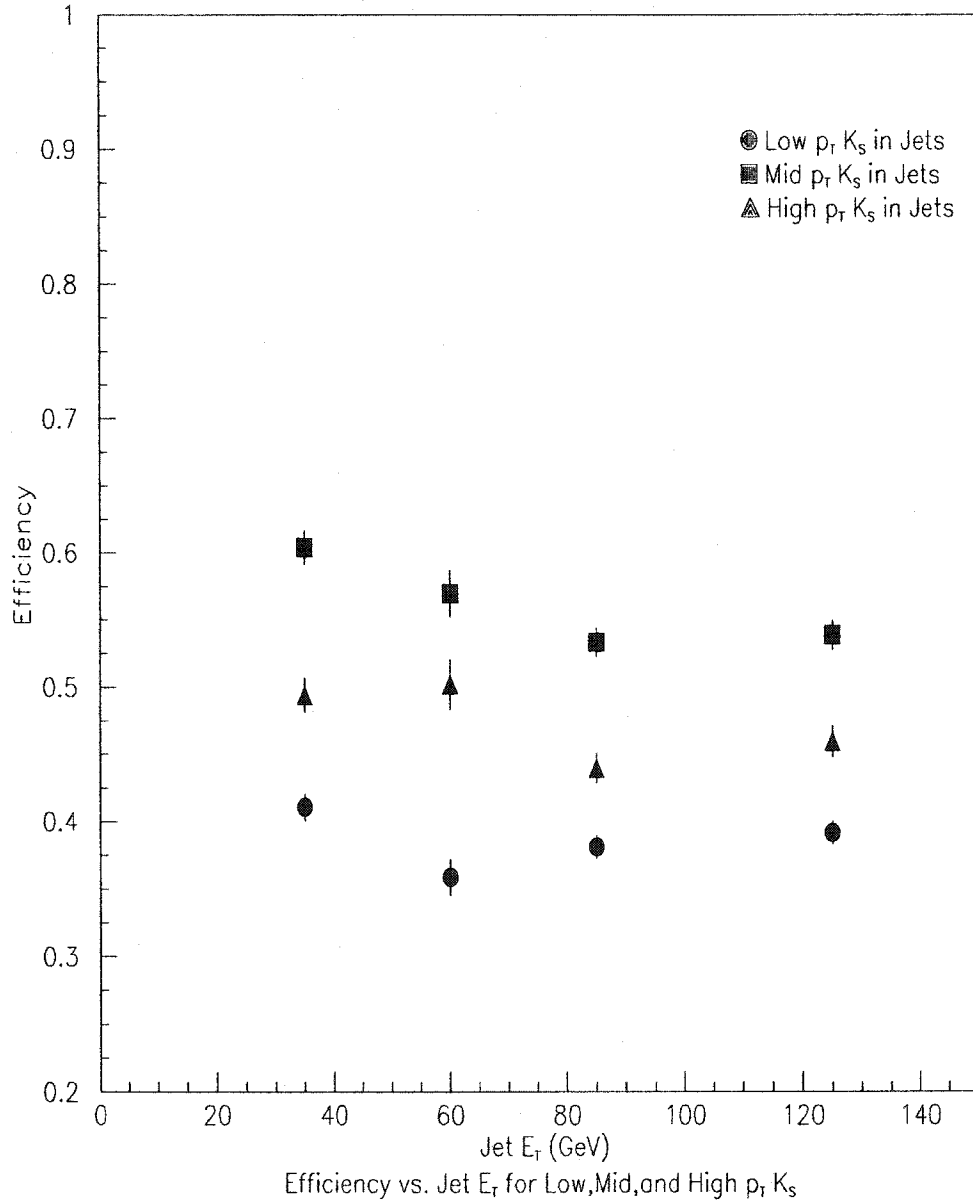
Figure 7.10: The K_S efficiency vs. jet E_T curve for the 3 groups of K_S p_T (low,mid,and high). The offsets in efficiency of each group to each other is due to the p_T efficiency of the K_S whereas the decrease in efficiency of every group is due to a jet E_T efficiency dependence that will taken into account with 3 separate K_S efficiency curves.
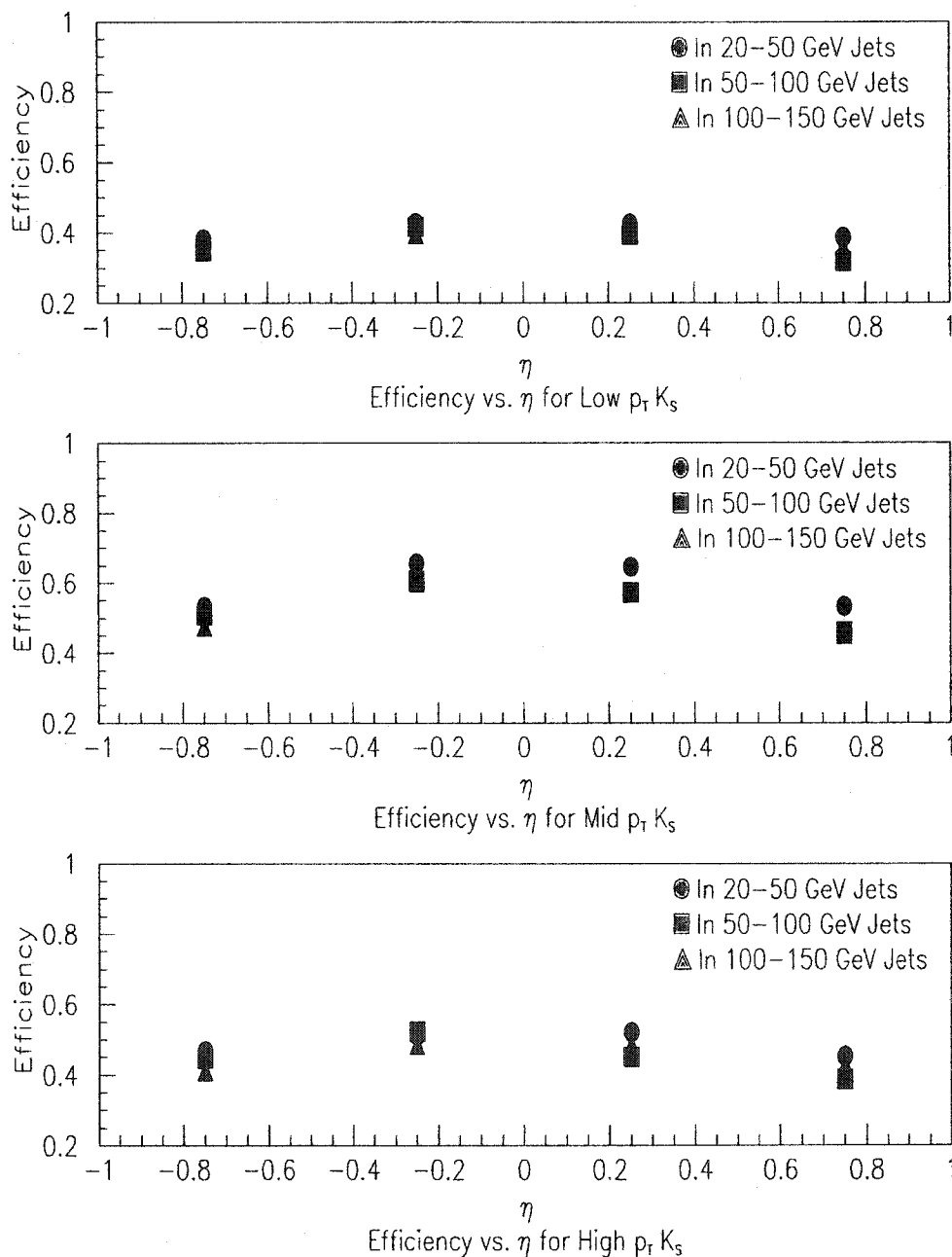
Figure 7.11: The K_S efficiency vs. η_{jet} curve for the 3 groups of K_S p_T (low,mid,and high).
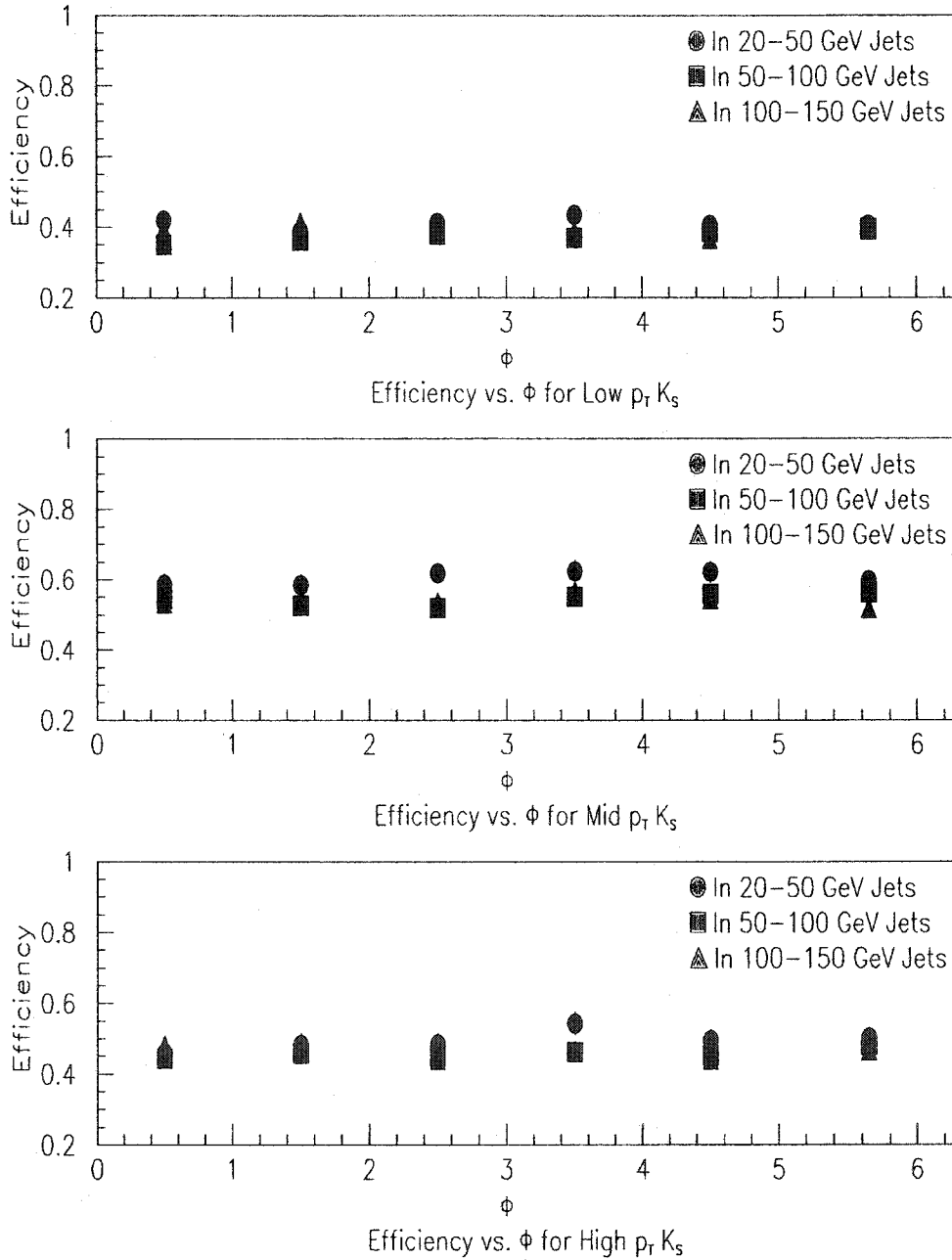
Figure 7.12: The K_S efficiency vs. ϕ_{jet} curve for the 3 groups of K_S p_T (low,mid,and high).
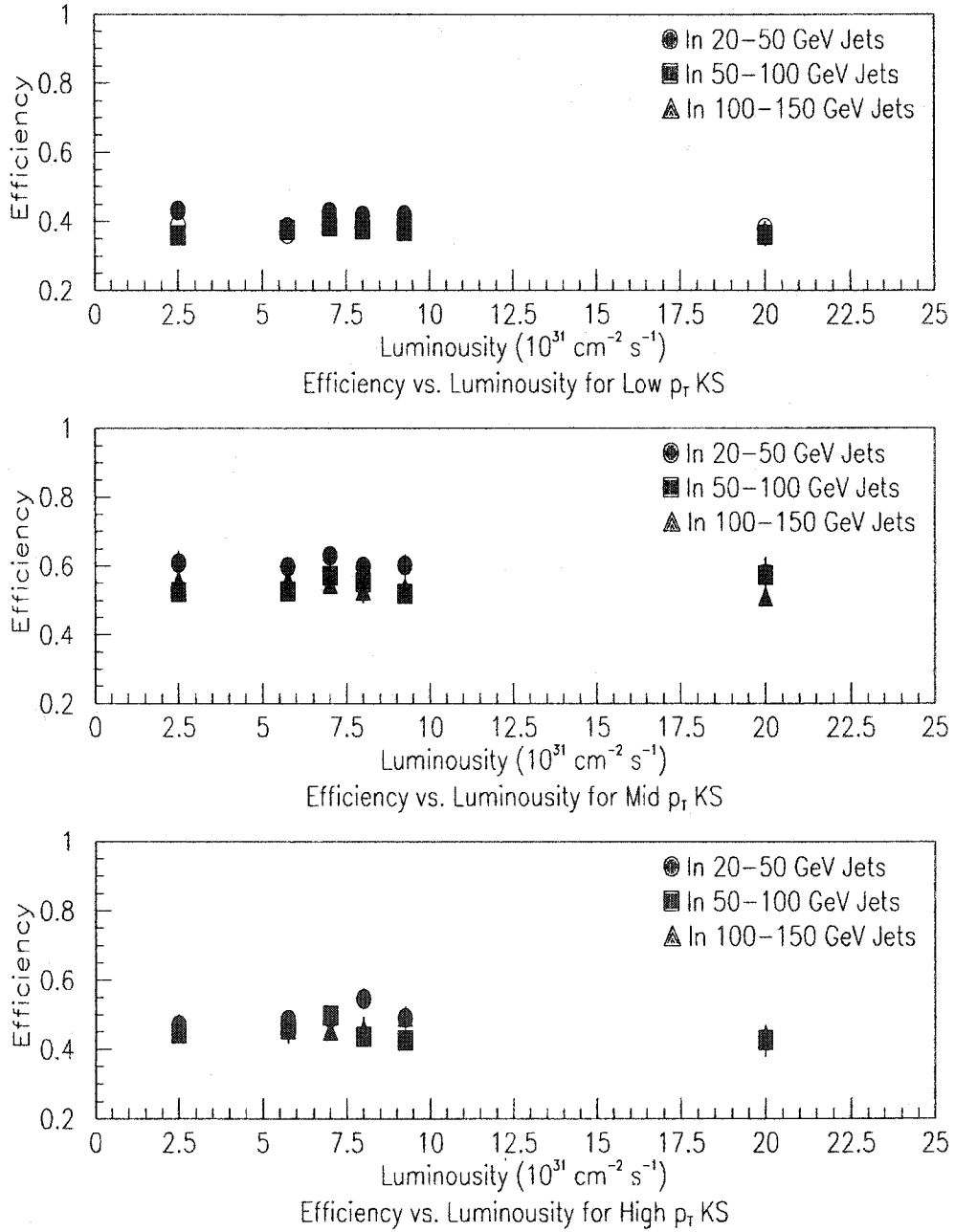
Figure 7.13: The K_S efficiency vs. luminosity curve for the 3 groups of K_S p_T (low,mid,and high).
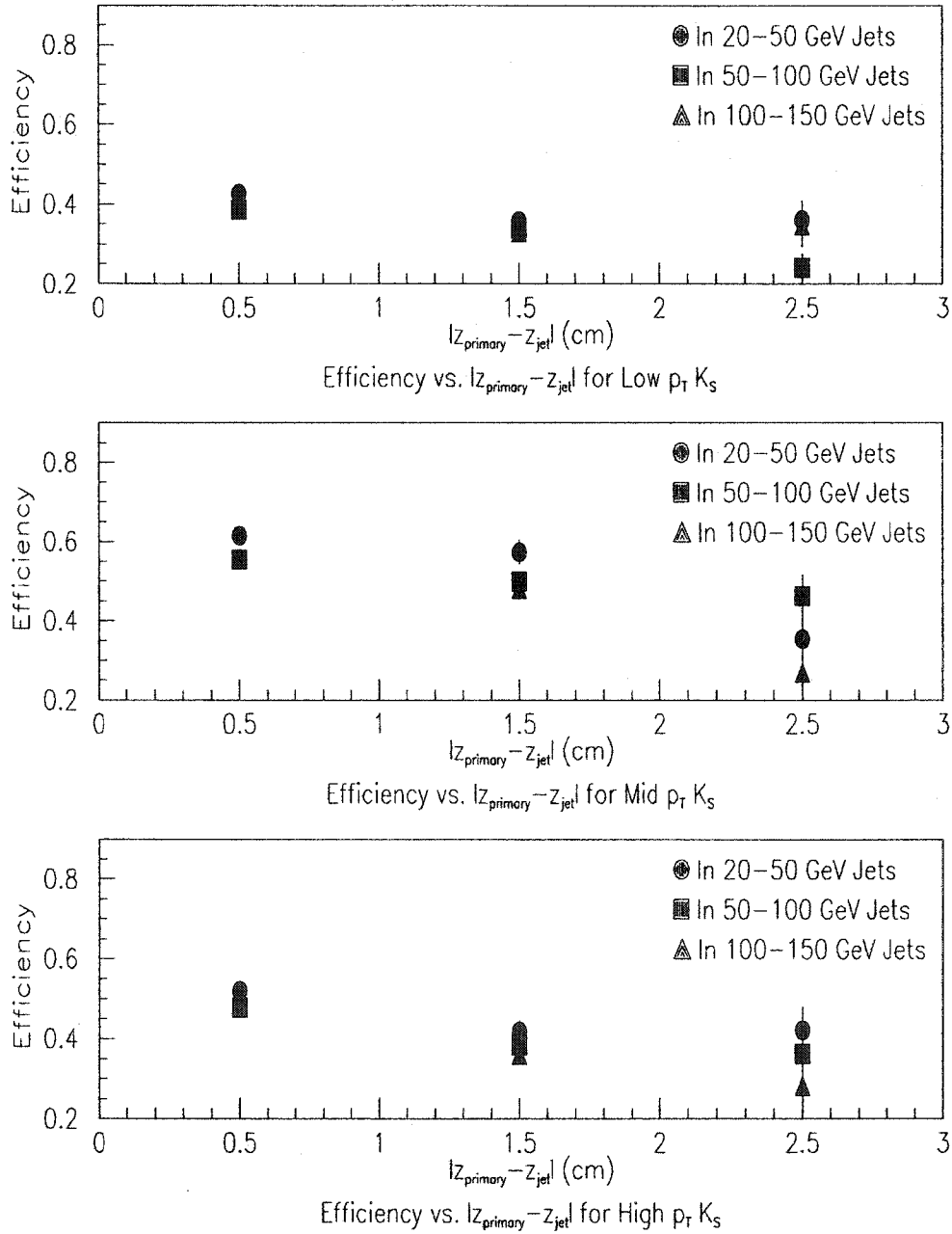
Figure 7.14: The K_S efficiency vs. $|z_{primary}-z_{jet}|$ curve for the 3 groups of K_S p_T (low,mid,and high).
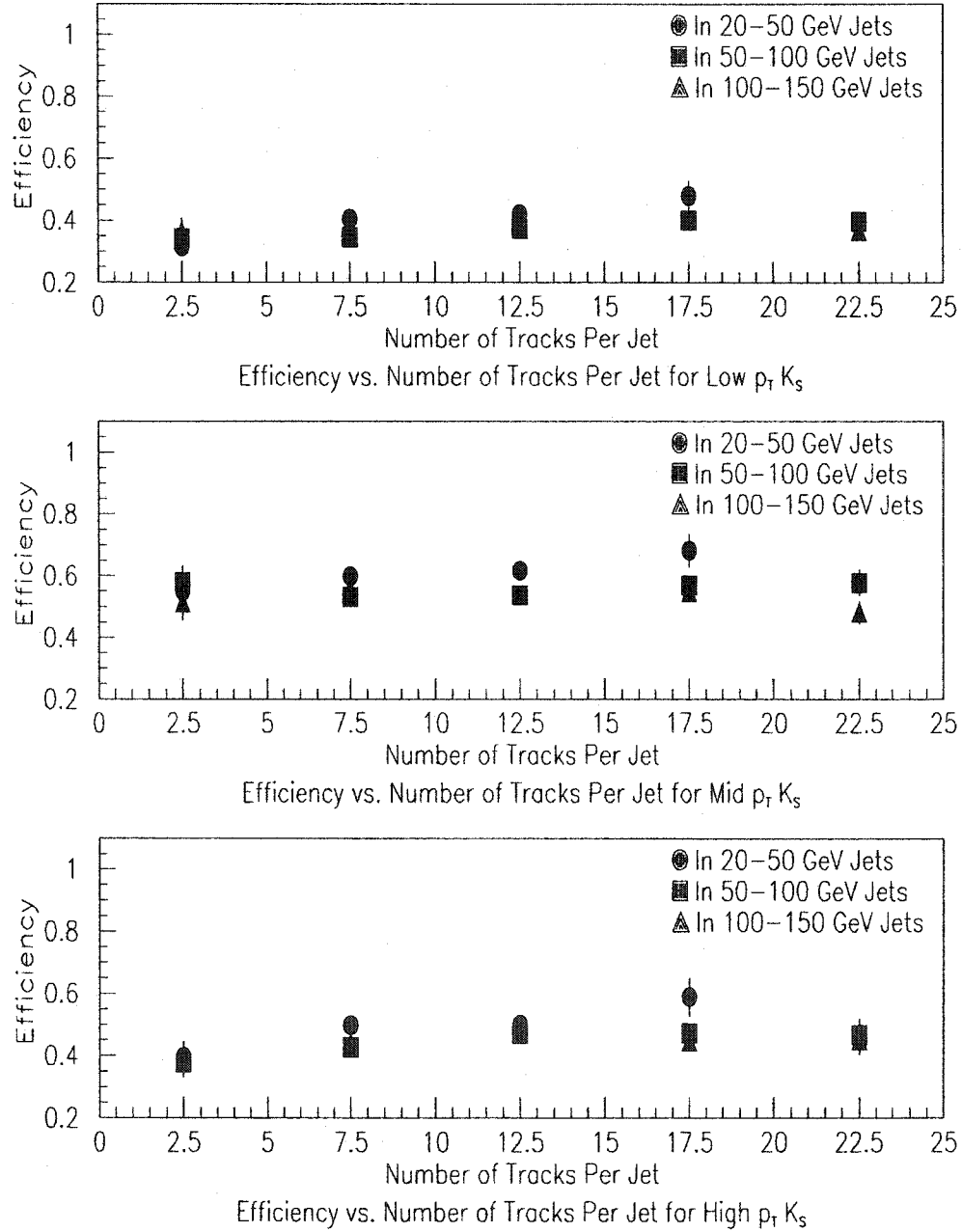
Figure 7.15: The K_S efficiency vs. the number of tracks per jet curve for the 3 groups of K_S p_T (low,mid,and high).
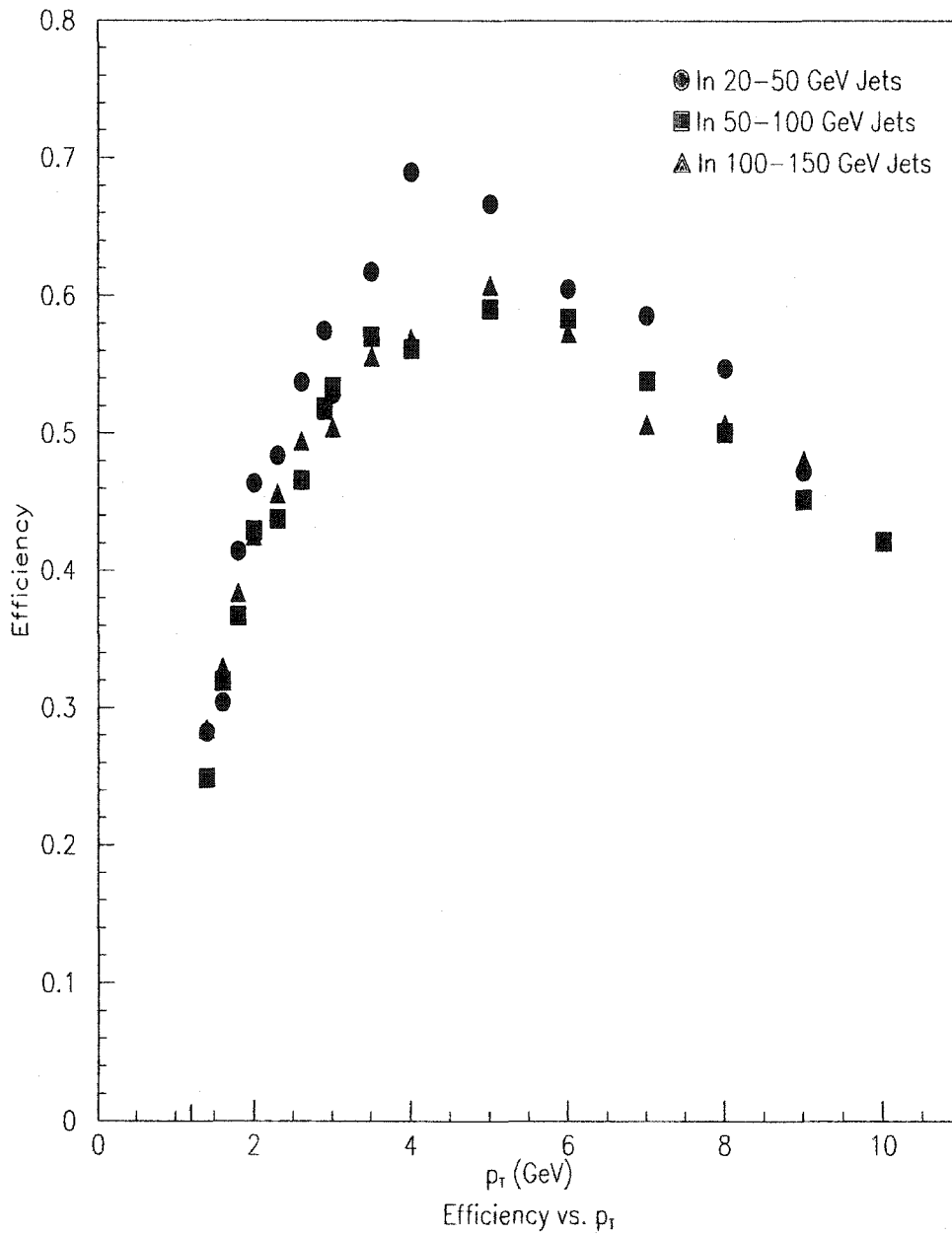
Figure 7.16: The K_S efficiency vs. p_T curve for K_S inside jets. Each point in the top figure represents a p_T value which implemented track-embedding. All three jet E_T ranges are shown.
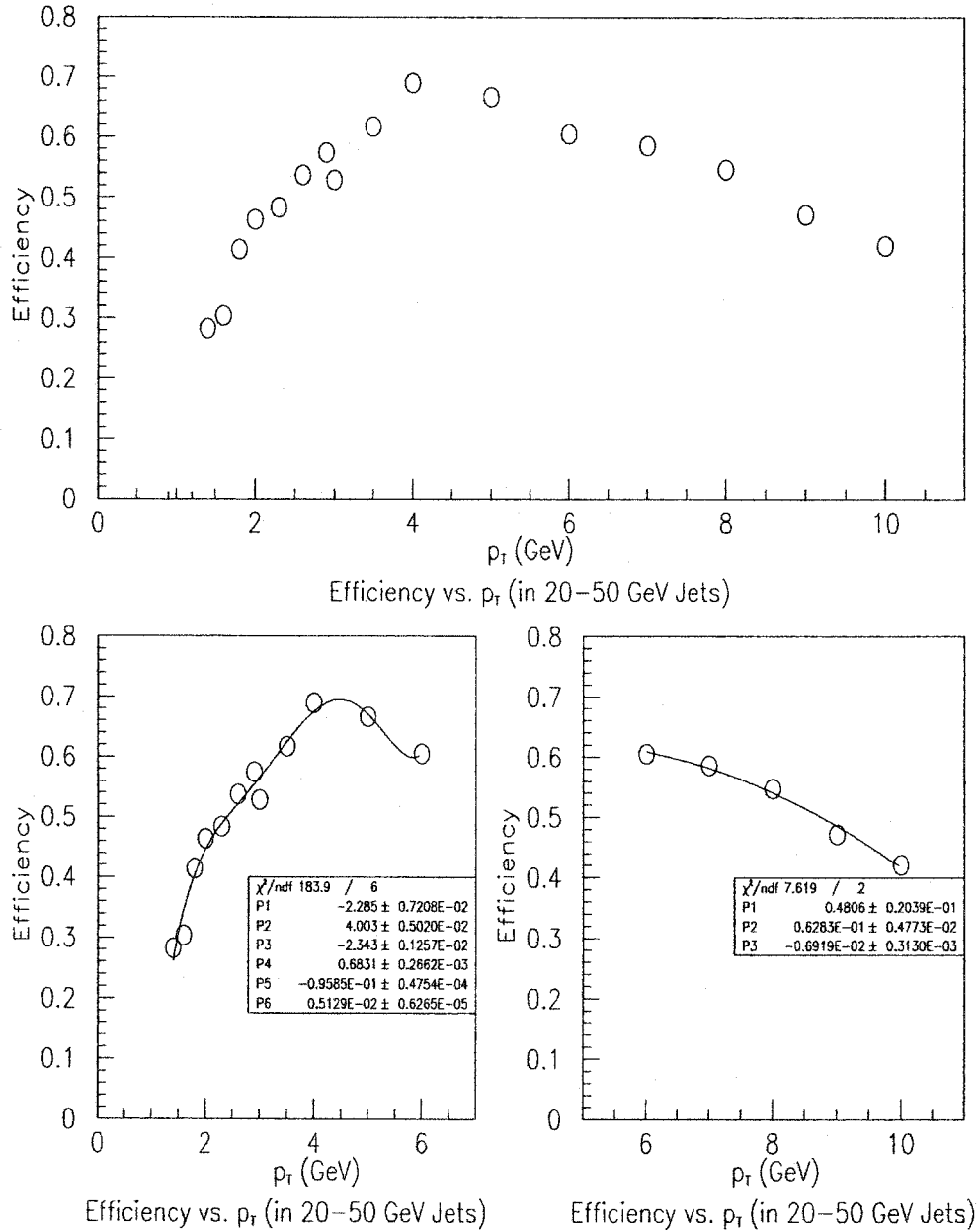
Figure 7.17: The K_S efficiency vs. p_T curve for K_S inside 20-50 GeV jets. Each point in the top figure represents a p_T value which implemented track-embedding. These points are divided into 2 distinct fit regions shown in the bottom diagrams.
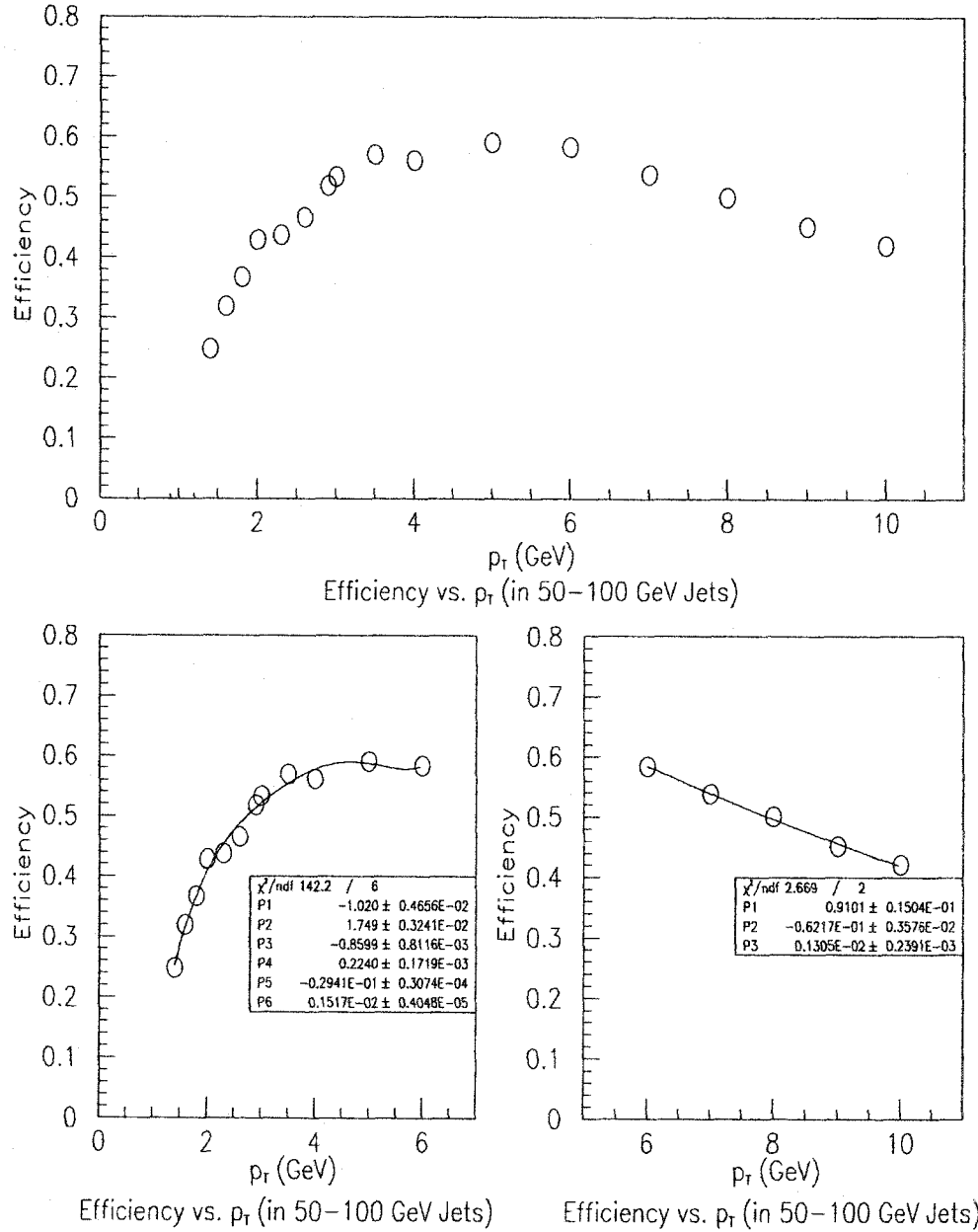
Figure 7.18: The K_S efficiency vs. p_T curve for K_S inside 50-100 GeV jets. Each point in the top figure represents a p_T value which implemented track-embedding. These points are divided into 2 distinct fit regions shown in the bottom diagrams.
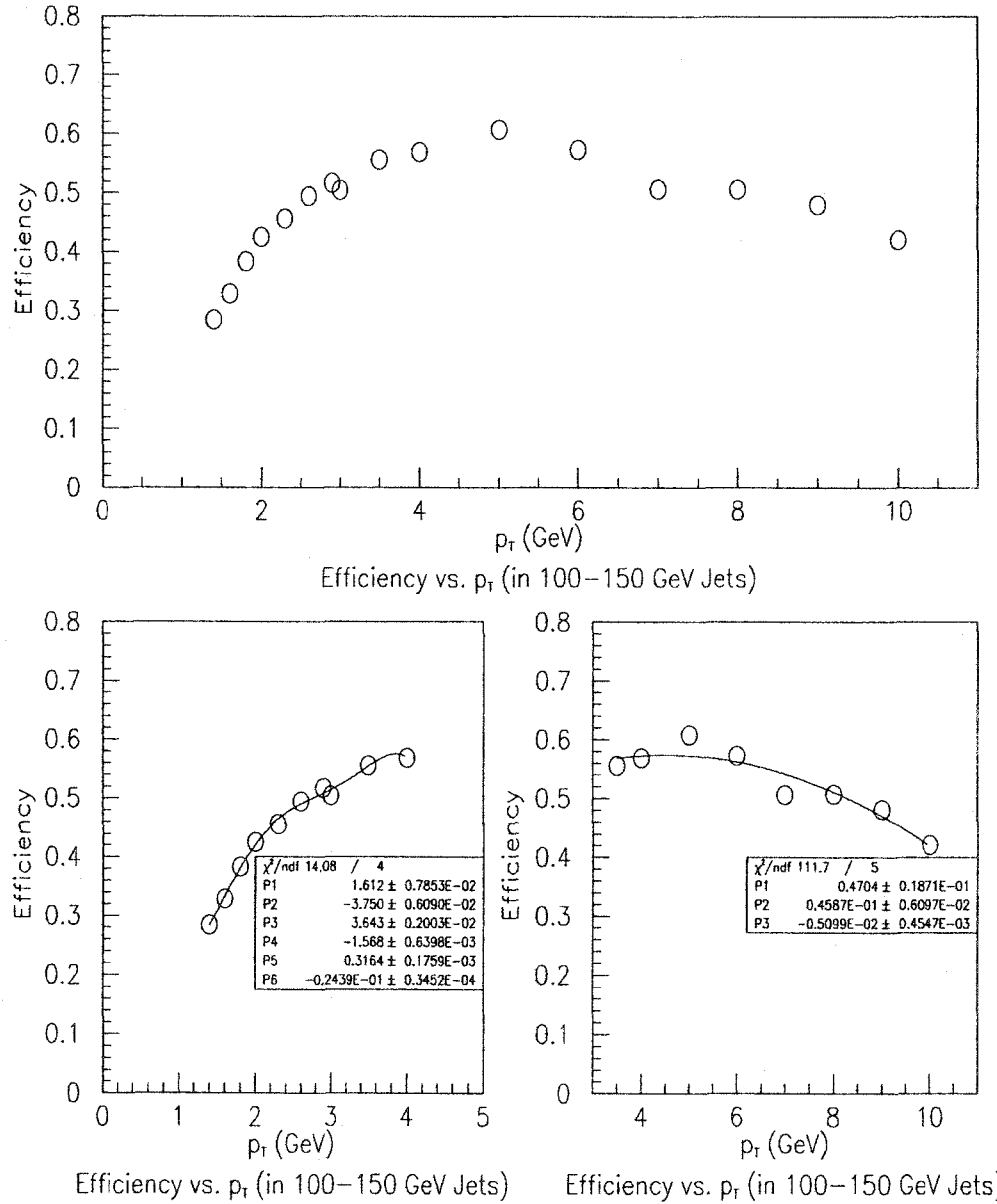
Figure 7.19: The K_S efficiency vs. p_T curve for K_S inside 100-150 GeV jets. Each point in the top figure represents a p_T value which implemented track-embedding. These points are divided into 2 distinct fit regions shown in the bottom diagrams.
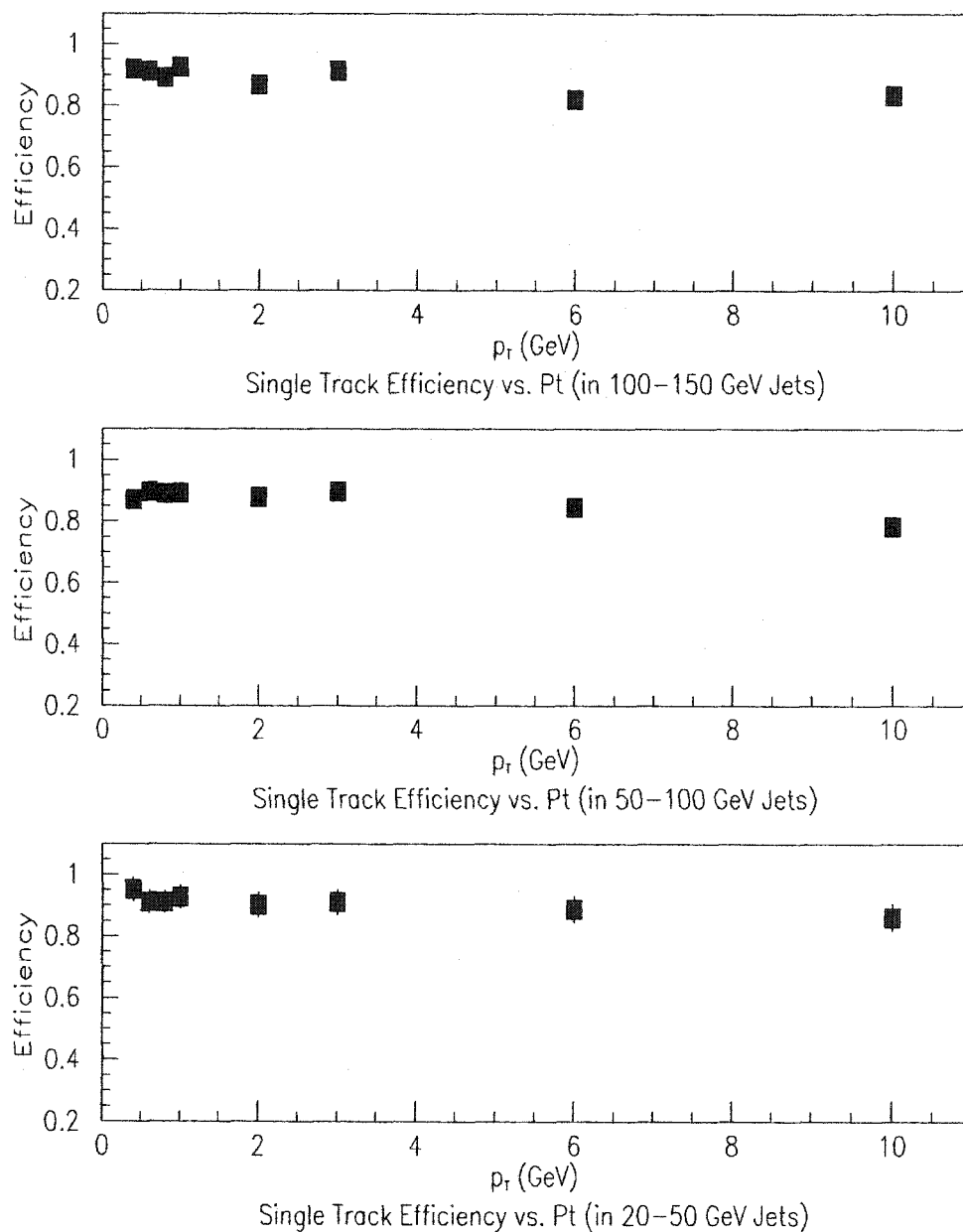
Figure 7.20: The single track efficiency vs. p_T curve for single tracks inside 100-150 GeV jets (top), 50-100 GeV jets (middle), and 20-50 GeV jets (bottom). Each point in the top figure represents a p_T value which implemented track-embedding.

Chapter 8

Jets: Additional Corrections

Aside from implementing the p_T efficiency corrections, there are two additional adjustments necessary before arriving at any conclusions regarding the production of K_S and tracks in jets. The first effect is due to the jet triggers which alter the jet E_T spectrum and the number of tracks per jet, and the second factor is the inclusion of unwanted background K_S originating from non-fragmentation processes. This chapter will discuss the trigger and background corrections applied to the jets, the tracks, and the K_S in the data.

8.1 Applying the p_T Efficiency Corrections

In regard to the types of physics plots generated in the analysis of K_S and track production inside jets, the treatment will be substantially altered from the scenario of K_S production described in Chapter 5. For the production of K_S in the Minimum Bias events, quantities such as $\frac{dN_{KS}}{d\eta}$ and $<p_T>$ are examined after fitting the $\frac{E}{N_{event}} \frac{d^3 N_{KS}}{d^3 p}$ spectra with a power law. These plots will be replaced in the jet study by the more relevant $\frac{1}{N_{jet}} \frac{1}{p_T} \frac{dN_{KS}}{dp_T}$ and $\frac{1}{N_{jet}} \frac{1}{p_T} \frac{dN_{track}}{dp_T}$ spectra. Furthermore, even though all of these plots from both the Minimum Bias and jet data originate from the p_T curves corrected for the p_T efficiencies, the way in which the p_T spectra

180

are generated and corrected for efficiencies will be quite different.

To generate the $\frac{E}{N_{event}} \frac{d^3 N_{KS}}{d^3 p}$ curve for Minimum Bias events, a single efficiency-corrected background-subtracted p_T curve must be produced. To achieve this goal, the K_S candidates passing the cuts (Chapter 3) are further divided into subsamples according to their mass. At this point, there are three p_T spectra, one for each corresponding mass region. Following the background subtraction (Chapter 5), a single uncorrected background-subtracted p_T curve for K_S remains. Next, the p_T efficiency corrections (Chapter 4) are applied bin-by-bin to this uncorrected background-subtracted p_T curve to yield the efficiency corrected background-subtracted p_T spectra for K_S. Once this the spectra is computed, the $\frac{E}{N_{event}} \frac{d^3 N_{KS}}{d^3 p}$ spectrum is obtained by dividing the number of K_S in each bin of the efficiency corrected $\frac{dN_{KS}}{dp_T}$ curve by the p_T value at the midpoint of the bin, the p_T bin width, the number of Minimum Bias events, and a constant of 8π. The generated $\frac{E}{N_{event}} \frac{d^3 N_{KS}}{d^3 p}$ spectra may now be fitted with a power law to compute $\frac{dN_{KS}}{d\eta}$ and $<p_T>$ values.

Although the same techniques applied in the Minimum Bias study may be used again, another method is implemented. In particular, correcting for p_T efficiencies will occur prior to background subtraction rather than after. These methods are equivalent. The latter method is preferred since other corrections will also be added in the form of weights. Also, since the particles contained within jets are measured with respect to the jet axis, producing the $\frac{E}{N_{event}} \frac{d^3 N_{KS}}{d^3 p}$ spectra from the efficiency-corrected background subtracted p_T curves is not the objective. This is the case because the K_S (and tracks) inside jets are not distributed randomly in η and ϕ space like the K_S in the Minimum Bias data. Hence, the quantities used in Chapter 5, like the $\frac{E}{N_{event}} \frac{d^3 N_{KS}}{d^3 p}$ and $\frac{dN_{KS}}{d\eta}$, are uninformative. Instead, the efficiency-

corrected background-subtracted p_T curves are converted into the $\frac{1}{N_{jet}} \frac{1}{p_T} \frac{dN_{KS}}{dp_T}$ and $\frac{1}{N_{jet}} \frac{1}{p_T} \frac{dN_{track}}{dp_T}$ spectra.

At this time, the computation of the $\frac{1}{N_{jet}} \frac{1}{p_T} \frac{dN_{KS}}{dp_T}$ and $\frac{1}{N_{jet}} \frac{1}{p_T} \frac{dN_{track}}{dp_T}$ curves with only the p_T efficiency corrections will be described. For every K_S candidate, there is associated along with it, a p_T and jet E_T value. Then, utilizing the efficiency curves determined in Chapter 7, each K_S and track candidate located inside a jet and passing all selection criteria in Chapter 6 is weighted by the corresponding p_T efficiency correction factor. By grouping the K_S inside jets into subsamples of different ranges of p_T, the number of K_S candidates inside jets having a particular reconstructed mass value is weighted. Next, the series of weighted mass plots have the background subtracted out. In the end, the number of K_S inside jets are tallied for a given interval of p_T, and they are plotted against p_T to yield the efficiency corrected p_T spectra. Similarly, the number of tracks inside jets with a particular p_T are also weighted and grouped according to p_T. Now, the number of K_S and tracks within each p_T bin is divided by the p_T value at the midpoint of the bin, the bin width, and the number of jets in a given jet E_T range (20-50 GeV, 50-100 GeV, or 100-150 GeV). In Figures 8.1 and 8.2, the $\frac{1}{N_{jet}} \frac{1}{p_T} \frac{dN_{KS}}{dp_T}$ and $\frac{1}{N_{jet}} \frac{1}{p_T} \frac{dN_{track}}{dp_T}$ spectra are shown following the p_T efficiency corrections for K_S and tracks inside 20-50 GeV, 50-100 GeV, and 100-150 GeV jets. In addition, the "p_T" notation in Tables 8.1-8.3 refer to values after the p_T efficiency corrections have been applied. At this time, the other corrections will be discussed.

8.2 Trigger Corrections to the Data

The jet data sample consists of the combination of all unique events passing the JET20, JET50, JET70, and JET100 triggers described in Chapter 2. Only the

effects of the jet triggers and the procedures followed to adjust the data will be outlined in this section. The origin as to why the triggers alter the data will not be studied in this analysis, but the jet triggers are known to be correlated to the jet E_T [73] [74]. Thus, by weighting the jets, the tracks in the jets, and the K_S in the jets by various functions of the jet E_T, both the jet E_T and the number of tracks per jet trigger corrections are made.

8.2.1 Jet E_T Effect

Since the production of K_S and tracks in jets is a function of the jet E_T, the results should be calculated with respect to a particular jet E_T spectrum. Although for the contrasting of the data with the Monte Carlo any jet E_T spectrum would suffice, it is best to incorporate the shape of the jet E_T cross-section curve as measured by CDF for the presentation of the results [73] [75] [76]. Hence, the effects of the trigger on the jet E_T will be undone by weighting the jet E_T spectra in the data and the Monte Carlo (to be discussed later) to be the same shape as the jet E_T cross-section. Furthermore, the K_S and tracks in jets are weighted along with the jets in order to undo the jet E_T effect of the trigger.

The jet data sample (JET 20, JET50, JET70, and JET100 sets) is ran through, and the jet E_T spectra for the 20-50 GeV, 50-100 GeV, and 100-150 GeV jets is histogramed in Figure 8.3. The bizarre jet E_T spectrum in Figure 8.3 shows the various peaks and dips caused by the combined effect of all the jet triggers of each set. The uniqueness of the jets is ensured by the removal of the events included in more than one data set as described in Chapter 6. Even though the distributions of the jet E_T vary upon the jet trigger data set, these effects can be corrected for all sets simultaneously.

Before adjusting the jet E_T histogram to be identical to the shape of the jet E_T cross-section, the jet E_T spectra is weighted to be flat. In Figure 8.4, all three jet energy ranges are weighted in this manner. The 20-50 GeV case has a pedestal equal to 30,000 and the 50-100 and 100-150 GeV cases have pedestals of 40,000. Any constant would do as long as it is fixed because the number of jets is divided out before particular quantities are computed. For the fragmentation measurement, it is better to quote results using the flat jet E_T spectra. In addition, K_S and tracks are weighted with the same values as the jets they are contained within.

This flat distribution is implemented because some other experiments have finely tuned e^+e^- collisions at a certain energy. This scenario is unlike the $p\bar{p}$ collisions at the Tevatron where the individual interacting quarks and gluons contain an arbitrary fraction of the energy of the proton and antiproton. The e^+e^- collisions give rise to back-to-back jets having energies on the order of $\frac{\sqrt{s}}{2}$. So when contrasting fragmentation results with other experiments, [9] [77] [78] [79] [80] [81], the jet energies produced from e^+e^- collisions are considered to be approximately constant.

For the $\frac{1}{N_{jet}} \frac{1}{p_T} \frac{dN_{KS}}{dp_T}$ and $\frac{1}{N_{jet}} \frac{1}{p_T} \frac{dN_{track}}{dp_T}$ as well as the number of K_S per jet and the number of tracks per jet calculations, the jet E_T is weighted so the resulting spectrum is similar to the shape of the jet cross-section as a function of jet E_T. This is accomplished by first obtaining the flat jet E_T distribution, and then weighting this spectrum in order to reproduce the structure of the jet cross-section as a function of jet E_T. In Figure 8.5, the jet E_T spectrum is shown after being corrected with this method. Again, the K_S and tracks inside jets are weighted according to the value of the jet E_T of the jet they are inside. The weighting of the Monte Carlo jets will be discussed later.

8.2.2 The Number of Tracks per Jet Effect

The number of tracks per jet is also effected by the jet trigger. For each jet trigger, the number of tracks per jet is approximately 10% too high around and below the trigger threshold. Since the number of tracks per jet is dependent upon the onset of the jet trigger, it follows that the number of tracks per jet is a function of jet E_T. Moreover, the K_S , by decaying into charged pions, behave similarly to the tracks and consequently may be corrected using the identical approach.

The number of tracks per jet as a function jet E_T is studied for each jet trigger sample separately. The examination of the jet trigger samples individually is different from the previous subsection where the jet E_T trigger correction is carried out simultaneously to a sample consisting of all the jet triggers. For each trigger set, a given track is tallied as being contained within a jet if the following criteria are satisfied:

- Track Cuts

    - $|z_{primary}| < 60.0$ cm

    - $z_{jet}^{rms} < 5.0$ cm

    - $|z_{primary}\text{-}z_{jet}| < 5.0$ cm

    - $|\eta^{jet}| < 1.0$

    - Tracks nearest $\Delta R = 0.7$ Jet

    - $|z_{primary}\text{-}z_{track}| < 5.0$ cm

    - $|\eta^{track}| < 1.0$

    - Saved According to jet E_T

Since the shape of the distribution is of concern, the properties that would alter the area of the distribution without changing the area normalized to unity are of little interest. The p_T track and the $|z_{primary}\text{-}z_{track}|$ cuts, the track background, and the track efficiencies falling under this category are irrelevant here.

Without the jet triggers, the number of tracks per jet is expected to be a smoothly increasing function of jet E_T. In Figure 8.6, the number of tracks per jet vs. the jet E_T is shown for each jet trigger set, and the data from each jet trigger set is denoted with the square symbols. Notice the bumps in around 50 GeV, 70-100 GeV, and 50-100 GeV for the JET50, JET70, and JET100 sets caused by the jet triggers. There is actually another such bump in the JET20 around 20-30 GeV but it is hardly noticeable using the current divisions. If left uncorrected, below the onset on the jet trigger, the number of K_S per jet and the number of tracks per jet would be approximately 10% too high.

Before adjusting the effect, the number of tracks per jet as a function of the jet E_T must be studied with a sample that lacks a jet E_T trigger. In this case, the muon trigger sample is selected. Either the electron or the photon data sets would have been sufficient; however, muons leave very little energy inside the calorimeter, unlike photons and electrons, and consequently the jets in the muon trigger sample would not require the removal of unwanted clusters prior to the calculation of jet E_T. Events passing both the muon trigger as well as any other jet trigger (JET20, JET50, JET70, and JET100) are excluded. In Figure 8.6, the number of tracks per jet vs. jet E_T for the muon set, devoid of any jet trigger dependence, are denoted with circles and are fitted with a 4th order polynomial.

By dividing each jet trigger result by those from the muon trigger, the corrections are made to every jet trigger set separately for a given jet E_T range. Hence, when

the data is rerun, each track with a given jet E_T is weighted to yield a smoothly increasing curve of the number of tracks per jet vs. jet E_T spectrum. The identical weights are also applied to the K_S in jets. Following the procedure just discussed, the trigger dependencies of the number of tracks per jet and the number K_S per jet are decoupled from the sample. Thus, the number of tracks per jet and the number K_S per jet are reduced by about 10% below the trigger threshold.

Other studies do not correct for the trigger effect on the number of tracks per jet in this manner. For example, in the inclusive cross-section study, [73] [74] [75] [76], jet E_T thresholds of 75, 100, and 130 GeV are applied to the 50, 70, and 100 GeV trigger samples in order to have a trigger efficiency above 95%. In the dijet analyses, [82] [83] [28] , the dijet masses are also selected to well above the 2.0 times the trigger thresholds. For another study of underlying events in low energy samples, [84] [85] [86], the 40 GeV threshold is placed on the leading jet for the jet 20 trigger sample. This method does indeed cure the trigger problem, but many jets are lost.

The jet E_T and the number of tracks per jet trigger corrections are simultaneously implemented on the jets, the tracks in jets, and the K_S in jets as a product of two weights which are functions of jet E_T. On the other hand, the jets are only adjusted for the jet E_T trigger effect. In the next section, the subtraction of the background K_S and tracks from the number of the K_S and tracks inside jets will be described.

8.3   Background Corrections to the Data

Not all of the K_S and tracks inside jets originate from fragmentation, some are produced by other low energy processes. The background K_S and tracks in jets

are considered to be "fake" since they are of no interest in this analysis. Though the particles are indeed real K_S and tracks, these are not the K_S and tracks in jets being sought out. These "fake" K_S and tracks in jets need to be subtracted from the total number of K_S and tracks in jets in order to prevent the resulting quantities from being at most 8% too high. This problem is dealt with by calculating how many K_S and tracks are in a random "fake" cone away from all other jets, and then subtracting this quantity from the number of K_S and tracks found in jets after trigger corrections are performed.

There are many differences between a "fake" jet and a "real" jet. A "real" jet is defined by the clustering algorithms and the jet energy corrections mentioned in Chapter 6. Also, for a "real" jet, the η_{jet}, the ϕ_{jet}, the jet E_T, and the jet vertex values are ultimately computed with the distributions of particles in a given event. In contrast, a "fake" jet does not exist in any material sense. A "fake" jet is not derived from the particles in the clusters found in the calorimeters, but rather via Monte Carlo techniques. Having just an η_{jet}^{fake} and a ϕ_{jet}^{fake}, a "fake" jet only exists if it is sufficiently isolated from all "real" jets. Moreover, a "fake" jet, not being calculated from particles, does not have either a jet E_T or a jet vertex. Apart from this, since there is not a jet E_T associated with this "fake" jet, the trigger corrections (jet E_T and the number of tracks per jet) are not made. A "fake" jet can be thought as an arbitrary cone away from the other jets in which the K_S and the tracks may be inside.

In order to determine whether either a track or a K_S is contained within a "fake jet", the direction of a "fake" jet is defined by a random η_{jet}^{fake} ($|\eta_{jet}^{fake}|<1.0$) and a random ϕ_{jet}^{fake} ($0\leq\phi_{jet}^{fake}<2\pi$). The η_{jet}^{fake} should also have the same shape as the η_{jet} distribution of the "real" jets from the data. The selection of random η_{jet}^{fake} and

ϕ_{jet}^{fake} values is repeated until $\Delta R_{jet-fake\ jet}$>1.0 for every "real" jet above 10.0 GeV where $\Delta R_{jet-fake\ jet}$ is given by:

$$\Delta R_{jet-fake\ jet} = \sqrt{(\eta_{jet} - \eta_{jet}^{fake})^2 + (\phi_{jet} - \phi_{jet}^{fake})^2}. \tag{8.1}$$

Once this iterative process of locating a "fake" jet direction sufficiently away from all other "real" jets above 10.0 GeV is complete, then the number of K_S and tracks within the "fake" jet is computed. In particular, if there is a K_S so $\Delta R_{KS-fake\ jet}$ <0.7 where $\Delta R_{KS-fake\ jet}$ is denoted by

$$\Delta R_{KS-fake\ jet} = \sqrt{(\eta_{KS} - \eta_{jet}^{fake})^2 + (\phi_{KS} - \phi_{jet}^{fake})^2} \tag{8.2}$$

, then the K_S is considered a background K_S . Equivalently, a track is tallied as a background track if $\Delta R_{track-fake\ jet}$<0.7 where $\Delta R_{track-fake\ jet}$ is defined by

$$\Delta R_{track-fake\ jet} = \sqrt{(\eta_{track} - \eta_{jet}^{fake})^2 + (\phi_{track} - \phi_{jet}^{fake})^2}. \tag{8.3}$$

Both K_S and tracks found inside "fake" jets should pass some of the cuts outlined in Chapter 6. Associating "fake" jets into E_T ranges or cutting on jet vertices is not possible since the "fake" jet is defined only by η_{jet}^{fake} and ϕ_{jet}^{fake}. However, most other cuts are utilized.

Once the p_T spectra for background K_S and tracks are obtained, the curves derived from K_S and tracks embedded inside 20-50 GeV jets are implemented in order to correct for efficiencies. This is done because the "fake" jets are believed not to contain many tracks. Since the 20-50 GeV have lower track multiplicities than either 50-100 GeV or 100-150 GeV jets, the track-embedding efficiency curves

from Chapter 7 obtained from K_S and tracks embedded into 20-50 GeV jets are incorporated.

In summary, the selection criteria of "fake" jets as well as for the background tracks and K_S inside the "fake" jets are listed below:

- Fake Jet Cuts

    - $|z_{primary}| < 60.0$ cm

    - Select η_{jet}^{fake} with $|\eta_{jet}^{fake}| < 1.0$

    - Select ϕ_{jet}^{fake} with $0 \leq \phi_{jet}^{fake} < 2\pi$

    - For all jets with $E_T > 10.0$ GeV, $|\Delta R_{jet-fake\ jet}| > 1.0$

- Track Cuts

    - $|z_{primary}| < 60.0$ cm

    - $\Delta R_{track-fake\ jet} < 0.7$

    - $|\eta^{track}| < 1.0$

    - $1.5 < p_T^{track} < 10.0$ GeV

    - Correct with p_T efficiency curve from tracks embedded into 20-50 GeV jets

- K_S Cuts

    - $|z_{primary}| < 60.0$ cm

    - $\chi_{KS}^2 < 20.0$

    - $|z_{KS} - z_{primary}| < 3.0$ cm

    - $p_T^{tracks\ from\ KS} > 500$ MeV

- $|\eta^{KS}| < 1.0$

- 3D Displacement$^{KS} > 1.0$ cm

- $\cos \theta_{PD}{}^{KS} > 0.990$

- $\Delta R_{KS-fake\ jet} < 0.7$

- $1.5 < p_T^{KS} < 10.0$ GeV

- Correct with p_T efficiency curve from K_S embedded into 20-50 GeV jets

The $\frac{1}{N_{jet}} \frac{1}{p_T} \frac{dN_{KS}}{dp_T}$ and $\frac{1}{N_{jet}} \frac{1}{p_T} \frac{dN_{track}}{dp_T}$ spectra for background K_S and tracks as a function of p_T are displayed in Figures 8.7 and 8.8. Although the HERWIG Monte Carlo results will be detailed in Chapter 9, it is shown along with the data. The square points represent the data whereas the three histograms generated with the HERWIG Monte Carlo correspond to three different jet E_T range settings. Both data and HERWIG Monte Carlo curves are computed from the K_S and tracks located within the "fake" jets. Notice that the data is higher than the HERWIG Monte Carlo (discussed in Chapter 9). The background curves are later subtracted bin-by-bin from the p_T spectra of K_S and tracks inside jets. Most of these background corrections are in low p_T regions.

In the end, after the trigger adjustments, the background rate of K_S and tracks in the data is at most an 8% effect. To be specific, of 2,078,760 fake jets, there are 25979 K_S between 1.5 and 10 GeV once the p_T and the branching ratio corrections are made. The background rate of K_S is 0.0125 ± 0.0003. Likewise, in the same ensemble of "fake" jets, there are 465099 tracks between 1.5 and 10 GeV after the single track p_T efficiency adjustments. This corresponds to a track background of 0.2237 ± 0.0003 tracks per jet.

8.4 Results from the Data

In Tables 8.1 through 8.3, the effect of the various corrections for the number of K_S per jet, the number of tracks per jet, and 2.0 times the number of K_S per track for data are listed for the K_S and tracks inside 20-50 GeV, 50-100 GeV, and 100-150 GeV jets. For example, in Table 8.1, the number of K_S per jet in 20-50 GeV jets is 0.175 ± 0.002. This number is taken after the branching ratio, the p_T efficiency, and the jet E_T trigger corrections have been taken into account. After the number of tracks per jet trigger adjustment, this number decreases to 0.168 ± 0.002. Moreover, after the background (or "fake") K_S have been removed, the number of K_S per jet is reduced to 0.156 ± 0.002. The number of tracks per jet and 2.0 times the number of K_S per track may be understood similarly.

The motivation for multiplying the number of K_S per track by 2.0 is to take into account K_L production. It is assumed that the sum of K_S and K_L are equal, so $2.0*K_S$ production is equal to K_S plus K_L production. Now, the sum of K_S and K_L production (2.0 K_S production) is equal to both the sum of K_0 and $\bar{K}_0$ production and the sum of K^+ and K^- production. It turns out that the ratio of the charged kaons to the charged pions is about 10% for Minimum Bias events. So in order to study this ratio inside high E_T jets, it becomes necessary to multiply K_S production by 2.0 and dividing this product by the number of tracks (approximately the number of charged pions).

From viewing Tables 8.1 through 8.3, various trends are observable. In general, the number of tracks per jet trigger correction has the largest effect on the number of K_S per jet and the number of tracks per jet below 100 GeV because most of the jet sample comes from the Jet100 set (mainly the jets below the threshold are effected). As for the background rate, every energy range is taken into account

Table 8.1: The number of K_S per jet in the data ($1.5 < p_T < 10.0$ GeV).

After Correction	$\frac{N_{KS}}{jet}$ in 20-50 Jets	$\frac{N_{KS}}{jet}$ in 50-100 Jets	$\frac{N_{KS}}{jet}$ in 100-150 Jets
P_T	0.175 ± 0.002	0.232 ± 0.003	0.218 ± 0.003
Trigger	0.168 ± 0.002	0.219 ± 0.003	0.213 ± 0.003
Fake Rate	0.156 ± 0.002	0.206 ± 0.003	0.200 ± 0.003

Table 8.2: The number of tracks per jet in the data ($1.5 < p_T < 10.0$ GeV).

After Correction	$\frac{N_{track}}{jet}$ in 20-50 Jets	$\frac{N_{track}}{jet}$ in 50-100 Jets	$\frac{N_{track}}{jet}$ in 100-150 Jets
P_T	3.095 ± 0.002	5.415 ± 0.003	6.282 ± 0.003
Trigger	3.026 ± 0.002	5.314 ± 0.003	6.181 ± 0.003
Fake Rate	2.802 ± 0.002	5.090 ± 0.003	5.957 ± 0.003

Table 8.3: The number of ($2.0 * K_S$) per track in the data ($1.5 < p_T < 10.0$ GeV).

After Correction	$2\,\frac{N_{KS}}{N_{track}}$ in 20-50 Jets	$2\,\frac{N_{KS}}{N_{track}}$ in 50-100 Jets	$2\,\frac{N_{KS}}{N_{track}}$ in 100-150 Jets
P_T	0.113 ± 0.001	0.086 ± 0.001	0.069 ± 0.001
Trigger	0.111 ± 0.001	0.082 ± 0.001	0.069 ± 0.001
Fake Rate	0.111 ± 0.001	0.081 ± 0.001	0.067 ± 0.001

following this procedure. For the data, after all the corrections, the number of K_S per jet increases from 0.156 ± 0.002 for K_S inside 20-50 GeV jets to 0.200 ± 0.003 for K_S inside 100-150 GeV jets. Hence, the number of K_S per jet increases by about 30%. The number of tracks per jet increases by more than a factor of 2.1 from 2.802 ± 0.002 to 5.957 ± 0.003 over a similar range. As for 2.0 times the number of K_S per track, this quantity decreases by approximately a factor of 0.60 from 0.111 ± 0.001 to 0.067 ± 0.001. In Chapter 9 and Chapter 10, the results from the data will be compared with those from the HERWIG Monte Carlo.

$1/N_{jet}$ $1/p_T$ dN_{track}/dp_T vs. p_T with Only p_T Efficiency and Jet E_T Corrections
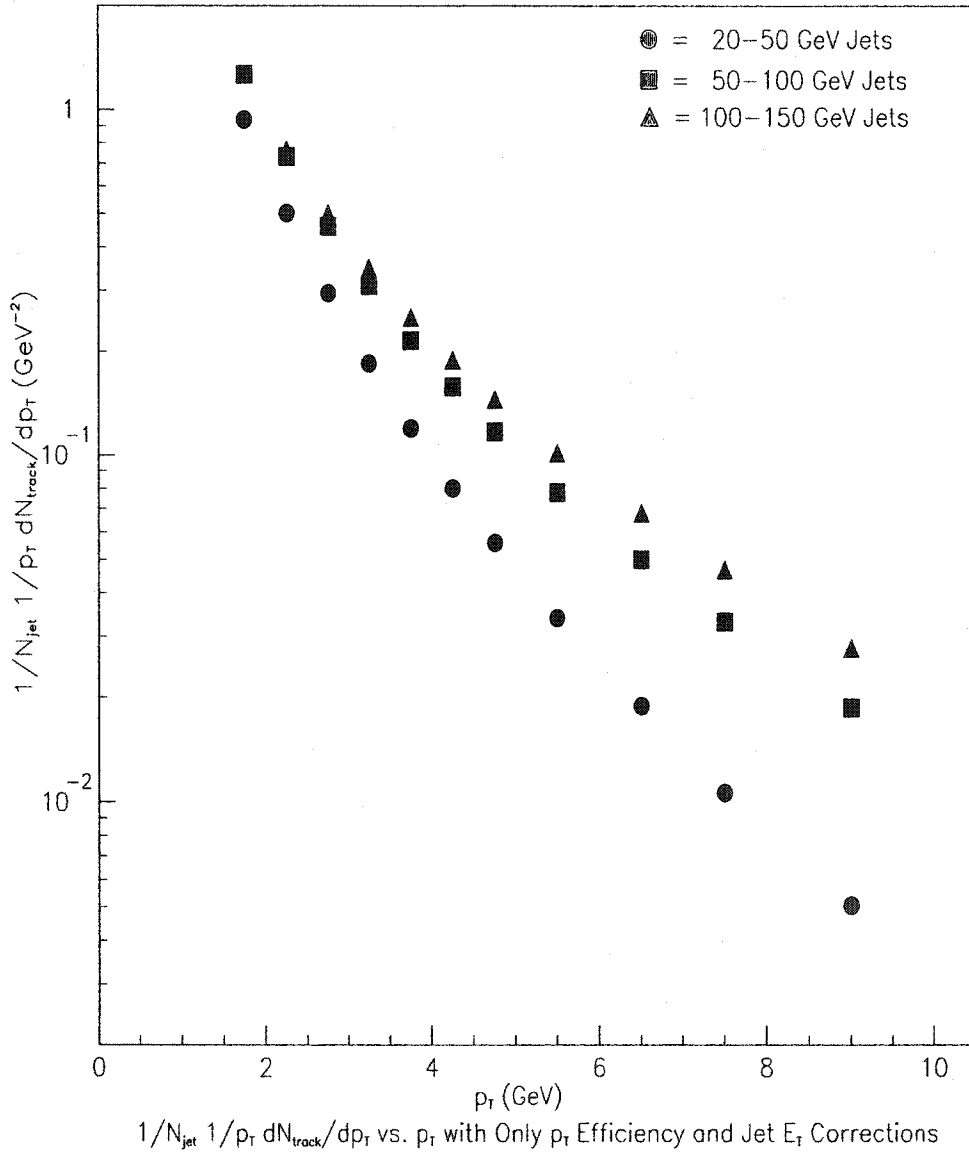
Figure 8.1: The $\frac{1}{N_{jet}} \frac{1}{p_T} \frac{dN_{KS}}{dp_T}$ spectra with only p_T efficiency and jet E_T trigger corrections for 20-50 GeV, 50-100 GeV, and 100-150 GeV jets.

$1/N_{jet}$ $1/p_T$ dN_{track}/dp_T vs. p_T with Only p_T Efficiency and Jet E_T Corrections
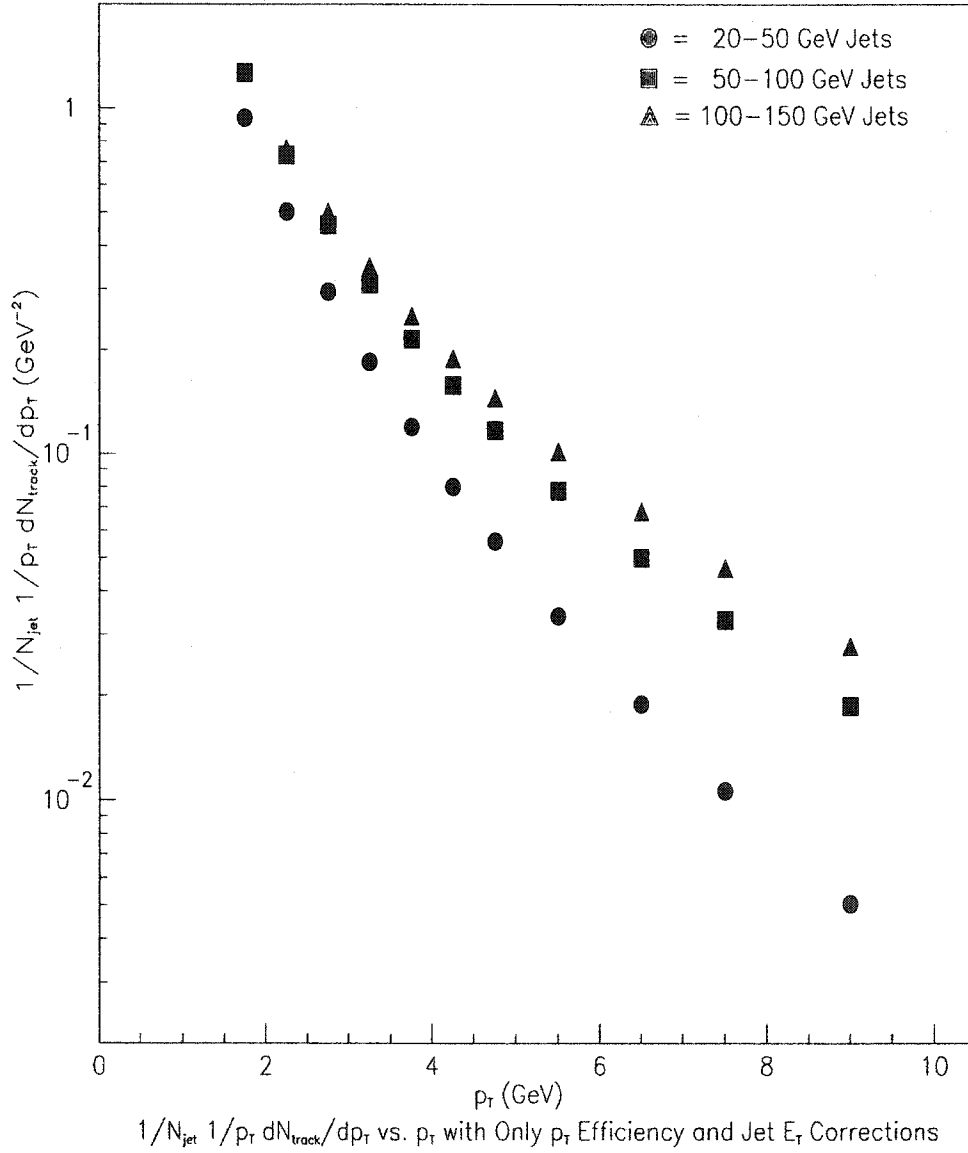
Figure 8.2: The $\frac{1}{N_{jet}}$ $\frac{1}{p_T}$ $\frac{dN_{track}}{dp_T}$ spectra with only p_T efficiency and jet E_T trigger corrections for 20-50 GeV, 50-100 GeV, and 100-150 GeV jets.
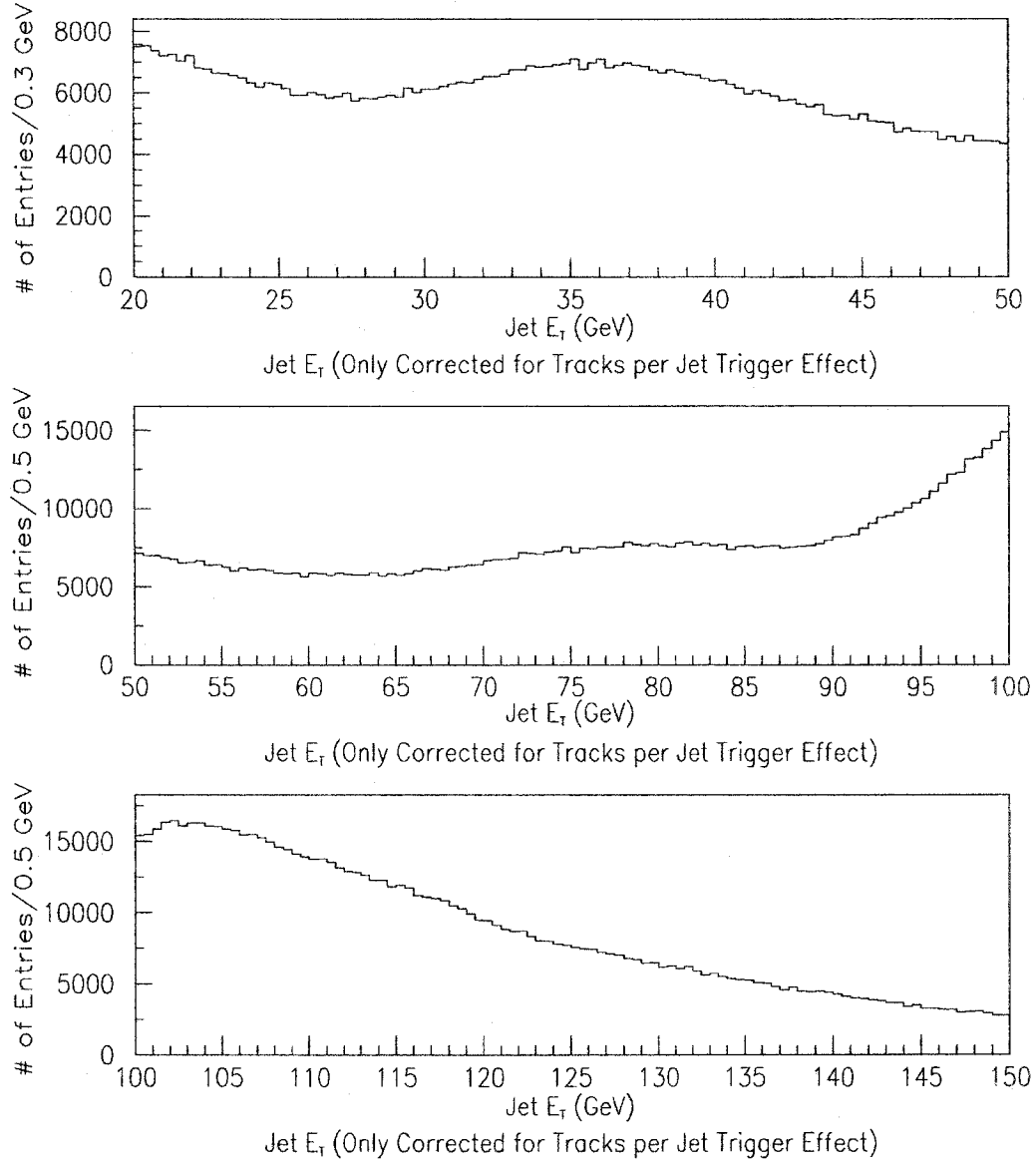
Figure 8.3: The unweighted jet E_T for 20-50 GeV (top), 50-100 GeV (middle), and 100-150 GeV (bottom) jets. For all jet E_T ranges, the jet E_T spectrum has not yet been corrected for the jet E_T dependence. Only the number of tracks per jet trigger effect has been taken into account.
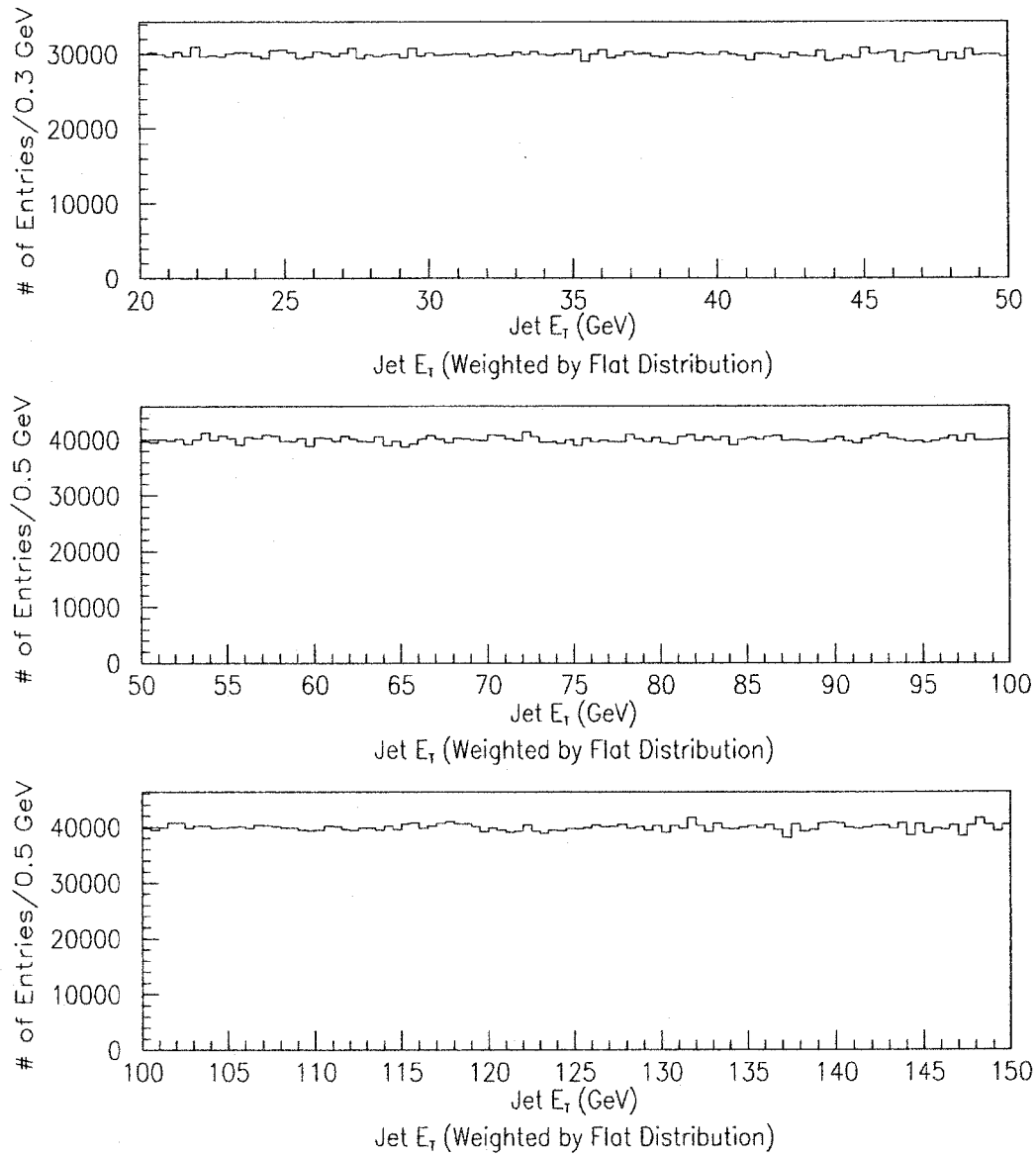
Figure 8.4: The weighted jet E_T for 20-50 GeV (top), 50-100 GeV (middle), and 100-150 GeV (bottom) jets. For all jet E_T ranges, the jet E_T spectrum has been weighted to yield the flat distribution vs. jet E_T. Both the number of tracks per jet and the jet E_T trigger effects have been taken into account.
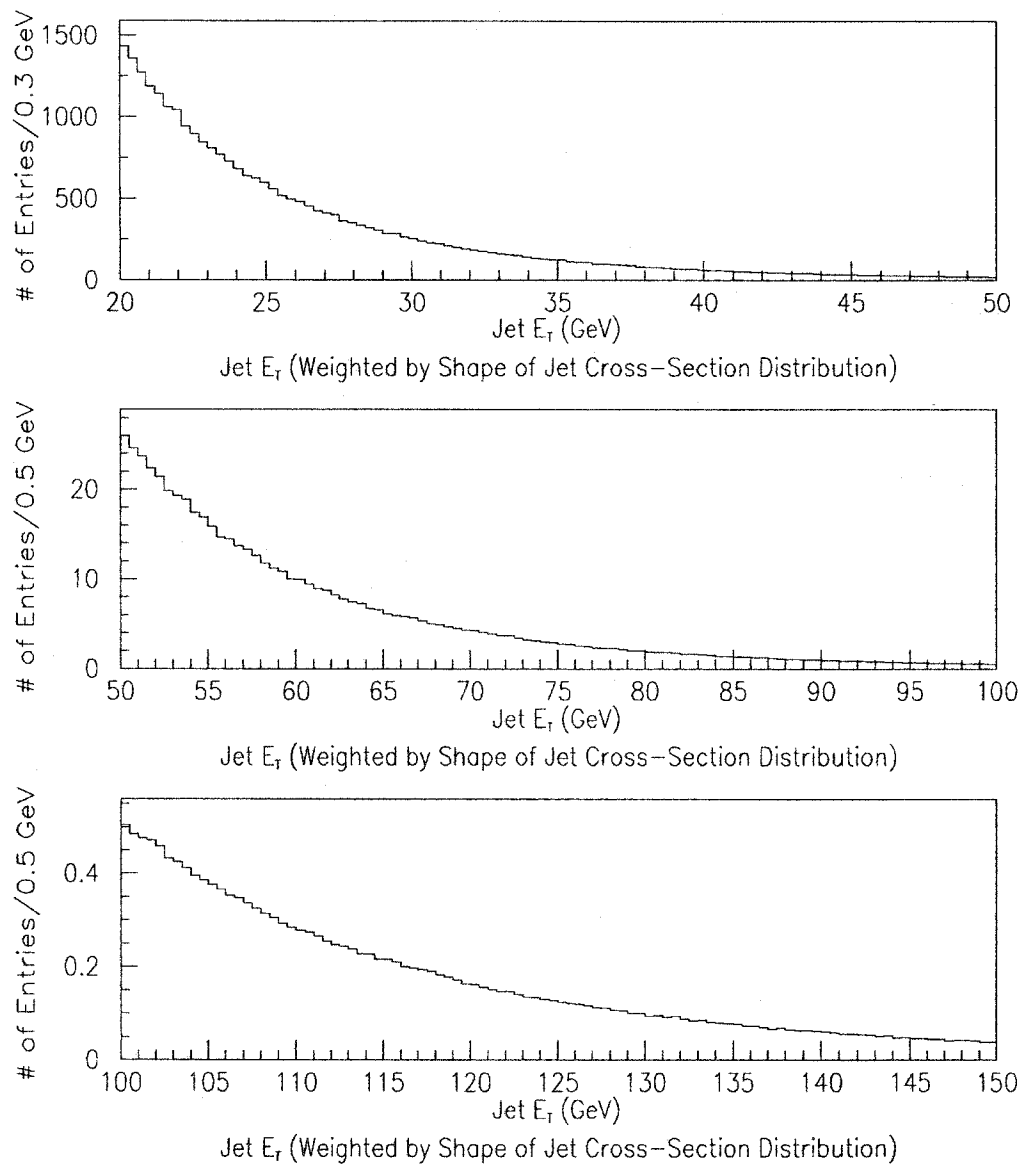
Figure 8.5: The weighted jet E_T for 20-50 GeV (top), 50-100 GeV (middle), and 100-150 GeV (bottom) jets. For all jet E_T ranges, the jet E_T spectrum has been weighted to yield the same distribution as the jet cross-section vs. jet E_T. Both the number of tracks per jet and the jet E_T trigger effects have been taken into account.
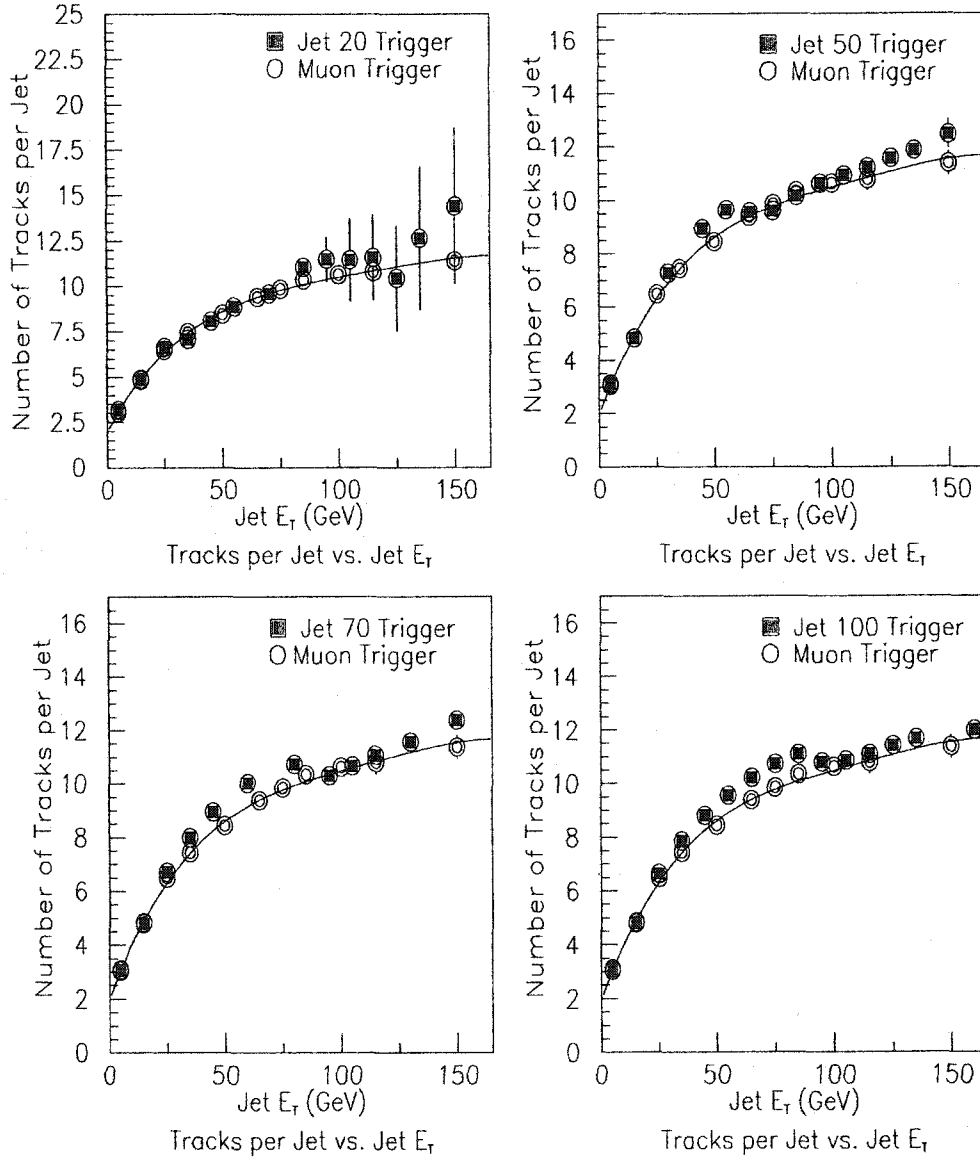
Figure 8.6: The jet trigger dependence on the number of tracks per jet vs. jet E_T. In top left, the number of tracks per jet vs. jet E_T dependence is plotted for both the JET20 and the muon sets. The squares are the JET20 set, and the circles are for the muon set. The muon set is fitted with a smooth curve. Similar, plots for JET50 (top right), JET70 (bottom left), and JET100 (bottom right) data sets are shown.

$1/N_{jet}\ 1/p_T\ dN_{KS}/dp_T$ vs. p_T for Fake K_s
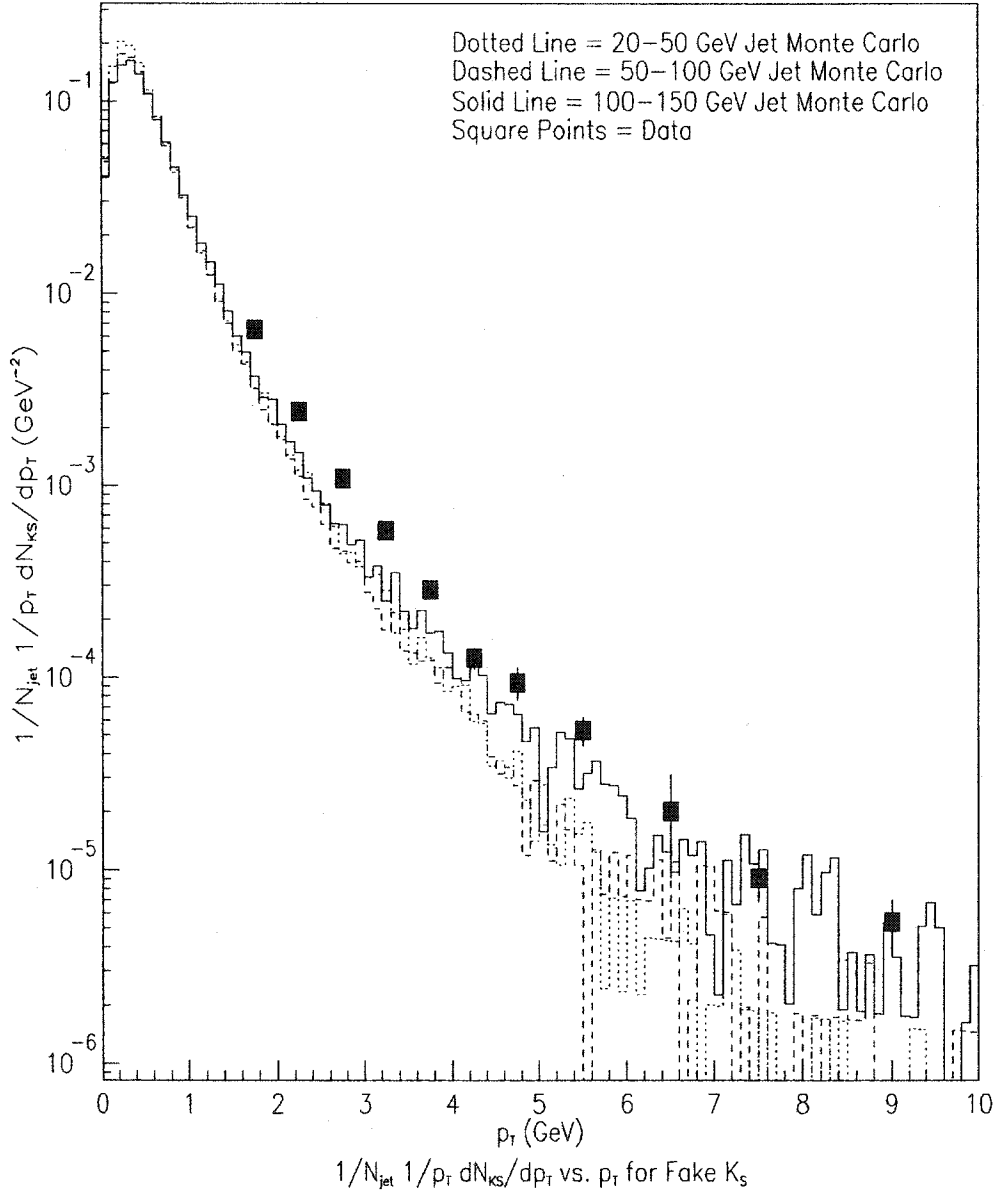
Figure 8.7: The $\frac{1}{N_{jet}}\ \frac{1}{p_T}\ \frac{dN_{KS}}{dp_T}$ distribution for background K_S in jets for data and HERWIG Monte Carlo. This is described further in Chapter 9. The statistical errors on the HERWIG Monte Carlo histograms are on the order of 1.2E-04, 1.2E-04, and 1.5E-04 at 2.0 GeV for 20-50 GeV, 50-100 GeV, and 100-150 GeV jets, 6.3E-06, 9.2E-06, and 1.3E-05 at 5.0 GeV for 20-50 GeV, 50-100 GeV, and 100-150 GeV jets, and 2.0E-06, 4.7E-06, and 3.3E-06 at 7.0 GeV for 20-50 GeV, 50-100 GeV, and 100-150 GeV jets.

1/N_jet 1/p_T dN_track/dp_T vs. p_T for Fake Tracks
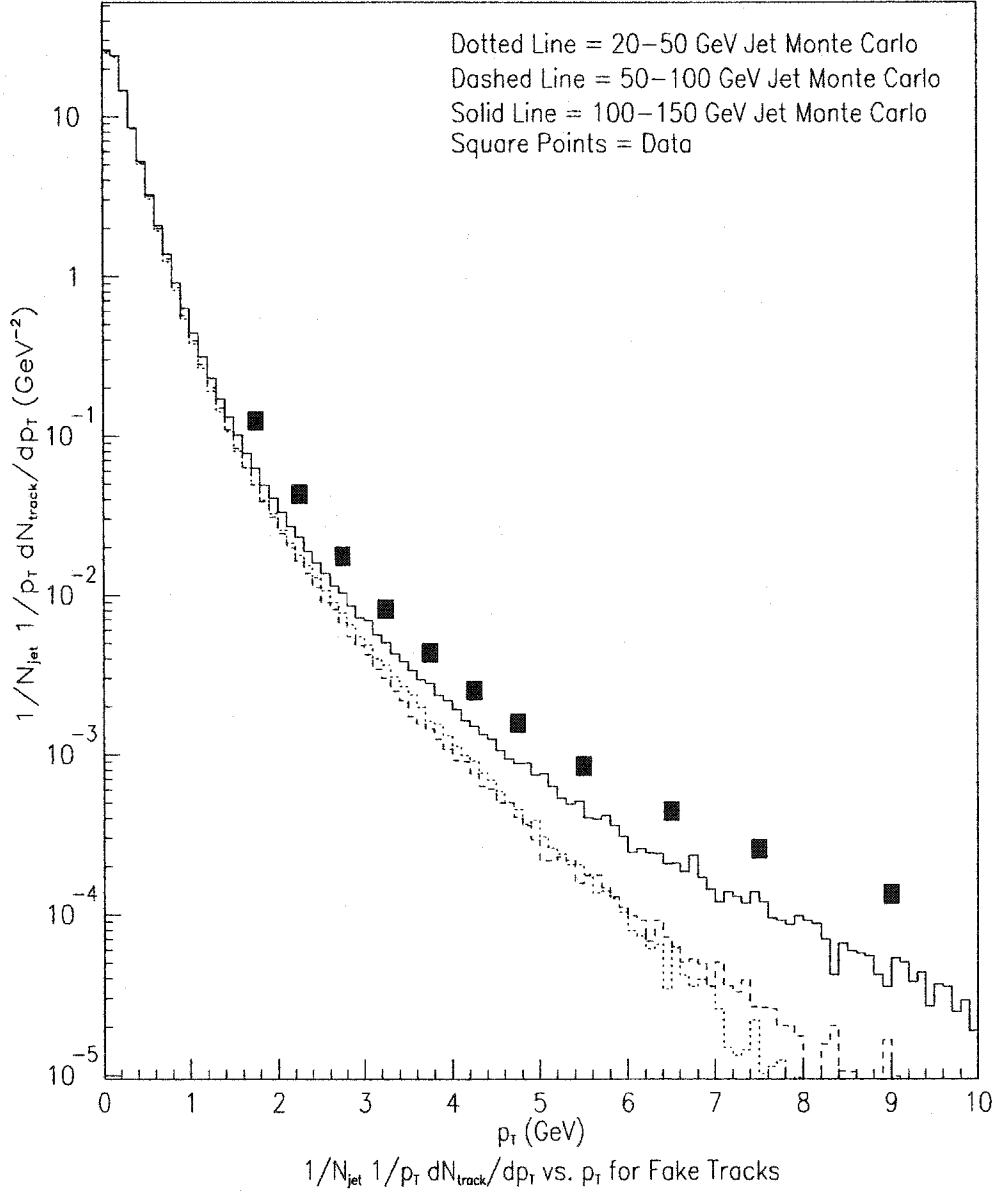
Figure 8.8: The $\frac{1}{N_{jet}} \frac{1}{p_T} \frac{dN_{track}}{dp_T}$ distribution for background tracks in jets for data and HERWIG Monte Carlo. This is described further in Chapter 9. The statistical errors on the HERWIG Monte Carlo histograms are on the order of 4.0E-04, 3.9E-04 and 4.7E-04 at 2.0 GeV for 20-50 GeV, 50-100 GeV, and 100-150 GeV jets, 2.7E-05, 2.4E-05, and 4.1E-05 at 5.0 GeV for 20-50 GeV, 50-100 GeV, and 100-150 GeV jets, and 7.1E-06, 7.1E-06, and 1.5E-05 at 7.0 GeV for 20-50 GeV, 50-100 GeV, and 100-150 GeV jets.

Chapter 9

Jets: HERWIG Monte Carlo

The comparison of the results from the data to those calculated via HERWIG Monte Carlo are an important part of this analysis. To initiate this discourse, the exact procedure of extracting the HERWIG Monte Carlo K_S and tracks contained within the jets will be described. The HERWIG Monte Carlo requires some adjustments reminiscent of those applied to the data in Chapter 8. For example, the setting of certain Monte Carlo parameters skews the jet E_T spectra in a manner which mirrors that of the data triggers. Furthermore, the HERWIG Monte Carlo background K_S and tracks from non-fragmentation processes also make their way inside the jets. Both of these effects need to be examined for prior to arriving at any conclusions about the track and K_S production inside jets. After these effects are accounted for in the HERWIG Monte Carlo, the stage is set to contrasting the data with the Monte Carlo.

9.1   HERWIG Monte Carlo

This would be an excellent time to briefly describe the Monte Carlo results employed in the comparison to the data. What is of interest is the various distributions of the K_S and tracks inside the jets, and to achieve this goal, the information of the

particles and the jets are extracted at different stages of the HERWIG generator and the QFL simulator procedure.

The particles of the jets are produced using the $2 \rightarrow 2$ parton hard-scattering processes in the HERWIG generator. For every proton and antiproton collision, a single parton from the proton will interact with another parton from the antiproton, and the two incoming partons will undergo $2 \rightarrow 2$ hard-scattering and leave just the two outgoing partons. These outgoing partons can fragment into groups of particles later clustered into jets. The hard-scattering momenta of the colliding partons are given by the default parton distribution functions. Besides this, the range of the transverse momenta of the interacting partons may be set by tuning the parameters which change the transverse momenta of the particles as well as the E_T of jets comprising of groups of particles [31].

The 4-vector information of the particles (the K_S and the tracks) is obtained directly after the HERWIG generator. At this level, the K_S are identified by their particle IDs. Equivalently, the tracks are considered as the particles having the particle IDs of charged pions (π^+ and π^-), charged kaons (K^+ and K^-), electrons (e^-), positrons (e^+), muons (μ^-), antimuons (μ^+), protons (p), and antiprotons ($\bar{p}$). At this point, the p_T corrected distributions of the K_S and the tracks are determined. Next, the K_S and the tracks contained within jets need to be identified.

A jet is an entity that depends upon the clustering algorithm applied to the energy clusters in the calorimeter. Clearly, at the HERWIG generator level, this calorimetry information has not yet been created. Hence, the HERWIG generator level is used as the input for the QFL simulator [90]. QFL is a simulator (CDFSIM described Chapter 7 is another) which does tracking poorly and calorimetry reasonably well. After the QFL simulator, the detector information produced is ran

through the same clustering algorithms and the jet energy corrections as the data in order to identify jets as well as compute the jet quantities like the jet vertices and the jet E_T.

If either a HERWIG level K_S or track is found within a $\Delta R = 0.7$ cone of a HERWIG+QFL+Cluster Code jet, then the particle is considered to be inside this jet. In particular, the following cuts are performed on the jets, the tracks, and the K_S :

- Jet Cuts

  - $|z_{primary}| < 60.0$ cm

  - $z_{jet}^{rms} < 5.0$ cm

  - $|z_{primary} - z_{jet}| < 5.0$ cm

  - $|\eta^{jet}| < 1.0$

  - $20.0 < E_T{}^{jet} < 50.0$ GeV, $50.0 < E_T{}^{jet} < 100.0$ GeV, or $100.0 < E_T{}^{jet} < 150.0$ GeV

- Track Cuts

  - $|z_{primary}| < 60.0$ cm

  - $z_{jet}^{rms} < 5.0$ cm

  - $|z_{primary} - z_{jet}| < 5.0$ cm

  - $|\eta^{jet}| < 1.0$

  - $|\eta^{track}| < 1.0$

  - Pass Particle ID Criteria ($\pi^+, \pi^-, K^+, K^-, e^-, e^+, \mu^-, \mu^+, p$, and $\bar{p}$)

  - Tracks within $\Delta R = 0.7$ Jet

- $20.0{<}E_T{}^{jet}{<}50.0$ GeV, $50.0{<}E_T{}^{jet}{<}100.0$ GeV, or $100.0{<}E_T{}^{jet}{<}150.0$ GeV

- K_S Cuts

  - $|z_{primary}|{<}60.0$ cm

  - $z_{jet}^{rms}{<}5.0$ cm

  - $|z_{primary}\text{-}z_{jet}|{<}5.0$ cm

  - $|\eta^{jet}|{<}1.0$

  - $|\eta^{track}|{<}1.0$

  - Pass Particle ID Criteria (K_S)

  - Tracks within $\Delta R = 0.7$ Jet

  - $20.0{<}E_T{}^{jet}{<}50.0$ GeV, $50.0{<}E_T{}^{jet}{<}100.0$ GeV, or $100.0{<}E_T{}^{jet}{<}150.0$ GeV

Since the QFL simulator reproduces tracking information poorly with 100% wire efficiency (most wires have efficiencies between 75-95%), the value of the Monte Carlo jet vertices computed from this tracking information may be called into question. However, the jets with E_T more than 20 GeV usually have at least 7 tracks with momenta above 0.5 GeV, and since the tracking efficiency is greater than 90%, a loss of a track or two would not radically alter the measurement. In addition, there are also tracks below 0.5 GeV incorporated into a given jet vertex calculation.

The Monte Carlo jet properties have been studied closely by others as well as in the course of this analysis. Both types of jets have been found to be consistent. In the next two sections, the corrections to the Monte Carlo jets, the tracks in jets, and the K_S in jets will be described.

9.2 "Trigger Corrections" to the Monte Carlo

In order to compare the Monte Carlo with the data, many Monte Carlo jets at various energies need to be generated. With default values, it would be inefficient to acquire a large number of jets at a particular E_T. The greater the E_T, the more impractical the rational for the implementation of the default parameters. However, by changing the allowable range of the transverse momenta of the interacting partons in the Monte Carlo, numerous jets at any desired energy can be obtained in a reasonable time.

By adjusting the upper and lower bounds of the transverse momenta of the hard-scattering partons, a Gaussian-like distribution of jet E_T about a jet E_T is produced. The exact values of these parameters are set so the falling edge of this Gaussian-like jet E_T distribution is contained within the jet E_T region of interest. In particular, for the production of 20-50 GeV, 50-100 GeV, and 100-150 GeV jets, the limits of the transverse momenta of the partons are fixed at 10.0 and 50.0 GeV, 40.0 and 100.0 GeV, and 80.0 to 150.0 GeV, respectively.

The setting of the hard-scattering transverse momenta parameters to mold the Monte Carlo jet E_T is analogous to how the jet triggers bias the jet E_T of the data. Likewise, the Monte Carlo jet E_T distributions are corrected similarly by weighting each jet E_T value so the jet E_T plots show a flat constant of 40,000 (any constant would do). Then, the jet E_T spectrum for each of the E_T ranges is weighted in order for the resulting histogram to be similar in shape to the jet cross-section as a function of jet E_T. The K_S and tracks inside jets are weighted according to the E_T of the jet in which they are embedded. As for the number of tracks per jet trigger correction for the Monte Carlo, there is none, since the setting of the hard-scattering transverse momenta range parameters do not effect the number of

tracks per jet.

9.3 Background Corrections to the Monte Carlo

The background K_S and tracks in jets are also removed from the K_S and tracks in jets in the HERWIG Monte Carlo. These fake rates for the K_S and tracks are expected to differ from the background rates of the data since multiple interactions, quite common in data, do not occur with the default Monte Carlo settings. However, like the case for the data, the background effect should not be more than 10% and most of the contribution should be confined to the first few low p_T bins.

The techniques incorporated to calculate the background K_S and tracks contained within jets in the Monte Carlo closely overlap those previously used for the data. An arbitrary cone with $|\eta_{jet}^{fake}| < 1.0$ and $0 \leq \phi_{jet}^{fake} < 2\pi$ is first isolated from all jets above 10 GeV, then the number of K_S and tracks inside the jets is tallied after making use of the particle ID and the 4-vector information taken directly from the HERWIG Monte Carlo. The isolation criteria depends on the jets above 10 GeV obtained after the HERWIG Monte Carlo and the QFL simulator stages. For the fake rates of the K_S and tracks in HERWIG Monte Carlo jets, the following cuts are employed for the jets, the tracks, and the K_S :

- Fake Jet Cuts

    - $|z_{primary}| < 60.0$ cm

    - Select η_{jet}^{fake} with $|\eta_{jet}^{fake}| < 1.0$

    - Select ϕ_{jet}^{fake} with $0.0 \leq \phi_{jet}^{fake} < 2\pi$

    - For all jets with $E_T > 10.0$ GeV, $|\Delta R_{jet-fake\ jet}| > 1.0$

- Track Cuts

  - $|z_{primary}|<60.0$ cm

  - Pass Particle ID Criteria ($\pi^+,\pi^-,K^+,K^-,e^-,e^+,\mu^-,\mu^+,p,$ and $\bar{p}$)

  - $\Delta R_{track-fake\ jet}<0.7$

  - $|\eta^{track}|<1.0$

  - $1.5<p_T^{track}<10.0$ GeV

- K_S Cuts

  - $|z_{primary}|<60.0$ cm

  - Pass Particle ID Criteria (K_S)

  - $\Delta R_{track-fake\ jet}<0.7$

  - $|\eta^{KS}|<1.0$

  - $1.5<p_T^{KS}<10.0$ GeV

On the other hand, since the hard-scattering variables are set separately for the 20-50 GeV, 50-100 GeV, and 100-150 GeV jets, there are actually three separate curves for the background K_S and tracks contained within jets. Furthermore, each separate HERWIG Monte Carlo background plot is subtracted bin by bin from the appropriate corresponding histogram of either the number of K_S per jet or the number of tracks per jet for a given jet E_T range. The number of HERWIG Monte Carlo background K_S per jet is 0.0073 ± 0.0001, 0.0059 ± 0.0001, 0.007 ± 0.0001 for the 20-50 GeV, 50-100 GeV, and 100-150 GeV cases, and the number of HERWIG Monte Carlo background track per jet is 0.1055 ± 0.0004, 0.0873 ± 0.0003, and 0.1081 ± 0.0003 for the 20-50 GeV, 50-100 GeV, and 100-150 GeV cases. The

background rates for the number of tracks and the number of K_S inside jets are at most a 5% effect.

9.4 Comparing the Background of the Data and the HERWIG Monte Carlo

In order to produce Figure 8.7 and 8.8, the p_T distributions of HERWIG Monte Carlo background K_S and tracks inside jets are divided by the number of jets, the bin size, and the p_T value at the midpoint of the bin. These $\frac{1}{N_{jet}} \frac{1}{p_T} \frac{dN_{KS}}{dp_T}$ and $\frac{1}{N_{jet}} \frac{1}{p_T} \frac{dN_{track}}{dp_T}$ are shown respectively for the 20-50, 50-100, and 100-150 GeV jet E_T ranges along with the equivalent background rates from the data. The data fake rate is greater than the Monte Carlo fake rates. Whereas in the data, the number of K_S and tracks per jet for 1.5 GeV $<p_T<10.0$ GeV are 0.0125±0.0003 and 0.2237±0.0003, respectively, the equivalent quantities from the HERWIG+QFL Monte Carlo are only around 0.005 to 0.007 for the background K_S per jet and .1 for the background tracks per jet. The data is approximately a factor of 2.0 higher than the HERWIG+QFL Monte Carlo. One reason for this is believed to be due to multiple interactions. There may be more than one interaction in a given data event whereas every default Monte Carlo event has only a single interaction. Thus, it is possible for the data to have either a K_S or a track originating from a different interaction point near the primary vertex be counted along with the other particles that do come from the primary.

Another reason for the discrepancy may originate from the limitations in characterizing the "fake" jets. Unlike the "real" jets, "fake" jets have neither a jet vertex nor a jet E_T associated with them. Moreover, correcting for the efficiencies

with the curve for the track-embedded K_S (and tracks) inside 20-50 GeV jets may be inappropriate. So if this efficiency is underestimated, then the correction factor might be larger than it should. Consequently, the background in the data would be computed to be too high.

Aside from the overall normalization factor, the shape of the background in the data closely resembles the 100-150 GeV Monte Carlo. This is believed to be so because the data is dominated by jets with E_T between 100-150 GeV. As for the 20-50 GeV and 50-100 GeV Monte Carlo cases having their distributions extending not as far in p_T as the 100-150 GeV Monte Carlo case, this is attributed to the likely possibility that the jets with greater E_T have a higher p_T background.

9.5 Comparing Background with Other Analyses

There are a couple of studies that should be mentioned, and both results have significantly higher track background rates than those stated here, referred to as "study 0", for both the data and HERWIG Monte Carlo.

In the first analysis, denoted by "study 1", [28] [82] [83], the background rate of tracks in dijets is computed by using a pair of "fake" 0.47 cones having the same jet η direction of the leading jet in a given dijet event but having the ϕ component of the "fake" jet rotated by 90° from that of the jet ϕ of the leading jet. Both "fake" 0.47 cones are collected statistically to yield a background rate of approximately 0.5-0.6 tracks per jet in the data.

In another analysis referred to as "study 2" ([84] [85] [86]), the background track rate in "fake" 0.7 cones is reported for all jet events. Likewise, a pair of "fake" jets are 90° in ϕ from the leading jet direction while having the same jet η as the leading jet. However, only the "fake" jet with the lowest E_T deposition in the calorimeter

of the two "fake" jets is considered in the track background rate computation. This track background rate is also calculated to be around 0.5 tracks per jet in the data, and this quantity appears to be constant for all jet E_T.

Both studies 1 and 2 have track background rates (for the data) larger than the 0.2237 ± 0.0003 tracks per jet value stated in study 0 (this analysis). However, these other analyses (study 1 and 2) use different p_T ranges to compute their values. In study 1 ([84] [85] [86]), the p_T range is from 0.4 GeV and above, and in study 2 ([28] [82] [83]), the p_T range is from 0.5 GeV and above. This analysis, study 0, implements a much higher p_T range, from 1.5 GeV to 10.0 GeV. Virturally all of this difference is expected to be between 0.4 GeV (or 0.5 GeV) and 1.5 GeV since the number of tracks above 10.0 GeV is small.

If study 0 implements similar ranges, these results may be contrasted with studies 1 and 2. For 0.4 GeV (0.5 GeV) to 10.0 GeV, this analysis, study 0, gets about 1.1 (0.95) tracks per jet for the data. This extrapolation is carried out into a region where there are no data points, and the uncertainty is large. In addition, multiple interactions included in the data that would increase this rate above the 0.5-0.6 tracks per jet values in study 2 ([28] [82] [83]), and the 0.5 tracks per jet quantity quoted in study 1 ([84] [85] [86]). In any case, even a factor of 2.0 difference in the background rate would only effect the first few p_T bins by at most 5%. There is not another analysis that examines the background K_S rate to make a similar comparison.

Despite the data rates, the HERWIG+Monte Carlo background rates are equivalent. From the other publications described in Chapter 8, the tracks in dijets in study 1 ([73], [74], and [75]) and the tracks in jets in study 2 ([76], [82], and [83]), the HERWIG+QFL track background rates are also quoted. For the former, study

1, the track background rate varies from 0.3 to 0.8 tracks per jet depending on the mass of the dijet, and for the latter, study 2, the background rate is approximately 0.6 tracks per jet. Although both quantities are above the 0.175 ± 0.002 track per jet calculated in study 0 (this study), once the p_T range is adjusted to be consistant, the agreement improves considerably. For p_T between 0.4 GeV and 10.0 GeV, study 0 gets around 0.55 tracks per jet for HERWIG+QFL. This is within the range of the 0.3-0.8 tracks per jet in study 1 ([28] [82] [83]). In addition, for 0.5 GeV to 10.0 GeV, this analysis yields between 0.45 to 0.49 tracks per jet. Again, this value is near the 0.6 tracks per jet quantity quoted in study 2 ([84] [85] [86]).

These differences are not expected to alter the results much since the total background correction is less than 8%, and they may be attributed to the differences in computation of these background rates from analysis to analysis such as the cone size and the definition of jet. The exact details will be spared, but in study 1 ([73], [74], and [75]), the cone-size is 0.47 and the η range is within $|\eta| < 0.7$. Furthermore, in study 2 ([76], [82], and [83]), the jets are defined through charged tracks rather than calorimetry information. Despite this, the background rates agree with the Monte Carlo, and the differences between in the background rate in the data is believed to be due to multiple interactions. The net effect will be small.

9.6   The HERWIG Monte Carlo Results

The number K_S per jet, the number of tracks per jet, and 2.0 times the number of K_S per track are shown for the HERWIG+QFL Monte Carlo after each correction in Tables 9.1-9.3. To render greater detail, in Table 9.1, after the jet E_T "trigger" correction, the number of K_S per jet inside the 20-50 GeV HERWIG Monte Carlo jets is 0.175 ± 0.002. These K_S are contained within jets which are distributed

according to the shape of the jet E_T cross-section. Being HERWIG Monte Carlo K_S , p_T efficiency corrections and the number of tracks per jet trigger adjustments are unnecessary. Hence, the number remains 0.162±0.002 in the next row. After the fake rate has been subtracted out, there are 0.155 ± 0.002 K_S per jet in the 20-50 GeV HERWIG Monte Carlo jets. Note that the tracks per jets behave equivalently in Table 9.2, and 2.0 times the K_S per track are virtually unchanged in Table 9.3.

In comparing the data with the HERWIG+QFL Monte Carlo, Tables 9.1-9.3 will be examined along with Tables 8.1-8.3. First, in Table 9.1, the number of K_S in jets in for 20-50 GeV, 50-100 GeV, and 100-150 GeV cases after all corrections in the HERWIG+QFL Monte Carlo is 0.155±0.002, 0.259±0.001, and 0.313±0.001. Note that there is definately an increase. However, in the data, the number of K_S inside jets is 0.156±0.002, 0.206±0.003, and 0.200±0.003. So, for the data, the K_S production inside jets reaches a plateau despite the agreement for 20-50 GeV. This is not the case with track production inside jets; the HERWIG+QFL and the data agree within 10% for all jet E_T. In addition, from Table 9.2, the number of tracks inside jets from the HERWIG+QFL Monte Carlo increases from 2.839±0.012 to 6.641±0.007 from the 20-50 GeV case to the 100-150 GeV case. Similarly, from Table 8.2, the number of tracks inside jets from the data increases from 2.802±0.002 to 5.957±0.003 from the 20-50 GeV case to the 100-150 GeV case. As a result of the K_S production discrepancy between the data and HERWIG+QFL increasing with jet E_T while the track production is in agreement, the (2^*K_S) per track ratios in Tables 9.3 and 8.3 diverge as well. This will be discussed further in Chapter 10.

At least two other analyses have discussed the topic of the number of tracks per jet. In study 1 ([28] [82] [83]), the number of tracks per jet as a function of dijet mass is examined. Granted there are differences from study 0, such as the

lower 400 MeV track cut among others; nonetheless, for the data, the number of tracks inside a 0.47 cone jet in study 1 increases from $6.1 \pm 0.0 \pm 0.5$ for dijets of mass 82 GeV/c^2 to $10.3 \pm 0.1 \pm 0.7$ for dijets of mass 293 GeV/c^2. Using a similar p_T range (0.4 GeV $<p_T<$ 10.0 GeV) for the data in study 0, the number of tracks per jet is 5.019 ± 0.013, 8.134 ± 0.013, and 8.763 ± 0.010 for 20-50 GeV, 50-100 GeV, and 100-150 GeV jets, respectively. Even though dijets are different objects than jet E_T, the number of tracks per jet appear to be comparable. For HERWIG+QFL and the identical p_T range in study 0, the number of tracks per jet is 4.752 ± 0.034, 7.770 ± 0.020, and 9.715 ± 0.015 for 20-50 GeV, 50-100 GeV, and 100-150 GeV jets, respectively. The important to note that in study 1, the data results are approximately 11% below those from the HERWIG Monte Carlo (not shown for study 1). This is also true for study 0.

The other analysis, study 2 ([87], [88], and [89]) calculates the number of tracks per jet in a manner similar to here, but the jets are computed strictly from tracks instead of calorimetry. Again, the details have no place here since there is an obvious bias of constructing jets from tracks. Now, a 20 GeV jet computed from just tracks would correspond to a much higher E_T jet calculated from the calorimeter. Nevertheless, there are about 6.0 tracks inside a 0.7 cone, 20 GeV p_T jet, and this value increases to 10.0 tracks per jet for 50 GeV p_T jets. This is not necessarily inconsistent with study 0 since the data also deviates from the HERWIG Monte Carlo as jet E_T increases. If study 0 uses the identical p_T (0.5 GeV$<p_T<$ 10.0 GeV) range, the number of tracks per jet is 4.809 ± 0.012, 7.837 ± 0.012, and 8.505 ± 0.010 for 20-50 GeV, 50-100 GeV, and 100-150 GeV jets, respectively. Similiarly, for the HERWIG+QFL results in study 0, the number of tracks per jet is 4.575 ± 0.033, 7.508 ± 0.020, and 9.410 ± 0.014 for 20-50 GeV, 50-100 GeV, and 100-150 GeV jets,

Table 9.1: The number of K_S per Jet in the HERWIG Monte Carlo ($1.5 < p_T < 10.0$ GeV).

After Correction	$\frac{N_{KS}}{jet}$ in 20-50 Jets	$\frac{N_{KS}}{jet}$ in 50-100 Jets	$\frac{N_{KS}}{jet}$ in 100-150 Jets
P_T	0.162 ± 0.002	0.265 ± 0.001	0.319 ± 0.001
Trigger	0.162 ± 0.002	0.265 ± 0.001	0.319 ± 0.001
Fake Rate	0.155 ± 0.002	0.259 ± 0.001	0.313 ± 0.001

Table 9.2: The number of tracks per jet in HERWIG Monte Carlo ($1.5 < p_T < 10.0$ GeV).

After Correction	$\frac{N_{track}}{jet}$ in 20-50 Jets	$\frac{N_{track}}{jet}$ in 50-100 Jets	$\frac{N_{track}}{jet}$ in 100-150 Jets
P_T	2.945 ± 0.012	5.170 ± 0.006	6.749 ± 0.007
Trigger	2.945 ± 0.012	5.170 ± 0.006	6.749 ± 0.007
Fake Rate	2.839 ± 0.012	5.083 ± 0.006	6.641 ± 0.007

Table 9.3: 2.0 times the number of K_S per track in HERWIG Monte Carlo ($1.5 < p_T < 10.0$ GeV).

After Correction	$2\frac{N_{KS}}{N_{track}}$ in 20-50 Jets	$2\frac{N_{KS}}{N_{track}}$ in 50-100 Jets	$2\frac{N_{KS}}{N_{track}}$ in 100-150 Jets
P_T	0.110 ± 0.001	0.102 ± 0.0003	0.095 ± 0.0003
Trigger	0.110 ± 0.001	0.102 ± 0.0003	0.095 ± 0.0003
Fake Rate	0.109 ± 0.001	0.102 ± 0.0003	0.094 ± 0.0003

respectively. Again, the agreement can be seen.

A detailed comparison between the data and HERWIG+QFL for the tracks and K_S production inside jets will occur later in Chapter 10 along with the conclusion.

Chapter 10

Jets: Results and Conclusions

The production of K_S and tracks inside jets will now be elaborated in greater detail. After summarizing the implementation of the p_T, trigger, and background corrections to the p_T curves, the $\frac{1}{N_{jet}} \frac{1}{p_T} \frac{dN_{KS}}{dp_T}$ and $\frac{1}{N_{jet}} \frac{1}{p_T} \frac{dN_{track}}{dp_T}$ spectra from the data and the HERWIG+QFL Monte Carlo are compared. Then, the number of K_S per jet $(\frac{N_{KS}}{jet})$, the number of tracks per jet $(\frac{N_{track}}{jet})$, and the $<p_T>$ for both K_S and tracks in jets are derived from the fit parameters of these spectra. Following this, the fragmentation plots of the K_S in jets are contrasted with e^+e^- results from other experiments. Finally, bringing this analysis to a close, the significance of the measurement in terms of the fragmentation model will be discussed.

10.1 Correcting for Tracks and K_S Inside Jets

As mentioned earlier in Chapter 8, to generate the $\frac{1}{N_{jet}} \frac{1}{p_T} \frac{dN_{track}}{dp_T}$ and $\frac{1}{N_{jet}} \frac{1}{p_T} \frac{dN_{KS}}{dp_T}$ spectra requires many steps and corrections. Once the K_S candidates and tracks in jets meet the selection criteria, the number of candidates with a given mass are grouped according to intervals of p_T. Moreover, prior to subtracting the background, these candidates are weighted by the p_T efficiency corrections and the trigger adjustments simultaneously. By doing this, the resulting background-

217

subtracted curve is already corrected for the p_T and the trigger biases. Note that for the p_T curve, the jet E_T is weighted to have the same shape as the jet cross-section as a function of jet E_T [73] [75] [76]. The fragmentation quantities, grouped into intervals of $\frac{p_T}{JetE_T}$, are also weighted so that the jet E_T has a flat distribution. Thus, by the application of three weights for every candidate (one for the p_T efficiency correction, one for the jet E_T trigger adjustment, and one for the number of tracks trigger effect), the number of K_S within a range of p_T creates a p_T curve needing only to account for the fake rate. As mentioned previously in Chapter 8, through bin-by-bin subtraction of the fake rate p_T curve from the p_T curve, the removal of the background contributions may be accomplished.

In summary, the cuts and the corrections for the tracks and K_S in 20-50 GeV, 50-100 GeV, and 100-150 GeV jets are listed below:

- Track Cuts

    - $|z_{primary}| < 60.0$ cm

    - $z^{rms}_{jet} < 5.0$

    - $|z_{primary} - z_{jet}| < 5.0$ cm

    - $|\eta^{jet}| < 1.0$

    - Tracks are inside the nearest $\Delta R = 0.7$ jet.

    - $|z_{primary} - z_{track}| < 5.0$ cm

    - $|\eta^{track}| < 1.0$

    - $1.5 < p_T^{track} < 10.0$ GeV

    - Weight with the p_T^{track} Efficiency Correction

    - Weight with the Number of Tracks per Jet Trigger Correction

  – Weight with the Jet E_T Trigger Correction

  – Group into bins according to the range of the p_T^{track}

- K_S Cuts

  – K_S candidates within $\Delta R = 0.7$ jet cone

  – $z_{jet}^{rms} < 5.0$

  – $|z_{primary} - z_{jet}| < 5.0$ cm

  – $\chi^2_{KS} < 20.0$

  – $|z_{KS} - z_{primary}| < 3.0$ cm

  – $p_T^{tracks\ from\ KS} > 500$ MeV

  – $|\eta^{KS}| < 1.0$

  – 3D Displacement$^{KS} > 1.0$ cm

  – $\cos\theta_{PD}{}^{KS} > 0.990$

  – $1.5 < p_T^{KS} < 10.0$ GeV

  – Weight with the p_T Efficiency Correction

  – Weight with the Number of Tracks per Jet Trigger Correction

  – Weight with the Jet E_T Trigger Correction

  – Group into bins according to the range of the p_T^{KS}

10.2 Comparing the Data with HERWIG+QFL Monte Carlo

To derive the $\frac{1}{N_{jet}} \frac{1}{p_T} \frac{dN_{KS}}{dp_T}$ and $\frac{1}{N_{jet}} \frac{1}{p_T} \frac{dN_{track}}{dp_T}$ curves, the number of entries in each bin of a weighted background subtracted p_T histogram is divided by the values of

the total number of jets in a given jet E_T range (20-50, 50-100, and 100-150 GeV), the midpoint of the p_T range, and the width of the p_T range. These results are displayed in Figures 10.1-10.6. The data is denoted as points while the overlapping solid curves represent the HERWIG+QFL Monte Carlo results derived Chapter 9.

Similar to the $\frac{E}{N_{event}} \frac{d^3 N_{KS}}{d^3 p}$ spectrum in Chapter 5, the $\frac{1}{N_{jet}} \frac{1}{p_T} \frac{dN_{KS}}{dp_T}$ and $\frac{1}{N_{jet}} \frac{1}{p_T} \frac{dN_{track}}{dp_T}$ plots are fitted with a power law. Each curve here will be fitted from 1.5 to 10.0 GeV on two consecutive occasions. At first 3 free parameters (A,n,p_0) are used, then p_0 is fixed and the spectrum is refitted with only 2 free parameters (A,n). This is done in order to simplify the error calculation. These parameters will be needed to compute the number of K_S and tracks per jet as well as $<p_T>$ for both K_S and tracks in jets.

After fitting the $\frac{1}{N_{jet}} \frac{1}{p_T} \frac{dN_{KS}}{dp_T}$ and $\frac{1}{N_{jet}} \frac{1}{p_T} \frac{dN_{track}}{dp_T}$ plots, the power law with its known parameters are incorporated in the calculation of interesting quantities. To compute the number of K_S $(\frac{N_{KS}}{jet})$ and tracks per jet $(\frac{N_{track}}{jet})$, the power law multiplied by p_T needs to be integrated. Moreover, as for the $<p_T>$ for K_S and tracks in jets, the ratio of the integral of the power law times the square of the p_T and the integral of the power law multiplied by p_T needs to be determined. The limits of integration are altered to generate quantities valid over different ranges of p_T. Equations 10.1 and 10.2 show the equations used to calculate $\frac{N_{KS}}{jet}$ and $\frac{N_{track}}{jet}$ whereas equations 10.3 and 10.4 are implemented in the computation of the $<p_T>$ of the tracks and K_S . The equations are given below:

$$\frac{N_{KS}}{jet} = \int_{1.0 GeV}^{10.0 GeV} \frac{A p_0^n p_T dp_T}{(p_T + p_0)^n} \tag{10.1}$$

$$\frac{N_{track}}{jet} = \int_{1.0 GeV}^{10.0 GeV} \frac{A p_0^n p_T dp_T}{(p_T + p_0)^n} \tag{10.2}$$

$$< p_T^{KS} > = \frac{\int_{1.0GeV}^{10.0GeV} \frac{A p_0^n p_T^2 dp_T}{(p_T + p_0)^n}}{\int_{1.0GeV}^{10.0GeV} \frac{A p_0^n p_T dp_T}{(p_T + p_0)^n}} \tag{10.3}$$

$$< p_T^{track} > = \frac{\int_{1.0GeV}^{10.0GeV} \frac{A p_0^n p_T^2 dp_T}{(p_T + p_0)^n}}{\int_{1.0GeV}^{10.0GeV} \frac{A p_0^n p_T dp_T}{(p_T + p_0)^n}}. \tag{10.4}$$

In Tables 10.1 through 10.6, the $\frac{N_{KS}}{jet}$, $\frac{N_{track}}{jet}$, $<p_T^{KS}>$, and $<p_T^{track}>$ for all three jet E_T ranges are listed for both the data and the HERWIG+QFL Monte Carlo with limits of integration from 1.0 GeV to 10.0 GeV and 1.5 GeV to 10.0 GeV. The results of the data with limits of integration from 1.5 GeV to 10.0 GeV in these tables are consistent with those non-fitted numbers computed in Chapter 8 and Chapter 9.

For the number of tracks inside jets with p_T between 1.5 and 10.0 GeV, the ratio between the results of the data and the HERWIG+QFL Monte Carlo grows from within 5% for 20-50 GeV and 50-100 GeV cases to almost 10% for the 100-150 GeV jets. This analysis is not the first to notice the 10% difference between the tracks in jets in the data and the HERWIG+QFL Monte Carlo for high transverse energy jets.

Since the K_S efficiency may be approximated by the product of two single track efficiencies, one might predict the discrepancy of the data and the HERWIG+QFL Monte Carlo for the production of the K_S inside jets. Doing this, one is led to believe that the data and the HERWIG+QFL Monte Carlo for K_S inside 20-50 GeV and 50-100 GeV jets would be in agreement because the corresponding cases for the tracks inside jets in the data are consistent with the HERWIG+QFL Monte Carlo. Thus, the K_S inside 100-150 GeV jets would be predicted to have the data about 20% (90%*90%=81%, assuming reconstruction efficiency $\sim$100%) lower than the HERWIG+QFL Monte Carlo.

Surprisingly, although the number of K_S inside 20-50 GeV jets in the data (with p_T between 1.5 and 10.0 GeV) agrees to within 5% of the HERWIG+QFL Monte Carlo, the disagreement grows to approximately 20% and 35% for the 50-100 GeV and 100-150 GeV jets, respectively. The number of K_S per jet in the data tends to be lower than what is expected from the HERWIG+QFL Monte Carlo. The disagreement is even 20% greater than what would be expected from a possible inaccuracy in the track efficiency in jets alone.

It is feasible that the data and the HERWIG+QFL Monte Carlo vary because detector efficiency issues, but even so, this is not believed to be the case. Instead, it more likely that the production of the K_S inside jets for the HERWIG Monte Carlo is overestimated, especially at higher and higher jet E_T.

On the other hand, the $<p_T^{track}>$ and $<p_T^{KS}>$ agree to within 5% for all jet E_T (with the exception of the 1.0-10.0 GeV case for K_S where it is within 10%). Consequently, the shape of the HERWIG+QFL Monte Carlo and the data are consistent for tracks and K_S inside jets for all jet E_T (20-150 GeV). Moreover, Figures 10.1-10.6 reflect these observations. Typically, the 1.0 to 10.0 GeV case is within 5% of the 1.5 to 10.0 GeV case, except for the 20-50 GeV case where it is within 10% for the number of K_S .

10.3 Comparing Fragmentation with Other Experiments

One of the motivations of this analysis is to compare the fragmentation function and hadronization of jets from 1.8 TeV $p\bar{p}$ collisions with those of e^+e^- collisions at other center of mass energies. It is expected that just the type and the momenta

of the outgoing partons determine the fragmentation function and hadronization, and that the fragmentation function might scale with the center of mass energy. Typically, the fragmentation function results from e^+e^- machines are quoted in terms of $x_T = \frac{p_{KS}}{p_{beam}}$ and charged kaons. It should be noted that the p_{beam} variable should be $\frac{\sqrt{s}}{2}$, and center of mass collisions at $\sqrt{s}$ usually give rise to back-to-back jets at energies of $\frac{\sqrt{s}}{2}$. On the other hand, the interaction energy of partons in $p\bar{p}$ collisions is only a fraction of the total momenta of proton and antiproton carried by the interaction quarks. In this case, most of this energy for hard-scattering in the central region is given by the jet E_T. Likewise, most of the momenta of the K_S in the central region consists of transverse momenta p_T. Thus, the fragmentation results in this analysis will be presented in terms of $x_T = \frac{p_T}{jetE_T}$. In order to compare with the charged kaons production from e^+e^- collisions, this result needs to be multiplied by a factor of 2 because charged kaons production is assumed to be twice that of K_S production.

There are a few of differences between the generation of the p_T spectra and the fragmentation curves. First, the K_S in jets are booked according to $\frac{p_T}{JetE_T}$ instead of p_T. Also, just the p_T efficiency and the jet E_T trigger weights are applied. As for the jet E_T trigger corrections for the fragmentation plots, the jet E_T spectra is examined at sufficiently narrow intervals. Consequently, the jet E_T of each desired range are adjusted to have a constant distribution. In particular, there are three plots for K_S in jets for the 35-45 GeV, 75-85 GeV, and 115-125 GeV jet E_T ranges.

The K_S candidates are weighted prior to background subtraction, and the number of weighted background subtracted K_S will be plotted against $x_T = \frac{p_T}{jetE_T}$. Neither the number of tracks per jet trigger corrections nor subtractions of background rates in the generation of fragmentation spectra are included. These other

corrections are left out because they are believed to small. To get the $\frac{p_T}{JetE_T}$ per jet, each bin in the $\frac{p_T}{JetE_T}$ curve is divided by the values of the total number of jets in the particular jet E_T range (35-45 GeV, 75-85 GeV, and 115-125 GeV) and the width of the $\frac{p_T}{JetE_T}$ range.

These results are shown in Figures 10.7-10.9 with the approximate e^+e^- results, [9] [77] [78] [79] [80] [81], overlapping the curves. Again, the shapes of the previous data are similar to this analysis although the Tevatron's points appear to be slightly lower. This could be evidence of scaling violations due to the greater collision energies at the Tevatron. To render greater detail, as the collision energy increases, the fragmentation curve is expected to shift to lower values of x_T. Clearly, this may case since the Tevatron's points appear to be lower. The results from all jet E_T ranges (20-50, 50-100, 100-150 GeV) are displayed together in Figure 10.10, and they overlap as they should since regardless of the jet E_T, all Tevatron fragmentation curves are generated at the same collision energy.

10.4 Estimation of Systematics

All errors quoted in this analysis are statistical. Although systematics has not been done in a rigorous sense, over the course of this analysis, a reliable estimation may be made. There are many potential sources of systematics: the variation of cuts, the particulars of the track embedding (such as incorporating the track density distribution), the fitting of the efficiency curves, the fitting of the mass curves, various implementations of trigger and efficiency corrections, and the fitting of the final spectra with a power law. The dominant systematic error is believed to arise from the fitting of the mass plus the background spectra, and it is on the order of 10%. All of the other systematic errors would be expected to alter the results by

around 5%. The overall systematic error, with all of these contributing factors, is believed to be approximately 15%.

10.5 Conclusions

In this thesis, the analysis of K_S production properties inside jets began with studying K_S production in Minimum Bias events. In order to compute the efficiencies, Monte Carlo K_S are embedded into real Minimum Bias data events. The K_S efficiency is found to be strongly correlated to the p_T of the K_S. After implementing the efficiencies, the corrected $c\tau$ of K_S is measured to be 2.6882 ± 0.0124 cm. This is within errors of the accepted value of 2.6786 ± 0.0024 cm. This implies that the generator and the simulator used for the track embedding are very reliable. In addition, the $\frac{E}{N_{event}} \frac{d^3 N_{KS}}{d^3 p}$ spectra as well as the invariant cross-section for K_S production are within 5% of previous analyses. By fitting the $\frac{E}{N_{event}} \frac{d^3 N_{KS}}{d^3 p}$ spectra with a power law, the number of K_S per eta $\frac{dN_{KS}}{d\eta}$ and the average p_T of the K_S $<p_T>$ are also computed. The $\frac{dN_{KS}}{d\eta} = 0.129 \pm 0.005$ and the $<p_T> = 1.022 \pm 0.005$ for K_S where 0.5 GeV$<p_T<$10.0 GeV. Other calculations find these values to be in accord with previous publications.

After verifying the track-embedding Monte Carlo to be valid by studying the K_S production in Minimum Bias events, K_S and track production inside jets became the focus. The efficiencies are calculated by embedding Monte Carlo K_S into jets in real data events, and the K_S efficiency is strongly correlated to the p_T of the K_S as well as jet E_T. Furthermore, the jet triggers also effect both the jet E_T spectra and the number of tracks per jet. By weighting K_S, tracks, and jets by correction factors, the K_S and track production may be determined for a jet distribution which resembles that of the jet E_T cross-section. Background corrections are made

by tallying the number of K_S or tracks inside an arbitrary cone away from all jets. Once this background is subtracted out, efficiency and trigger adjusted $\frac{1}{N_{jet}}$ $\frac{1}{p_T} \frac{dN_{track}}{dp_T}$ and $\frac{1}{N_{jet}} \frac{1}{p_T} \frac{dN_{KS}}{dp_T}$ spectra are determined for K_S and tracks inside jets having E_T ranges of 20-50 GeV, 50-100 GeV, and 100-150 GeV.

Once the $\frac{1}{N_{jet}} \frac{1}{p_T} \frac{dN_{track}}{dp_T}$ and $\frac{1}{N_{jet}} \frac{1}{p_T} \frac{dN_{KS}}{dp_T}$ spectra are fitted with a power law, the number of K_S per jet $\frac{N_{KS}}{jet}$ and the number of tracks per jet $\frac{N_{track}}{jet}$ may be studied and compared with the HERWIG+QFL generator+simulator results. If the fragmentation and hadronization models are accurate, the agreement between the data and the Monte Carlo should be quite close. The HERWIG+QFL Monte Carlo predicts that both the $\frac{N_{KS}}{jet}$ and $\frac{N_{track}}{jet}$ values increase with jet E_T. On the other hand, the data shows that although the $\frac{N_{track}}{jet}$ quantity increases, the $\frac{N_{KS}}{jet}$ value eventually becomes constant. This latter point is in stark contrast to the HERWIG+QFL predictions.

To render greater detail, in the data, for track production in jets, the $\frac{N_{track}}{jet}$ quantity for $1.5 < p_T < 10.0$ GeV grows from 2.816±0.008, 5.107±0.009, 5.972±0.008 for the 20-50 GeV, 50-100 GeV, and 100-150 GeV cases. This is inline with the expectations for the HERWIG+QFL values of 2.785±0.004, 4.999±0.015, 6.536±0.011 for the 20-50 GeV, 50-100 GeV, and 100-150 GeV cases. Even at high jet E_T, the discrepancy is only 10%. The HERWIG+QFL reproduces the data reasonably well.

As for the $\frac{N_{KS}}{jet}$ variable, the data and HERWIG+QFL results diverge with jet E_T. For the data, the $\frac{N_{KS}}{jet}$ quantities are 0.156±0.007 for the 20-50 GeV jets, 0.206±0.011 for the 50-100 GeV jets, and 0.199±0.011 100-150 GeV jets. Clearly, for jets above 50 GeV jets, the $\frac{N_{KS}}{jet}$ value is constant. The HERWIG+QFL values for $\frac{N_{KS}}{jet}$ increase for all measured jet E_T from 0.150±0.008 for the 20-50 GeV jets to 0.254±0.004 for the 50-100 GeV jets and to 0.308±0.005 for the 100-150 GeV

jets. Thus, the HERWIG+QFL values are greater than those of the data by about 5%, 20%, and 35% for the 20-50 GeV, 50-100 GeV, and 100-150 GeV cases. The differences are believed to be due to HERWIG overestimating K_S production inside jets for the higher jet E_T ranges.

In addition, although the number of K_S per jet and the number of tracks increases for both the data and the Monte Carlo, at higher jet E_T, the K_S production levels off for the data. As a result, 2.0 times the number of K_S per track is almost constant for the Monte Carlo whereas it decreases substantially for the data. To give more details, the quantity of 2.0 times the number of K_S per track decreases by approximately a factor of 0.60 from 0.111±0.001 to 0.067±0.001 for the K_S and tracks inside the 20-50 GeV and 100-150 GeV jets. For the HERWIG Monte Carlo, this value is approximately constant, 0.109±0.001 to 0.094±0.0003 for the 20-50 GeV and 100-150 GeV cases, respectively.

The average p_T of the tracks and the K_S, $<p_T^{track}>$ and $<p_T^{KS}>$, are consistent for all three jet E_T ranges. For the tracks with $1.5 < p_T < 10.0$ GeV, the data predicts the $<p_T^{track}>$ of 3.354±0.001 GeV, 3.880±0.001 GeV, and 4.148±0.001 GeV for the 20-50 GeV, 50-100 GeV, and 100-150 GeV cases. Moreover, for the K_S with $1.5 < p_T < 10.0$ GeV, the data predicts the $<p_T^{KS}>$ of 3.809±0.026 GeV, 4.348±0.031 GeV, and 4.458±0.036 GeV for the 20-50 GeV, 50-100 GeV, and 100-150 GeV cases. Over all measured jet E_T ranges, the values for $<p_T^{track}>$ and $<p_T^{KS}>$ increase with jet E_T, and the data and the HERWIG+QFL Monte Carlo are within a few percent of each other. Consequently, the fragmentation model in HERWIG predictions are valid.

In contrasting the fragmentation functions of the Tevatron with those from e^+e^- experiments, the overall shapes of the fragmentation distributions are in fair agree-

ment. However, in general, the Tevatron data is lower than the e^+e^- data. The fragmentation spectra for all of the jet E_T ranges overlap for the Tevatron, and this indicates that fragmentation functions for the Tevatron are independent of jet E_T.

10.6 Overview

Since quarks and gluons have never been observed in isolation, various fragmentation models have attempted to address how these partons are converted into mesons and baryons. These groups of hadrons directed in region a phase space produced from a fragmenting parton are called "jets". Through the study of particle production within jets, greater insight to the particulars of the fragmentation process may be tested. Most of the fragmentation data comes from e^+e^- collisions, and these theories are also applied to those from $p\bar{p}$ collisions. To do so, many models assume that only the type and kind of outgoing parton from an interaction, rather than the process itself, governs the fragmentation process. In particular, an outgoing parton from a hard-scattering process will shower into other partons, and this is explained with perturbative QCD down to an energy scale of around a few hundred MeV.

At this point, in order to describe how groups of gluons and quarks are transformed into mesons and baryons, various hadronization models must be implemented. There are two major types of hadronization models: the string and the cluster model. The string model is based upon the breaking of strong force lines from separating quarks into quark-antiquark pairs, and the cluster model consists of grouping and decaying clusters of quarks and gluons in regions of phase space. Both of these models predict that strange quark production (and particles containing strange quarks) will be suppressed. In this analysis, charged particle and strangeness production in the data will be compared with HERWIG, an event gen-

erator based upon the cluster model. Moreover, strangeness production will be contrasted with e^+e^- experiments. Due to the higher mass of the strange quarks, studies in strange quark production reveal additional information as to how partons are converted into hadrons that is not otherwise provided through the examination of the fragmentation of only the lighter up and down quarks.

It is found that HERWIG generates too many tracks and K_S inside high E_T jets. However, the discrepancy between the data and HERWIG may not all be attributed to an overall discrepancy in track production inside jets. Through comparing K_S fragmentation functions from $p\bar{p}$ collisions with those of other experiments, the premise of fragmentation depending only upon the type and the energy of the outgoing parton is tested. In addition, possible scaling violations may be observed. The Tevatron $p\bar{p}$ results are below those from e^+e^- machines. Also, the shapes of the fragmentations is in fair agreement, but conclusions as to the existence of scaling violations are indeterminate.

This study indicates that the HERWIG cluster hadronization model needs to be adjusted in regard to strangeness and track production for high E_T jets, though $<p_T>$ of K_S and tracks inside jets are consistent.

Table 10.1: The $\frac{N_{particle}}{jet}$ and $<p_T>$ values for tracks and K_S inside 20-50 GeV jets in the data. Systematic errors are not included.

	tracks in 20-50 Jets	K_S in 20-50 Jets
Fit Range	$1.5<p_T<10.0$GeV	$1.5<p_T<10.0$ GeV
Function Fitted	$\frac{Ap_0^n}{(p_0+p_T)^n}$	$\frac{Ap_0^n}{(p_0+p_T)^n}$
Resulting Fit Parameters	$A = 10.313 \pm 0.022$ $n = 5.345 \pm 0.003$ $p_0 = 2.826(fixed)$	$A = 0.155 \pm 0.005$ $n = 6.845 \pm 0.076$ $p_0 = 6.583(fixed)$
$\frac{N_{particle}}{jet}$ from 1.0-10.0 GeV	3.725 ± 0.010	0.185 ± 0.008
$\frac{N_{particle}}{jet}$ from 1.5-10.0 GeV	2.816 ± 0.008	0.156 ± 0.007
$<p_T>$ from 1.0-10.0 GeV	2.838 ± 0.001	3.404 ± 0.029
$<p_T>$ from 1.5-10.0 GeV	3.354 ± 0.001	3.809 ± 0.026

Table 10.2: The $\frac{N_{particle}}{jet}$ and $<p_T>$ values for tracks and K_S inside 20-50 GeV jets in HERWIG Monte Carlo. Systematic errors are not included.

	tracks in 20-50 Jets	K_S in 20-50 Jets
Fit Range	$1.5<p_T<10.0$ GeV	$1.5<p_T<10.0$ GeV
Function Fitted	$\frac{Ap_0^n}{(p_0+p_T)^n}$	$\frac{Ap_0^n}{(p_0+p_T)^n}$
Resulting Fit Parameters	$A = 7.985 \pm 0.048$ $n = 5.821 \pm 0.009$ $p_0 = 3.493(fixed)$	$A = 0.801 \pm 0.031$ $n = 3.606 \pm 0.029$ $p_0 = 1.296(fixed)$
$\frac{N_{particle}}{jet}$ from 1.0-10.0 GeV	3.625 ± 0.028	0.194 ± 0.010
$\frac{N_{particle}}{jet}$ from 1.5-10.0 GeV	2.785 ± 0.023	0.150 ± 0.008
$<p_T>$ from 1.0-10.0 GeV	2.883 ± 0.004	3.137 ± 0.024
$<p_T>$ from 1.5-10.0 GeV	3.378 ± 0.004	3.694 ± 0.021

Table 10.3: The $\frac{N_{particle}}{jet}$ and $<p_T>$ values for tracks and K_S inside 50-100 GeV jets in the data. Systematic errors are not included.

	tracks in 50-100 Jets	K_S in 50-100 Jets
Fit Range	$1.5<p_T<10.0$ GeV	$1.5<p_T<10.0$ GeV
Function Fitted	$\frac{Ap_0^n}{(p_0+p_T)^n}$	$\frac{Ap_0^n}{(p_0+p_T)^n}$
Resulting Fit Parameters	$A = 16.448 \pm 0.022$ $n = 3.503 \pm 0.001$ $p_0 = 1.511(fixed)$	$A = 0.163 \pm 0.006$ $n = 3.805 \pm 0.049$ $p_0 = 3.259(fixed)$
$\frac{N_{particle}}{jet}$ from 1.0-10.0 GeV	6.351 ± 0.011	0.236 ± 0.012
$\frac{N_{particle}}{jet}$ from 1.5-10.0 GeV	5.107 ± 0.009	0.206 ± 0.011
$<p_T>$ from 1.0-10.0 GeV	3.362 ± 0.001	3.961 ± 0.035
$<p_T>$ from 1.5-10.0 GeV	3.880 ± 0.001	4.348 ± 0.031

Table 10.4: The $\frac{N_{particle}}{jet}$ and $<p_T>$ values for tracks and K_S inside 50-100 GeV Jets in HERWIG Monte Carlo. Systematic errors are not included.

	tracks in 50-100 Jets	K_S in 50-100 Jets
Fit Range	$1.5<p_T<10.0$ GeV	$1.5<p_T<10.0$ GeV
Function Fitted	$\frac{Ap_0^n}{(p_0+p_T)^n}$	$\frac{Ap_0^n}{(p_0+p_T)^n}$
Resulting Fit Parameters	$A = 13.639 \pm 0.029$ $n = 3.562 \pm 0.002$ $p_0 = 1.669(fixed)$	$A = 0.309 \pm 0.003$ $n = 3.591 \pm 0.011$ $p_0 = 2.422(fixed)$
$\frac{N_{particle}}{jet}$ from 1.0-10.0 GeV	6.162 ± 0.017	0.298 ± 0.004
$\frac{N_{particle}}{jet}$ from 1.5-10.0 GeV	4.999 ± 0.015	0.254 ± 0.004
$<p_T>$ from 1.0-10.0 GeV	3.407 ± 0.001	3.774 ± 0.009
$<p_T>$ from 1.5-10.0 GeV	3.910 ± 0.001	4.204 ± 0.007

Table 10.5: The $\frac{N_{particle}}{jet}$ and $<p_T>$ values for tracks and K_S inside 100-150 GeV Jets in the data. Systematic errors are not included.

	tracks in 100-150 Jets	K_S in 100-150 Jets
Fit Range	$1.5<p_T<10.0$ GeV	$1.5<p_T<10.0$ GeV
Function Fitted	$\frac{Ap_0^n}{(p_0+p_T)^n}$	$\frac{Ap_0^n}{(p_0+p_T)^n}$
Resulting Fit Parameters	$A = 13.547 \pm 0.014$ $n = 3.107 \pm 0.001$ $p_0 = 1.419(fixed)$	$A = 0.084 \pm 0.003$ $n = 5.749 \pm 0.093$ $p_0 = 7.815(fixed)$
$\frac{N_{particle}}{jet}$ from 1.0-10.0 GeV	7.161 ± 0.009	0.221 ± 0.012
$\frac{N_{particle}}{jet}$ from 1.5-10.0 GeV	5.972 ± 0.008	0.199 ± 0.011
$<p_T>$ from 1.0-10.0 GeV	3.666 ± 0.001	4.135 ± 0.040
$<p_T>$ from 1.5-10.0 GeV	4.148 ± 0.001	4.458 ± 0.036

Table 10.6: The $\frac{N_{particle}}{jet}$ and $<p_T>$ values for tracks and K_S inside 100-150 GeV jets in HERWIG Monte Carlo. Systematic errors are not included.

|	tracks in 100-150 Jets	K_S in 100-150 Jets
Fit Range	$1.5<p_T<10.0$ GeV	$1.5<p_T<10.0$ GeV
Function Fitted	$\frac{Ap_0^n}{(p_0+p_T)^n}$	$\frac{Ap_0^n}{(p_0+p_T)^n}$
Resulting Fit Parameters	$A = 17.172 \pm 0.023$ $n = 2.994 \pm 0.001$ $p_0 = 1.239(fixed)$	$A = 0.383 \pm 0.004$ $n = 2.947 \pm 0.009$ $p_0 = 1.717(fixed)$
$\frac{N_{particle}}{jet}$ from 1.0-10.0 GeV	7.866 ± 0.012	0.355 ± 0.006
$\frac{N_{particle}}{jet}$ from 1.5-10.0 GeV	6.536 ± 0.011	0.308 ± 0.005
$<p_T>$ from 1.0-10.0 GeV	3.664 ± 0.001	3.987 ± 0.009
$<p_T>$ from 1.5-10.0 GeV	4.156 ± 0.001	4.411 ± 0.008
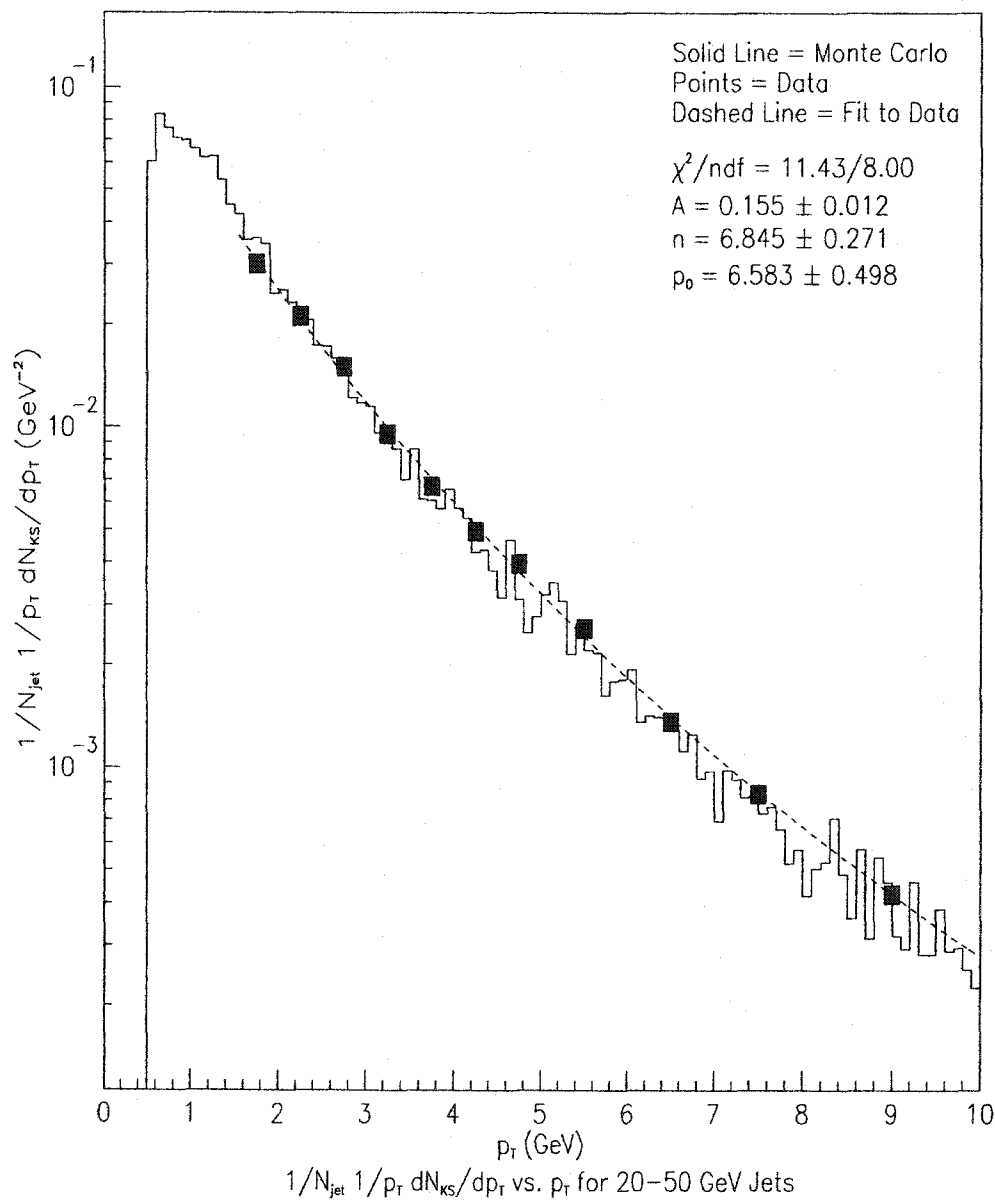
Figure 10.1: The $\frac{1}{N_{jet}} \frac{1}{p_T} \frac{dN_{KS}}{dp_T}$ spectrum K_S inside 20-50 GeV jets. Both the data and the Monte Carlo have been corrected for trigger and background effects. The errors on the HERWIG Monte Carlo are 0.0016, 0.0003, and 0.0002 at 2.0 GeV, 5.0 GeV, and 7.0 GeV, respectively. Systematic errors are not included.
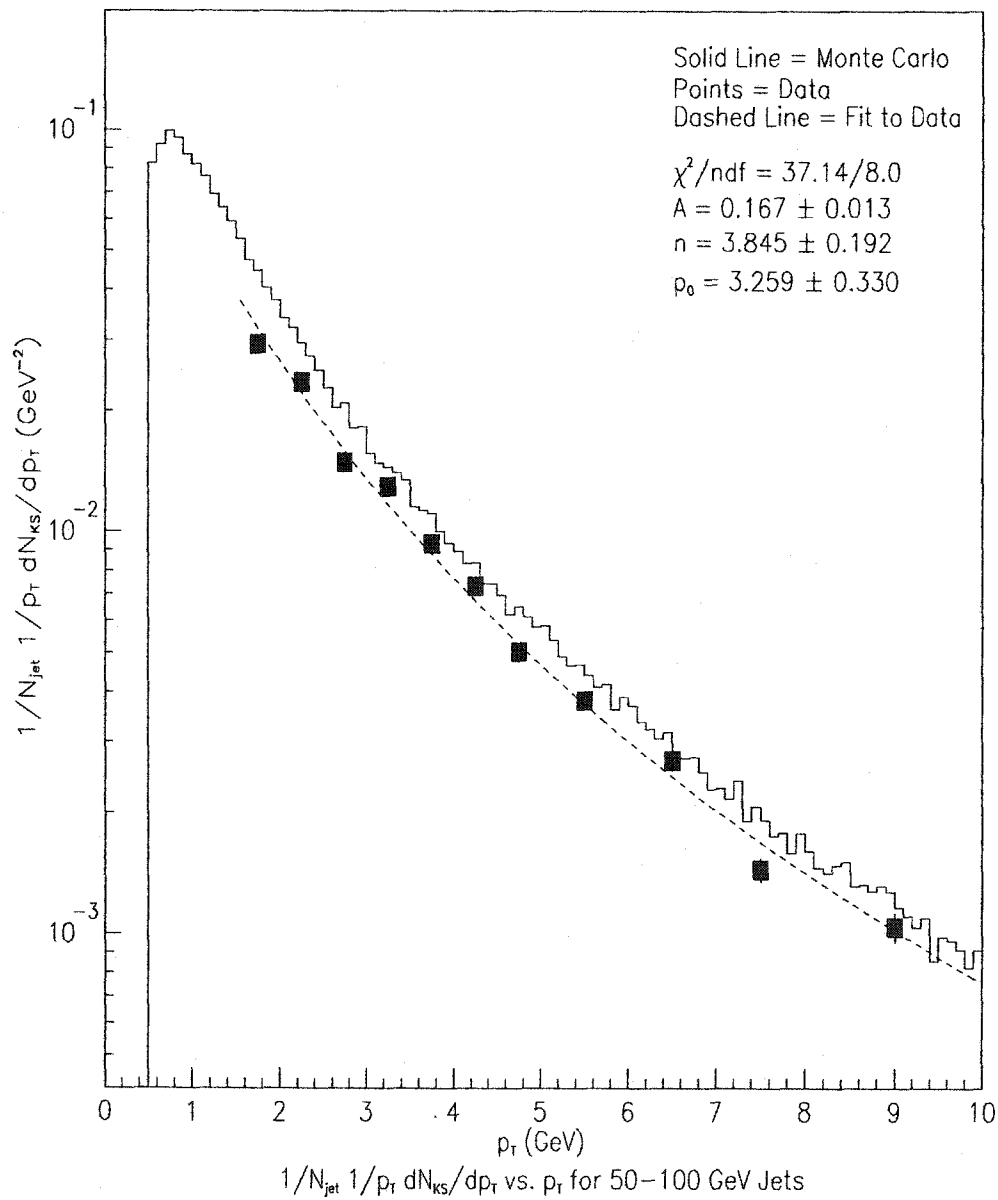
Solid Line = Monte Carlo
Points = Data
Dashed Line = Fit to Data

$\chi^2/ndf = 37.14/8.0$
$A = 0.167 \pm 0.013$
$n = 3.845 \pm 0.192$
$p_0 = 3.259 \pm 0.330$

$1/N_{jet}$ $1/p_T$ dN_{KS}/dp_T vs. p_T for 50−100 GeV Jets

Figure 10.2: The $\frac{1}{N_{jet}} \frac{1}{p_T} \frac{dN_{KS}}{dp_T}$ spectrum for K_S inside 50-100 GeV jets. Both the data and the Monte Carlo have been corrected for trigger and background effects. The errors on the HERWIG Monte Carlo are 0.0009, 0.0002, and 0.0001 at 2.0 GeV, 5.0 GeV, and 7.0 GeV, respectively. Systematic errors are not included.
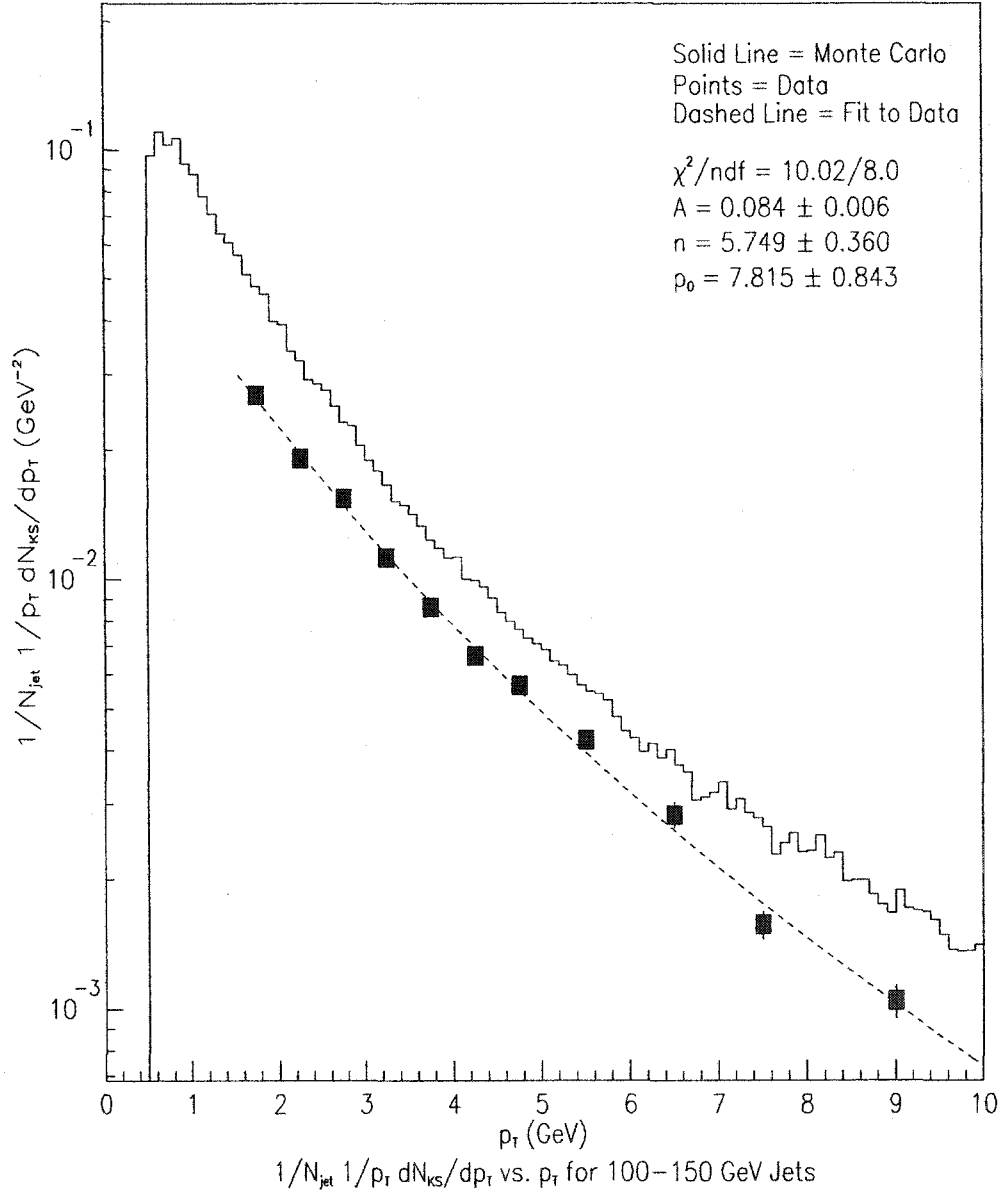
Solid Line = Monte Carlo
Points = Data
Dashed Line = Fit to Data

$\chi^2/ndf = 10.02/8.0$
$A = 0.084 \pm 0.006$
$n = 5.749 \pm 0.360$
$p_0 = 7.815 \pm 0.843$

$1/N_{jet}$ $1/p_T$ dN_{KS}/dp_T vs. p_T for 100–150 GeV Jets

Figure 10.3: The $\frac{1}{N_{jet}} \frac{1}{p_T} \frac{dN_{KS}}{dp_T}$ spectrum for K_S inside 100-150 GeV jets. Both the data and the Monte Carlo have been corrected for trigger and background effects. The errors on the HERWIG Monte Carlo are 0.0009, 0.0002, and 0.0001 at 2.0 GeV, 5.0 GeV, and 7.0 GeV, respectively. Systematic errors are not included.
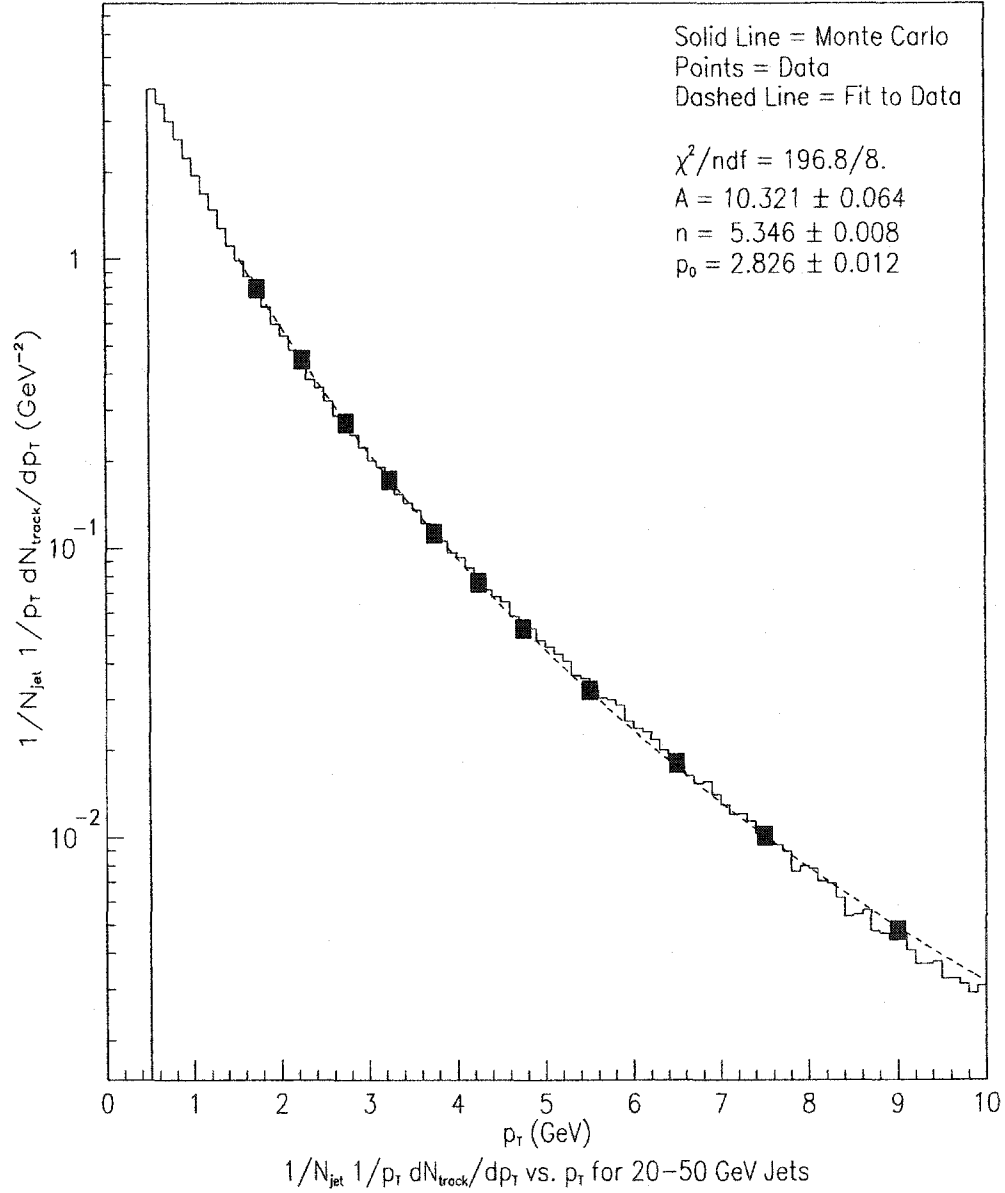
Figure 10.4: The $\frac{1}{N_{jet}}\frac{1}{p_T}\frac{dN_{track}}{dp_T}$ spectrum for tracks inside 20-50 GeV jets. Both the data and the Monte Carlo have been corrected for trigger and background effects. The errors on the HERWIG Monte Carlo are 0.0065, 0.0011, and 0.0005 at 2.0 GeV, 5.0 GeV, and 7.0 GeV, respectively. Systematic errors are not included.
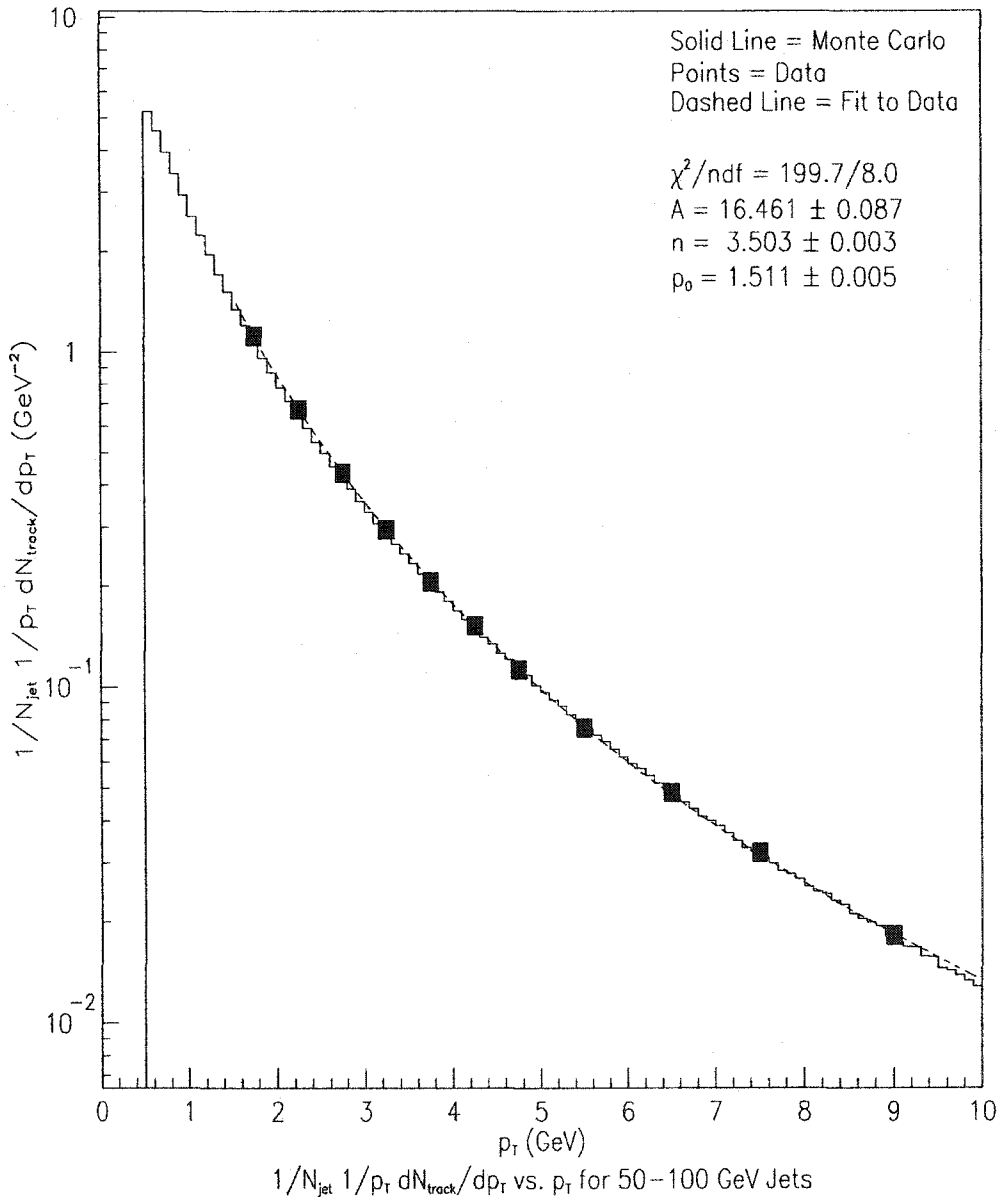
Solid Line = Monte Carlo
Points = Data
Dashed Line = Fit to Data

$\chi^2/\mathrm{ndf} = 199.7/8.0$
A = 16.461 ± 0.087
n = 3.503 ± 0.003
p_0 = 1.511 ± 0.005

$1/N_{jet}\ 1/p_T\ dN_{track}/dp_T$ vs. p_T for 50–100 GeV Jets

Figure 10.5: The $\frac{1}{N_{jet}}\ \frac{1}{p_T}\ \frac{dN_{track}}{dp_T}$ spectrum for tracks inside 50-100 GeV jets. Both the data and the Monte Carlo have been corrected for trigger and background effects. The errors on the HERWIG Monte Carlo are 0.0034, 0.0007, and 0.0004 at 2.0 GeV, 5.0 GeV, and 7.0 GeV, respectively. Systematic errors are not included.
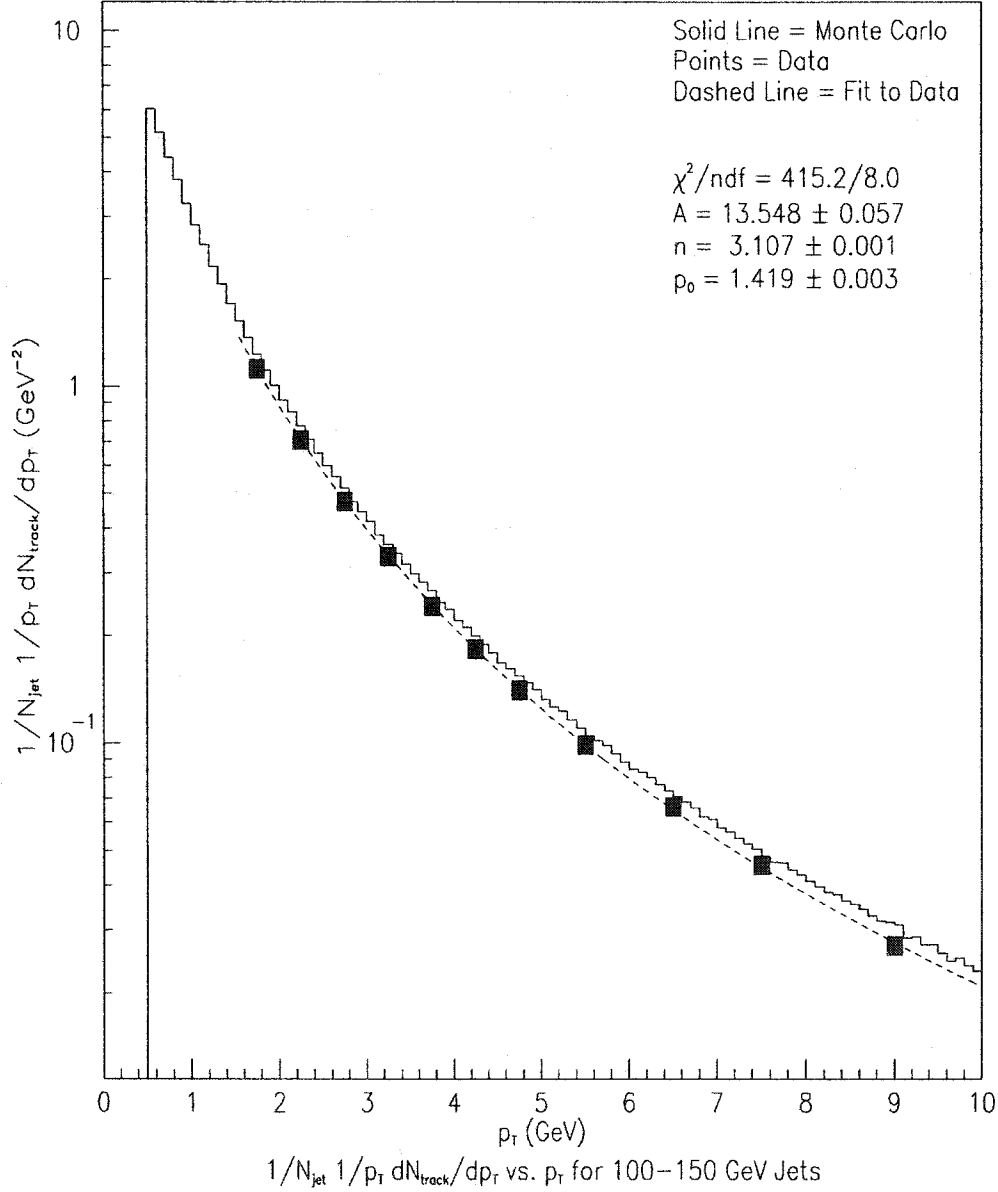
Figure 10.6: The $\frac{1}{N_{jet}} \frac{1}{p_T} \frac{dN_{track}}{dp_T}$ spectrum for tracks inside 100-150 GeV jets. Both the data and the Monte Carlo have been corrected for trigger and background effects. The errors on the HERWIG Monte Carlo are 0.0039, 0.0009, and 0.0005 at 2.0 GeV, 5.0 GeV, and 7.0 GeV, respectively. Systematic errors are not included.
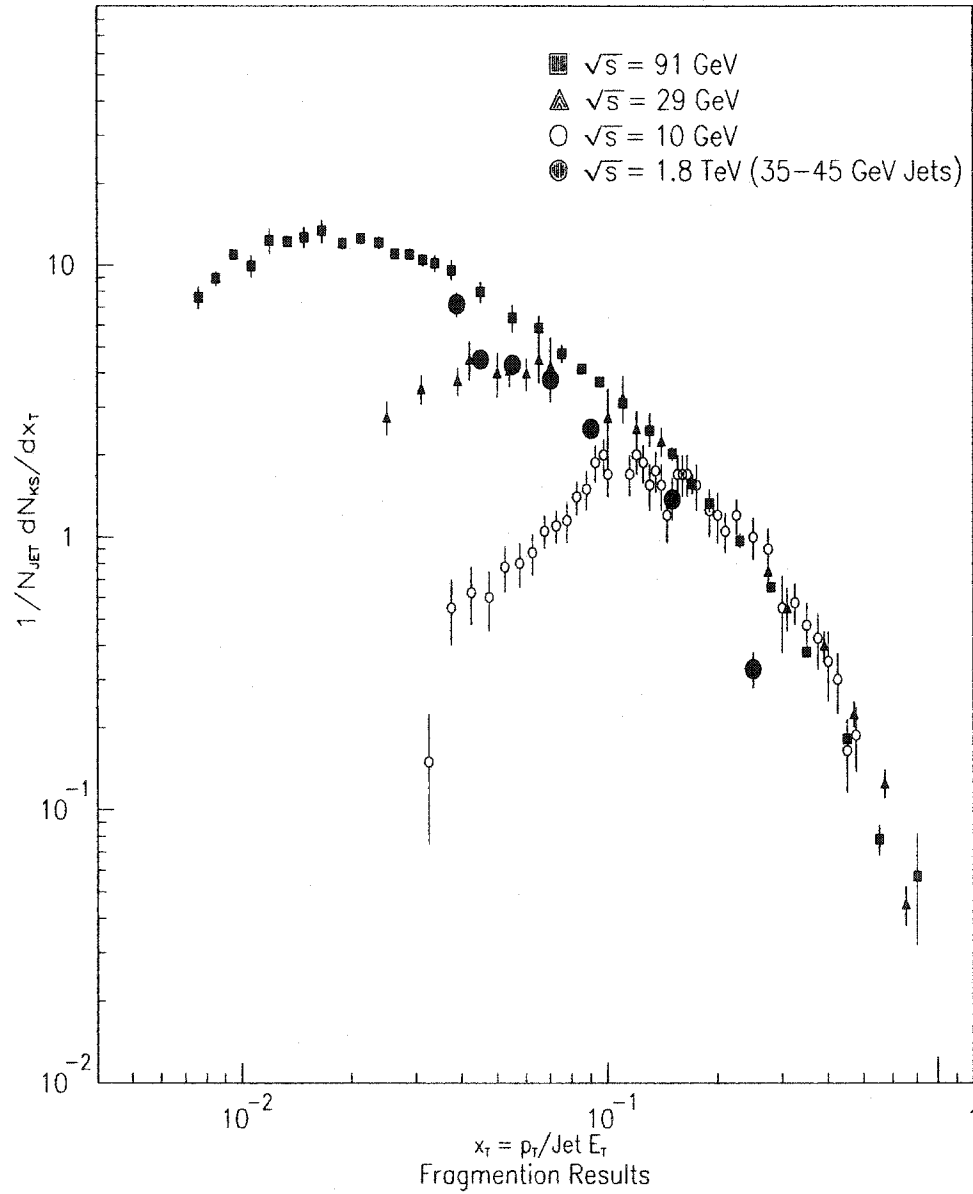
Figure 10.7: The fragmentation spectrum K_S inside 20-50 GeV jets. The solid circular symbols are the $p\bar{p}$ results whereas the triangles, the squares, and hollow circles represent the results from e^+e^- collisions. The data has been corrected for the trigger effect. Systematic errors are not included.
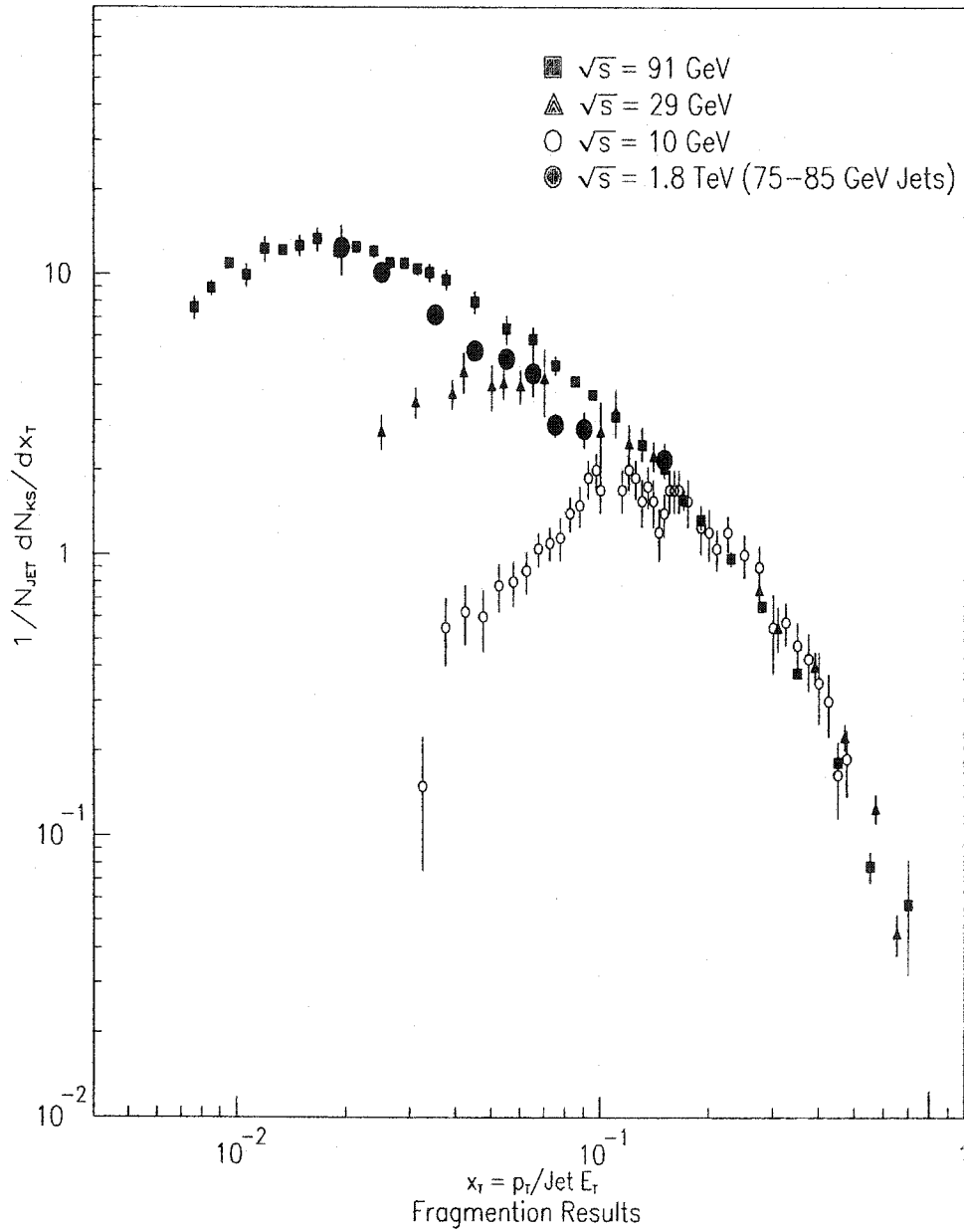
Figure 10.8: The fragmentation spectrum K_S inside 50-100 GeV jets. The solid circular symbols are the $p\bar{p}$ results whereas the triangles, the squares, and hollow circles represent the results from e^+e^- collisions. The data has been corrected for the trigger effect. Systematic errors are not included.

Figure 10.9: The fragmentation spectrum K_S inside 100-150 GeV jets. The solid circular symbols are the $p\bar{p}$ results whereas the triangles, the squares, and hollow circles represent the results from e^+e^- collisions. The data has been corrected for the trigger effect. Systematic errors are not included.
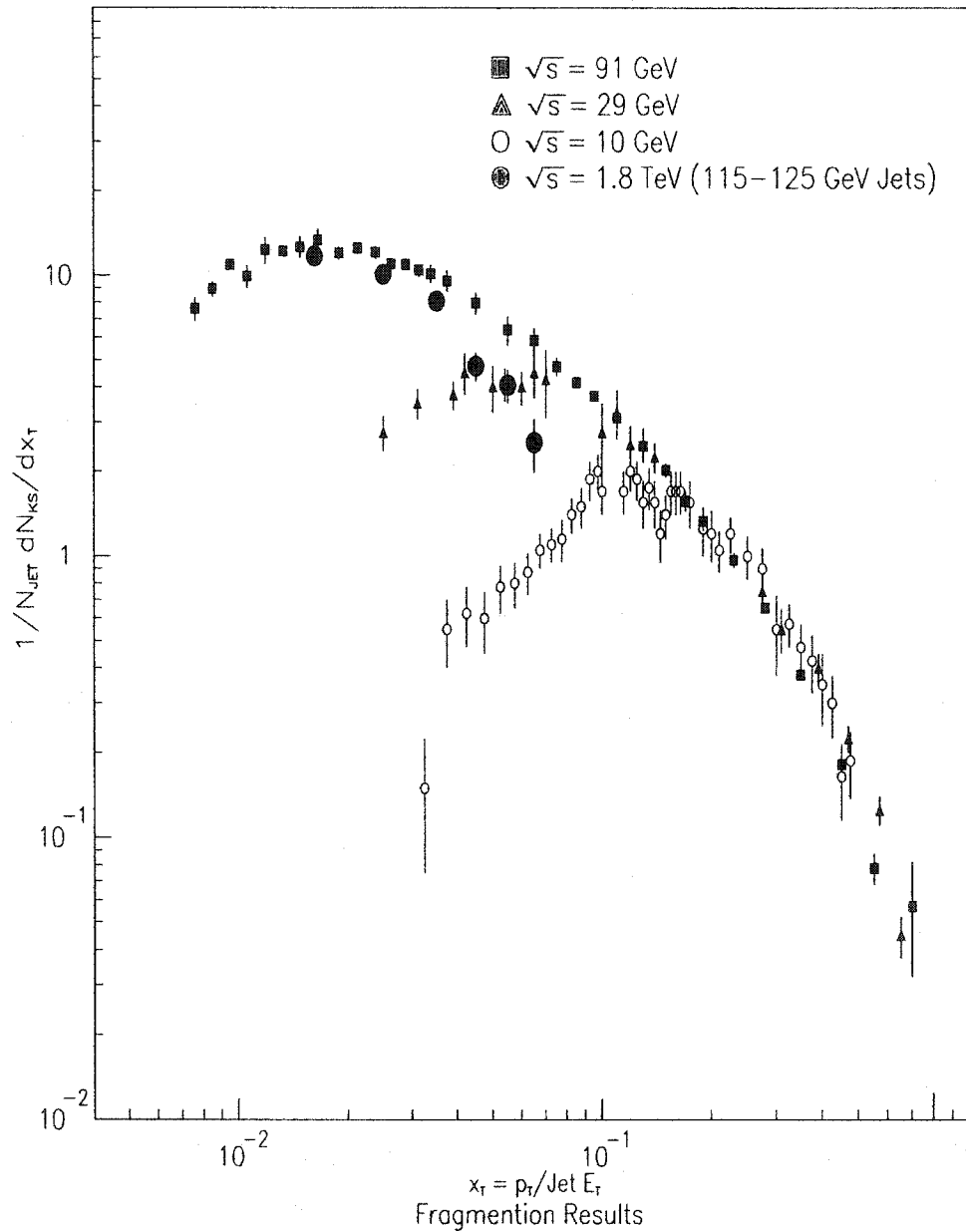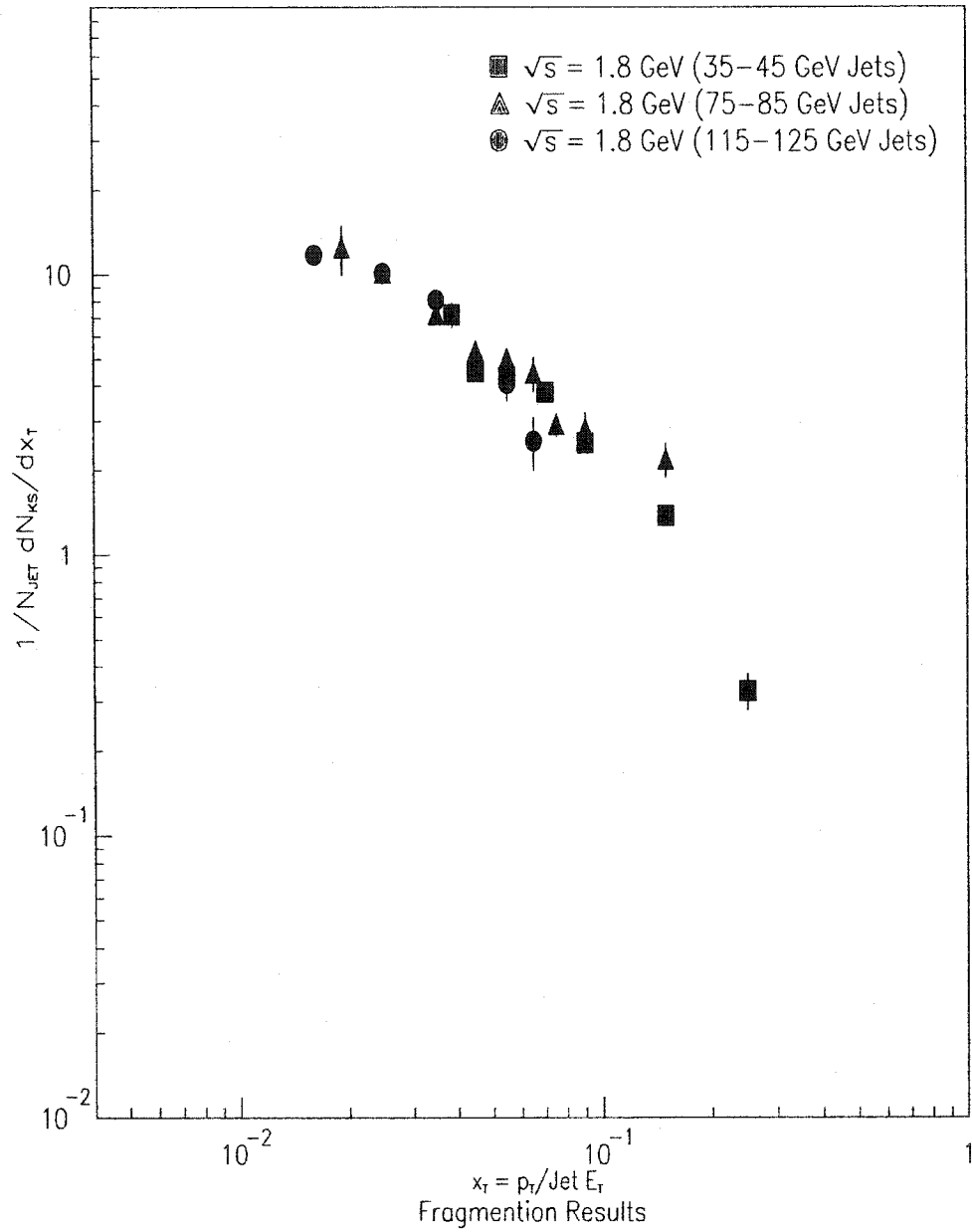
Figure 10.10: The fragmentation spectrum tracks inside 20-50,50-100,100-150 GeV jets. The data has been corrected for the trigger effect. Systematic errors are not included.

Bibliography

[1] G.D. Rochester and C.C. Butler, "Evidence for the Existence of New Unstable Elementary Particles", Nature 160:855-857, 1947.

[2] C. Powell et al., "Observations with Electron Sensitive Plates Exposed to Cosmic Radiation", Nature 163:82, 1949.

[3] David Griffiths, "Introduction to Elementary Particles", John Wiley & Sons, 1987

[4] M. Gell-Mann, Phys. Lett. 8, 218(1964); G. Zweig, CERN-8419-TH-412 (1964).

[5] B.R. Martin, G. Shaw, "Particle Physics", John Wiley & Sons, 1992.

[6] D.Cronin-Hennessy, CDF thesis - "Tests of perturbative QCD in W + jets events produced in $\sqrt{s} = 1.8\ TeV\ \bar{p}p$ collisions", 1997.

[7] J.R.Dittmann, CDF thesis - "Measurement of the W + $\leq$ 1 jet cross section in proton-antiproton collisions at $\sqrt{s} = 1.8\ TeV$, 1998.

[8] M. Brozovic, CDF thesis - "Studies of the WZ Production Associated with Direct Photons, 2002.

[9] C. Caso et al. (Particle Data Group), The European Physical Journal C3(1998)

[10] Leslie S. Groer, CDF thesis - "A Search for Charged Higgs Boson Decays of the Top Quark Using Hadronic Decays of the Tau Lepton, in Proton-Antiproton Collisions at $\sqrt{s}$=1.8 TeV at CDF, 1998.

[11] Michael Schmelling, "Status of the Strong Coupling Constant", Plenary talk given at the XXVIII Intern. Conf. on High Energy Physics, Warsaw, July 25-31, 1996.

[12] W. Bardeen et al., Phys. Rev. D. 18, 3998 (1978).

[13] CCFR Collaboration: W.G. Seligman et al., Phys. Rev. Lett. 79, 1213 (1997); NMC Collaboration: M. Arneodo et al., Phys. Lett. B309, 222 (1993); L.W. Whitlow, Ph.D. thesis, SLAC Report 357 (1990).

[14] S. L. Glashow et al., Phys. Rev. D2, 1285(1970); S. Weinberg, Phys. Rev. Lett. 19, 1264 (1967); A. Salam, p. 367 of Elementary Particle Theory, Almquist and Wiksells, Stockholm (1969).

[15] G. Arnison et al., Phys. Lett. 122B, 103 (1983).

[16] M. Banner et al, Phys. Lett. B 122, 476 (1983).

[17] G. Arnison et al., Phys. Lett. 126B, 398 (1983).

[18] P. Bagnaia et al, Phys. Lett. B 129, 130 (1983).

[19] C. Caso et al, European Physical Journal C3, 1 (1998).

[20] V. Berger, R. Phillips, "Collider Physics", Addison-Wesley, 1987.

[21] B. Webber, "Fragmentation and Hadronization", e-conference C990809.

[22] B. Webber, P. Nason, and O. Biebel, "Jet Fragmentation in e^+e^- Annihilation", hep-ph/0109282, Nov 2001.

[23] L. N. Lipatov, Sov. J. Nucl. Phys. 20, 95 (1975); V.N. Gribov and L.N. Lipatov, Sov. J. Nucl. Phys. 15, 438 (1972); G. Altarelli and G. Parisi, Nucl. Phys. B126, 298 (1977); Yu.L. Dockshitzer, Sov. Phys. JETP 46, 641 (1977).

[24] D. J. Fox et al., Phys. Rev. Lett 33, 494 (1979).

[25] V.N. Gribov and L.N. Lipatov, Sov. J. Nucl. Phys. 15, 438 (1972); L.N. Lipatov, Sov. J. Nucl. Phys. 20, 94 (1975); G. Altarelli and P. Parisi, Nucl. Phys. B 126, 298 (1977); Yu. L. Dokshitzer, Sov. Phys. JETP, 46, 641 (1977).

[26] Yu. L. Dokshitzer and S. L. Troyan, Proc. 19th Winter School of the LNPI, Vol. I, p. 144; A. H. Mueller, Nucl. Phys. B 213, 85 (1983).

[27] Yu. Dokshitzer, S. Troyan, XIX Winter School of LNPI, vol. 1, p. 144 (1984); A. H. Mueller, Nucl. Phys. B 213, 85 (1983).

[28] A.N. Safonov, CDF thesis - "Jet Fragmentation and Predictions of the Resummed Perturbative QCD", 2001

[29] X. Artru and G. Mennessier, Nucl. Phys. B70, 93 (1974); B. Andersson, G. Gustafson, G. Ingelman, T. Sjostrand, Phys. Reports 97, 31 (1983).

[30] Ya. I. Azimonv, Yu. Dokshitzer, V. Khoze, and S. Troyan, Z. Phys. C 27, 65 (1985).

[31] Marechesini et al., HERWIG v 5.1 a Monte Carlo generator that simulates the initial and final state radiation and hadronization, 1992.

[32] V.S. Fadin, Sov. Journ. Nucl. Phys. 37, 245 (1983).

[33] G. Marchesini et al., Comp. Phys. Comm. 67, 465 (1992); G. Corcella et al., JHEP 0101, 010 (2001).

[34] Torbjorn Sjostrand, "PYTHIA v5.7" and "JETSET 7.4" Physics and Manual, Comput. Phys. Commun. **82**, 74 1994.

[35] CDF collaboration, "The Collider Detector at Fermilab"- A Compilation of Articles Reprinted from Nuclear Instruments and Methods in Physics Research, 1988.

[36] K. Burkett, "Trigger Tables", 1995.

[37] E. Buckley-Geer and S. Lammel, "How to Find Out What Run1B Data is Available", 1994.

[38] Anwar Ahmad Bhatti CDF note 3642

[39] Anwar Ahmad Bhatti CDF note 5286

[40] T. Daniels, CDF thesis - "Charmoniun Production in $p\bar{p}$ Collisions at $\sqrt{s} = 1.8$ TeV$1800GeV$", 1997

[41] M.H. Schub, CDF thesis - "Strange Particle Production in Proton-Antiproton Collisions at Center of Mass Energies of 630 GeV and 1800 GeV, 1989

[42] J.B. Gonzalex, J. G. Heinrich, N. S. Lockyer CDF note 3010

[43] M. Deninno, N. Moggi, F. Rimondi, CDF note 6075

[44] T. A. Keaffaber, CDF thesis - "Measurement of the B^+ Meson Cross Section in Proton-Antiproton Collisions at 1.8 TeV Using the Fully Reconstructed Decay $B^+ \rightarrow J/\psi K^+$", 2000

[45] J. Marriner CDF note 1996

[46] N. Moggi, F. Rimondi CDF note 5575

[47] S. Oh and C. Wang CDF note 4343

[48] T. Devlin CDF note 4205

[49] P. Perchonok, fakeevent.cdf, 1995

[50] CDF collaboration, CDF detector simulator CDFSIM

[51] N. Moggi, F. Rimondi CDF note 6043

[52] F. Bedeschi and A. Mukherjee, qtrkpr.cdf, 1993

[53] A. Caner and A. Mukherjee, ctaddh.cdf, 1994

[54] M.W. Bailey, A. F. Garinkel, S. M. Tkaczyk CDF note 2815

[55] Andreas Warburton CDF note 4139

[56] Todd A. Keaffaber, Jonathan D. Lewis, Mark W. Bailey, Daniela Bortoletto, Slawek Tkaczyk, Arthur F. Garfinkel CDF note 4768

[57] A. Caner, A. Mukherjee, A. Yagil CDF note 2363

[58] William Trischuk, Andreas Warburton CDF note 4423

[59] Ting Miao CDF note 3843

[60] Petar Maksimovic, G. Bauer, J. Friedman, T. Shah, P. Sphicas, J. Tseng CDF note 4487

[61] Fumihiko Ukegaw CDF note 5204

[62] Personal Correspondence with M. Kirk, P. Maksimovic, and S. Oh on separate occassions.

[63] "Measurement of B Meson Lifetimes using Fully Reconstructed B Decays Produced in $p\bar{p}$ Collisions at $\sqrt{s} = 1.8$ TeV", D. Acosta et al., The CDF Collaboration, Phys. Rev. D65, 092009 (2002).

[64] "B Lifetimes, Mixing and CP Violation at CDF", M. Paulini, Int. J. Mod. Phys. A14, 2791 (1999).

[65] "K_S production in $p\bar{p}$ interactions at $\sqrt{s} = 630$ and 1800 GeV", F. Abe et al., The CDF Collaboration, Phys. Rev. D 40, 3791 (1989).

[66] "Topology of three-jet events in $p\bar{p}$ Collisions at $\sqrt{s} = 1.8$ TeV", Phys. Rev. D 45,1448 (2001)

[67] B. Flaugher et al CDF note 2902

[68] N. Eddy CDF note 3534

[69] J.R. Dittmann CDF note 4001

[70] L. Galtieri et al CDF note 3253

[71] Anwar Ahmad Bhatti CDF note 4440

[72] Anwar Ahmad Bhatti CDF note 5285

[73] "Measurement of the Inclusive Jet Cross Section in $p\bar{p}$ Collisions at $\sqrt{s} = 1.8\ TeV$", Phys. Rev. D64,032001(2001)

[74] Anwar Bhatti, 'CDF note 5108

[75] Anwar Bhatti, CDF note 4678

[76] Anwar Bhatti and B. Flaugher, CDF note 4890

[77] R. Akers et al., Z. Phys. C63, 181 (1994).

[78] P. Abreau et al., Nucl. Phys. B444, 3 (1995).

[79] D. Buskulic et al., Z. Phys. C66, 355 (1995).

[80] H. Aihara et al., Phys. Rev. Lett. 61, 1263 (1988).

[81] H. Albrecht et al., Z. Phys. C44, 547 (1989).

[82] "Momentum Distribution of Charged Particles in Dijet Events in $p\bar{p}$ Collisions at $\sqrt{s} = 1.8\ TeV$ and Comparisons to Perturbative QCD Predictions", Phys. Rev. D65,092002(2002)

[83] "Charged Particle Multiplicity in $p\bar{p}$ Collisions at $\sqrt{s} = 1.8\ TeV$", Phys. Rev. Letters 87,211804(2001) the Resummed Perturbative QCD", 2001

[84] Valeria Tano CDF note 5757

[85] Anwar Bhatti, Eve Kovacs, Joey Huston, Valeria Tano CDF note 5600

[86] Anwar Bhatti, Joey Huston, Eve Kovacs, Valeria Tano CDF note 5214

[87] "Charged Jet Evolution and the Underlying Event in Proton-Antiproton Collisions at 1.8 TeV", Phys. Rev. D65,092002(2002)

[88] Rick Field CDF note 5746

[89] Rick Field CDF note 5245

[90] CDF collaboration, CDF detector simulator QFL v3.59
$\sqrt{s} = 1.8$ TeV", 1998

ProQuest
Start here.
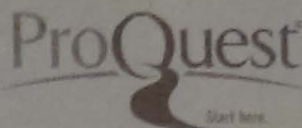
2017 ProQuest Distribution Agreement

Agreement is between the author (Author) and ProQuest LLC, through its ProQuest Dissertation Distribution business (formerly
Quest/UMI). Under this Agreement, Author grants ProQuest certain rights to preserve, archive and distribute the dissertation or thesis (the
k), abstract, and index terms provided by Author to ProQuest.

tion I. License for Inclusion of the Work in ProQuest Publishing Program

nt of Rights. Author hereby grants to ProQuest the non-exclusive, worldwide right to reproduce, distribute, display and transmit the Work (in
le or in part) in such tangible and electronic formats as may be in existence now or developed in the future. Author further grants to ProQuest
right to include the abstract, bibliography and other metadata in the ProQuest Dissertations & Theses database (PQDT) and in ProQuest
ertation Abstracts International and any successor or related index and/or finding products or services.

Quest Publishing Program - Election and Elements. The rights granted above shall be exercised according to the publishing option selected by
hor in Section III, Author Options, and subject to the following additional Publishing Program requirements:

Distribution of the Work. Except as restricted by Author in the publishing option selected, the rights granted by Author automatically include
(1) the right to allow sale and distribution of the Work, in whole or in part, by ProQuest and its sales agents and distributors and (2) the right
to make the Abstract, bibliographic data and any meta data associated with the Work available to search engines and harvesters.

Restrictions. ProQuest will use commercially reasonable efforts to restrict the distribution of the Work as provided under the publishing option
selected by Author or as later elected by Author through direct contact with ProQuest. Such election is subject to Author's Degree Granting
Institution Directives. With respect to restrictions requested after submission of the Work, Author acknowledges that ProQuest cannot recall
or amend previously distributed versions of the Work.

Removal of Work from the Program. ProQuest may elect not to distribute the Work if it believes that all necessary rights of third parties have
not been secured. Refer to the website http://www.proquest.com/products_umi/dissertations/ for information about copyright and your
dissertation or thesis. If Author's degree is rescinded, and/or the degree-granting institution so directs, ProQuest will expunge the Work from
its publishing program in accordance with its then current publishing policies.

Degree Granting Institution Directives. Author is solely responsible for any conflict between policies and directions of Author's degree-granting
institution, Author's choice of publishing model, and/or any restriction Author places on the use of the Work. For the avoidance of doubt,
ProQuest is not responsible for access to the Work that is provided by Author's degree-granting institution through its library or institutional
repository. Author must work directly with Author's degree granting institution to ensure application of any restrictions to access relating to
the Work by Author's degree granting institution.

elivery of the Work. Author shall provide to ProQuest the Work and all necessary supporting documents during the online submission process,
cording to the Instructions accompanying this agreement.

ghts Verification. Author represents and warrants that Author is the copyright holder of the Work and has obtained all necessary rights to permit
oQuest to reproduce and distribute third party materials contained in any part of the Work, including all necessary licenses for any non-public
ird party software necessary to access, display, and run or print the Work. Author is solely responsible and will indemnify ProQuest for any third
arty claims related to the Work as submitted for publication.

pen Access Publishing Plus
☐ I want the broadest possible dissemination of my work, and I want to provide free global access to the electronic copy of my
work via the internet.
☑ I understand that I will not be eligible to receive royalties.

want major search engines (e.g. Google, Yahoo) to discover my work. Learn more: http://www.proquest.com/en-
s/products/dissertations/google.shtml
☑ Yes
☐ No

cknowledgment. I have read, understand and agree to this ProQuest Publishing Agreement, including all rights and restrictions included within
he publishing option chosen by me as indicated above.

Date __07/07/17__

EQUIRED Author's signature __Dr. Justn Lancaster__

Print Name) __Dr. Justin Lancaster__

nstitution conferring degree __Duke University__